ELASTO-CAPILLARITY: COUPLING OF INTERFACE STRESS AND ELASTICITY

A Dissertation

Presented to the Faculty of the Graduate School

of Cornell University

In Partial Fulfillment of the Requirements for the Degree of

Doctor of Philosophy

by

Tianshu Liu

January 2017

© 2017 Tianshu Liu

ELASTO-CAPILLARITY: COUPLING OF INTERFACE STRESS AND ELASTICITY

Tianshu Liu, Ph. D.

Cornell University 2017

This dissertation studies several elasto-capillary phenomena. We first experimentally demonstrate that the coupling of familiar liquid/air interface tension and elasticity can be used to drive droplet motion. Specifically, we show that droplets placed on different sides of a thin elastic film tend to repel each other. An evaluation of the intermediate state energy is carried out to explain the phenomenon and a "satellite" droplet pattern is designed and observed. In a separate experiment, we put a droplet on a fibrillar structure terminated by a thin film and find that the droplet move spontaneously and chaotically. The surface tension of the droplet cause a significant deformation of the substrate and generate a periodic driving force. This periodic driving force together with evaporation induce an instability of the droplet that cause the spontaneous chaotic motion.

The second part of this dissertation aims to extend the classical adhesive contact and fracture mechanics theory to include the effect of surface tension. Specifically, we consider the contact between a rigid spherical/cylindrical indenter and an elastic substrate. The surface of the substrate has both adhesion and surface stress included. We also study the effects of surface tension on mode-I cracks and find that the linearization of curvature is not valid near the crack tip because of the singularity. Using an asymptotic analysis, we show that surface tension can reduce the energy release rate which is consistent with our own finite element calculations.

Finally, we consider the effect of solid surface stress on problems with large deformation. A closed-form large deformation solution is found for the pure bending of a long plate. We find that surface stress can significantly increase the bending stiffness and we also discover an instability under load control. In Chapters 8 and 9, we use a large deformation finite element method to study the effect of surface stress on a penny-shaped crack inflated by internal pressure and the contact between a rigid circular punch and an elastic substrate. Our results suggest that surface stress can resist deformation and reduce energy release rate.

BIOGRAPHICAL SKETCH

Tianshu Liu was born in Beijing, P. R. China. He spent his first 22 years in his hometown. He received a bachelor degree in Engineering Mechanics and Aerospace Engineering from Tsinghua University. After graduation from college, he came to Ithaca to start his graduate studies in the field of Theoretical and Applied Mechanics at Cornell University and expects to complete his Ph.D. in Jan 2017. Upon completion of his program at Cornell, Tianshu Liu will join Hyperloop One as a structural analyst to bring the future of transportation into reality.

To my mom, for her support and love.

ACKNOWLEDGMENTS

I would like to first express my sincerest gratitude to my advisor, Prof. Chung-Yuen Hui, for his support and invaluable guidance throughout my Ph.D. research. It is enjoyable to work with him and I learned a lot from him, from critical thinking to technical writing. He always encourage me to pursue the direction of research that I am interested in and provide valuable suggestions that help me bring an idea into a complete research. Besides academic advisor, he is also a true friend. The Thanksgiving dinners he cooked is always the most enjoyable meal of the year and we spent quite some time on discussing how to improve the skills of table tennis.

I would like to thank Prof. Anand Jagota from Lehigh University. He provided a lot of great insights and suggestions for most of my research. I spent a summer doing experiments in his lab where I learned most of the experimental skills I have so far. The discussion with him helped me establish a much better intuition and greatly improved the quality of this dissertation. I am also thankful to Prof. Paul Steen and Prof. Charles Williamson for serving in my committee and advising me about courses and research.

I also need to thank all my group mates, Jing, Abhishek, Xuejuan, Xinzeng, Pankaj, Jingyi and Haibin. Through the discussion with them, I have a better understanding of some basic mechanics and mathematical concepts. Thanks are also due to my friends, Huichan, Yuxing, Zhe, Yi, Lin, Liang, Xuetian, Julia and Saien without whom my graduate life would not be so enjoyable.

I wish to take this opportunity to express my deepest thanks and gratitude to my mom. Without her love and constantly supporting me of pursuing what I like, I would not become who I am today. During my time at Cornell, I am so lucky that I meet my girl friend, Yishuo, who always support me by offering her company, encouragement and confidence in me.

Finally, I would also like to acknowledge the sources of financial support that have made my graduate studies possible. I first need to thank Department of Mechanical and Aerospace Engineering for offering me Fellowships and Teaching Assistantships. Support through Research Assistantships from U.S. Department of Energy are also acknowledged.

TABLE OF CONTENTS

BIOGRAPHICAL SKETCH v
ACKNOWLEDGMENTS vii
TABLE OF CONTENTS ix
LIST OF FIGURES xii
PREFACE xxii
CHAPTER 1 INTRODUCTION 1
REFERENCES 6
CHAPTER 2 INTERACTION OF DROPLETS SEPARTED BY AN ELASTIC FILM 9
2.1 Introduction 9
2.2 Methods 11
2.3 Experiments: Interaction of two droplets 12
2.4 Energy landscape and stability of the droplet pair 14
2.5 Satellite droplet pattern 20
2.6 Conclusion and Discussion 22
APPENDIX 2.1 ENERGY LANDSCAPE CALCULATION 23
REFERENCES 28
CHAPTER 3 SPONTANEOUS DROPLET MOTION ON A PERIODIC COMPLIANT STRUCTURE 32
3.1 Introduction 32
3.2 Experimental Results 34
3.3 Model for droplet motion 37
3.4 Conclusion and discussion 44
3.5 Methods 45
APPENDIX 3.1 1-D MODEL SET-UP 47
APPENDIX 3.2 TRAJECTORIES AND VELOCITY DISTRIBUTION FOR SAMPLES WITH DIFFERENT FIBRIL HEIGHT AND SPACING 54
REFERENCES 68
CHAPTER 4 INDENTATION OF A RIGID SPHERE INTO AN ELASTIC SUBSTRATE WITH SURFACE TENSION AND ADHESION 70
4.1 Introduction 70
4.2 Statement of Problem and Summary of Approach 72
4.2.1 The JKR limit 74
4.2.2 The surface tension dominated or the partial wetting liquid-like limit 75
4.2.3 Comparison between the JKR limit and the partial wetting liquid-like limit 77
4.3 General case: transition between JKR and partial wetting liquid-like limits: 79
4.3.1 Determination of P_H, δ_H and C 79
4.3.2 Asymptotic results 81
4.3.3 General relation between load and contact radius for the adhesive problem 83
4.3.4 Numerical results: $\bar{P}_H(\beta), \bar{\delta}_H(\beta), \phi(\beta)$ and $\Lambda\ \beta$ 84

4.3.5 Pull-off and zero load cases 87
4.3.6 Contact radius versus applied load 88
4.3.7 Indentation depth versus contact radius 89
4.4 Comparison with experiments 91
4.5 Summary and discussion 93
APPENDIX 4.1 NUMERICAL IMPLEMENTATION 95
APPENDIX 4.2 DERIVATION OF EQUATIONS (4.20) AND (4.28) 98
REFERENCES 99
CHAPTER 5 ADHESIVE CONTACT OF A RIGID CIRCULAR CYLINDER TO A SOFT ELASTIC SUBSTRATE – THE ROLE OF SURFACE TENSION 101
5.1 Introduction 101
5.2 Statement of Problem and Summary of Approach 104
5.2.1 The elasticity dominated limit 107
5.2.2 The surface tension dominated limit 108
5.3 Transition between the elasticity and surface-tension-dominated limits 110
5.3.1 Formulation of the Hertz problem with surface tension 110
5.3.2 Determination of P_H and $\Lambda_H = -dC/da$ 113
5.3.3 Extended JKR theory with surface tension 116
5.4 Summary and discussion 119
APPENDIX 5.1 NUMERICAL IMPLEMENTATION 122
APPENDIX 5.2 CALCULATION OF $\overline{\Lambda_H}$ 124
REFERENCES 126
CHAPTER 6 HOW DOES SURFACE TENSION AFFECTS ENERGY RELEASE RATE OF CRACKS LOADED IN MODE I? 129
6.1 Introduction 129
6.2 Formulation and analysis 133
6.3 Discussion 136
APPENDIX 6.1 ASYMPTOTIC BEHAVIOR OF (6.13) 140
REFERENCES 143
CHAPTER 7 A CLOSED FORM LARGE DEFORMATION SOLUTION OF PLATE BENDING WITH SURFACE EFFECT 145
7.1 Introduction 145
7.2 Large deformation surface elasticity 147
7.2.1 Kinematics: Surface deformation gradient 147
7.2.2 Constitutive Model 148
7.2.3 Isotropic surface 150
7.2.4 Linearized theory – Classical Shuttleworth equation 152
7.2.5 Indicial form for given curvilinear coordinates 153
7.3 Bending of a plate with finite thickness 155
7.4 Results and discussion 160
7.5 Summary and conclusions 167
REFERENCES 170

CHAPTER 8 ENERGY RELEASE RATE OF A PENNY-SHAPED CRACK SUBJECTED TO INTERNAL PRESSURE: EFFECT OF SURFACE TENSION AND LARGE DEFORMATION 173
8.1 Introduction 173
8.2 Geometry and derivation of Energy Release Rate 177
8.3 Finite Element Method 181
8.4 Results 183
8.5 Approximation for energy release rate 188
8.6 Summary and discussion 190
REFERENCES 193
CHAPTER 9 EFFECT OF SURFACE TENSION ON THE ADHESION BETWEEN A RIGID FLAT PUNCH AND A SEMI-INFINITE NEO-HOOKEAN HALF-SPACE 195
9.1 Introduction 195
9.2 Statement of problem 196
9.2.1 Problem definition 196
9.2.2 Limiting cases: Elasticity and Liquid-like limit 198
9.3 Finite Element (FE) Method 201
9.4. Calculation of energy release rate G 203
9.5 Numerical Results 204
9.6. Discussion and summary 210
9.6.1 Discussion 210
9.6.2 Summary 212
APPENDIX 9.1 INDENTATION BEHAVIOR 214
APPENDIX 9.2 DERIVATION OF ENERGY RELEASE RATE 217
APPENDIX 9.3 PULL-OFF LOAD AND DISPLACEMENT NORMALIZATION 218
APPENDIX 9.4 COMPARISON WITH KARPITSCHA ET AL. 219
CHAPTER 10 CONCLUSIONS AND FUTURE WORK 224
REFERENCES 226

LIST OF FIGURES

Fig. 2.1 Schematic side view of the supported-film sample. Both film and support are made of Vinyl Polysiloxane (VPS). The film has a diameter of 8mm and a thickness of 20.5μm……..12

Fig. 2.2 Process of repulsion between two droplets on either side of a VPS film. (a) Using an air displacement pipette, a DI droplet was placed underneath the film, and the film bulged out due to the Laplace pressure *P* (see insert). (b) Another DI droplet of same volume was placed on the top side of the film, overlapping the bottom droplet. (c) The configuration in (b) was unstable and the two droplets separated. (d) Snapshot of the initial (unstable) overlapped configuration (top view). (e) Snapshot of the stable configuration with a small overlap (top view)…….....13

Fig. 2.3 (a) Initial configuration of the two drops in which $2c_r$ is the equilibrium contact width at zero separation. The film has no deformation as the Laplace pressure and surface tension at the contact line from two droplets cancel each other. (b) Configuration of two separated droplets. Part 1 is identical to part 5 and part 2 is identical to part 6 due to symmetry…….……..16

Fig. 2.4 (a) Total energy of the system vs a/c_r for different elasto-capillary number β. The local energy minimum is achieved when $a/c_r \approx 1.77$ for $\beta = 0.1$, and 1.75 for $\beta = 1$. (b) Minimum energy configuration for $\beta = 0.1$. The red line is the thin film and the blue line is the surface of the droplets……..19

Fig. 2.5 (a) Schematic of the experimental setup. The glass beaker was heated to increase the evaporation rate, and the sample together with a droplet was held by two glass slides on top of the glass beaker. Small droplets condensed on the bottom of the

film due to evaporation (not shown in figure) (b) Satellite droplet pattern: four "satellite" droplets underneath the film formed around the top droplet……....21

Fig. A2.1 Parameter θ_1^* and θ_2^* can be used to determine the parameter equation of arc 1 and 2……...24

Fig. A2.2 Energy landscape for $\bar{a} = 1.5,\ \beta = 0.1$……26

Fig. 3.1 Droplet on a film-terminated fibrillar surface. (a-d) Beginning at $t = t_0$, micrographs of a droplet of de-ionized water placed atop a film-terminated fibrillar surface show (i) significant distortion of interferometric contours, indicating out-of-plane deformation driven by liquid surface tension, and (ii) spontaneous movement of the droplet. In this series of optical micrographs, the droplet moves over a distance much larger than its own size and the interfibrillar distance. (e) Scanning electron micrograph image of the film-terminated fibrillar surface. (f) A schematic showing a droplet on the structured surface, and the deformation caused by droplet surface tension. The experiments are repeated on samples with height h varied from 10 – 40 μm and interfibrillar spacing a varied from 20 – 110 μm. (g) Contours and 3D representation of the vertical displacement of the substrate caused by surface tension of the drop…….34

Fig. 3.2 (a) Trajectories and (b) velocities of the droplet centroid for different drops placed on the same substrate. Different colors correspond to different experiments. The fibril spacing a is 20 μm and the fibril height is 10 μm. Measured trajectories for samples with different fibril spacing and fibril heights are given in the SI. The circular markers are centered at the droplet's centroid. The marker size is proportional to the contact area of the drop, thus showing how the drop shrinks by evaporation. The time between two consecutive markers is 3 sec. For a specific region of the sample, the

experiments could only be repeated about 3-7 times, after which new droplets lost their ability to move. This is likely due to the deposition of some impurities during droplet drying, which increases the contact angle hysteresis……....36

Fig. 3.3 Schematic of a cross-section of a droplet on a periodic surface, which consists a thin film on top of identical fibrils, with interfibrillar spacing *a*. The contact line on the left causes little deformation since it lies directly on top of a fibril, where the film is least compliant. In contrast, the contact line on the right lies between two ridges, where the film is most compliant. Note that since the contact line can move, the contact angle at A can be fixed at θ_c while θ decreases at *B* without violating volume conservation. Surface tension pulls the film upward, thereby deforming the structure surface. This uplifting reduces the apparent contact angle, and the difference in contact angle at the two contact lines provides a driving force to move the drop…….38

Fig. 3.4 (a) The blue lines and red lines represent locations of the droplet center of mass that are stable and unstable, respectively. The black arrows represent the velocity of the center of mass (dX_{cm}/dt) if it deviates from the stationary point. (b) Potential energy landscape (red denotes high potential and blue low potential)…….42

Fig. A3.1.1 Evaporating droplet is modeled as two *point* masses connected by a shrinking spring of stiffness k_s with decreasing equilibrium length $l(t)$. Periodic variation of substrate stiffness causes a periodic force (with period *a*) $F(x)$ acting on the masses where $F_1 = F(x_1)$ and $F_2 = F(x_2)$ ……48

Fig. A3.1.2 (a), (b) The motion and velocity of droplet center of mass for $\epsilon = 0.001$. Note here that since L represents a backward time variable (see (A3.1.3)), $\frac{dX_{CM}}{dL}$ is a

measure of velocity. (c), (d) The motion and velocity of droplet center of mass for $\epsilon = 0.5$ ……...51

Fig. A3.2.1 (10.20) – (30.125)…….55-67

Fig. 4.1 A rigid sphere of radius R is indented by a vertical force P, bringing it into no-slip contact with the surface of an incompressible isotropic elastic half-space. The indentation is resisted by the elasticity of the substrate as well as the substrate-air surface tension σ ……..73

Fig. 4.2: Free body diagram showing the forces acting on the sphere in the partial wetting liquid-like limit……..……..76

Fig. 4.3(a), (b) Normalized contact radius versus normalized indentation load for the JKR limit and the partial wetting liquid-like limit. Insets show different scaling behaviors. Note that load is normalized differently in (a) and (b). The inserts in these figures show different scaling behaviors……..…78

Fig. 4.4 The vertical axis is the ratio of the Hertz like load/displacement with surface tension to the classical Hertz load/displacement without surface tension. The horizontal axis is the normalized surface tension β. These figures quantify the deviation from classical Hertz theory due to air-substrate surface tension. (a) Normalized Hertz-like load $\bar{P}_H$ against β (b) Normalized Hertz-like displacement $\bar{\delta}_H$ against β ……..…85

Fig. 4.5 Dimensionless compliance $\phi(\beta)$ and $\Lambda(\beta)$ versus β ……....86

Fig. 4.6 (a) Normalized contact radius at pull-off versus ω. (b) Normalized pull-off force versus ω. The pull-off radius and load of the elastic limit are calculated using (4.10a) and (4.10b)……88

Fig. 4.7 Normalized contact radius versus normalized load for different ω ……89

Fig. 4.8 Normalized contact radius versus normalized indentation depth for 4 different elasto-capillary numbers. Curves are generated using (4.30b) and (4.33) with $\bar{W}_{ad} = 0.1$. For $\omega = 0.001$ the JKR solution and the prediction given by (4.33) lies on top of each other……..…..90

Fig. 4.9 Normalized load versus normalized indentation depth for different α with $\bar{W}_{ad} = 0.1$. Note that JKR and the solution for $\alpha = 0.001$ lies on top of each other.....90

Fig. 4.10 Comparison with experimental data of Style *et al*. [5]. Symbols are experimental data. Solid lines are predictions based on small deformation theory with air-substrate surface tension. Dotted lines are based on small deformation theory without surface tension. Prediction of large strain solution in partial wetting liquid-like limit (4.34) is shown as a dashed-dotted line. The parameters used for these fits are based on the paper by Xu *et al.* [6]……..……...92

Fig. A.4.1.1 Pressure distributions for different β ……..…..96

Fig. 5.1 A long rigid cylinder of radius *R* and length *L* >> *R* indents an isotropic and incompressible elastic half-space under the influence of a vertical line force *P*……104

Fig. 5.2 Force balance and geometry in the surface tension limit……...109

Fig. 5.3 Normalized Hertz-like load $\bar{P}_H$ versus normalized surface tension β. In this plot, the numerical solution is indistinguishable from (5.29). This result matches well with the results of Long *et al*. [33], and here a fitted formula is provided……115

Fig. 5.4 Normalized contact radius versus normalized indentation force for different values of ω……117

Fig. 5.5 (a) Normalized pull-off load versus ω (b) Normalized contact half width versus ω……118

Fig. A5.2.1 $\overline{\Lambda_H}$ vs elasto-capillary number……...124

Fig. 7.1 Thermodynamic analysis for an arbitrary region of surface in the reference configuration. Unit vector **v** are tangent to the surface but normal to the boundary. η and ω are the entropy and heat from the bulk or environment and **q** is the heat flow to the adjacent surface..……...…....148

Fig. 7.2 (a) Cross-section plot for the reference configuration of a finite thickness plate, axis X^3 is perpendicular to the plane. (b) Cross-section plot for the deformed configuration of the plate…….……...……156

Fig. 7.3 Normalized moment versus normalized curvature. (a) surface stress is a constant. (b) surface stress linearly depends on surface strain with different surface stiffness.……..161

Fig. 7.4 (a) Schematic of the cross-section stress distribution, the two line forces represent surface stress. By removing the skin which carries surface stress, a radial traction (Laplace pressure) is felt on the surface of the remaining solid. (b) Circumferential stress distribution for different value of residue isotropic surface stress

at fixed curvature $\bar{\kappa}=1.5$ with surface stiffness $\overline{k_s}=0$. (c) Radial stress distribution for different value of residue isotropic surface stress at fixed curvature $\bar{\kappa}=1.5$ with surface stiffness $\overline{k_s}=0$ (d) Plate thickness decreases with bending curvature. Note that when there is residue surface stress, the plate is thicker than the un-deformed plate even at zero curvature. This is because the plate is under compression due to surface stress……..…….…….164

Fig. 7.5 Stress distribution for different value of surface stiffness. The curvature $\bar{\kappa}$ is fixed to be 1.5 and residue surface stress $\overline{\sigma_0}=0.5$ (a) circumferential stress component distribution (b) radial stress distribution…….. ……...165

Fig. 7.6 On $\bar{r}=\bar{r}_2$, $\overline{\sigma_0}=\overline{k_S}=0$, on $\bar{r}=\bar{r}_1$, $\overline{\sigma_0}>0$ while $\overline{k_S}=0$. (a) The normalized equilibrium curvature $\overline{\kappa_0}$ increase with $\overline{\sigma_0}$ on $\bar{r}=\bar{r}_1$ surface. (b) Schematic of bulk stress distribution induced by the self-bending…….…….. ……...167

Fig. 8.1 Surface tension on crack face……....177

Fig. 8.2 Schematic of the mechanical loading process……...179

Fig. 8.3: The geometry and boundary conditions used in our finite element calculation. All lengths are normalized by initial crack radius *a*. The right and upper boundaries are traction free. Symmetry boundary conditions are applied on the left and lower boundaries. Internal pressure and surface tension are applied on crack faces……....182

Fig. 8.4 Mesh used in our FEM calculation: (a) mesh of the full model. (b) zoom-in view of the original coarse mesh near the crack tip. (c) Re-mesh on deformed configuration……...……183

Fig. 8.5 (a) Normalized crack volume versus elasto-capillary number ω for different pressures. (b) Crack opening displacements for different elasto-capillary numbers when $p = 0.5E$ ……..184

Fig. 8.6 (a) Normalized crack volume versus elasto-capillary number ω for $P = 0.02E$. (b) Crack opening displacements for different elasto-capillary numbers when $P = 0.02E$ ……186

Fig. 8.7 Change of normalized energy release rate with respect to normalized pressure for different elasto-capillary number……..187

Fig. 8.8 Change of normalized energy release rate with respect to elasto-capillary number for different normalized pressure……...…187

Fig. 8.9 Normalized energy release rate versus normalized pressure $\bar{P}$, when $\omega = 0$ ……...189

Fig. 8.10 $s\left(\bar{P}\right) = \partial\Gamma / \partial\omega\big|_{\omega=0}$ versus normalized pressure $\bar{P}$ ……190

Fig. 9.1 the contact between a rigid punch with radius *a* and a semi-infinite elastic half-space under retraction P. The retraction displacement is Δ, and the contact angle between the substrate-air interface and the punch bottom is denoted by θ ……...197

Fig. 9.2 During retraction, the edge of contact can be seen as the front of an external interface crack. This is because the indenter is rigid, so changing its shape outside the contact zone does not affect the stress and strain field in the substrate. ……..…199

Fig. 9.3 Deformed shape of the substrate surface (zero mean curvature surface when gravity is neglected) in the liquid like limit, θ denotes the contact angle of the contact line……...200

Fig. 9.4 A schematic of our model used in finite element calculation. All length are normalized by the punch radius. The elastic half-space is approximated by a square with length equal to 100 unit……..……202

Fig. 9.5 Near edge deformation field for retraction of punch. The gray part is the deformed shape of the substrate near the punch edge. With increase of elasto-capillary number, the substrate becomes more flat and the local contact angle becomes larger……...205

Fig. 9.6 (a) Normalized load-displacement relation for retraction of punch for three different elasto-capillary numbers. The three red lines are the corresponding SSLE results given by Wang et al [29]. (b) Comparison of stiffness with SSLE results. SSLE tends to underestimate the stiffness……206

Fig. 9.7 (a) Normalized energy release rate vs normalized load for different values of elasto-capillary number (b) Normalized energy release rate vs elaso-capillary number for different normalized load……..207

Fig. 9.8 (a) normalized pull-off load vs elasto-capillary number (b) normalized pull-off displacement vs elasto-capillary number. The curves with different normalized work of adhesion $\overline{W_{ad}} = \dfrac{\pi W_{ad}}{4Ea}$ essentially lie on top of each other……..209

Fig. 9.9 Apparent contact angle vs elasto-capillary number for $\bar{\Delta} = 1.0$ ……..……..211

Fig. A9.1.1 Scheme of a rigid punch indenting on an elastic solid, i.e. $P,\ \Delta < 0$ ..…214

Fig. A9.1.2 Near edge deformation field for indentation……...….215

Fig. A9.1.3 Normalized load-displacement relation for indentation with different elasto-capillary number……...216

Fig. A9.4.1 Comparison between the contact angle at pull-off predicted by both FEM results and liquid theory when $\overline{W_{ad}}$ is fixed to be 0.05……..220

PREFACE

Eight Chapters (2 to 9) in this dissertation were originally prepared as individual research papers. Chapter 2, 3 and 7 are based on papers that are under review. Editorial changes were made to make the writing styles consistent but some mathematical symbols may have different physical meanings for different chapters.

CHAPTER 1

INTRODUCTION

Elasto-capillarity refers to the coupling effect of interface stress and elasticity. The elastic deformation caused by liquid/vapor, solid/vapor or liquid/solid interface stress is on the order of σ / E, where σ is the magnitude of interface stress (unit of force/length) and E is the Young's modulus of the involved material. When this elasto-capillary length is comparable to the size of the structure, the effect of elasto-capillarity is significant. Therefore, it is necessary to consider interfacial stress effect for nano/micro structures [1] and soft materials [2,3]. It is also for this reason that it is very important to have a good understanding of elasto-capillary phenomena when designing MEMS/NEMS or controlling the shape of ultra-soft material such as hydrogels.

Because liquid has little resistance to shear, it is easy to observe the existence of liquid/vapor surface tension. The liquid/vapor surface stress is isotropic and hence called surface tension and can be represented by a scalar σ. It is well known that liquid/vapor surface tension and surface energy density are numerically equal even though they have completely different physical meaning [4,5]. When liquid are in contact with materials that are either soft or have a slender ratio, the materials can be significantly deformed. For example, fibers or hairs can be bent and bundled together due to water surface tension [6]; micro-structures can be deformed and damaged due to capillary forces [7]; thin planar structures can be deformed by droplet surface tension and form beautiful 3-D structures [8]; thin films or slender beams can be buckled by liquid/vapor surface tension [9,10]. More references can be found in the review paper of Roman and Bico [11]. More recently, Style et al. [12] studied the reverse effect where a gradient in substrate stiffness was used to drive the liquid drop motion. For most of the work reviewed above, the interactions between liquid and

solid structures are “one-way”, that is either surface tension can deform material or elasticity properties can affect and drive droplet motion. Here we demonstrate by two examples that this interaction can also be “two-way”, that is soft structure can be deformed by liquid/vapor surface tension and the deformation in turn will drive the motion of liquids. Chapter 2 presents the first example where we find that droplets placed on different sides of a thin film can sense and interact with each other through the elastic deformation of the film. Intuitively, this phenomenon can be understood as the droplets create an equivalent stiffness gradient which cause them to interact with each other. In our system, droplets can not coalesce since they are separated by the thin film. A second example of “two-way” interaction is given in Chapter 3. We observe that a droplet placed on a fibrillar structure terminated by a thin film can spontaneously move and cover large distances before it completely vaporize. This phenomenon is very counterintuitive as there is no overall gradient and it is unclear what drives the motion. Using a white light interferometer, we find that the film is significantly deformed by the liquid/air surface tension and the deformation is non-uniform as the parts that are supported by pillars are much stiffer than the rest. The driving force can be produced by this non-uniform deformation. Using a one dimensional shrinking droplet model, we are able to reproduce a motion that has similar features observed in our experiments. Our toy model suggests that shrinkage due to evaporation coupled with periodic potential can lead to an instability which may cause the droplets motion.

Solid/vapor or solid/liquid interface stress effects are much harder to observe as conventional materials or structures are either too stiff or too large so that the deformation induced by interfacial stresses is negligible compared with the dimension of the materials. However, this is no longer true with the development of nano/micro structures and ultra-soft materials. Compared with liquid/vapor interface stress, solid

interface stress is much more complex and less understood. In general, solid interface stress tensor is not isotropic and hence can not be represented by a scalar, it may have a shear component and can be surface strain-dependent. A formal mathematical description of solid surface stress was first proposed by Gurtin and Murdoch [13] but the subject was not extensively studied until it was experimentally observed that both the bending and tensile stiffness of a nano beam are strongly size-dependent [14–18]. This size-dependency is attributed to solid/air interface stress and a linearized beam model superimposed with a Laplace pressure caused by solid surface stress is found to be in good agreement with experiments [19–25]. More recently, ultra-soft materials such as hydro-gels can have elastic modulus as low as tens of Pascals [26]. These low modulus gels extend elasto-capillary deformation into macroscale [2,3]. For example, it is observed that a soft gel can resist contact mostly by its surface stress just like a liquid would [27]; a Rayleigh-Plateau type instability, an instability commonly seen for liquid, was observed for ultra-soft gels [28]. These experiments implies that there is a transition from solid-like to liquid-like behaviors as the modulus of solids go down. To capture this transition, it is necessary to modify the classical solid mechanics equations to include the effect of surface stress. In this dissertation, we consider how surface stress affect fracture and contact mechanics. Based on the Hertz contact theory with solid surface tension [29,30], we extend the well-known Johnson-Kendall-Robert (JKR) theory to regimes where surface stress are important [31,32]. Our results fit very well with Style et al's experimental data [27] even though small deformation and linear elasticity are assumed in our theory. In Chapter 6, we presents an asymptotic analysis for a mode-I crack with surface stress effect. We point out that a linearization of curvature at crack tip is not possible due to the singularity. By keeping the nonlinear curvature term, we are able to show that surface stress can decrease but not

necessarily cancel the energy release rate. This result is consistent with the conclusion of our finite element simulation [33].

For ultra-soft gels, the deformation is naturally large. The small deformation theory, though useful in understanding the physics, in general can not be used to quantitatively predict the deformed shape of a soft solid. Using an analog to 3-D elasticity, a surface constitutive law can be established from thermodynamic inequalities [34–41]. Combine the constitutive law with kinematics and equilibrium equations set up by Gurtin and Murdoch [13], one can formulate the effect of surface stress as the boundary conditions of a 3-D elasticity problem. Even though the problem can be analytically formulated, solving the nonlinear governing equations is not trivial as the principle of superposition is no longer valid. In Chapter 7, we consider the pure bending of a plate with finite thickness. With plane strain assumption, we find an analytical solution of this problem. In our model, we assume that the surface stress consists a residue isotropic tension and a part that is linearly proportional to the stretch of the surface. We found that both the residue tension and surface stiffness can increase the overall bending stiffness of the plate. The possibility of self-bending due to un-symmetric surface behavior is also explored. For a general elasticity problem with large deformation and surface stress, it is impossible to obtain an analytical solution and a finite element solution is necessary. In Chapters 8, we present a large deformation calculation for a penny-shaped crack. The surface stress is implemented by a user-defined surface element and a re-mesh technique is used to guarantee the convergence and accuracy of the calculation. We find that the presence of surface stress can decrease energy release rate and hence makes it harder for crack propagation. Furthermore, the energy release rate can be even negative when surface stress is sufficiently large. In Chapter 9, we use a similar finite element technique to study the contact between a rigid circular punch and a semi-infinite substrate. Our

results show that the linearized solution can not correctly capture the deformation near the contact line. We further show that the local “contact angle” at the contact line is quite sensitive to the magnitude of surface stress. This property can be used to measure the solid surface stress when it is small compared with elastic modulus.

REFERENCES

[1] J. Wang, Z. Huang, H. Duan, S. Yu, X. Feng, G. Wang, W. Zhang, and T. Wang, Acta Mech. Solida Sin. **24**, 52 (2011).

[2] R. W. Style, A. Jagota, C.-Y. Hui, and E. R. Dufresne, (2016).

[3] B. Andreotti, O. Baeumchen, F. Boulogne, K. E. Daniels, E. R. Dufresne, H. Perrin, T. Salez, J. H. Snoeijer, and R. W. Style, Soft Matter **12**, 2993 (2016).

[4] R. W. Style, A. Jagota, C.-Y. Hui, and E. R. Dufresne, (2016).

[5] C.-Y. Hui and A. Jagota, Langmuir **29**, 11310 (2013).

[6] J. Bico, B. Roman, L. Moulin, and A. Boudaoud, Nature **432**, 690 (2004).

[7] T. Tanaka, M. Morigami, and N. Atoda, Jpn. J. Appl. Phys. **32**, 6059 (1993).

[8] D. H. Gracias, V. Kavthekar, J. C. Love, K. E. Paul, and G. M. Whitesides, Adv. Mater. **14**, 235 (2002).

[9] J. Huang, M. Juszkiewicz, W. H. de Jeu, E. Cerda, T. Emrick, N. Menon, and T. P. Russell, Science (80-.). **317**, (2007).

[10] S. Neukirch, B. Roman, B. de Gaudemaris, and J. Bico, J. Mech. Phys. Solids **55**, 1212 (2007).

[11] B. Roman and J. Bico, J. Phys. Condens. Matter **22**, 493101 (2010).

[12] R. W. Style, Y. Che, S. J. Park, B. M. Weon, J. H. Je, C. Hyland, G. K. German, M. P. Power, L. A. Wilen, J. S. Wettlaufer, and E. R. Dufresne, Proc. Natl. Acad. Sci. U. S. A. **110**, 12541 (2013).

[13] M. Gurtin and A. Ian Murdoch, Arch. Ration. Mech. Anal. **57**, (1975).

[14] K. Babaei Gavan, H. J. R. Westra, E. W. J. M. van der Drift, W. J. Venstra, and H. S. J. van der Zant, Appl. Phys. Lett. **94**, 233108 (2009).

[15] G. Y. Jing, H. L. Duan, X. M. Sun, Z. S. Zhang, J. Xu, Y. D. Li, J. X. Wang, and D. P. Yu, Phys. Rev. B **73**, 235409 (2006).

[16] S. Cuenot, C. Frétigny, S. Demoustier-Champagne, and B. Nysten, Phys. Rev.

B **69**, 165410 (2004).

[17] K. R. Pirota, E. L. Silva, D. Zanchet, D. Navas, M. Vázquez, M. Hernández-Vélez, and M. Knobel, Phys. Rev. B **76**, 233410 (2007).

[18] C. Q. Chen, Y. Shi, Y. S. Zhang, J. Zhu, and Y. J. Yan, Phys. Rev. Lett. **96**, 75505 (2006).

[19] J. He and C. M. Lilley, Nano Lett. **8**, 1798 (2008).

[20] J. He and C. M. Lilley, Appl. Phys. Lett. **93**, 263108 (2008).

[21] G.-F. Wang and X.-Q. Feng, J. Phys. D. Appl. Phys. **42**, 155411 (2009).

[22] G.-F. Wang and X.-Q. Feng, Appl. Phys. Lett. **94**, 141913 (2009).

[23] Z.-Q. Wang, Y.-P. Zhao, and Z.-P. Huang, Int. J. Eng. Sci. **48**, 140 (2010).

[24] G. Yun and H. S. Park, Phys. Rev. B **79**, 195421 (2009).

[25] R. Ansari and S. Sahmani, Int. J. Eng. Sci. **49**, 1244 (2011).

[26] A. Chakrabarti and M. K. Chaudhury, Langmuir **30**, 4684 (2014).

[27] R. W. Style, C. Hyland, R. Boltyanskiy, J. S. Wettlaufer, and E. R. Dufresne, Nat. Commun. **4**, 2728 (2013).

[28] S. Mora, T. Phou, J. M. Fromental, L. M. Pismen, and Y. Pomeau, Phys. Rev. Lett. **105**, 214301 (2010).

[29] J. M. Long and G. F. Wang, Mech. Mater. **56**, 65 (2013).

[30] J. M. Long, G. F. Wang, X. Q. Feng, and S. W. Yu, Int. J. Solids Struct. **49**, 1588 (2012).

[31] C.-Y. Hui, T. Liu, T. Salez, E. Raphael, and A. Jagota, Proc. R. Soc. A Math. Phys. Eng. Sci. **471**, 20140727 (2015).

[32] T. Liu, A. Jagota, and C.-Y. Hui, Soft Matter (2015).

[33] T. Liu, R. Long, and C.-Y. Hui, Soft Matter **10**, 7723 (2014).

[34] G. Yun and H. S. Park, Comput. Methods Appl. Mech. Eng. **197**, 3337 (2008).

[35] A. Papastavrou, P. Steinmann, and E. Kuhl, J. Mech. Phys. Solids **61**, 1446

(2013).

[36] A. Javili and P. Steinmann, Comput. Methods Appl. Mech. Eng. **198**, 2198 (2009).

[37] A. Javili and P. Steinmann, Comput. Methods Appl. Mech. Eng. **199**, 755 (2010).

[38] P. H. Saksono and D. Perić, Comput. Mech. **38**, 251 (2005).

[39] P. H. Saksono and D. Perić, Comput. Mech. **38**, 265 (2005).

[40] Z. P. Huang and J. Wang, Acta Mech. **182**, 195 (2006).

[41] X. Gao, Z. Huang, J. Qu, and D. Fang, J. Mech. Phys. Solids **66**, 59 (2014).

CHAPTER 2

INTERACTION OF DROPLETS SEPARTED BY AN ELASTIC FILM[1]

2.1 Introduction

The ability to manipulate and transport droplets is important in a variety of industrial applications such as micro-fluidic devices [1–3] and self-cleaning surfaces [4–6]. Motion of individual droplets on a surface by the Marangoni effect [7] typically requires some form of spatially varying surface tension force [7] which can be achieved by gradients of geometry [8,9] or interfacial energy [10]. There are various ways to create a gradient in interfacial energy, from chemical [11–16] to electrical [17] and thermal [18–22]. However, these mechanisms require careful preparation of the surface or substrate. Recently, Cira *et al*. have demonstrated that two-component droplets of well-chosen miscible liquids can sense and move in response to the vapor emitted by neighboring droplets [23], with no other gradient on the surface.

For the phenomena discussed above, the substrate is basically un-deformable and there is little interaction between droplets unless they make contact. A contrasting situation is one in which rigid particles float on a liquid. In this case, particles distort the liquid-vapor interface, leading to long range interactions, a phenomenon dubbed the "Cheerios effect" because of the common observation that toruses of the breakfast cereal by that name tend to agglomerate [24]. Related phenomena have recently been reported in which rigid particles placed in very soft but solid gels exhibit long-range interaction [25]. When a liquid drop is placed on a soft solid, recent experiments and theories have shown that capillary force can significantly deform soft materials, such as elastomers and hydrogels [26–30]. The large deformation caused by liquid drops themselves can provide a driving force for drop transportation. This mechanism was

[1] Liu T. , Xu X., Nadermann N., He Z., Jagota A., Hui C.Y., (2016) submitted to Langmuir

first proposed by Style *et al*. [31] where they created a gradient of substrate stiffness by changing its thickness. In their experiments, they found the droplets prefer to move toward a softer substrate where the local apparent contact angle is lower. This idea was further pursued by Karpitschka *et al.* who reported both attraction and repulsion between droplets on a soft elastic substrate, depending on the thickness of the substrate solid [32], a reverse Cheerios effect [33]. To explain their observation, they computed the deformed shape of the substrate using a small strain linear elasticity theory and found that the imbalance of surface tension in horizontal direction provides the driving force.

High substrate deformation in the forgoing examples is achieved by using compliant materials; it can also be achieved using a relatively stiffer material but with slender aspect, such as a thin film [26,34–40] or a slender rod [41,42]. In this work, we show that droplets placed on a uniform thin film can sense and move in response to the deformation of the film caused by the droplets on the other side of the film. This interaction mechanism results in droplet motion without chemical modification of surfaces, nor is it necessary to have two-component droplets. The droplets are separated by an impermeable thin elastic film which prevents them from coalescing. Further to demonstrate this mechanism, we designed and experimentally observed a "satellite" droplet pattern where a larger droplet on one side of the film is surrounded by a series of droplets on the other side. A full, large-deformation, analysis of the total system energy landscape is conducted to establish a quantitative basis for droplet interaction and stability.

The new mode of droplet interaction we report here can also be intuitively understood as being driven by droplets seeking a softer regions of the substrate. However, unlike the results of Style *et al.* [31], in which individual droplets move on an externally created stiffness gradient, the phenomenon we report is active only for

interaction between two or more droplets where each droplet moves in the effective potential energy landscape created by film deformation caused by all the droplets.

In addition to its relevance for droplet fluidics, we believe that the phenomenon we report could potentially be helpful in understanding and studying other processes, such as the role of substrate compliance on behavior of cells, where it is well known that cell motility and fate is strongly dependent on substrate stiffness [43–48].

2.2 Methods

The samples used in our experiments comprise a circular thin Vinyl Polysiloxane (VPS, Zhermack Elite Double 8, 1:1 mass ratio between base and catalyst) film suspended on a VPS substrate with a hole 8mm in diameter. A schematic cross-sectional view of the sample is shown in Fig. 1. To prepare this sample, a VPS substrate a few millimeters thick with a hole 8mm in diameter was molded in a Plexiglas mold. The VPS film was fabricated by spin-coating liquid VPS onto a Polystyrene-coated glass slide at 2000rpm for 2 minutes. The VPS substrate was placed onto the thin film immediately, and they were cured together at room temperature for over 30 minutes. The thickness of the film was measured by a white-light interferometer (Zegage; Zygo Corporation) to be 20.5μm.

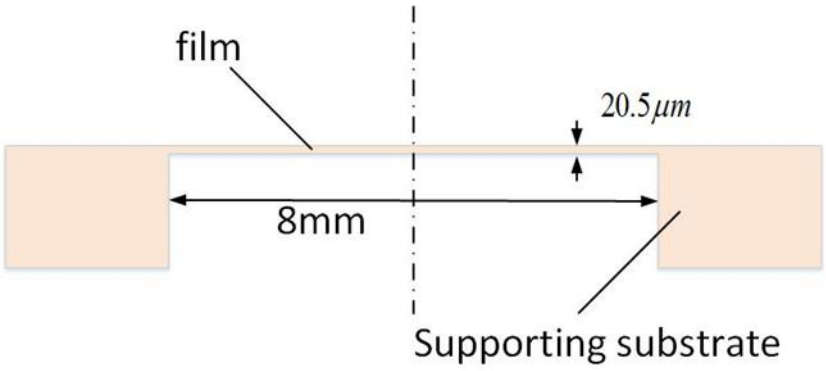

Fig. 2.1 Schematic side view of the supported-film sample. Both film and support are made of Vinyl Polysiloxane (VPS). The film has a diameter of 8mm and a thickness of 20.5µm.

2.3 Experiments: Interaction of two droplets

We study the interaction between two droplets placed on different sides of the thin elastic VPS film. A 5 μL de-ionized water (DI) droplet was placed on the bottom side of the film using an air displacement pipette as shown in Fig. 2.2 (a). In this configuration, the film bulges upwards due to the Laplace pressure p of the liquid drop, as shown by Nadermann *et al*. [34]. After this, another DI droplet of the same volume was placed on the top side of the film. The position of this droplet was controlled so that the two droplets, to begin with, were practically on top of each other (see Figs. 2.2(b, d)). Since the two droplets were nearly identical, neglecting gravity, the film became flat everywhere and went back to its undeformed state. However, this equilibrium configuration was not stable; the two droplets started to separate after a few seconds and eventually stopped at a stable configuration with a small overlap (see SI, movies 1,2).

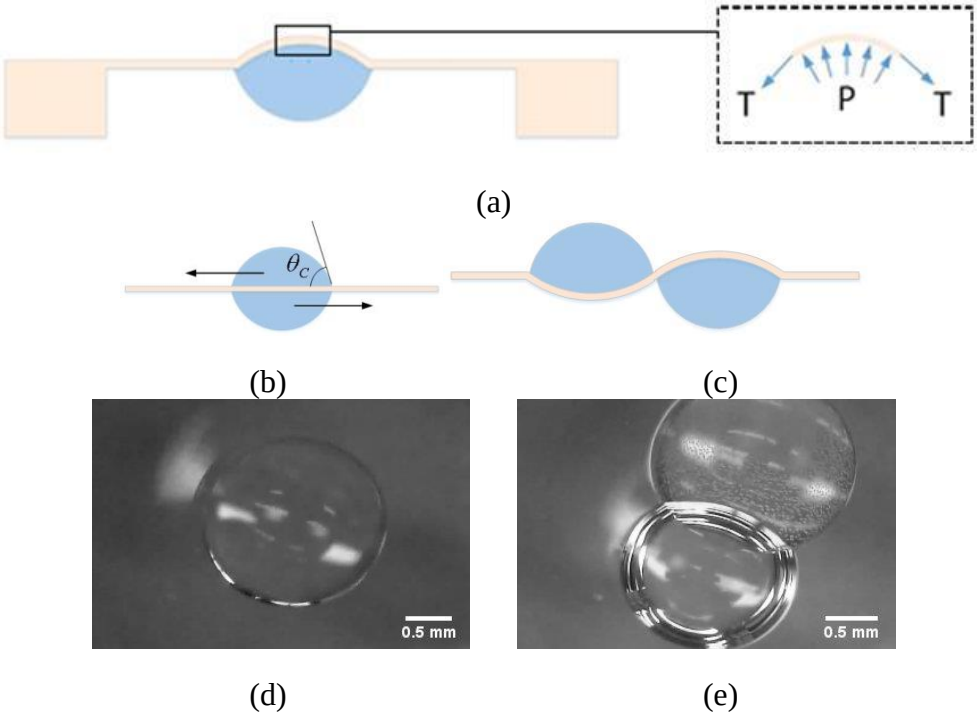

Fig. 2.2 Process of repulsion between two droplets on either side of a VPS film. (a) Using an air displacement pipette, a DI droplet was placed underneath the film, and the film bulged out due to the Laplace pressure *P* (see insert). (b) Another DI droplet of same volume was placed on the top side of the film, overlapping the bottom droplet. (c) The configuration in (b) was unstable and the two droplets separated. (d) Snapshot of the initial (unstable) overlapped configuration (top view). (e) Snapshot of the stable configuration with a small overlap (top view).

When two droplets overlap exactly (Fig. 2.2 (b)), the out-of-plane deformation of the film caused by one droplet is cancelled by the other. Therefore, the influence of the second droplet is effectively to increase the stiffness of the film. When two droplets are separated, the film again bulges out due to Laplace pressure (Fig. 2.2 (c)); both droplets are "sensing" the compliant elastic film. According to Style *et al.* [31], droplets tend to move toward a configuration where the substrate is softer. This durotaxis arises because a gradient in stiffness translates into a gradient in contact

angle, and a gradient in contact angle drives a drop towards the region of smaller apparent contact angle [49]. So, qualitatively, this argument suggests that the separation process can be understood as droplets seeking a softer place on which to sit.

2.4 Energy landscape and stability of the droplet pair

To understand our observation quantitatively, we analyze the energy landscape of two droplets that are infinitely long in the out-of-plane direction (Fig. 2.3). This plane problem is mathematically much more tractable than the fully 3D problem of interacting circular drops. Usually, the results of a plane strain problem differ from those of an axisymmetric or 3D calculation only within constant factors on the order of unity. These droplets lie on the opposite sides of an elastic film *clamped* at its edges. The initial undeformed width of the film is $2l_0$. We assume the droplets are sufficiently small so we can ignore gravity. Initially, the droplets are right on top of each other (Fig. 2.3 (a)). In this position, the droplets have identical width $2c_r$ and the film is completely flat since the Laplace pressure acting on the liquid/film interface exactly cancels as shown in Fig. 2.3 (a). In the absence of residual stress (due to fabrication), the film should have no elastic strain in the overlap configuration.

From this initial configuration, we allow the droplets to separate and compute the total energy of the system as a function of separation (see Fig. 2.3(b)). Any separation will cause the film to deform and the drops to change their shape. Specifically, the portion of the film (labeled 2 and 6 in Fig. 2.3 (b)) that is exposed to air on one side and liquid on the other will bulge into circular arcs due to Laplace pressure [34,35], while the region of film between the liquid drops (labeled 4 in Fig. 2.3 (b)) is flat since the pressure is the same on both its sides. Note that the film exterior to the drops (3 in Fig. 2.3 (b)) also remains flat since we ignore gravity. However, this part of the film is stretched due to the bulging of the film.

The extent of the film jointly covered by the two droplets is denoted by *2a*, and a/c_r serves as a parameter that characterizes the separation between the two droplets (Note that $a/c_r = 1$ when the two droplets overlap completely). To compute the elastic energy and the deformation of the film, we assume the film is a membrane with no bending stiffness (This approximation is accurate if the length $\sqrt{EI/\sigma} << a$ [50]. For our system, the length is about 25 microns and *a* > 1mm). To model large deformation, the film is taken to be an incompressible neo-Hookean solid with shear modulus μ. The strain energy density *W* of a neo-Hookean membrane subjected to uniform stretch ratio λ is given by

$$W(\lambda) = \frac{\mu h}{2}\left(\lambda^2 + \lambda^{-2} - 2\right) \tag{2.1}$$

where h is the undeformed thickness of the film.

To reduce the number of parameters in the problem, we further assume that the surface stresses of the film that is exposed to air and liquid is isotropic, independent of surface strains and are numerically equal to the surface energies γ_{SV}, γ_{SL}, respectively. We define an elasto-capillary number β as the ratio of liquid-vapor surface energy γ_{LV} to the effective modulus of the film μh. For our system, β is on the order of 0.1.

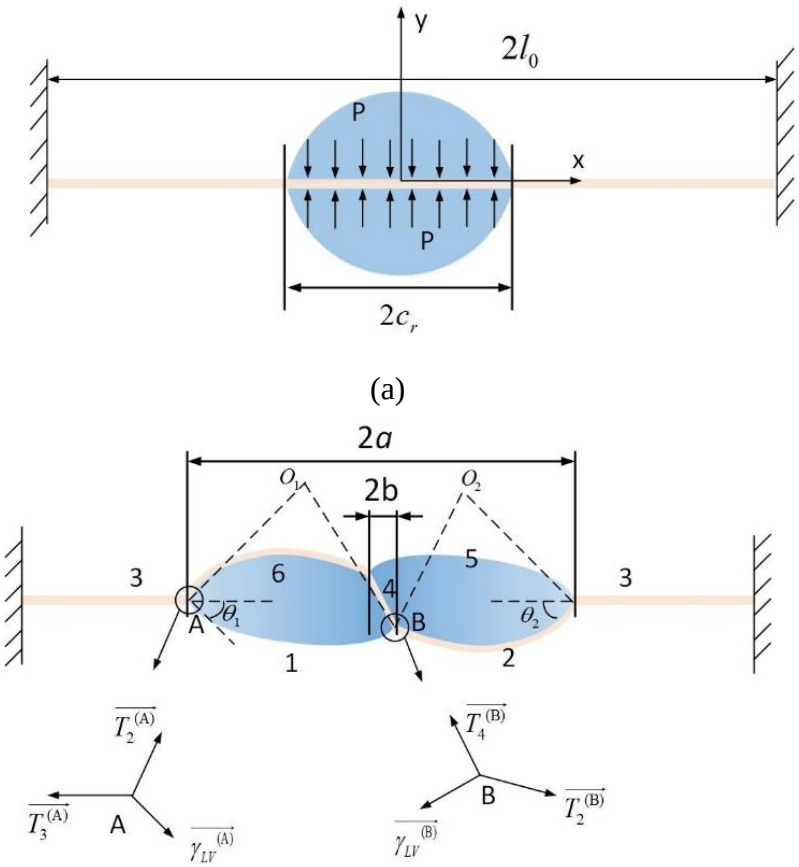

Fig. 2.3 (a) Initial configuration of the two drops in which $2c_r$ is the equilibrium contact width at zero separation. The film has no deformation as the Laplace pressure and surface tension at the contact line from two droplets cancel each other. (b) Configuration of two separated droplets. Part 1 is identical to part 5 and part 2 is identical to part 6 due to symmetry.

In the following, we summarize the key steps in our calculation of the total energy, which consists of contributions from the surface and elastic stretching. Details of our analysis are given in the Appendix.

The liquid drops (1 in Fig. 2.3 (b)) and the film (2 in Fig. 2.3 (b)) deform into circular arcs with unknown radii r_1 and r_2, respectively. In addition, the unknown

stretch ratios in each region (2,3,4, and 6) are constant and denoted by $\lambda_2, \lambda_3, \lambda_4$, and ($\lambda_6 = \lambda_2$ due to symmetry), respectively. For any given values of *a* and *b*, one can fully constrain the deformed geometry by specifying r_1, r_2 and the angles θ_1, θ_2 in Fig. 2.3 (b). As a result, the energy of the system is completely determined by 7 unknowns ($r_1, r_2, \theta_1, \theta_2, \lambda_2, \lambda_3, \lambda_4$). Specifically, the surface energies of the droplets and the deformed films (part 2 and 3) can be directly obtained from the deformed geometry, they are given by the first four terms in (A2.12). The elastic energies in part 2, 3 and 4 of the film can be determined using (2.1), the unknowns $\lambda_2, \lambda_3, \lambda_4$ and the undeformed length of these parts, and these energies are given by the last three terms in (A2.12).

To determine these 7 unknowns as a function of *a, b* and known surface energy densities $\gamma_{SV}, \gamma_{SL}, \gamma_{LV}$, we enforce force balance and volume conservation. From the free body diagram of A and B (shown in Fig. 2.3 (b)), the equilibrium equations can be written as

$$\overrightarrow{T_2^{(A)}} + \overrightarrow{T_3^{(A)}} + \overrightarrow{\gamma_{LV}^{(A)}} = \vec{0} \tag{2.2}$$

$$\overrightarrow{T_2^{(B)}} + \overrightarrow{T_4^{(B)}} + \overrightarrow{\gamma_{LV}^{(B)}} = \vec{0} \tag{2.3}$$

where $\vec{T}_2, \vec{T}_3$ and $\vec{T}_4$ denote the tensions in parts 2, 3 and 4 of the film respectively; the superscript () denotes that these tensions are to be evaluated at points A and B. These tensions (unit = force/length) are given by

$$\begin{aligned} T_2 &= \mu h(\lambda_2 - \lambda_2^{-3}) + \gamma_{SV} + \gamma_{SL} \\ T_3 &= \mu h(\lambda_3 - \lambda_3^{-3}) + 2\gamma_{SV} \\ T_4 &= \mu h(\lambda_4 - \lambda_4^{-3}) + 2\gamma_{SL} \end{aligned} \tag{2.4}$$

Equation (2.4) indicates that the tensions have two contributions, one is due to elastic stretch of the neo-Hookean membrane [51,52] and the rest is from the surface stress of the interface.

Since the droplet volume is a constant during separation, we impose the condition

$$V(\text{droplet}) = \mathrm{V}_0 \tag{2.5}$$

where V_0 is the volume of the liquid drop before deformation. In addition, since the boundary of the film is clamped at the edges, the total *undeformed* width of the film should be $2l_0$. This condition is

$$\frac{l_3}{\lambda_3} + \frac{l_2}{\lambda_2} + \frac{l_4}{2\lambda_4} = l_0 \tag{2.6}$$

where l_2, l_3 and l_4 are the deformed length of parts 2,3 and 4 of the film respectively. The fact that the *x* coordinate of point *B* is equal to *b* yields one more equation, that is, the *y* coordinate of point *B* must be given by

$$r_1 \cos\theta_1 - \sqrt{r_1^2 - (b + a - r_1 \sin\theta_1)^2} = r_2 \cos\theta_2 - \sqrt{r_2^2 - (b - a + r_2 \sin\theta_2)^2} \tag{2.7}$$

The equilibrium equations (2.2) and (2.3) provides 4 scalar equations, which, together with (2.5-2.7) give 7 equations which allows us to solve numerically for the 7 unknowns $r_1, r_2, \theta_1, \theta_2, \lambda_2, \lambda_3, \lambda_4$.

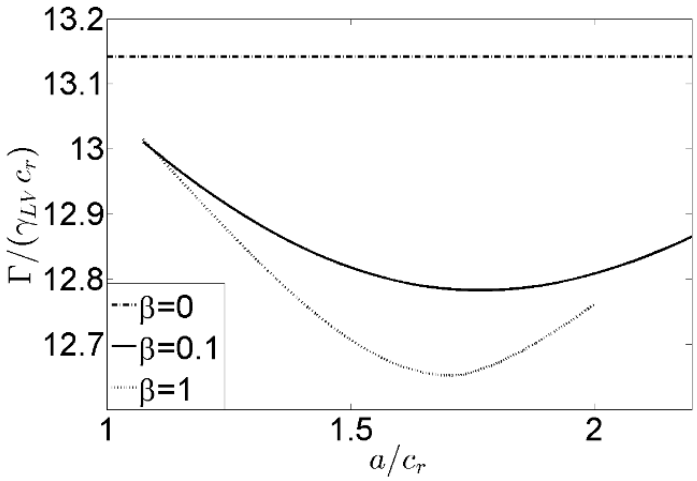

(a)

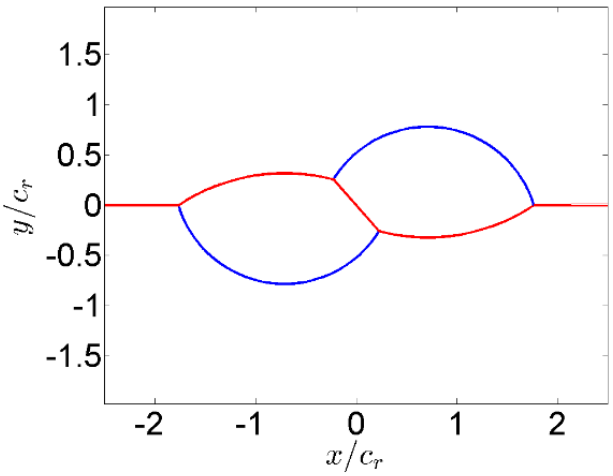

(b)

Fig. 2.4 (a) Total energy of the system vs a/c_r for different elasto-capillary number β. The local energy minimum is achieved when $a/c_r \approx 1.77$ for $\beta = 0.1$, and 1.75 for $\beta = 1$. (b) Minimum energy configuration for $\beta = 0.1$. The red line is the thin film and the blue line is the surface of the droplets.

Next, for a given separation *a*, we minimize the energy of the system by varying *b*. Repeating this calculation for different values of *a*, we obtain the result in Fig. 2.4 (a). Fig. 2.4 (a) shows that, once the system is perturbed from the complete overlap case, the total energy starts to decrease indicating that the overlap scenario is unstable. Once separation starts, the two droplets will continue to repel each other until a local energy minimum is achieved, as shown in Fig. 2.4 (a). That there is a local energy minimum for partial overlap between the two drops explains the experimental observation that there is always a small overlap between drops on two sides of the film, as shown in Fig. 2.2 (e). A computed equilibrium configuration for the case of $\beta = 0.1$ is shown in Fig. 2.4 (b). When the film is more compliant i.e. β becomes larger, the energy well will be deeper, but the local energy minimum position only changes slightly. This suggests that for a softer film, it will be easier to observe the separation process but the final equilibrium configuration will not change much.

2.5 Satellite droplet pattern

To demonstrate further the mechanism for inter-droplet interaction just described, we show its use to create a "satellite" droplet pattern where small drops surround a large one. In this experiment, a single $1\mu L$ DI droplet was placed on the top side of the film. The sample together with the droplet was then placed on the top of a glass beaker filled with DI water as shown in Fig. 2.5 (a). We heated the glass beaker to increase the evaporation rate, and small droplets continued to condense on the bottom of the film as shown in SI (movie 2.3). As these small droplets coalesced to form bigger droplets under the pre-placed droplet on the top side of the film, they were repelled to the boundary of the top droplet. This process continued until a ring of droplets formed around the top droplet as shown in Fig. 2.5 (b).

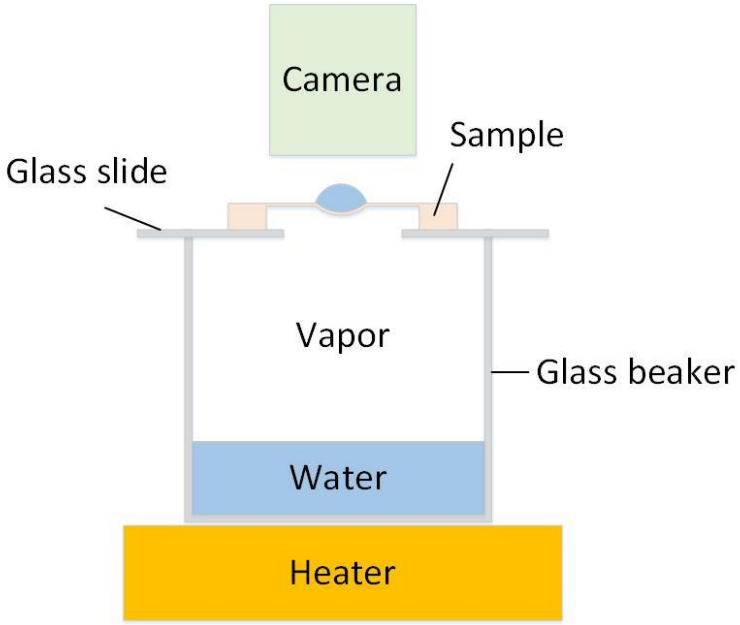

(a)

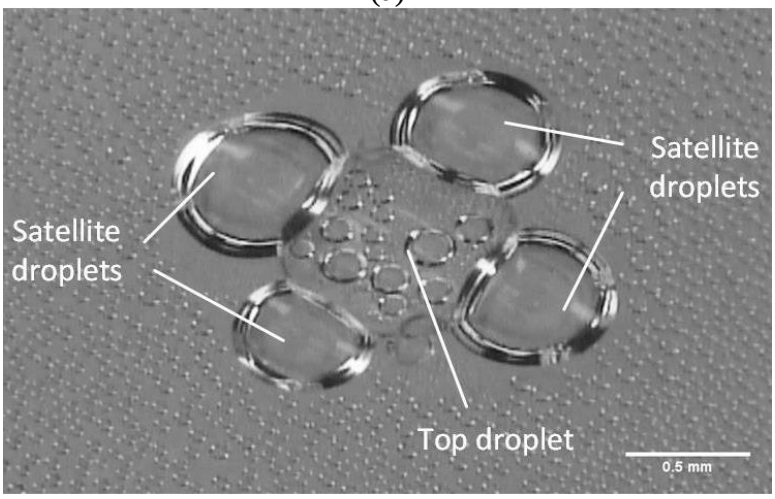

(b)

Fig. 2.5 (a) Schematic of the experimental setup. The glass beaker was heated to increase the evaporation rate, and the sample together with a droplet was held by two glass slides on top of the glass beaker. Small droplets condensed on the bottom of the film due to evaporation (not shown in figure) (b) Satellite droplet pattern: four "satellite" droplets underneath the film formed around the top droplet.

2.6 Conclusion and Discussion

We report a short range interaction between droplets sitting on different sides of a thin elastic film. When droplets overlap completely, the system is in an unstable state, and a small perturbation will lead to rapid separation between the two droplets. The process stops when there is a small overlap between the two droplets (about 1/3 of droplet size). The phenomenon is explained quantitatively by computing the surface and elastic energy of the system and finding the configuration where the total energy is minimized. This new interaction mechanism can be potentially useful for pattern formation, an example of "satellite" droplet pattern is proposed and tested by experiment.

It should be noted that our plane strain model assumes that the droplets are infinitely long in the out of plane direction, which is not true in most cases. Indeed, if the two droplets were completely separated, the plane strain model, in the absence of gravity, predicts that the film stretches uniformly and remains flat outside the droplets. This is not the case for 3D droplets. Such non-uniform deformation would result in spatially varying apparent contact angle leading to more complex interaction between droplets. This interaction is short range since we did not observe any interaction between droplets that are placed more than one diameter away from each other. The deformation of the film caused by two 3-D droplets and how their interaction depends on the spacing between them will be studied in a future work.

APPENDIX 2.1

ENERGY LANDSCAPE CALCULATION

To simplify the geometry, we consider a 2-D system where both the droplets and film are assumed to be infinitely long in the out of plane direction. The droplets are assumed to be partially separated as shown in Fig. 2.3 (b). As gravity is neglected, the pressure inside the drop is a constant. Hence, part 1 and 2 are both circular arcs [51,52]. Part 4 has to be flat as the pressure from different sides cancels each other. The origin of our coordinate system is shown in Fig. 2.3 (a). Note, after deformation, the material point at the origin remain fixed and is located at the midpoint of part 4.

For any given value of *a* and *b*, one can fully constrain the geometry by determining the radius of curvature for part 1 and 2 (r_1, r_2) and the angles θ_1, θ_2. The amount of elastic stretch λ_2, λ_3, λ_4 needs to be determined separately. The total energy of the system can be calculated once these 7 unknowns ($r_1, r_2, \theta_1, \theta_2, \lambda_2, \lambda_3, \lambda_4$) are known.

We select c_r as the characteristic length scale for this problem and normalize all the lengths by it, i.e., $\overline{r_1} = \frac{r_1}{c_r}, \overline{r_2} = \frac{r_2}{c_r}, \overline{l_0} = \frac{l_0}{c_r}$. The force per unit out of plane length is normalized by γ_{LV}. The condition of force balance at point A can be written as:

$$\overline{\sigma_{LV}} \cos\theta_1 + \overline{T_2} \cos\theta_2 = \overline{T_3} \tag{A2.1}$$

$$\overline{\sigma_{LV}} \sin\theta_1 = \overline{T_2} \sin\theta_2 \tag{A2.2}$$

where $\overline{\sigma_{LV}} = \frac{\sigma_{LV}}{\gamma_{LV}} = 1$, $\overline{T_2} = \frac{1}{\beta}(\lambda_2 - \lambda_2^{-3}) + \overline{\sigma_{SV}} + \overline{\sigma_{SL}}$ and $\overline{T_3} = \frac{1}{\beta}(\lambda_3 - \lambda_3^{-3}) + 2\overline{\sigma_{SV}}$.

Here $\beta = \frac{\gamma_{LV}}{\mu h}$ is the elasto-capillary number for this system, σ_{LV}, σ_{SV} and σ_{SL} are the liquid-vapor, solid-vapor and solid-liquid interface tension. In our system, interface surface stress is assumed to be isotropic, independent of surface strain and numerically equal to surface energy.

Using the coordinate system defined in Fig. 2.3(a), the position of O_1 and O_2 can be determined by geometry, they are:

$$\begin{aligned} O_1 &: (-\bar{a} + \bar{r_1}\sin\theta_1, \bar{r_1}\cos\theta_1) \\ \mathrm{O}_2 &: (\bar{a} - \bar{r_2}\sin\theta_2, \bar{r_2}\cos\theta_2) \end{aligned} \tag{A2.3}$$

Point *B* is the intersection between arcs 1 and 2. The *x* coordinate of *B* is $\bar{b}$ while its *y* coordinate y_B can be determined from both arc 1 and arc 2. Using (A2.3), we find

$$\begin{aligned} \bar{y}_B &= \bar{r_1}\cos\theta_1 - \sqrt{\bar{r_1}^2 - (\bar{b} + \bar{a} - \bar{r_1}\sin\theta_1)^2} \\ &= \bar{r_2}\cos\theta_2 - \sqrt{\bar{r_2}^2 - (\bar{b} - \bar{a} + \bar{r_2}\sin\theta_2)^2} \end{aligned} \tag{A2.4}$$

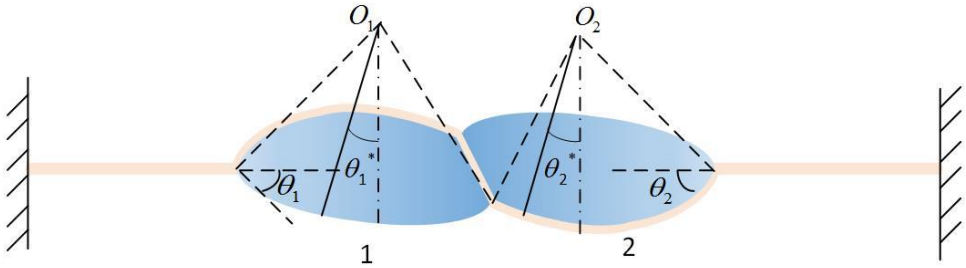

Fig. A2.1 Parameter θ_1^* and θ_2^* can be used to determine the parameter equation of arc 1 and 2.

The equation of the circular arc 1 connecting *A* and *B* can be determined by the angle θ_1^* (see Fig. A2.1):

$$\bar{x}_1(\theta_1^*) = -\bar{a} + \bar{r_1}\sin\theta_1 + \bar{r_1}\sin\theta_1^*,\ \bar{y}_1(\theta_1^*) = \bar{r_1}\cos\theta_1 - \bar{r_1}\cos\theta_1^* \tag{A2.5}$$

where $\theta_1^* \in (-\theta_1, \sin^{-1}(\dfrac{\bar{b} + \bar{a} - \bar{r_1}\sin\theta_1}{\bar{r_1}}))$. Similarly, the equation of arc 2 can described by the angle θ_2^* (see Fig. A2.1)

$$\bar{x}_2(\theta_2^*) = \bar{a} - \bar{r_2}\sin\theta_2 + \bar{r_2}\sin\theta_2^*,\ \bar{y}_2(\theta_2^*) = \bar{r_2}\cos\theta_2 - \bar{r_2}\cos\theta_2^*, \tag{A2.6}$$

where $\theta_2^* \in (\sin^{-1}(\dfrac{\bar{b} - \bar{a} + \bar{r_2}\sin\theta_2}{\bar{r_2}}), \theta_2)$. Using these parametric equations, we integrate to obtain the volume of the droplet. This volume is conserved through the separation process:

$$-\int \overline{y_1} d\overline{x_1} - \int \overline{y_2} d\overline{x_2} = \overline{V_0} \tag{A2.7}$$

where $\overline{V_0} = \dfrac{V_0}{c_r^{\,2}}$ is the normalized volume of a droplet.

Next we enforce force balance at *B*. The forces acting there are shown in Fig. 2.3 (b):

$$\frac{\overrightarrow{T_4^{(B)}}}{\gamma_{LV}} = \overline{T_4}\overrightarrow{e_4^{(B)}}, \quad \frac{\overrightarrow{\gamma_{LV}^{(B)}}}{\gamma_{LV}} = \overrightarrow{e_\sigma^{(B)}}, \quad \frac{\overrightarrow{T_2^{(B)}}}{\gamma_{LV}} = \overline{T_2}\overrightarrow{e_2^{(B)}} \tag{A2.8}$$

where $\overrightarrow{e_4^{(B)}}$, $\overrightarrow{e_\sigma^{(B)}}$ and $\overrightarrow{e_2^{(B)}}$ are unit vectors pointing in the direction of these forces respectively. They are given by

$$\begin{aligned}
\overrightarrow{e_4^{(B)}} &= \frac{1}{\sqrt{\overline{y_B}^2 + \overline{b}^2}} \begin{pmatrix} -\overline{b} \\ -\overline{y_B} \end{pmatrix}, \\
\overrightarrow{e_\sigma^{(B)}} &= \frac{1}{\overline{r_1}} \begin{pmatrix} \overline{y_B} - \overline{r_1}\cos\theta_1 \\ \overline{r_1}\sin\theta_1 - \overline{a} - \overline{b} \end{pmatrix}, \\
\overrightarrow{e_2^{(B)}} &= \frac{1}{\overline{r_2}} \begin{pmatrix} \overline{r_2}\cos\theta_2 - \overline{y_B} \\ \overline{b} - \overline{a} + \overline{r_2}\sin\theta_2 \end{pmatrix}
\end{aligned} \tag{A2.9a}$$

where $\overline{y_B} = \overline{r_2}\cos\theta_2 - \sqrt{\overline{r_2}^2 - \left(\overline{b} - \overline{a} + \overline{r_2}\sin\theta_2\right)^2}$ is the *y* coordinate of point *B*. The magnitude of the forces, $\overline{T_2}, \overline{T_4}$ are:

$$\overline{T_2} = \frac{1}{\beta}(\lambda_2 - \lambda_2^{-3}) + \overline{\sigma_{SV}} + \overline{\sigma_{SL}}, \; \overline{T_4} = \frac{1}{\beta}(\lambda_4 - \lambda_4^{-3}) + 2\overline{\sigma_{SL}} \tag{A2.9b}$$

Using (A2.8-A2.9) and (2.2-2.3), the force balance at point *B* is

$$\frac{\overline{T_4}}{\sqrt{\overline{y_B}^2 + \overline{b}^2}} \begin{pmatrix} -\overline{b} \\ -\overline{y_B} \end{pmatrix} + \frac{1}{\overline{r_1}} \begin{pmatrix} \overline{y_B} - \overline{r_1}\cos\theta_1 \\ \overline{r_1}\sin\theta_1 - \overline{a} - \overline{b} \end{pmatrix} + \frac{\overline{T_2}}{\overline{r_2}} \begin{pmatrix} \overline{r_2}\cos\theta_2 - \overline{y_B} \\ \overline{b} - \overline{a} + \overline{r_2}\sin\theta_2 \end{pmatrix} = \begin{pmatrix} 0 \\ 0 \end{pmatrix} \tag{A2.10a,b}$$

Finally, the total undeformed length of the system should remain as a constant $2\overline{l_0}$, and this constraint is (2.6) in the main text and can be expanded as:

$$\frac{\overline{l_0} - \overline{a}}{\lambda_3} + \frac{\left(\theta_2 - \sin^{-1}\left(\dfrac{\overline{b} - \overline{a} + \overline{r_2}\sin\theta_2}{\overline{r_2}}\right)\right)\overline{r_2}}{\lambda_2} + \frac{\sqrt{\overline{b}^2 + \overline{y_B}^2}}{\lambda_4} = \overline{l_0} \tag{A2.11}$$

Equations (A2.1), (A2.2), (A2.4), (A2.7), (A2.10a,b), (A2.11) allows us to determine $\bar{r}_1, \bar{r}_2, \theta_1, \theta_2, \lambda_2, \lambda_3, \lambda_4$ for any given $\bar{a}, \bar{b}$.

Because of symmetry, we consider the energy stored in half of the film. This energy is:

$$\begin{aligned}\bar{\Gamma} = {} & 2\left(\bar{l}_0 - \bar{a}\right)\overline{\sigma_{SV}} + \bar{r}_2\left(\theta_2 - \sin^{-1}\left(\frac{\bar{b} - \bar{a} + \bar{r}_2 \sin\theta_2}{\bar{r}_2}\right)\right)\left(\overline{\sigma_{SL}} + \overline{\sigma_{SV}}\right) \\ & + 2\sqrt{\overline{y_b}^2 + \bar{b}^2}\,\overline{\sigma_{SL}} \\ & + \left(\sin^{-1}\left(\frac{\bar{b} + \bar{a} - \bar{r}_1 \sin\theta_1}{\bar{r}_1}\right) + \theta_1\right)\bar{r}_1 + \frac{1}{2\beta}\left(\lambda_3^{\,2} + \frac{1}{\lambda_3^{\,2}} - 2\right)\frac{\bar{l}_0 - \bar{a}}{\lambda_3} \\ & + \frac{1}{2\beta}\left(\lambda_2^{\,2} + \frac{1}{\lambda_2^{\,2}} - 2\right)\frac{\left(\theta_2 - \sin^{-1}\left(\frac{\bar{b} - \bar{a} + \bar{r}_2 \sin\theta_2}{\bar{r}_2}\right)\right)\bar{r}_2}{\lambda_2} \\ & + \frac{1}{2\beta}\left(\lambda_4^{\,2} + \frac{1}{\lambda_4^{\,2}} - 2\right)\frac{\sqrt{\bar{b}^2 + \overline{y_B}^2}}{\lambda_4}\end{aligned} \tag{A2.12}$$

First, we compute the energy for a fixed $\bar{a}$ and varying $\bar{b}$. For example, if we set $\bar{a} = 1.5$, $\beta = 0.1$, the energy landscape is shown in Fig. A2.2:

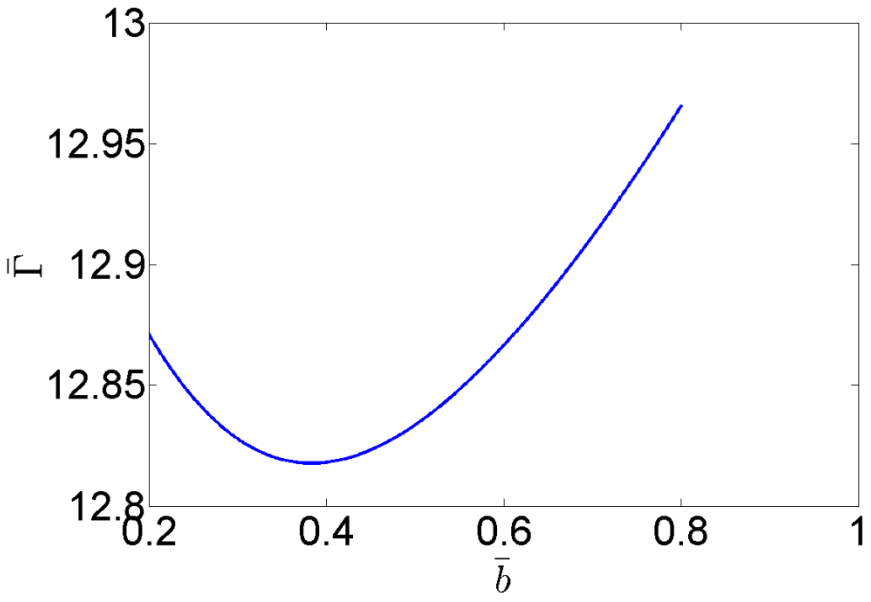

Fig. A2.2 Energy landscape for $\bar{a} = 1.5$, $\beta = 0.1$

The lowest energy is defined as the equilibrium energy for $\bar{a} = 1.5$. We repeat this process for different $\bar{a}$ to obtain Fig. 2.4(a) in the main text.

REFERENCES

[1] T. M. Squires and S. R. Quake, Rev. Mod. Phys. **77**, 977 (2005).

[2] M. Srinivasarao, Science (80-.). **292**, 79 (2001).

[3] M. G. Pollack, A. D. Shenderov, and R. B. Fair, Lab Chip **2**, 96 (2002).

[4] X. Zhang, F. Shi, J. Niu, Y. Jiang, and Z. Wang, J. Mater. Chem. **18**, 621 (2008).

[5] P. Kim, T.-S. Wong, J. Alvarenga, M. J. Kreder, W. E. Adorno-Martinez, and J. Aizenberg, ACS Nano **6**, 6569 (2012).

[6] F. Schellenberger, J. Xie, N. Encinas, A. Hardy, M. Klapper, P. Papadopoulos, H.-J. Butt, and D. Vollmer, Soft Matter **11**, 7617 (2015).

[7] D. A. Edwards, H. Brenner, and D. T. Wasan, *Interfacial Transport Processes and Rheology* (Butterworth-Heinemann, 1991).

[8] C. Lv, C. Chen, Y.-C. Chuang, F.-G. Tseng, Y. Yin, F. Grey, and Q. Zheng, Phys. Rev. Lett. **113**, 26101 (2014).

[9] M. Prakash, D. Quéré, and J. W. M. Bush, Science **320**, 931 (2008).

[10] M. K. Chaudhury, A. Chakrabarti, and S. Daniel, Langmuir **31**, 9266 (2015).

[11] M. K. Chaudhury and G. M. Whitesides, Science **256**, 1539 (1992).

[12] K. Ichimura, Science (80-.). **288**, 1624 (2000).

[13] Y. Zheng, H. Bai, Z. Huang, X. Tian, F.-Q. Nie, Y. Zhao, J. Zhai, and L. Jiang, Nature **463**, 640 (2010).

[14] H. A. Stone, A. D. Stroock, and A. Ajdari, Annu. Rev. Fluid Mech. **36**, 381 (2004).

[15] Y. Sumino, N. Magome, T. Hamada, and K. Yoshikawa, Phys. Rev. Lett. **94**, 68301 (2005).

[16] S. Daniel, S. Sircar, J. Gliem, and M. K. Chaudhury, Langmuir **20**, 4085 (2004).

[17] B. S. Gallardo, V. K. Gupta, F. D. Eagerton, L. I. Jong, V. S. Craig, R. R. Shah, and N. L. Abbott, Science (80-.). **283**, 57 (1999).

[18] A. M. Cazabat, F. Heslot, S. M. Troian, and P. Carles, Nature **346**, 824 (1990).

[19] S. Daniel, M. K. Chaudhury, and J. C. Chen, Science **291**, 633 (2001).

[20] P. Lazar and H. Riegler, Phys. Rev. Lett. **95**, 136103 (2005).

[21] J. B. Brzoska, F. Brochard-Wyart, and F. Rondelez, Langmuir **9**, 2220 (1993).

[22] G. Lagubeau, M. Le Merrer, C. Clanet, and D. Quéré, Nat. Phys. **7**, 395 (2011).

[23] N. J. Cira, A. Benusiglio, and M. Prakash, Nature **519**, 446 (2015).

[24] D. Vella and L. Mahadevan, Am. J. Phys. **73**, 817 (2005).

[25] A. Chakrabarti and M. K. Chaudhury, Langmuir **29**, 15543 (2013).

[26] E. R. Jerison, Y. Xu, L. A. Wilen, and E. R. Dufresne, Phys. Rev. Lett. **106**, 186103 (2011).

[27] R. W. Style, R. Boltyanskiy, Y. Che, J. S. Wettlaufer, L. A. Wilen, and E. R. Dufresne, Phys. Rev. Lett. **110**, 66103 (2013).

[28] C.-Y. Hui and A. Jagota, Proc. R. Soc. A Math. Phys. Eng. Sci. **470**, 20140085 (2014).

[29] L. Limat, Eur. Phys. J. E. Soft Matter **35**, 9811 (2012).

[30] L. A. Lubbers, J. H. Weijs, L. Botto, S. Das, B. Andreotti, and J. H. Snoeijer, J. Fluid Mech. **747**, R1 (2014).

[31] R. W. Style, Y. Che, S. J. Park, B. M. Weon, J. H. Je, C. Hyland, G. K. German, M. P. Power, L. A. Wilen, J. S. Wettlaufer, and E. R. Dufresne, Proc. Natl. Acad. Sci. U. S. A. **110**, 12541 (2013).

[32] S. Karpitschka, A. Pandey, L. A. Lubbers, J. H. Weijs, L. Botto, S. Das, B. Andreotti, and J. H. Snoeijer, Proc. Natl. Acad. Sci. U. S. A. **113**, 7403 (2016).

[33] A. Jagota, Proc. Natl. Acad. Sci. U. S. A. **113**, 7294 (2016).

[34] N. Nadermann, C.-Y. Hui, and A. Jagota, Proc. Natl. Acad. Sci. U. S. A. **110**,

10541 (2013).

[35] C.-Y. Hui and A. Jagota, Soft Matter (2015).

[36] R. D. Schulman and K. Dalnoki-Veress, Phys. Rev. Lett. **115**, 206101 (2015).

[37] J. Huang, M. Juszkiewicz, W. H. de Jeu, E. Cerda, T. Emrick, N. Menon, and T. P. Russell, Science (80-.). **317**, (2007).

[38] G. Lagubeau, M. A. Fontelos, C. Josserand, A. Maurel, V. Pagneux, and P. Petitjeans, Phys. Rev. Lett. **105**, 184503 (2010).

[39] R. D. Schroll, M. Adda-Bedia, E. Cerda, J. Huang, N. Menon, T. P. Russell, K. B. Toga, D. Vella, and B. Davidovitch, Phys. Rev. Lett. **111**, 14301 (2013).

[40] C. Py, P. Reverdy, L. Doppler, J. Bico, B. Roman, and C. N. Baroud, Phys. Rev. Lett. **98**, 156103 (2007).

[41] S. Mora, C. Maurini, T. Phou, J.-M. Fromental, B. Audoly, and Y. Pomeau, Phys. Rev. Lett. **111**, 114301 (2013).

[42] B. Roman and J. Bico, J. Phys. Condens. Matter **22**, 493101 (2010).

[43] Y. S. Choi, L. G. Vincent, A. R. Lee, K. C. Kretchmer, S. Chirasatitsin, M. K. Dobke, and A. J. Engler, Biomaterials **33**, 6943 (2012).

[44] L. Trichet, J. Le Digabel, R. J. Hawkins, S. R. K. Vedula, M. Gupta, C. Ribrault, P. Hersen, R. Voituriez, and B. Ladoux, Proc. Natl. Acad. Sci. U. S. A. **109**, 6933 (2012).

[45] D. E. Discher, P. Janmey, and Y. Wang, Science (80-.). **310**, (2005).

[46] C. M. Lo, H. B. Wang, M. Dembo, and Y. L. Wang, Biophys. J. **79**, 144 (2000).

[47] R. Zhang, L. Ni, Z. Jin, J. Li, and F. Jin, Nat. Commun. **5**, 5541 (2014).

[48] W. Guo, M. T. Frey, N. A. Burnham, and Y. Wang, Biophys. J. **90**, 2213 (2006).

[49] P.-G. de Gennes, F. Brochard-Wyart, and D. Quéré, *Capillarity and Wetting*

Phenomena (Springer New York, New York, NY, 2004).

[50] R. W. Style, A. Jagota, C.-Y. Hui, and E. R. Dufresne, (2016).

[51] A. Srivastava and C.-Y. Hui, Proc. R. Soc. London A Math. Phys. Eng. Sci. **469**, (2013).

[52] A. Srivastava and C.-Y. Hui, Proc. R. Soc. London A Math. Phys. Eng. Sci. **469**, (2013).

CHAPTER 3

SPONTANEOUS DROPLET MOTION ON A PERIODIC COMPLIANT STRUCTURE [2]

3.1 Introduction

Spontaneous droplet motion is of great importance in a variety of industrial applications such as the design and fabrication of microfluidic devices [1–3] and super-hydrophobic coatings [4]. Typically, droplet motion is induced using a surface with gradients in curvature [5], in droplet apparent contact angle, or by external stimuli such as vibration [6–8]. Spatial gradient in apparent contact angle can be induced by variation in thermal [9–12], chemical [13–17], electrical [18] and elastic [19] properties of the surface. Continuous transportation of a droplet requires a continuous input of energy. Besides surface gradient, this energy can be also provided by the evaporation of droplets. For example, by controlling the direction of vapor flow, a droplet placed on a hot ratchet can propel itself in a specified direction [20]. More recently, Cira *et al.* [21] have demonstrated that two-component droplets of well-chosen miscible liquids on a clean glass slide can move and interact with each other by emitting vapor.

Here, we report a new phenomenon in which a water droplet can spontaneously move on a surface with periodic variation in compliance but with no surface energy gradient or external stimuli. Specifically, we fabricated an elastomeric substrate with periodic variation of surface compliance. We found that a small droplet placed on such a substrate *undergoes random motion over distances significantly larger than the drop size and the spatial period over which compliance varies*. This phenomenon is surprising because it is unclear what drives it; there is no overall gradient in surface energy or in surface compliance. This phenomenon is quite different from that

[2] Liu T., Nadermann N., He Z., Strogatz, S., Hui C.Y., Jagota A., (2016) submitted to Langmuir.

reported by Style *et al.* [19], where droplet motion is driven by a monotonically decreasing gradient in substrate stiffness. Indeed, if the motion observed in our system were driven by a stiffness gradient, our droplet would be trapped in a position of minimum substrate stiffness and will not able to move more than one period. Hence, there should be some other energy sources beyond stiffness gradient that powers the droplet motion. What makes the phenomenon even more counterintuitive is that increasing surface compliance and surface undulations should both lead to an increase of contact angle hysteresis [22]. Therefore, going from a flat, unstructured control, which does not show drop motion, to a structured surface with a periodic variation in compliance should, according to the arguments above, make drop motion *less* likely, not more. However, we observe the reverse.

Fig. 1 shows a top view of the phenomenon: a droplet of deionized water moves spontaneously on a compliant surface whose stiffness varies periodically in both directions. Before analyzing the details and the cause of the motion, let us clarify the experimental setup. A typical micrograph of the structure used in our studies, and a schematic of the cross-section with a droplet on top, are shown in Figs. 1(e) and 1(f), respectively. The structure is a thin poly(dimethylsiloxane) (PDMS) film (thickness $\approx 10\mu m$) bonded to a periodic square array of fibrils with center to center spacing *a*. The fibrils are circular pillars of diameter 10 m. The architecture of this surface was inspired by biology – many insects and small animals use arrays of fibrils to make contact, to increase adhesion and friction [23,24]. Naturally the film is much stiffer when it is directly above a fibril than when it is between them. Therefore the surface compliance of this structure varies periodically with fibril spacing.

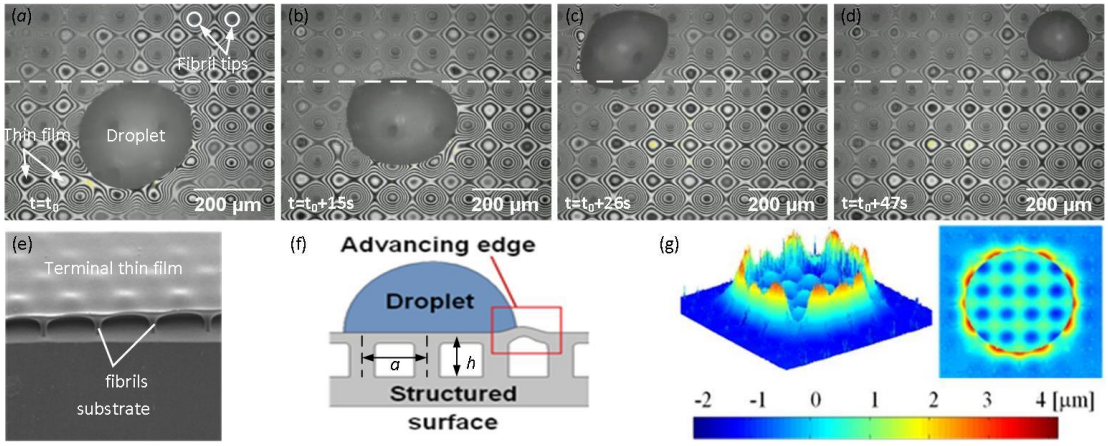

Fig. 3.1 Droplet on a film-terminated fibrillar surface. (a-d) Beginning at $t = t_0$, micrographs of a droplet of de-ionized water placed atop a film-terminated fibrillar surface show (i) significant distortion of interferometric contours, indicating out-of-plane deformation driven by liquid surface tension, and (ii) spontaneous movement of the droplet. In this series of optical micrographs, the droplet moves over a distance much larger than its own size and the interfibrillar distance. (e) Scanning electron micrograph image of the film-terminated fibrillar surface. (f) A schematic showing a droplet on the structured surface, and the deformation caused by droplet surface tension. The experiments are repeated on samples with height h varied from 10 – 40 μm and interfibrillar spacing a varied from 20 – 110 μm. (g) Contours and 3D representation of the vertical displacement of the substrate caused by surface tension of the drop.

3.2 Experimental Results

A single deionized water droplet of volume 0.1 μL was placed on the film. The volume of the droplet was controlled by an air displacement pipette. The sample together with the droplet was then placed under a white light interferometer (Zegage; Zygo Corporation) for observation. Initially, the droplet has the shape of a spherical cap and the contact line between the droplet and the film is roughly circular (Fig.

3.1(g)), with small undulations near the fibrils. Typical snapshots of the deformed and moving droplet are shown in Figs. 3.1(a)-(d). The droplet gradually becomes smaller as it evaporates and the contact line becomes irregular. As evaporation continues, the droplet starts to move spontaneously, as shown in the SI movie. The motion of the droplet is relatively slow at first, then picks up speed as it becomes smaller with further evaporation, and eventually slows down and stops when the size of the droplet becomes much smaller than the spacing between fibrils. The surface tension and Laplace pressure of the droplet can induce large deformation of the substrate (see Fig. 3.1(g)). As expected, deformation is smaller at or near the fibrils, where the compliance is lowest. This variation of spatial deformation leads to local variation of apparent contact angle along the contact line. [19]

As the video in the Supplementary Information indicates, droplet motion has the appearance of a random walk. To test if the motion is truly random, or if there is some unknown gradient on the surface driving the motion, we repeated the experiment several times using a new droplet deposited on the same sample, and recorded the motion of the droplet. (A Matlab® program was used to detect the droplet contact line and to compute the centroid of its contact area for every frame of the video.) Trajectories of the centroid for different drops placed on the same substrate are shown in Fig. 3.2 (a). In Figs. 3.2 (a) and (b), different color corresponds to different trials. The size of the markers (circles centered at droplet's centroid) are proportional to the contact area between the drop and the substrate. The time between two consecutive markers is 3 seconds.

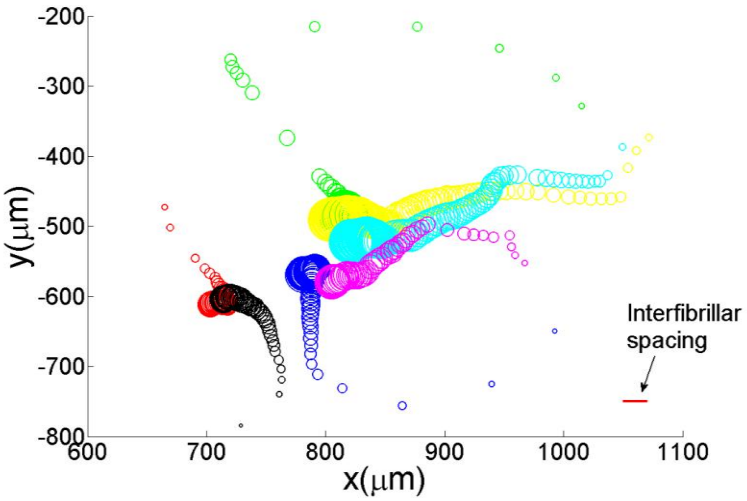

(a)

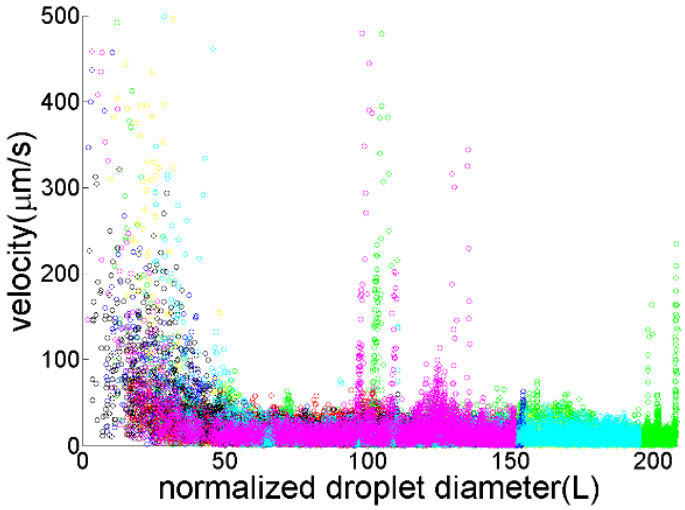

(b)

Fig. 3.2 (a) Trajectories and (b) velocities of the droplet centroid for different drops placed on the same substrate. Different colors correspond to different experiments. The fibril spacing a is 20 μm and the fibril height is 10 μm. Measured trajectories for samples with different fibril spacing and fibril heights are given in the SI. The circular markers are centered at the droplet's centroid. The marker size is proportional to the contact area of the drop, thus showing how the drop shrinks by evaporation. The time between two consecutive markers is 3 sec. For a specific region of the sample, the

experiments could only be repeated about 3-7 times, after which new droplets lost their ability to move. This is likely due to the deposition of some impurities during droplet drying, which increases the contact angle hysteresis.

From both the SI movie and Fig. 3.2(a), we see that the motion of the drop is quite substantial and that the distance it travels is typically much larger than the interfibrillar spacing *a*. From the recorded trajectories, the drop motion is apparently random and is very sensitive to initial conditions. For example, the black and the red paths in Fig. 2(a) start at almost the same location, but the trajectories are completely different. In several instances, for example the case illustrated by the purple and cyan paths, the droplets follow similar paths in the beginning but deviate from each other later on. These observations rule out a hidden gradient driving the process and suggest that the dynamics of droplet motion may be chaotic. Large droplets move slowly or not at all; their sluggishness is probably due to inertia or contact angle hysteresis. As a drop evaporates and becomes smaller, the speed of its motion increases. When the size of a droplet becomes smaller than the interfibrillar spacing *a*, the drop starts to slow down and eventually stops and dries out.

The SI movie and the velocity data in Fig. 3.2(b) show that the motion of droplets can be jerky. Fig. 3.2 (b) indicates that most of the time the drop moves slowly and continuously but suddenly speeds up and darts across the surface at certain locations, as indicated by the spikes in Fig. 3.2(b). Similar trends are observed for samples with different fibril spacing and height, as shown in SI.

3.3 Model for droplet motion

The chaotic motion observed in our experiments rule out the possibility that an overall gradient drives the droplet motion. Furthermore, compared with a flat surface,

the structured surface should make contact angle hysteresis larger [22]. So, what provides the force to overcome the hysteresis and induce the motion? A clue comes from Fig. 3.1(g), when the interfibrillar spacing a is $20\,\mu m$ the film deformation caused by surface tension can be as large as $4\,\mu m$. Such large deformation can reduce the apparent contact angle θ from its equilibrium value on a rigid substrate, θ_c, as illustrated in Fig. 3.3 for a particular position of the droplet. As reported by Chaudhury [25], the difference between contact angles on two sides of a drop, say θ and θ_c in the example drawn in Fig. 3.3, will give an unbalanced force, which drives the motion of the drop. In our system, this force is periodic and depends on the shape of the contact line as well as the position of the drop on the periodic structure

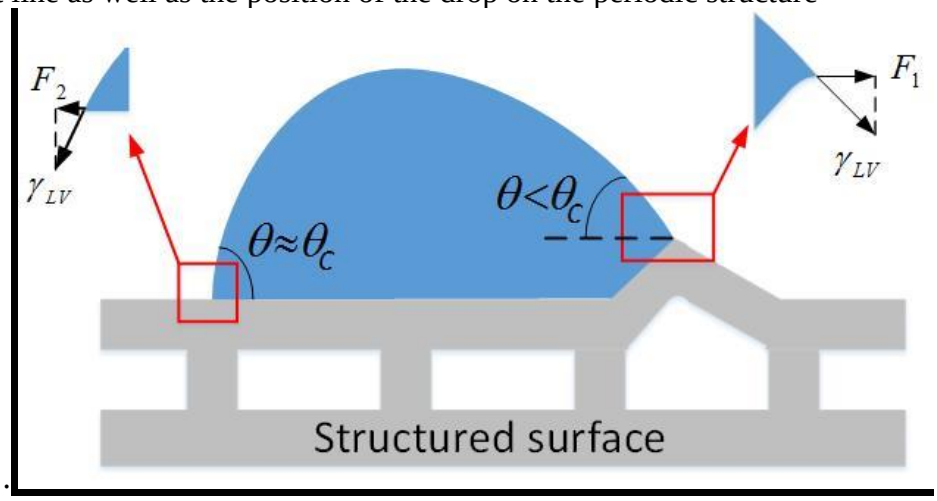

Fig. 3.3 Schematic of a cross-section of a droplet on a periodic surface, which consists a thin film on top of identical fibrils, with interfibrillar spacing *a*. The contact line on the left causes little deformation since it lies directly on top of a fibril, where the film is least compliant. In contrast, the contact line on the right lies between two ridges, where the film is most compliant. Note that since the contact line can move, the contact angle at A can be fixed at θ_c while θ decreases at *B* without violating volume conservation. Surface tension pulls the film upward, thereby deforming the structure

surface. This uplifting reduces the apparent contact angle, and the difference in contact angle at the two contact lines provides a driving force to move the drop.

In our experiments, the contact line of the droplet is irregular, parts of it lie on fibrils and the rest are on the compliant film. The elastic deformation of the film is coupled to the dynamics of motion. Furthermore, the amount of hysteresis depends on the position of the contact line and it can be very sensitive to surface impurities. Due to all these difficulties, it is extremely difficult to develop a quantitative model to compare against the experiment. In the following, we use a simple one-dimensional model that captures the key feature in this system, namely, the periodic driving force and the shrinking volume of the droplet. We use it to show that the dynamics of droplet motion can be extremely sensitive to the shape, size, and position of the droplet.

Consider a 2D droplet (a droplet that is infinitely long in the out-of-plane direction) on a one-dimensional periodic structure consisting of a thin film on top of identical parallel ridges with center-to-center spacing *a*. The geometry is the same as Fig. 3.3 except now there is only one cross-section. The droplet is constrained to move along the *x*-axis, which is perpendicular to the ridges. We choose the origin $x = 0$ to be midway between two ridges, where the film is most compliant. At time t, the coordinates of the contact lines are $x_2(t), x_1(t)$ respectively. The size of the droplet is $l(t) \equiv x_2(t) - x_1(t)$, which decreases linearly according to (see SI)

$$l(t) = l_0(1 - \beta t), \tag{3.1}$$

where l_0 is the initial size and β is an evaporation rate. As argued above, the net driving force is given by the difference in horizontal component of liquid vapor surface tension γ. We take the configuration $\theta = \theta_c$ as a reference and define a local force *F* on each of the two contact lines such that the difference between the forces,

thus defined, is the net driving force. Periodicity of the structure implies that F has the same period a. Specifically, when the contact line is on top of a ridge, that is, when $x=(2n+1)a/2$, where n is an integer, $\theta=\theta_c$ and F is at its minimum. When the contact line lies midway between two ridges, $x=na$, θ is at its minimum $\theta_{\min}$ and F reaches its maximum. Here we assume F varies sinusoidally between these two limits,

$$F(x)=\frac{1}{2}\gamma_{LV}\left(\cos\theta_{\min}-\cos\theta_c\right)\left(1+\cos\left(\frac{2\pi x}{a}\right)\right)+\gamma_{LV}\cos\theta_c \tag{3.2}$$

where γ is the surface energy of the liquid/air interface. Since the net horizontal force acting on the droplet is $F(x_2)-F(x_1)$, the center of mass $x_{cm}=(x_1+x_2)/2$ moves according to

$$M(t)\frac{d^2x_{cm}}{dt^2}=F(x_2)-F(x_1)+\mu\frac{dx_{cm}}{dt} \tag{3.3}$$

where M is the mass of the droplet which decreases with time as given by (1). The last term in (3) models the damping due to viscous flow [26]. Here we have neglected the resistance due to contact line hysteresis. We further simplify the dynamics by ignoring inertia and assume the droplet is so stiff so it is rigidly shrinking in size (justification is given in SI). With these approximations, (1-3) can be combined into one equation (see SI for details):

$$\varepsilon\frac{dX_{cm}}{dL}=\sin(L/2)\sin X_{cm}\ , \tag{3.4}$$

where $\varepsilon=\mu\beta l_0/\gamma_{LV}\left(\cos\theta_{\min}-\cos\theta_c\right)$ is a dimensionless parameter, and $X_{cm}=\pi(x_2+x_1)/a$ and $L=2\pi l/a$ are the normalized center-of-mass coordinate and length of the droplet, respectively. Since L is monotonically related to t via Eq. (3.1), it can play the role of a new time variable, as it does in Eq. (3.4), though it is important to keep in mind that L shrinks as t grows; hence, L plays the role of a *backward* time variable. Note when $X_{cm}=n\pi$, $\frac{dX_{cm}}{dt}=0$, center of mass would not move , therefore, $X_{cm}=n\pi$ are called fixed or equilibrium points. Also, notice that as L decreases

monotonically in time, the time-dependent coefficient $\sin(L/2)$ in Eq. (3.4) oscillates periodically from positive to negative values. This has the effect of alternately stabilizing or destabilizing any given fixed point. For example, the fixed point at $X_{cm}=0 \pmod{2\pi}$ is stable when the coefficient $\sin(L/2) > 0$, and unstable when $\sin(L/2) < 0$.

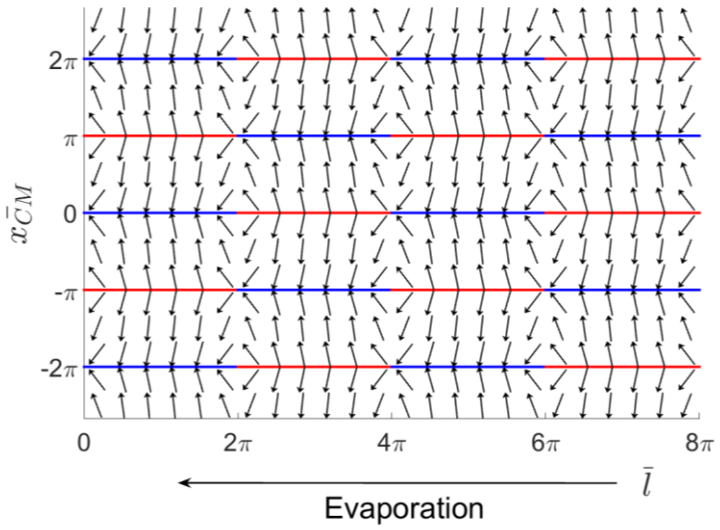

(a)

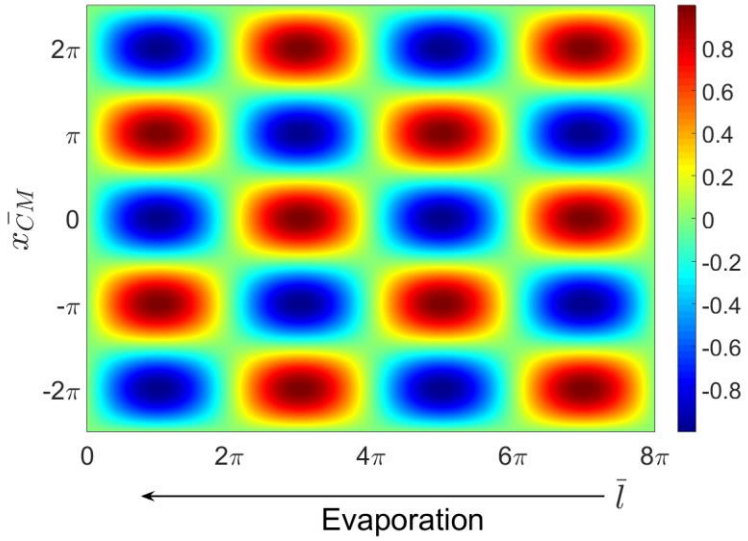

(b)

Fig. 3.4 (a) The blue lines and red lines represent locations of the droplet center of mass that are stable and unstable, respectively. The black arrows represent the velocity of the center of mass (dX_{cm}/dt) if it deviates from the stationary point. (b) Potential energy landscape (red denotes high potential and blue low potential)

Define $\Omega = (0, 2\pi] \cup (4\pi, 6\pi] \cup (8\pi, 10\pi] \cup \cdots$, $\Omega^C = (0, 2\pi] \cup (4\pi, 6\pi] \cup (8\pi, 10\pi] \cup \cdots$. Then, the stability of a general fixed point $X_F = n\pi,\ n \in Z$ can be summarized as:

$$X_F = 2k\pi \begin{cases} \text{stable if } L \in \Omega \\ \text{unstable if } L \in \Omega^C \end{cases} \tag{3.5a}$$

$$X_F = 2k\pi + \pi \begin{cases} \text{stable if } L \in \Omega^C \\ \text{unstable if } L \in \Omega \end{cases} \tag{3.5b}$$

Where *k* is any integer. If the center of mass of the drop lies at a stable fixed point, it will stay there until evaporation reduces its size by *a* so this fixed point becomes unstable; the droplet then moves to one of its neighboring fixed points. Which one of the neighboring fixed points the droplet eventually ends up is extremely sensitive to the slightest perturbation of the environment. Fig. 3.4 (a) plots the slope field of (3.4) for $\varepsilon = 0.1$ which indicates the direction of movement once the droplet is perturbed from the fixed points. The value of ε controls the speed of motion: the smaller the ε the faster the drop moves.

Another way to visualize the dynamics is to note that the right hand side of (3.4) can be interpreted as the force due to the potential $-\sin(L/2)\cos X_{cm}$ which depends on *both the normalized droplet size and position*. Fig. 3.4(b) shows the periodic energy landscape. Regions of high or low potential energies are labeled red or blue, respectively. As a drop shrinks, it will move towards regions of lower potential. In our one-dimensional system, this means that it can move right or left. Note that this simple one dimensional model would predict a "stick and go" motion, whereas in experiment the droplet motion is much more continuous even though some sudden fast motion can be observed (see Fig. 3.2(b)). This can be attributed to the three dimensional nature of the droplet where it can be stuck in one direction but ready to go in another direction.

3.4 Conclusion and discussion

We report spontaneous random motion of water droplets on a periodic film-terminated fibrillar structure. A droplet placed on such a substrate gradually becomes smaller due to evaporation. When the size of the droplet becomes small enough, it overcomes inertia and moves spontaneously and randomly. A droplet can move a considerable distance before it finally slows down and vanishes. This motion is counterintuitive for a number of reasons. First, it occurs in the absence of any overall gradients such as often drive droplet motion. Second, surface undulation and compliance usually increase contact angle hysteresis and hence might be expected to work against drop motion. However, here these are the very features that are necessary for drop motion.

Our conjecture is that the process is driven by surface free energy released during evaporation. Whereas under normal conditions this energy is dissipated, in this case our explanation is that the released energy is partially stored as elastic energy by the compliant surface. The resulting inhomogeneous deformation of the film causes spatial variation of the apparent contact angle which provides a periodic driving force, leading to large-scale spontaneous motion of the drop.

Many of the key features in our experiments, such as sensitivity to initial condition and randomness of motion, can be explained using a simple one-dimensional lattice model in which the evaporating droplet is subjected to an unbalanced (sinusoidal) force with period equal to the spacing between fibrils. The source of this force is the difference in contact angles on the two sides of the drop due to differences in deformability. The motion is damped by a viscous force that is much greater than the inertial force. This simple model explains both the observed randomness of the motion and its significant extent compared to the lattice spacing of the substrate.

There are obvious limitations in our 1D model. For example, the contact line can only occupy two positions and hence the drop can only move left or right, whereas in reality, the contact line is irregular, and both it and the drop itself can move in different directions. Also, our analysis neglects contact line hysteresis, which is an important damping mechanism. Thus our model overestimates the speed of droplet motion. Because of these simplifications, our model cannot be used to quantify observations. Nevertheless, we believe that our model captures the essential physics of the phenomenon, namely that the stability of fixed points can flip depending on the size of the droplet relative to the lattice spacing.

Our experiments have revealed a novel mechanism for spontaneous drop motion driven by the drop's own internal energy, with no external stimulus or overall gradient. Further work is needed to clarify the role of humidity in controlling droplet motion, as well as how motion is affected by drop chemistry.

3.5 Methods

The sample preparation method is similar to the process described in Glassmaker *et al.* [27]. Briefly, using standard photolithography and deep reactive ion etch techniques, arrays of circular holes of diameter $10\,\mu m$ are formed on silicon wafers. Next, the etched master silicon wafers are coated by a hydrophobic self-assembled monolayer so that the molded PDMS structure can be easily peeled off. After this step, liquid PDMS (Sylgard 184; Dow Corning;10:1 mass ratio of elastomer base to curing agent) was cast into the master silicon wafer. A clean glass slide is used to confine the material and is separated from the master by 0.635mm using a clean spacer to form the backing layer (see Fig. 1(a)). The liquid PDMS is cured at $80^{\circ}C$ for 1 hour and manually removed from the master. The resulting PDMS array with backing layer is then placed on a thin liquid PDMS film spin-coated on a glass slide. The entire

structure is then cured at $80^{\circ}C$ for an hour and then peeled off from the glass slide. In our experiment, the height *h* of the fibrils is set to be 10, 20, 30 and 40 μm and the center to center spacing *a* between the fibrils is 20, 35, 50, 65, 80, 95 and 110 μm. Fig. 3.1(f) shows a schematic of this structure.

APPENDIX 3.1

1-D MODEL SET-UP

We present a more detailed model which reduces to Eq. (3.4) in the main text under certain approximations discussed below. We consider a 2-D droplet which is constrained to move along the *x* axis only (see Fig. 3 in the main text). As noted by Chaudhury [25], when a drop is slightly out of mechanical equilibrium, the increase in energy is parabolic, so the energy profile of a drop near equilibrium can be identified with the potential energy of a spring with spring constant

$$k_s = \left.\frac{d^2U}{dl^2}\right|_V = \frac{\gamma_{LV}\sin\theta_c}{2l}\left(\frac{\sin 2\theta_c - 2\theta_c}{\theta_c\cot\theta_c - 1}\right), \qquad \text{(A3.1.1)}$$

where θ_c is the equilibrium contact angle and *l* is the contact length. Note that this is the 2-D version of the previous theory [25]. We model the drop as two equal point masses *m* connected by a spring with stiffness k_s and subjected to a periodic potential force (with period *a*) $F(x)$ at $x = x_i, i = 1,2$ (see eq. (3.2) in main text). Due to evaporation, the equilibrium length of the spring $l(t)$ is assumed to decrease linearly with time from its initial value l_0 with rate constant β. Since at equilibrium, the droplet is a spherical cap (part of a circle in 2-D), the mass of the drop *m* is related to $l(t)$ by the following relation,

$$m = \rho\frac{[l(t)]^2}{4\sin^2\theta_c}\left(\theta_c - \cos\theta_c\sin\theta_c\right), \qquad \text{(A3.1.2)}$$

where ρ is the density of water. If we assume that the rate of loss of mass is proportional to the surface area of the cap, then a simple analysis shows that $l(t)$ is a linear function of time, i.e.,

$$l(t) = l_0(1-\beta t) \qquad \text{(A3.1.3)}$$

where l_0 is the equilibrium distance at time zero and β is the evaporation rate.

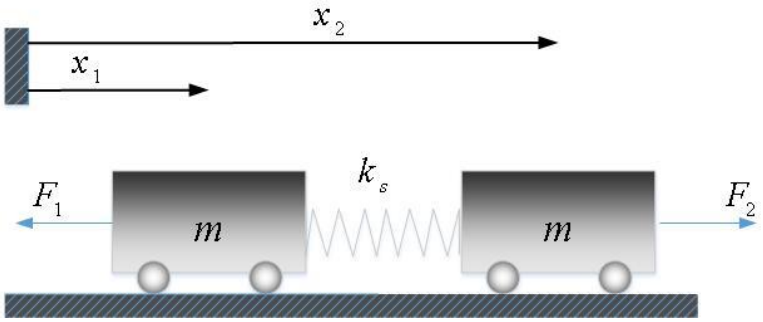

Fig. A3.1.1 Evaporating droplet is modeled as two *point* masses connected by a shrinking spring of stiffness k_s with decreasing equilibrium length $l(t)$. Periodic variation of substrate stiffness causes a periodic force (with period *a*) $F(x)$ acting on the masses where $F_1 = F(x_1)$ and $F_2 = F(x_2)$.

The periodic force F in Eq. (3.2) in main text represents the change of apparent contact angle due to variation of substrate stiffness. The motion of the drop is damped by viscous flow. Using a result due to deGennes [24], this damping force is estimated as

$$\frac{3\pi\eta}{2}\frac{dx_i}{dt} \tag{A3.1.4}$$

where η is the viscosity of the droplet. The equations of motion of the droplet, as required by Newton's law, are:

$$\begin{aligned} m\frac{d^2x_1}{dt^2} &= k_S\left(x_2 - x_1 - l(t)\right) - F(x_1) - \frac{3\pi\eta}{2}\frac{dx_1}{dt} \\ m\frac{d^2x_2}{dt^2} &= F(x_2) - k_S\left(x_2 - x_1 - l(t)\right) - \frac{3\pi\eta}{2}\frac{dx_2}{dt} \end{aligned} \tag{A3.1.5a-b}$$

Note (A3.1.5a,b) neglected damping due to contact line hysteresis.

In the following, we neglect the inertia terms since mass is proportional to l^3 which is orders of magnitude smaller than the other terms in (A3.1.5 a,b). Adding Eq. 3.4 (a) and 3.4(b), we have

$$3\pi\eta\frac{dx_{cm}}{dt}=F\left(x_2\right)-F\left(x_1\right)$$
$$=-\gamma_{LV}\left(\cos\theta_{\min}-\cos\theta_c\right)\sin\left(\frac{\pi\left(\mathrm{x}_2-x_1\right)}{a}\right)\sin\left(\frac{2\pi x_{cm}}{a}\right), \tag{A3.1.6}$$

where $x_{cm}=\left(x_1+x_2\right)/2$ is the center of mass coordinate. Since the spring constant k_s is found to be very large, the spring is approximated as a rigid bar whose length decreases linearly with time given by Eq. 3.3, that is,

$$\mathrm{x}_2-x_1=l\left(t\right). \tag{A3.1.7}$$

Next we substitute (A3.1.7) into (A3.1.6) and eliminate time by changing the independent variable from t to l and then normalize all lengths by $2\pi/a$, i.e.,

$$L=2\pi l/a,\ \ X_{cm}=2\pi x_{cm}/a, \tag{A3.1.8}$$

where *a* is the interfibrillar spacing. Finally, substitute (A3.1.8) into (A3.1.6). Then the governing equation reduces to

$$\varepsilon\frac{dX_{cm}}{dL}=\sin\left(L/2\right)\sin\left(X_{cm}\right), \tag{A3.1.9a}$$

where

$$\varepsilon\equiv\frac{3\pi\eta\beta l_0}{\gamma_{LV}\left(\cos\theta_{\min}-\cos\theta_c\right)}. \tag{A3.1.9b}$$

Although (A3.1.9a) has an exact solution

$$\frac{\left|\tan\left(X_{cm}/2\right)\right|}{\left|\tan\left(X_{cm0}/2\right)\right|}=\exp\left[\frac{2}{\varepsilon}\left(\cos\left(L_0/2\right)-\cos\left(L/2\right)\right)\right], \tag{A3.1.10}$$

where $X_{cm0}\equiv X_{cm}(L_0=2\pi l_0/a)$, it is difficult to interpret, particularly because we are interested in the stability of the dynamical system. The equilibrium or fixed points of (A3.1.9a) are the roots of $\sin X_{cm}$, which are $X_F=n\pi$. For even n, the center of mass sits on the middle of two fibrils, whereas for odd *n*, it sits on top of a fibril. Because the system is non-autonomous, the stability of these fixed points depends on the droplet size, *L*. Since $\sin X_{cm}$ has period 2π, it is sufficient to consider the stability of the fixed points at $X_F=0,\pi$. Note since $dt=-dl$, X_F is a stable (unstable) equilibrium point if and only if $dX_{cm}/dL>0$ (<0) in a small punctured

neighborhood about 0 or π). Expansion about $X_{cm}=0$ shows that $X_F=0$ is a stable fixed point if and only if $\sin(L/2)>0$, that is, if

$$L\in\Omega=\bigcup_{k=1}\left(4k\pi,4k\pi+2\pi\right]. \tag{A3.1.11}$$

Conversely, $X_F=0$ is an unstable fixed point if and only if $\sin(L/2)<0$, that is, when L lies in the complement of Ω, i.e.,

$$L\in\Omega^c=\bigcup_{k=1}\left(4k\pi+2\pi,4k\pi+4\pi\right] \tag{A3.1.12}$$

The same line of reasoning allows us to conclude that

$$X_F=\pi\ \begin{cases}\text{stable if } L\in\Omega^c\\ \text{unstable if } L\in\Omega\end{cases} \tag{A3.1.13a,b}$$

Note since L always decreases with time, the boundary points at $2\pi,6\pi,\cdots,(4k+2)\pi,\cdots$ are the specific sizes when the transition of stability can occur. When drop size reaches these values, with a slight perturbation, it can move from one stable equilibrium point to another. The rate of this movement between adjacent equilibrium points depends on ε. For small ε, the center of mass of the droplet moves rapidly to one of its neighboring fixed points when $X_{cm}\neq X_F$ ((A3.1.10) shows that the approach is exponentially fast). In this case, the droplet spends most of its time resting at a stable fixed point, until evaporation reduces its size so this fixed point becomes unstable, after which the droplet moves rapidly to one of its neighboring fixed points. This scenario is shown in Fig. A3.1.2 (a) where (A3.1.9a) is integrated numerically using $\varepsilon=0.001$ with initial condition $X_{CM}=0.1$. The choice of equilibrium point depends on numerical errors. On the other hand, if ε is of order 1, then droplet spends more time transitioning from fixed point to fixed point and the motion appears to be continuous. This scenario is shown in Fig. A3.1.2 (b) where (A3.1.9 (a)) is integrated numerically using $\varepsilon=0.5$ with the same initial condition. In both cases, which one of the neighboring fixed points the droplet eventually ends up at

is extremely sensitive to the slightest perturbation of the environment (e.g. the time step in our integration scheme).

The value of ε estimated using (A3.1.9 (b)) and the viscosity of water is found to be very small. This gives velocity distributions that are almost discontinuous: the velocity of a drop is either almost zero or infinite (see Fig. A3.1.2 (b)). This feature is qualitatively consistent with the data given in Fig. A3.2.1 which indicates that the velocity distribution with time is interspersed with spikes. However, the velocities observed in the experiments are neither zero nor infinity which indicates that our estimate of ε is too small. We attribute this discrepancy to the fact that PDMS is a viscoelastic solid, so most of the dissipation occurs by viscoelastic dissipation due to the motion of contact line, instead of by local fluid flow.

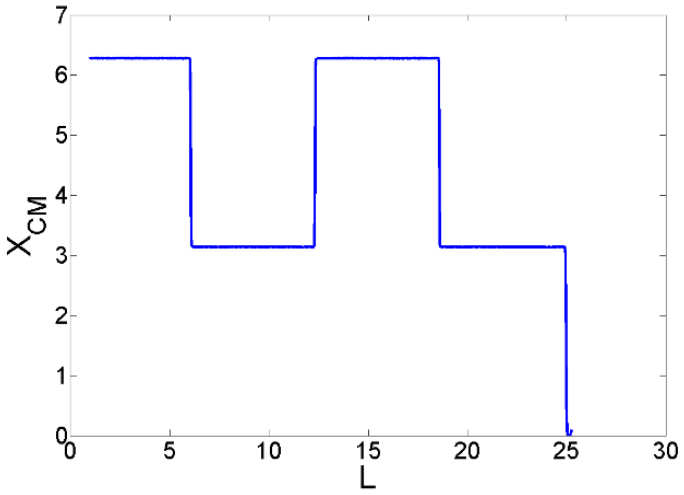

(a)

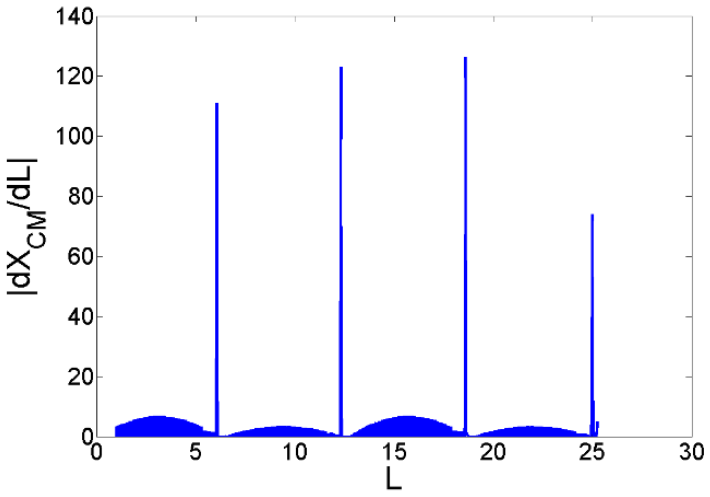
140
120
100
80
60
40
20
0
0
5
10
15
20
25
30
L
|dX_CM/dL|

(b)

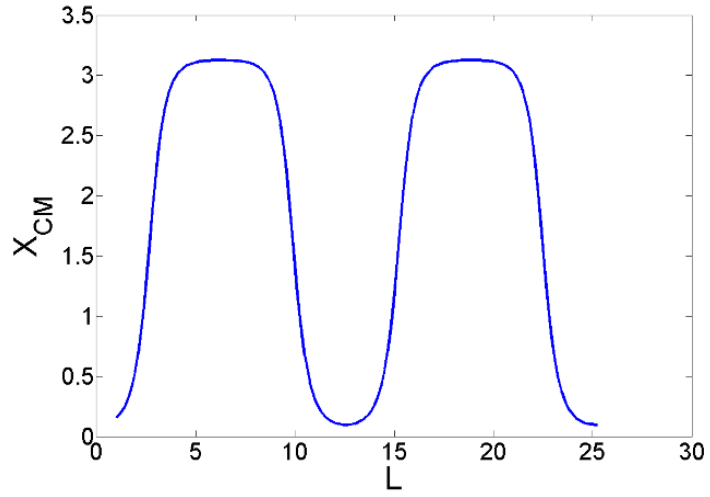
3.5
3
2.5
2
1.5
1
0.5
0
0
5
10
15
20
25
30
L
X_CM

(c)

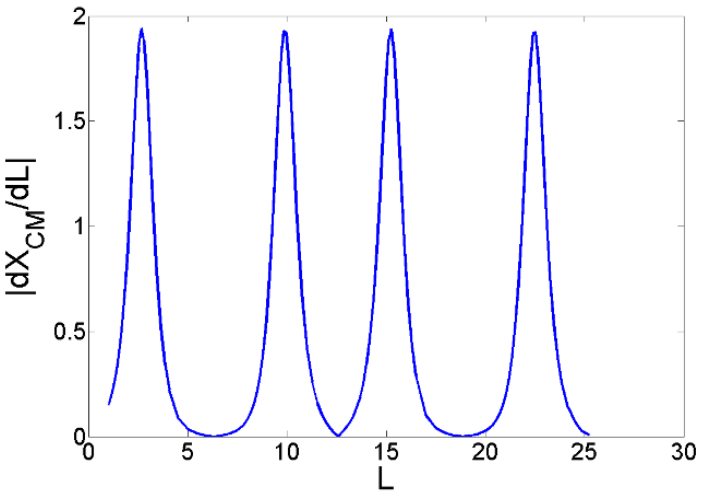

(d)

Fig. A3.1.2 (a), (b) The motion and velocity of droplet center of mass for $\epsilon = 0.001$. Note here that since L represents a backward time variable (see (A3.1.3)), $\frac{dX_{CM}}{dL}$ is a measure of velocity. (c), (d) The motion and velocity of droplet center of mass for $\epsilon = 0.5$.

APPENDIX 3.2

TRAJECTORIES AND VELOCITY DISTRIBUTION FOR SAMPLES WITH DIFFERENT FIBRIL HEIGHT AND SPACING

Trajectories and velocity distributions for samples with different fibril height and spacing are given in figures below. We indicate the fibril height and spacing in a figure by the notation xx.yy. Here xx denote the fibril height and yy denote the spacing. For example, Fig.A3.2.1 (10.20) means that the fibril height and spacing are 10 and 20 μm respectively. The fibril spacing are indicated by a scale bar in all the trajectory figures. These trajectory figures support our claim that droplet motion is random and droplets can move distances much greater than spacing. The velocity distribution figures show that motion of droplets is jerky which is in qualitative agreement with our model.

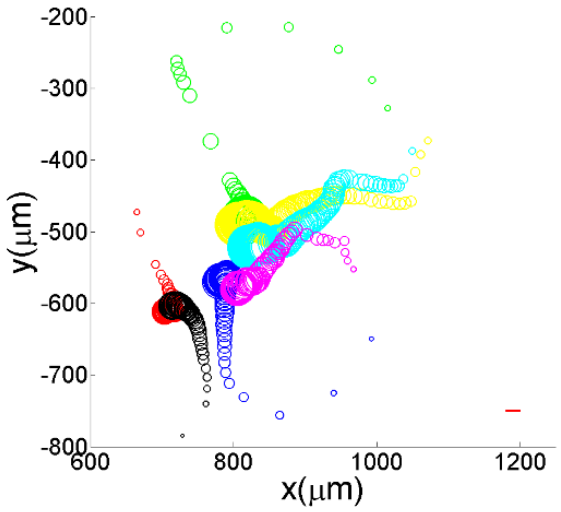

(a)

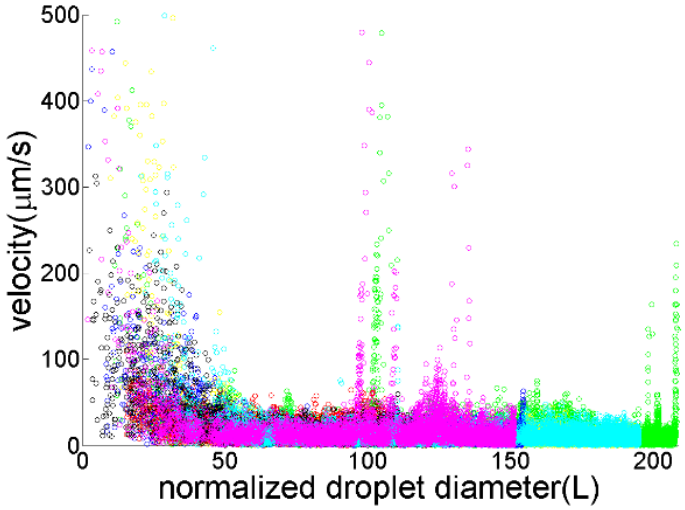

(b)

Fig. A3.2.1 (10.20)

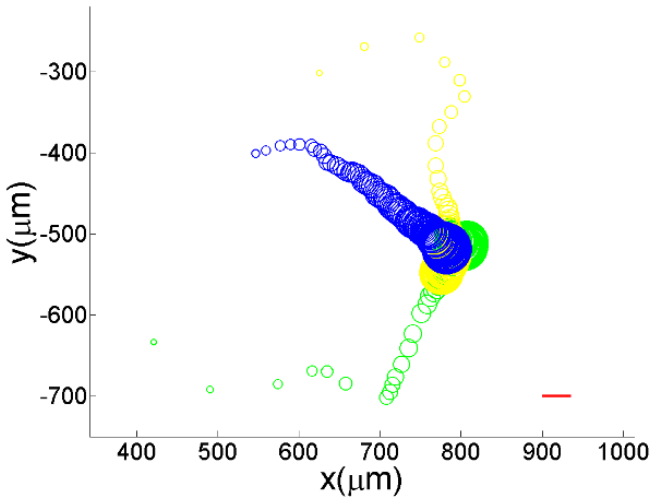

(a)

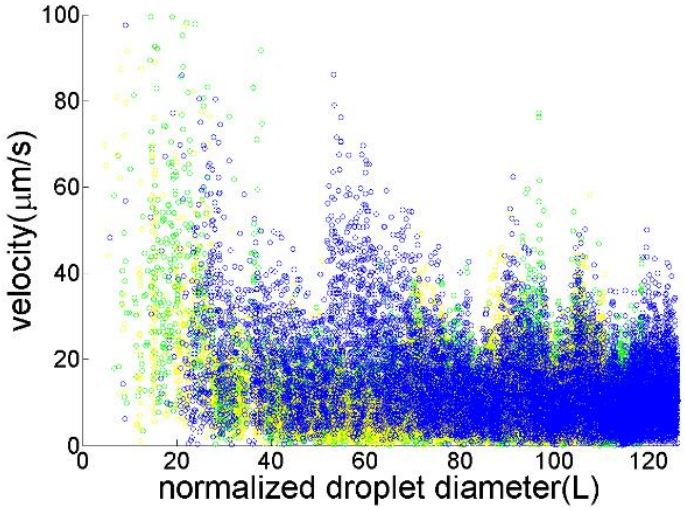

(b)

Fig. A3.2.1 (10.35)

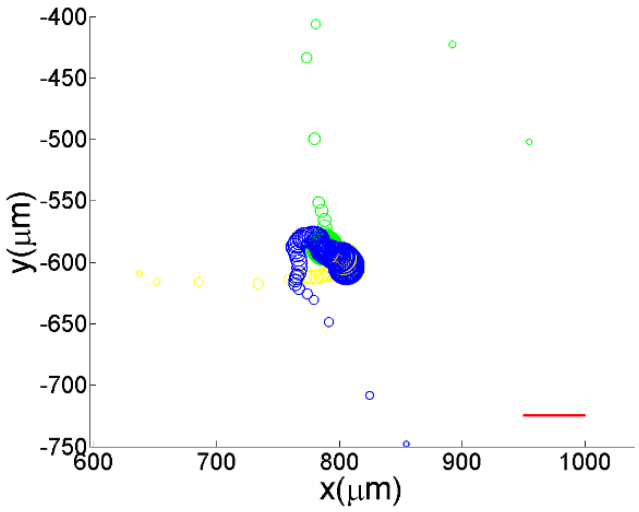

(a)

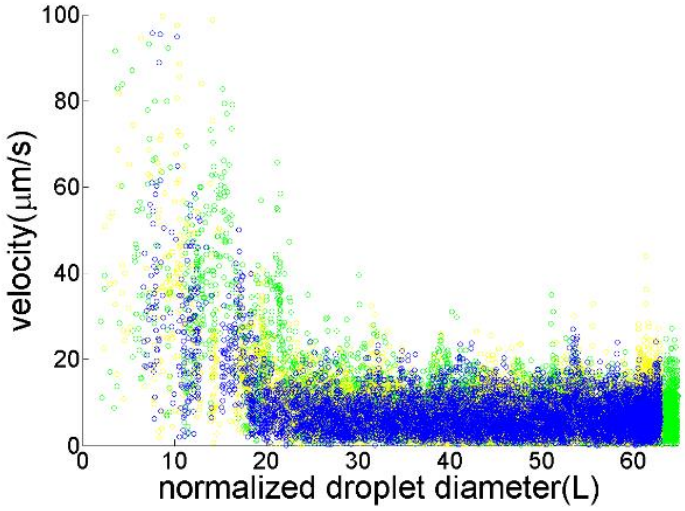

(b)

Fig. A3.2.1 (10.50)

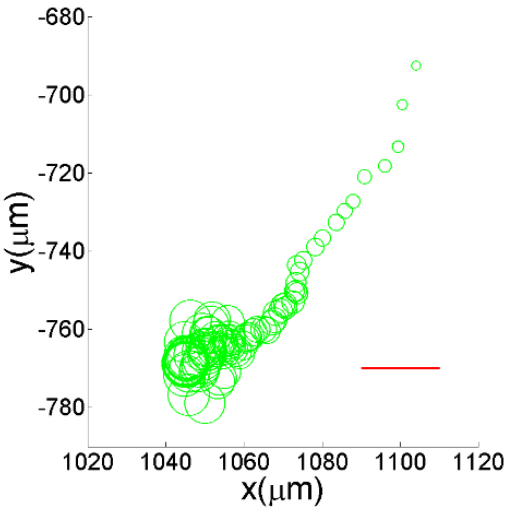

(a)

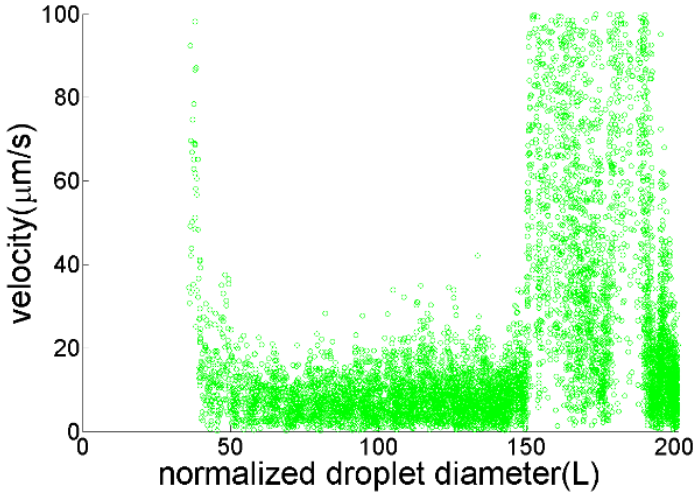

(b)

Fig. A3.2.1 (20.20)

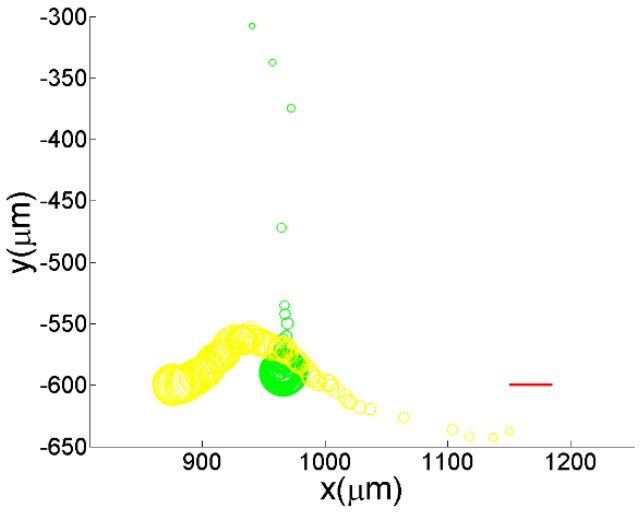

(a)

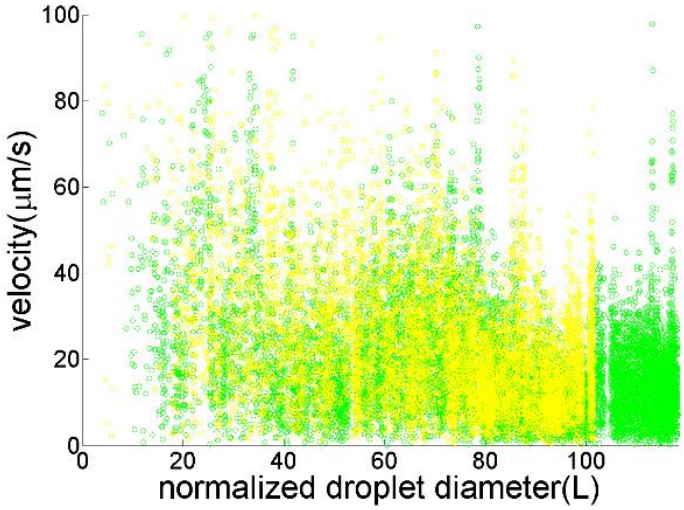

(b)

Fig. A3.2.1 (20.35)

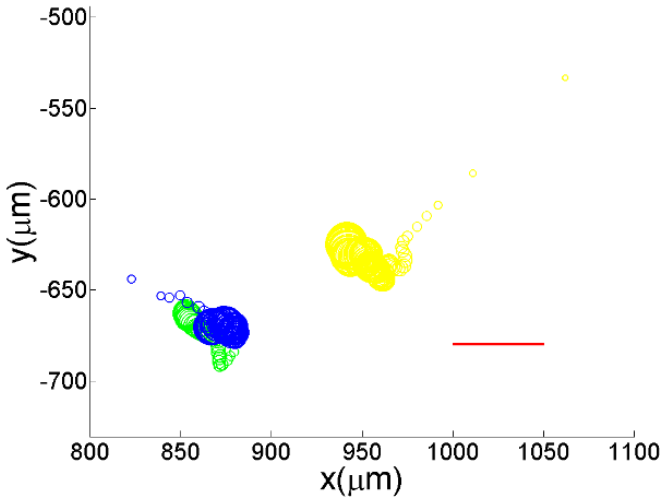

(a)

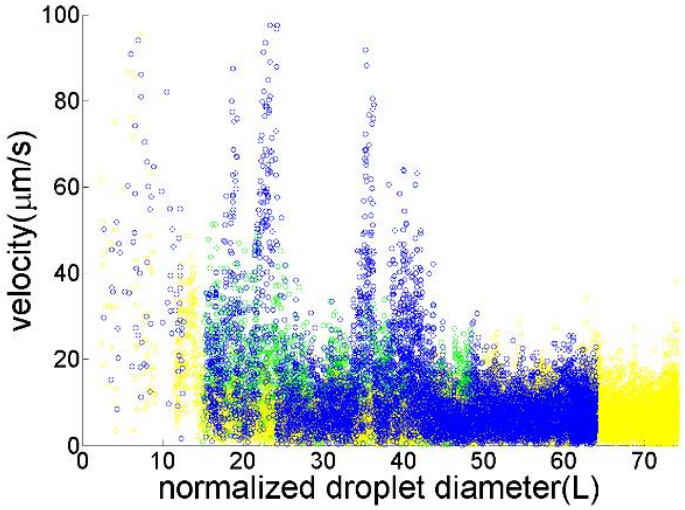

(b)

(Fig. A3.2.1) (20.50)

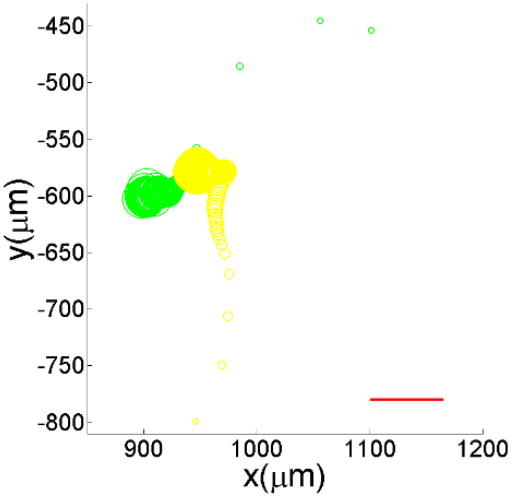

(a)

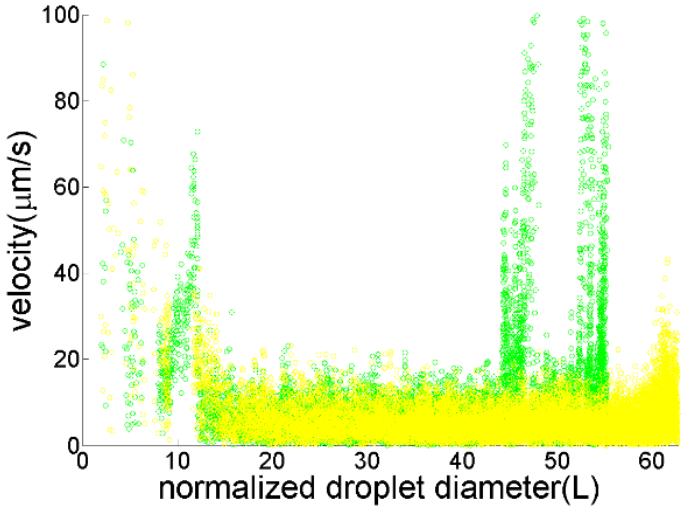

(b)

Fig. A3.2.1 (20.65)

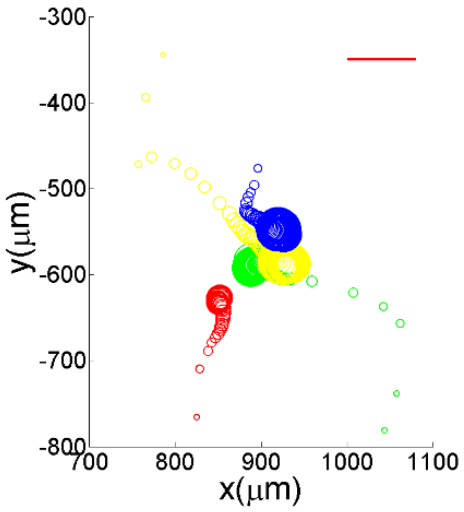

(a)

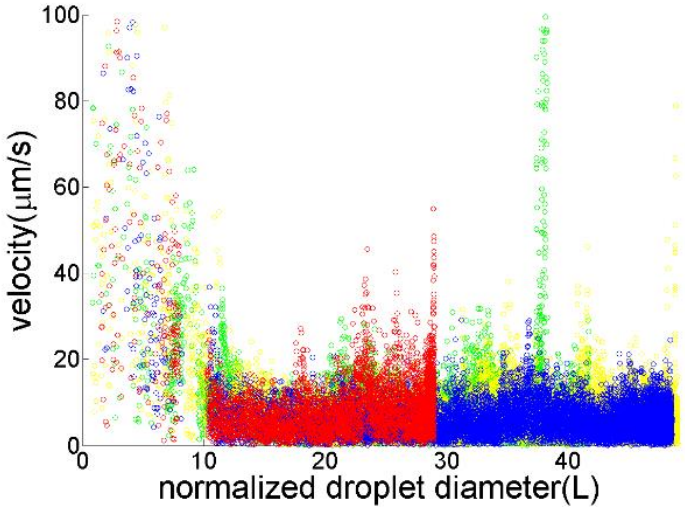

(b)

Fig. A3.2.1 (20.80)

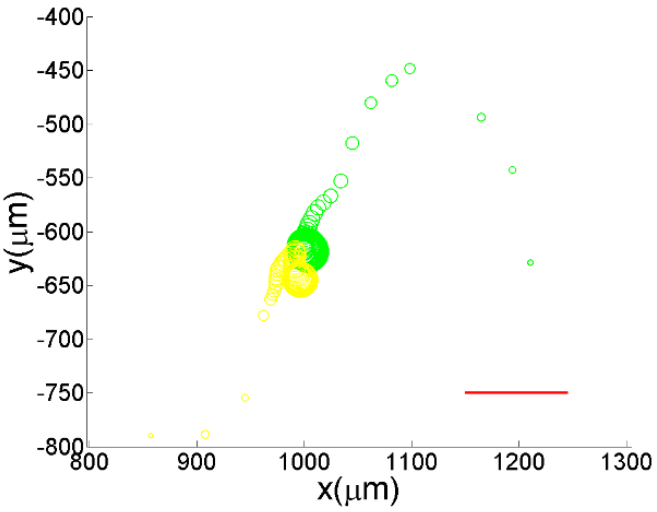

(a)

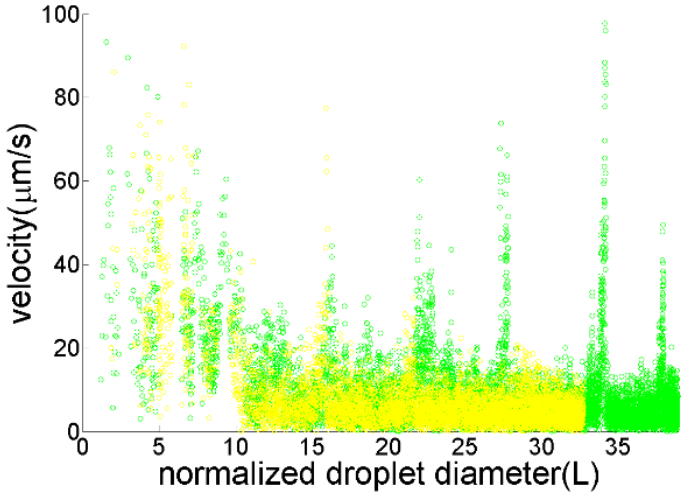

(b)

Fig. A3.2.1 (20.95)

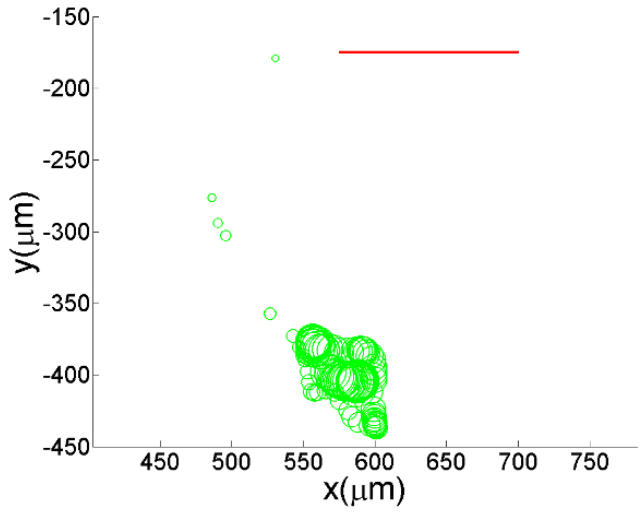

(a)

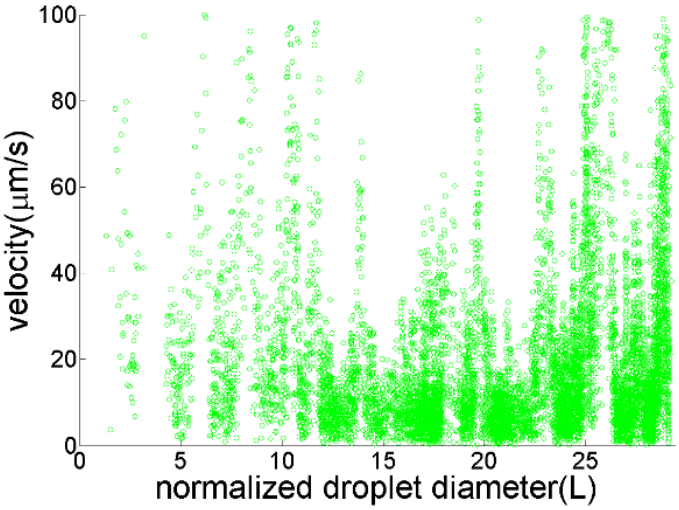

(b)

Fig. A3.2.1 (20.125)

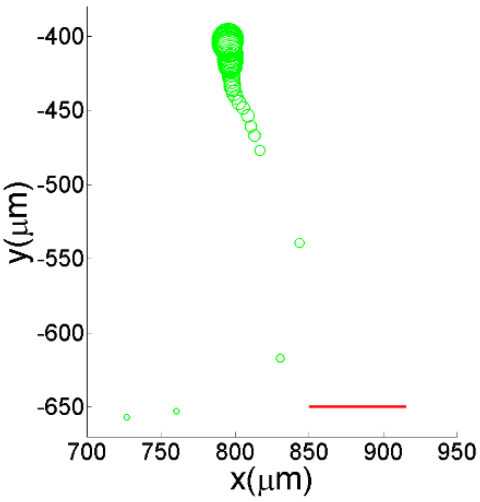

(a)

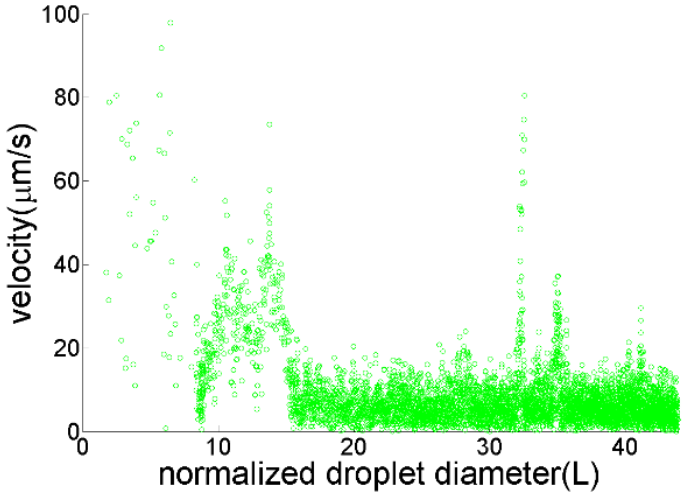

(b)

Fig. A3.2.1 (30.65)

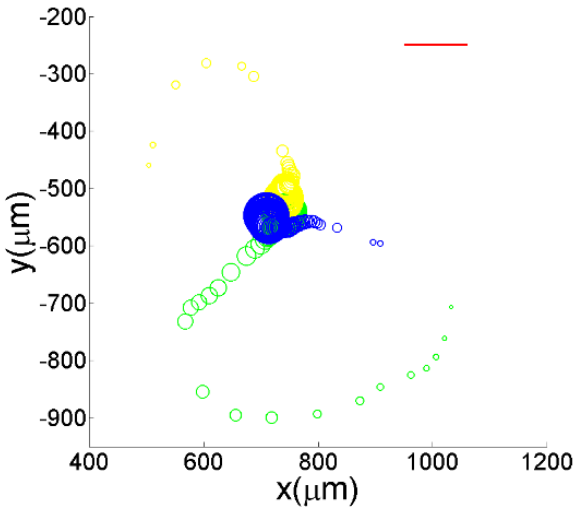

(a)

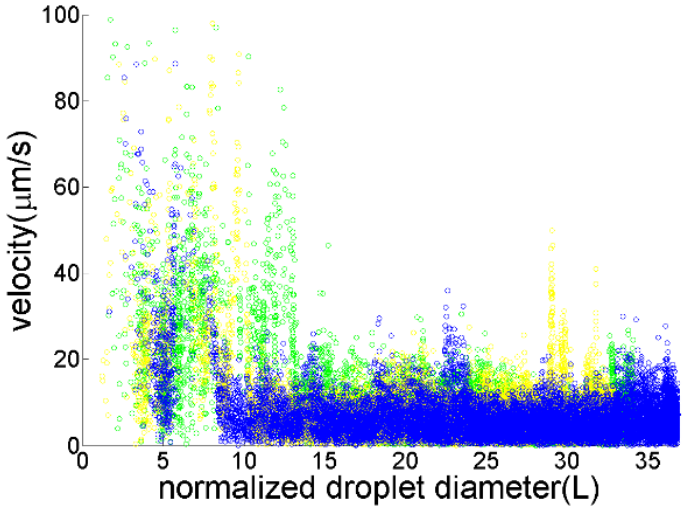

(b)

Fig. A3.2.1 (30.110)

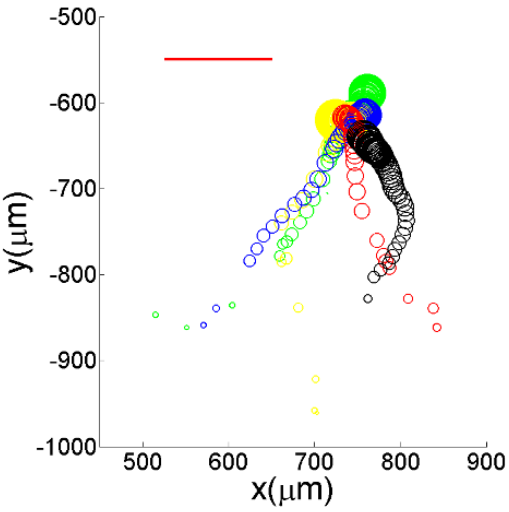

(a)

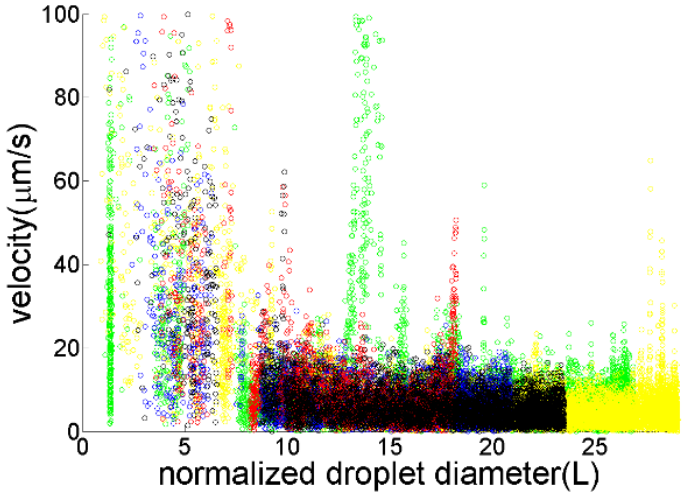

(b)

Fig. A3.2.1 (30.125)

REFERENCES

[1] T. M. Squires and S. R. Quake, Rev. Mod. Phys. **77**, 977 (2005).

[2] M. Srinivasarao, Science (80-.). **292**, 79 (2001).

[3] M. G. Pollack, A. D. Shenderov, and R. B. Fair, Lab Chip **2**, 96 (2002).

[4] X. Zhang, F. Shi, J. Niu, Y. Jiang, and Z. Wang, J. Mater. Chem. **18**, 621 (2008).

[5] C. Lv, C. Chen, Y.-C. Chuang, F.-G. Tseng, Y. Yin, F. Grey, and Q. Zheng, Phys. Rev. Lett. **113**, 26101 (2014).

[6] S. Daniel and M. K. Chaudhury, Langmuir **18**, 3404 (2002).

[7] S. Daniel, M. K. Chaudhury, and P.-G. de Gennes, Langmuir **21**, 4240 (2005).

[8] C. Lv and P. Hao, Langmuir **28**, 16958 (2012).

[9] A. M. Cazabat, F. Heslot, S. M. Troian, and P. Carles, Nature **346**, 824 (1990).

[10] S. Daniel, M. K. Chaudhury, and J. C. Chen, Science **291**, 633 (2001).

[11] P. Lazar and H. Riegler, Phys. Rev. Lett. **95**, 136103 (2005).

[12] J. B. Brzoska, F. Brochard-Wyart, and F. Rondelez, Langmuir **9**, 2220 (1993).

[13] M. K. Chaudhury and G. M. Whitesides, Science **256**, 1539 (1992).

[14] K. Ichimura, Science (80-.). **288**, 1624 (2000).

[15] Y. Zheng, H. Bai, Z. Huang, X. Tian, F.-Q. Nie, Y. Zhao, J. Zhai, and L. Jiang, Nature **463**, 640 (2010).

[16] H. A. Stone, A. D. Stroock, and A. Ajdari, Annu. Rev. Fluid Mech. **36**, 381 (2004).

[17] Y. Sumino, N. Magome, T. Hamada, and K. Yoshikawa, Phys. Rev. Lett. **94**, 68301 (2005).

[18] B. S. Gallardo, V. K. Gupta, F. D. Eagerton, L. I. Jong, V. S. Craig, R. R. Shah, and N. L. Abbott, Science (80-.). **283**, 57 (1999).

[19] R. W. Style, Y. Che, S. J. Park, B. M. Weon, J. H. Je, C. Hyland, G. K.

German, M. P. Power, L. A. Wilen, J. S. Wettlaufer, and E. R. Dufresne, Proc. Natl. Acad. Sci. U. S. A. **110**, 12541 (2013).

[20] G. Lagubeau, M. Le Merrer, C. Clanet, and D. Quéré, Nat. Phys. **7**, 395 (2011).

[21] N. J. Cira, A. Benusiglio, and M. Prakash, Nature **519**, 446 (2015).

[22] S. Vajpayee, A. Jagota, and C.-Y. Hui, J. Adhes. **86**, 39 (2010).

[23] A. Jagota and C.-Y. Hui, Mater. Sci. Eng. R Reports **72**, 253 (2011).

[24] M. Scherge and S. S. Gorb, *Biological Micro- and Nanotribology* (Springer Berlin Heidelberg, Berlin, Heidelberg, 2001).

[25] M. K. Chaudhury, A. Chakrabarti, and S. Daniel, Langmuir **31**, 9266 (2015).

[26] P. de Gennes, Rev. Mod. Phys. **57**, 827 (1985).

[27] N. J. Glassmaker, A. Jagota, C.-Y. Hui, W. L. Noderer, and M. K. Chaudhury, Proc. Natl. Acad. Sci. U. S. A. **104**, 10786 (2007).

CHAPTER 4

INDENTATION OF A RIGID SPHERE INTO AN ELASTIC SUBSTRATE WITH SURFACE TENSION AND ADHESION [3]

4.1 Introduction

A fundamental problem in adhesion science is the contact between a rigid sphere and an elastic substrate. For small deformation where the contact radius a is small in comparison with the radius of the sphere R, the solution was derived by Hertz [1]. Hertz theory assumes adhesion-less contact; as a result, the traction on the contact region is compressive everywhere and vanishes at the contact line. In 1971, Johnson, Kendall and Roberts (JKR) [2] extended Hertz theory to allow for adhesion. In essence, they treated the contact line as the tip of an external crack; the equilibrium relation between the applied load and the contact radius was obtained by equating the energy release rate of this crack to the interfacial work of adhesion.

The JKR theory has been extremely successful in describing the adhesive contact of elastic spheres. It is therefore surprising to find that recently observed deformations of soft substrates, such as plasticized polystyrene [3], hydrogels [4] and silicone gels [5] caused by adhesion of hard microparticles or nanoparticles, in the absence of external load, deviate considerably from JKR theory. For example, Style *et al.* [5] have reported that the power-law relation between the contact radius a (indentation depth δ) and sphere radius R changes from $a \propto R^{2/3}$ $\left(\delta \propto R^{1/3}\right)$ to $a \propto R$ $\left(\delta \propto R\right)$ as the sphere reduces in size or the substrate becomes softer. The transition in scaling observed in these experiments has been interpreted as a corresponding underlying transition from the JKR limit where the adhesion-driven deformation is primarily

[3] Hui C.Y., Liu T., Salez T., Raphael E., Jagota A., (2015). Proc. R. Soc. A Math. Phys. Eng. Sci. **471**, 20140727.

resisted by bulk elasticity, to the "liquid" limit where the adhesion-driven deformation is primarily resisted by the substrate-air surface tension.

Style *et al.* [5] noted that these deviations can be explained by the fact that JKR theory does not account for the role of the substrate-air surface tension in resisting deformation. More specifically, in JKR theory, the work done by the surface tensions upon change in surface area is neglected in the calculation of the energy release rate. Since decreasing the substrate elastic modulus or the sphere radius increases the relative contribution of surface tension to the energy release rate, it is not surprising that the JKR theory breaks down for sufficiently soft substrates or small spheres.

Using a large deformation Finite Element Model which incorporates both substrate –air surface tension and nonlinear-elasticity, Xu *et al.* [6] have computed the energy release rate for the problem of a rigid sphere in adhesive contact with a neo-Hookean substrate in the absence of external load. Their numerical results show a transition from the elasticity dominated regime where $a \propto R^{2/3}$ to the surface tension dominated regime where $a \propto R$. This transition depends on the single elasto-capillary number $\alpha \equiv \sigma/(2\mu R)$ - small α favors elasticity whereas large α favors surface tension. Their results are found to be in good agreement with the experiments reported by Style *et al.* [5]. This transition in scaling has been verified using molecular dynamics simulations by Cao *et al.* [7].

Although hard particles are used in the above reported experiments, a similar transition is expected for soft particles on a rigid surface. For example, Lau *et al.* reported some preliminary observation of such effects with spontaneous adhesion of latex nanoparticles [8]. The transition from the JKR limit to the liquid limit for a soft sphere on a rigid substrate in the absence of external load was also studied by Salez *et al.* [9] using an ad-hoc thermos-dynamical approach. These works illustrate that the

departure from JKR scaling represents the increasing influence of solid surface stress in resisting the adhesion-driven deformation.

The spheres in the aforementioned experiments and theories are subjected to zero external load. This is a special case of the more general situation in which deformation and contact are driven by some combination of external load and work of adhesion at the contacting interface. The solution for Hertzian contact between a rigid cylinder and an elastic half-space with indentation force was given by Long *et al.* [10]. For the case of a soft sphere on a rigid half space, a molecular dynamics simulation and a scaling analysis of this problem were reported by Carrillo and Dobrynin [11]. The theoretical analysis is much more complicated if an external load is applied, and the goal of this article is to provide a rigorous analysis of this problem using a continuum mechanics approach.

4.2 Statement of Problem and Summary of Approach

Our system is shown in Fig. 4.1. A rigid sphere of radius R is brought into contact with the flat surface of a substrate by a vertical force P. The substrate initially occupies the half-space $z > 0$ and is assumed to be linearly elastic, isotropic and incompressible, with shear modulus μ and Poisson's ratio $\nu = 0.5$. Just as in JKR theory, our analysis is based on small deformation theory where the displacements and strains are small. We also assumed that the surface stress tensor is isotropic, so it can be represented by the scalar surface tension σ. Since the materials with which we are concerned are isotropic in the plane of the surface, the surface stress is expected to be isotropic as well and can be represented by a single number, σ, the scalar surface tension. This assumption has also been made by a number of other investigators and is validated by the good agreement between the resulting models and experiments [12].

Note that, in general, the surface tension of a solid does not need to be the same as its surface tension. For a detailed discussion, consult [13,14].

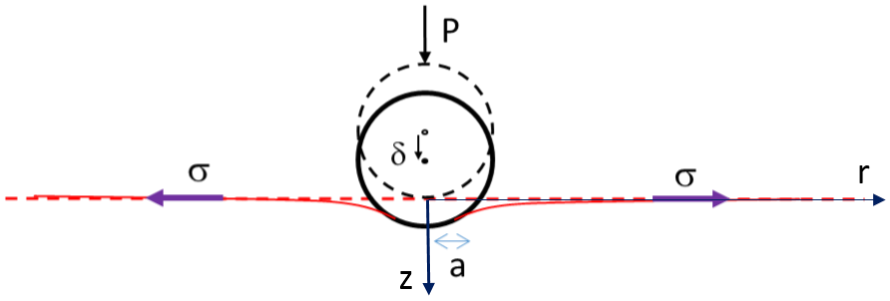

Fig. 4.1 A rigid sphere of radius R is indented by a vertical force P, bringing it into no-slip contact with the surface of an incompressible isotropic elastic half-space. The indentation is resisted by the elasticity of the substrate as well as the substrate-air surface tension σ.

In contrast to JKR theory, which assumes frictionless contact, we assume a no-slip contact condition. That is, a material point on the substrate surface is held fixed once it comes into contact with the rigid sphere. Under this boundary condition, we only need to specify the surface tension of the non-contacting part of the substrate surface. Without the no-slip condition, one would have to introduce a new parameter into the model – the interfacial surface tension in the contact region. In general, the no-slip contact condition will induce shear stress in the contact region. However, a classical result in linear elasticity states that the no-slip boundary condition is consistent with a vanishing shear stress provided that the sphere is rigid and the substrate is incompressible and infinite in extent [1]. Fortunately, for most elastomers and hydrogels, incompressibility is an excellent approximation.

As in JKR theory, our approach is based on energy balance, that is, the relation between the contact radius and the applied load is obtained by setting the energy release rate G of the external crack (the air gap between the sphere and the surface of

the substrate outside the contact zone) equal to the interfacial work of adhesion, W_{ad}. The key novel feature is the inclusion of the substrate-air surface tension in the calculation of G.

Suppose we are able to obtain the "Hertz-like" solution of the contact problem, that is, the relation between force, $P_H(a)$, indentation displacement, $\delta_H(a)$, and contact radius, *a*, in the absence of any adhesive forces. Note that the subscript *H* in P_H and δ_H refers to adhesion-less contact, and these quantities in general depend on the air-substrate surface tension. For the special case of zero surface tension, P_H and δ_H reduce to the classical Hertz solution. Having this solution automatically also means that we know the contact compliance,

$$C(a) = d\delta_H / dP_H = \frac{d\delta_H}{da} / \frac{dP_H}{da}. \tag{4.1}$$

This information suffices to determine the change of potential energy of the system (not counting interfacial work of adhesion) per unit change in contact area, i.e., the energy release rate, as a function of contact area. Specifically, as previously shown by Vajpayee *et al*. [15], the energy release rate, G, is given by

$$G = -\frac{1}{4\pi a}\frac{dC}{da}\left(P - P_H\right)^2 = -\frac{1}{4\pi a C^2}\frac{dC}{da}\left(\delta - \delta_H\right)^2. \tag{4.2a,b}$$

where *P* and δ are respectively the applied load and indentation depth (see Fig. 4.1) of the adhesive contact problem.

4.2.1 The JKR limit

As an example, consider the classical Hertz theory without surface tension [1],

$$P_H = \frac{16\mu a^3}{3R},\ \delta_H = \frac{a^2}{R} \Rightarrow C = \frac{1}{8\mu a}, \tag{4.3a}$$

Substituting (4.3a) into (4.2a) and enforcing the energy balance equation $G = W_{ad}$ recovers the JKR theory for a rigid sphere in adhesive contact with an incompressible elastic half-space,

$$P = \frac{16\mu a^3}{3R} - 4\sqrt{2\pi\mu a^3 W_{ad}}\,. \tag{4.3b}$$

The indentation depth versus contact radius relation can be obtained using (4.2b) and (4.3a):

$$\delta = \frac{a^2}{R} - \sqrt{\frac{\pi a W_{ad}}{2\mu}}\,. \tag{4.3c}$$

Thus, the main thrust of our analysis is to determine how the Hertz-like load and Hertz-like displacement (and hence the instantaneous compliance) are affected by the presence of substrate-air surface tension.

4.2.2 The surface tension dominated or the partial wetting liquid-like limit

Before tackling the general problem of the transition from the regime where resistance to deformation is dominated by elasticity (Eqns. 4.3a-c) to the surface tension dominated limit, we examine the limiting "liquid-like" case in which substrate-air surface tension dominates over elasticity. The free-body diagram in Fig. 4.2 shows that force balance requires

$$P = 2\pi\sigma a \sin\left(\theta - \theta_p\right), \tag{4.4}$$

where $\theta = \sin^{-1}(a/R)$ and θ_p is the peel angle. The energy release rate G can be computed using Kendall's peel theory [16]:

$$G = \sigma\left(1 - \cos\theta_p\right)\,. \tag{4.5}$$

By setting $W_{ad} = \sigma + \gamma_{RA} - \gamma_{RS}$, the energy balance equation $G = W_{ad}$ is equivalent to the Young-Dupre equation

$$\gamma_{RS} + \sigma\cos\left(\pi - \theta_p\right) = \gamma_{RA}\,, \tag{4.6}$$

where the γ's are the surface energies and where the subscripts R, S, A stand for rigid sphere, compliant substrate and air atmosphere respectively. Note that in (6) we have used surface energies instead of surface tensions, since the Young-Dupre equation is based on energy balance; for a detailed discussion see [17]. Note also that in the liquid-like limit, we have assumed the surface tension and surface energy of the air-

substrate interface to have the same value. Using the small angle approximation, the energy balance equation becomes

$$\frac{\sigma\theta_p^2}{2} = W_{ad}\,. \tag{4.7}$$

Substituting (4.7) into (4.4) and using the small angle approximation $\sin\theta_p \approx \theta_p$ gives the relation between applied load and contact radius in the liquid limit:

$$P = \frac{2\pi\sigma a^2}{R} - 2\pi a\sqrt{2\sigma W_{ad}}\,. \tag{4.8}$$

Eq. (4.8), which, when specialized to the zero force case, gives a contact radius of

$$a_0^{Liquid} = R\sqrt{2W_{ad}/\sigma}\ , \tag{4.9}$$

that is directly proportional to the sphere radius *R*. The scaling predicted by (4.9) is consistent with the experiments of Style *et al*. [5] who showed that when a small sphere is placed on the surface of a soft gel (with practically zero external force), the contact radius scales linearly with the radius instead of to the power 2/3 predicted by JKR theory.

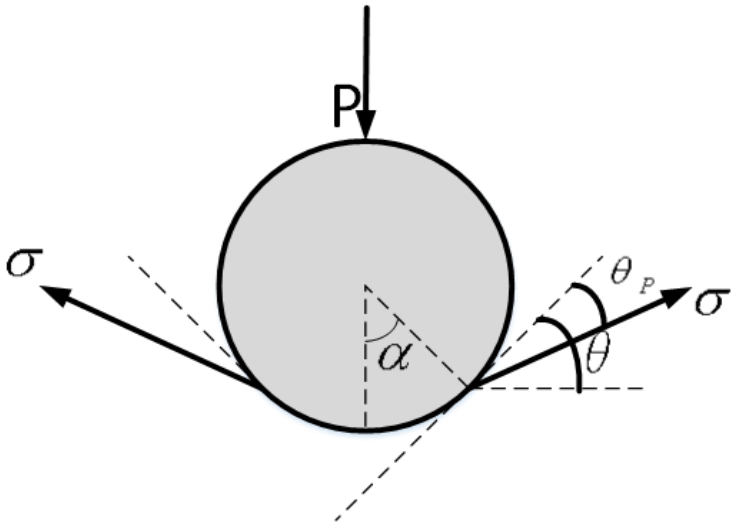

Fig. 4.2: Free body diagram showing the forces acting on the sphere in the partial wetting liquid-like limit.

4.2.3 Comparison between the JKR limit and the partial wetting liquid-like limit

The effect of surface tension is most evident by comparing the JKR limit with the partial wetting liquid-like limit by plotting (4.3b) and (4.8) in Fig. 4.3 (a,b). As noted by Chaudhury *et al.* [18], in the JKR limit a plot of $\left(a/R\right)^{3/2}$ versus $P/\left(4\sqrt{2\pi\mu W_{ad}a^3}\right)$ gives a straight line with slope $3/\left(4\sqrt{\mu R/(2\pi W_{ad})}\right)$ and horizontal intercept -1 (see insert of Fig. 4.3 (a)). In the surface tension dominated limit, this plot is not a straight line. Instead, as shown in the insert of Fig. 4.3b, a/R versus $P/\left(2\pi a\sigma\right)$ is a straight line with slope 1 and horizontal intercept $-\sqrt{2W_{ad}/\sigma}$.

In a load controlled test [1], the sphere jumps out of contact at a contact radius of

$$a_{off}^{Elastic} = \frac{1}{2}\left(\frac{9\pi W_{ad}}{4\mu}\right)^{1/3} R^{2/3} \ . \tag{4.10a}$$

The pull-off load at this instability is

$$P_{off}^{Elastic} = -\frac{3}{2}\pi R W_{ad} \ . \tag{4.10b}$$

The corresponding quantities in the surface tension dominated limit are:

$$a_{off}^{Liquid} = \sqrt{\frac{W_{ad}}{2\sigma}}R \, , \tag{4.11a}$$

$$P_{off}^{Liquid} = -\pi W_{ad} R \, , \tag{4.11b}$$

respectively. Comparing (4.10b) and (4.11b), one sees that in the liquid limit the magnitude of the pull-off load is reduced by 1/3 compared with the JKR limit. More importantly, (4.10a) and (4.11a) show that the contact radius at pull-off scales very differently with the sphere radius, despite the fact that the scaling for the pull-off forces are the same.

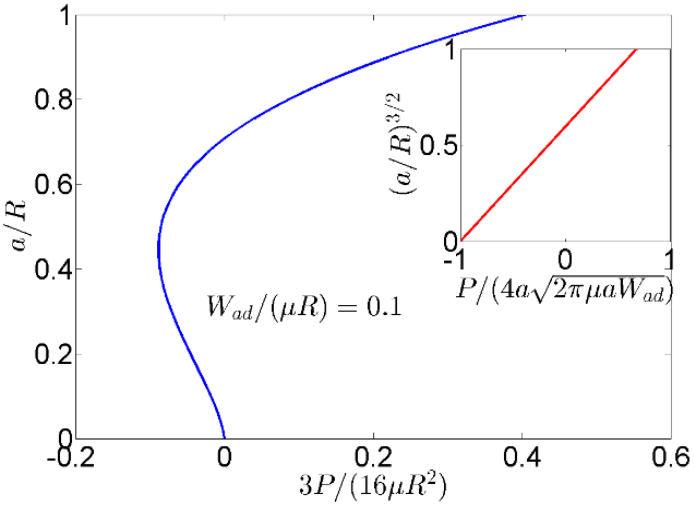

(a) JKR solution

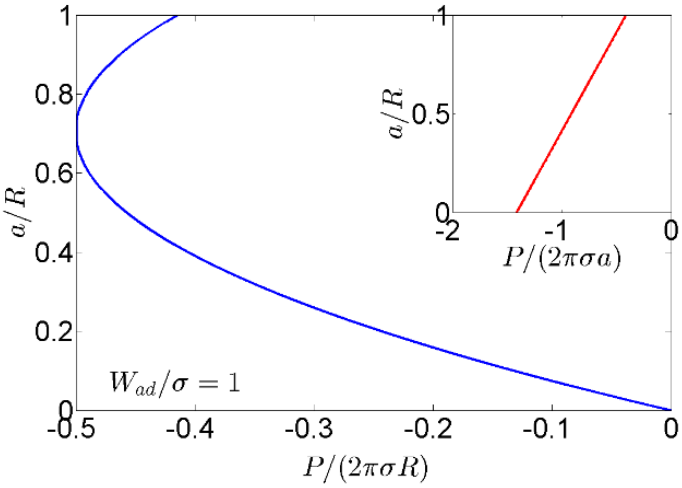

(b) partial wetting liquid- like solution

Fig. 4.3(a), (b) Normalized contact radius versus normalized indentation load for the JKR limit and the partial wetting liquid-like limit. Insets show different scaling behaviors. Note that load is normalized differently in (a) and (b). The inserts in these figures show different scaling behaviors.

4.3 General case: transition between JKR and partial wetting liquid-like limits:

4.3.1 Determination of P_H, δ_H and C

The adhesion-less contact of a rigid sphere to an infinite elastic substrate with surface tension has recently been studied by Long *et al.* [19]. Here we use their formulation specialized to an incompressible elastic substrate. For reasons stated in the 2nd paragraph of section 4.2.1, their formulation is strictly valid only for this case. Their numerical results are presented for specific values of sphere radius, applied load and material properties. Since our goal is to determine the relation between applied load and contact radius for all material and loading parameters, a different approach is needed.

Using the point source solution of Hajji [20], Long *et al.* [19] showed that the contact pressure P acting on the sphere satisfies the integral equation.

$$\frac{1}{2\sigma}\int_0^a tp(t)\int_0^\pi \psi\left(l/s\right)d\theta dt = \delta_H - \frac{r^2}{2R},\ \text{r < a} \tag{4.12a}$$

where

$$l=\sqrt{r^2+t^2-2rt\cos\theta},\ \ s=\sigma/2\mu, \tag{4.12b}$$

$$\psi\left(\eta\right)=H_0\left(\eta\right)-Y_0\left(\eta\right). \tag{4.12c}$$

Here (r,θ) is the polar coordinate system on the surface of the substrate with origin at the initial contact point, δ_H is the displacement of the rigid sphere in the absence of adhesion, and H_0, Y_0 are the Struve function and Bessel function of the 2nd kind (both of order 0), respectively. By setting $r=0$ in (4.12a), δ_H is found to be:

$$\delta_H = \frac{\pi}{2\sigma}\int_0^a tp(t)\psi\left(\mathrm{t}/s\right)dt. \tag{4.13a}$$

Substituting (4.13a) into (4.12a) allows us to eliminate δ_H and the integral equation becomes:

$$\frac{\pi}{2\sigma}\int_0^a tp(t)\left[\psi\left(t/s\right)-\frac{1}{\pi}\int_0^\pi \psi\left(l/s\right)d\theta\right]dt = \frac{r^2}{2R},\ \text{r < a}. \tag{4.13b}$$

Force balance implies that the load P_H acting on the sphere is related to the pressure distribution by

$$2\pi\int_0^a tp(t)dt = P_H\,. \tag{4.13c}$$

To reduce the number of material parameters in the calculation, we introduce the following normalization:

$$r = a\bar{r}, t = a\bar{t}, l = a\bar{l}\,,\ p = \frac{8\mu a}{\pi R}\,\bar{p}, P_H = \frac{16\mu a^3}{3R}\,\bar{P}_H, \delta_H = \frac{a^2}{R}\,\bar{\delta}_H \tag{4.14}$$

Thus, all length scales are normalized by the unknown contact radius *a*. In particular, the total load (Hertz-like load) and the displacement of the sphere (Hertz-like displacement) are normalized by the Hertz load and displacement of the classical Hertz theory without surface tension, respectively (see (4.3a)). Thus, in the absence of surface tension, the *normalized* Hertz-like load $\bar{P}_H$ and displacement $\bar{\delta}_H$ are both exactly equal to one.

Our normalization yields a very important result. The integral equation (4.13b), the Hertz-like displacement (4.13a) and load (4.13c), after normalization, become:

$$2\beta^{-1}\int_0^1 \bar{t}\bar{p}(\bar{t},\beta)\left[\psi\left(\bar{t}\,/\,\beta\right) - \frac{1}{\pi}\int_0^\pi \psi\left(\bar{l}\,/\,\beta\right)d\theta\right]d\bar{t} = \frac{\bar{r}^2}{2},\ \bar{r} < 1 \tag{4.15a}$$

$$\bar{P}_H\left(\beta\right) = 3\int_0^1 \bar{t}\bar{p}(\bar{t},\beta)d\bar{t} \tag{4.15b}$$

$$\bar{\delta}_H\left(\beta\right) = \frac{2}{\pi\beta}\int_0^1 \bar{t}\bar{p}(\bar{t},\beta)\psi\left(\bar{t}\,/\,\beta\right)d\bar{t} \tag{4.15c}$$

$$\beta = \sigma/\left(2\mu a\right). \tag{4.15d}$$

The important result is that the normalized Hertz-like load and displacement depend on a *single* dimensionless parameter β, which is the ratio of the elasto-capillary length σ/μ to the contact diameter. Physically, a small β corresponds to the classical Hertz limit, where elasticity dominates, whereas a large β corresponds to the non-wetting liquid limit, where surface tension dominates.

Although useful from a theoretical standpoint, the integral equation (4.15a) is not suitable for numerical solution. Numerical solution is carried out using the equivalent form

$$\frac{2}{\pi\beta}\int_0^1 \bar{t}\bar{p}(\bar{t},\beta)\int_0^{\pi}\psi\left(\bar{l}/\beta\right)d\theta d\bar{t} = \bar{\delta}_H - \frac{\bar{r}^2}{2},\ \bar{r}<1. \tag{4.16}$$

Details of our numerical scheme are given in the Appendix. Briefly, for a fixed value of β, we first set $\bar{\delta}_H = 1$ in (4.16) and solve it for the pressure distribution. In general, the pressure at the contact line will diverge to positive or negative infinity. Then, the Hertz-like solution is obtained by varying the normalized indentation depth $\bar{\delta}_H$ until the pressure at the contact line is bounded. The corresponding Hertz-like load $\bar{P}_H$ is determined by numerically integrating the pressure distribution using (4.15b).

Using the fact that the *normalized* Hertz-like load and displacement are functions only of β, i.e.,

$$\delta_H = \left(a^2/R\right)\bar{\delta}_H(\beta);\ P_H = \left(16\mu a^3/3R\right)\bar{P}_H(\beta), \tag{4.17a,b}$$

the instantaneous compliance can be found using (4.1) resulting in

$$C = \frac{1}{8\mu a}\phi(\beta),\ \phi(\beta) \equiv \frac{\bar{\delta}_H - \frac{\beta}{2}\frac{d\bar{\delta}_H}{d\beta}}{\bar{P}_H - \frac{\beta}{3}\frac{d\bar{P}_H}{d\beta}}. \tag{4.18a,b}$$

Here ϕ is the normalized compliance. Recall that $1/(8\mu a)$ is the instantaneous compliance of the classical Hertz theory (with no surface tension) so the normalized compliance specifies the deviation due to substrate-air surface tension.

4.3.2 Asymptotic results

Of particular interest is the transition from the elasticity dominated limit to the surface tension dominated limit. It is therefore appropriate to study the behavior of the normalized Hertz-like load and displacement in these limits. The behavior of these

functions in the elastic dominated limit is a direct consequence of our choice of normalization, i.e.,

$$\bar{P}_H\left(\beta\to 0\right)=\bar{\delta}_H\left(\beta\to 0\right)=1. \tag{4.19}$$

Eqs. (4.18b) and (4.19) imply that the normalized compliance $\phi\left(\beta\to 0\right)=1$, as expected. It is also possible to show that the integral equation (4.16), in the limit of $\beta\to 0$, reduces to the integral equation governing the classical Hertz theory without surface tension.

The surface tension dominated or non-wetting liquid like (no adhesion) limit requires more analysis. Using properties of special functions and after some calculations, the integral equation (4.15a) is reduced to (see Appendix for details):

$$\frac{4}{\pi\beta}\int_0^{\bar{r}}\bar{t}\bar{p}\left(\bar{t},\beta\right)\ln\left(\bar{r}/\bar{t}\right)d\bar{t}=\bar{r}^2/2\ ,\ \beta\to\infty. \tag{4.20}$$

Since the right hand side of (4.20) does not go to zero as $\beta\to\infty$, we conclude that there exists a function χ which depends *only* on $\bar{\mathrm{t}}$, such that

$$\bar{\mathrm{p}}\left(\bar{\mathrm{t}},\beta\to\infty\right)=\chi\left(\bar{\mathrm{t}}\right)\beta. \tag{4.21}$$

Furthermore, it is easy to verify that $\chi\left(\bar{\mathrm{t}}\right)=\pi/2$ satisfies the integral equation (4.20) exactly. Substituting (4.21) into (4.15b), we have

$$\bar{P}_H\left(\beta\to\infty\right)=3\beta\int_0^1\bar{t}\,\chi\left(\bar{t}\right)d\bar{t}\equiv\frac{3\pi}{4}\beta\Leftrightarrow P_H\left(\beta\to\infty\right)=2\pi\sigma a^2/R. \tag{4.22}$$

Reverting to dimensional quantity, (4.21) implies that the pressure distribution in the contact zone is

$$p(t,\beta\to\infty)=2\sigma/R, \tag{4.23}$$

which is recognizable as the (uniform) Laplace pressure required to balance the force of surface tension. This result is consistent with the fact that in the surface tension dominated limit and in the absence of adhesion, it is the surface tension that fully supports the applied force. The behavior of the Hertz-like displacement can be found by substituting (4.21) into (4.15c), it is:

$$\bar{\delta}_H\left(\beta\to\infty\right)\to\ln\beta\Rightarrow\delta_H=\frac{P_H}{2\pi\sigma}\ln\left(\frac{\sigma}{2\mu a}\right). \tag{4.24}$$

The normalized compliance $\phi(\beta)$ is computed using (4.18b), (4.22) and (4.24) and is given by

$$\phi\left(\beta\to\infty\right)\to\frac{2}{\pi\beta}\ln\beta-\frac{1}{\pi\beta}\Rightarrow\frac{1}{2\pi a}\frac{dC}{da}=-\frac{1}{4\pi^2\sigma a^2}\,. \tag{4.25}$$

The energy release rate in the surface tension dominated limit is obtained using (4.2a), (4.25) and (4.22) and is:

$$G=\frac{\left(P-2\pi\sigma a^2/R\right)^2}{8\pi^2\sigma a^2}\,. \tag{4.26}$$

The relation between applied load and contact radius can be obtained using the energy balance equation $G=W_{ad}$, which results in (4.8).

4.3.3 General relation between load and contact radius for the adhesive problem

The relation between load and contact radius is given by setting the energy release rate given by (4.2a) equal to the interfacial work of adhesion. It is convenient to introduce a new normalization for the applied load that is independent of the unknown contact radius *a:*

$$\hat{P}=\frac{P}{\frac{3}{2}\pi RW_{ad}}\,,\ \hat{a}=\frac{a}{\frac{1}{2}\left(\frac{9\pi W_{ad}}{4\mu}\right)^{1/3}R^{2/3}}\,. \tag{4.27a,b}$$

Eq. (4.2a) and the energy balance equation $G=W_{ad}$ become (see Appendix for details):

$$\hat{P}=\overline{P_H}(\beta)\hat{a}^3-2\sqrt{\frac{\hat{a}^3}{\Lambda(\beta)}}\,, \tag{4.28a}$$

where we have used (4.18a,b) to determine the compliance, and

$$\Lambda\left(\beta\right)\equiv-16\pi\mu a^3\frac{dC}{dA}=\phi\left(\beta\right)+\beta\frac{d\phi\left(\beta\right)}{d\beta}\,. \tag{4.28b}$$

where $A=\pi a^2$ is the contact area. Although β is convenient to use from a theoretical standpoint, it depends on the contact radius, which is usually an unknown. In the following, we use a dimensionless parameter ω,

$$\omega=\beta\hat{a}=\frac{2\sigma}{\left(\mu R\right)^{2/3}\left(\frac{9\pi}{4}W_{ad}\right)^{1/3}}. \tag{4.29a}$$

Equation (4.28a) is a key result: it generalizes the JKR theory to include surface tension. The modified theory is simple, in that two scalar factors $\bar{P}_H\left(\beta\right)$ and $\Lambda\left(\beta\right)$ that depend only on β needs to be appended to the JKR theory to account for surface tension. It states that the relation between the normalized contact radius and the normalized applied load depends on a single dimensionless parameters ω.

Note that in the JKR theory, $\beta=0\Leftrightarrow\Lambda\left(\beta=0\right)=\bar{P}_H\left(\beta=0\right)=1$ in (4.28a), as a result, the normalized load versus contact radius relation is specified by the single parameter $W_{ad}/\mu R$ - the normalized work of adhesion. Finally, all that remains is to determine $\bar{P}_H\left(\beta\right)$ and $\bar{\delta}_H\left(\beta\right)$ numerically which allows us to find $\Lambda\left(\beta\right)$ defined by (4.28b).

4.3.4 Numerical results: $\bar{P}_H\left(\beta\right),\bar{\delta}_H\left(\beta\right),\ \phi\left(\beta\right)$ ***and*** $\Lambda\ \beta$

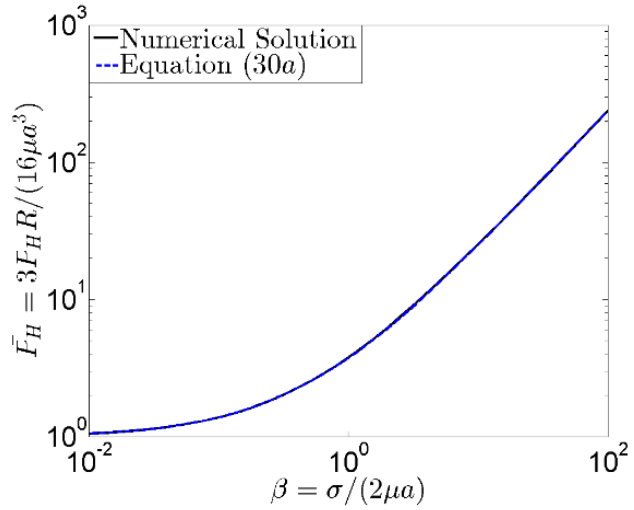

(a)

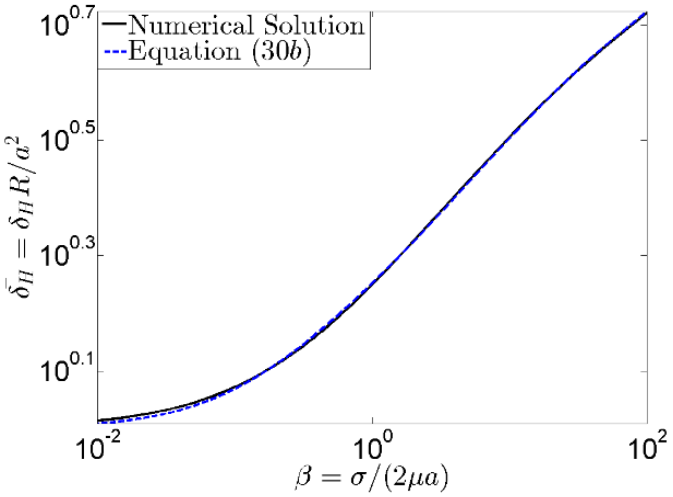

(b)

Fig. 4.4 The vertical axis is the ratio of the Hertz like load/displacement with surface tension to the classical Hertz load/displacement without surface tension. The horizontal axis is the normalized surface tension β. These figures quantify the deviation from classical Hertz theory due to air-substrate surface tension. (a) Normalized Hertz-like load $\bar{P}_H$ against β (b) Normalized Hertz-like displacement $\bar{\delta}_H$ against β.

Fig. 4.4 (a,b) plot the normalized Hertz-like load $\bar{P}_H$ and normalized Hertz-like displacement $\bar{\delta}_H$ against β. As shown in Fig. 4.4 (a,b), these numerical results are very well fitted by

$$\bar{P}_H = 1 + \frac{3\pi\beta}{4}\left[\frac{\beta^2 + 0.6016\beta + 0.0171}{\beta^2 + 0.3705\beta + 0.0063}\right] \quad , \tag{4.30a}$$

$$\bar{\delta}_H = 1 + \frac{1}{3}\ln(1 + 6.582\beta + 2.759\beta^2 + 0.3782\beta^3) . \tag{4.30b}$$

It should be noted that (4.30a,b) give the correct asymptotic behaviors for small and large β. Eqs. (4.30a,b), together with (4.18b) and (4.28b) allow us to compute the scalar factor $\Lambda(\beta)$. Since the final expression is very complicated, it is not given here explicitly. A plot of $\phi(\beta)$ and $\Lambda(\beta)$ versus β is given in Fig. 4.5. Also, for the sake of completeness, we plotted the normalized pressure distribution of the Hertz – like problem for different elasto-capillary numbers α. These results are given in the Appendix.

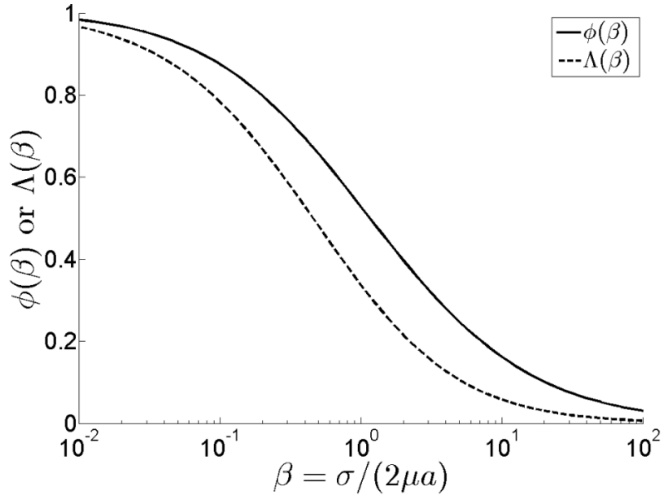

Fig. 4.5 Dimensionless compliance $\phi(\beta)$ and $\Lambda(\beta)$ versus β

The results in Fig. 4.5 is calculated using a local fit method. $\phi(\beta)$ and $\Lambda(\beta)$ can be fitted by:

$$\Lambda(\beta) = \frac{2\beta^2 + 7.4\beta + 1}{\pi\beta^3 + 15.78\beta^2 + 10.92\beta + 1} \tag{4.31a}$$

$$\phi(\beta) = \frac{0.6425\beta^2 + 4.284\beta + 1}{0.2039\beta^3 + 3.994\beta^2 + 6.011\beta + 1} \tag{4.31b}$$

4.3.5 Pull-off and zero load cases

Of particular interest are the contact radius at zero load (a_0) and the pull-off force (P_{off}), which can be readily determined from (4.28a). The contact radius at zero load satisfies the implicit equation

$$\hat{a}_0 = \frac{1}{2}\left(\frac{9\pi}{\Lambda\left(\omega / \hat{a}_0\right)\left[\bar{P}_H\left(\omega / \hat{a}_0\right)\right]^2} \frac{W_{ad}}{\mu R} \right)^{1/3} . \tag{4.32}$$

The normalized pull-off force $\hat{P}_{off}$ and the contact radius at pull-off $\hat{a}_{off}$ are determined from (4.28a) using the condition $d\hat{P} / d\hat{a} = 0$. To show the deviation from the classical JKR theory, the pull-off force and radius are re-normalized by the pull-off force and radius of JKR theory determined by (4.10a) and (4.10b). These results are shown in Fig. 4.6 for different values of $\bar{W}_{ad}$.

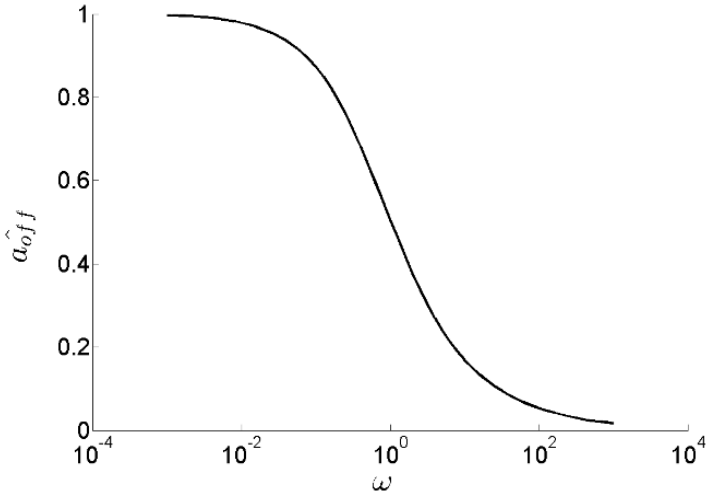

(a)

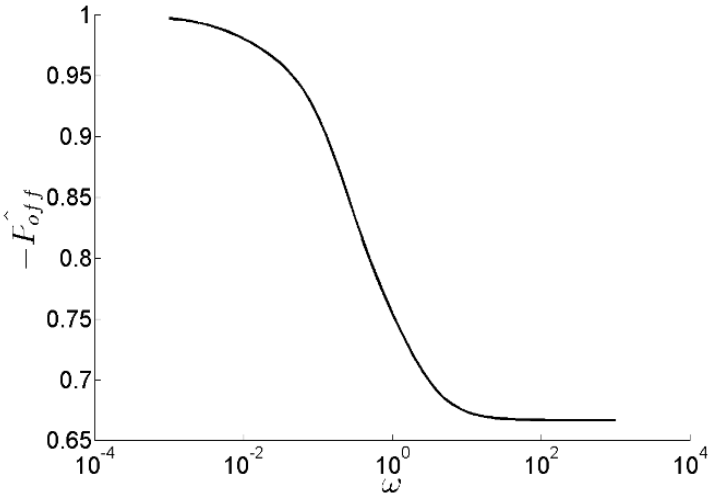

(b)

Fig. 4.6 (a) Normalized contact radius at pull-off versus ω. (b) Normalized pull-off force versus ω. The pull-off radius and load of the elastic limit are calculated using (4.10a) and (4.10b).

4.3.6 Contact radius versus applied load

The contact radius versus load relation for various ω is shown in Fig. 4.7 for $\bar{W}_{ad} = 0.1$. Note that the small contact requires that $\overline{W_{ad}}$ to be much less than $\max\{1, \alpha\}$. As expected, increasing elasto-capillary number (e.g. increasing surface

tension at fixed modulus and sphere radius) increases the substrate's resistance to deformation, resulting in much smaller contact at the same indentation load.

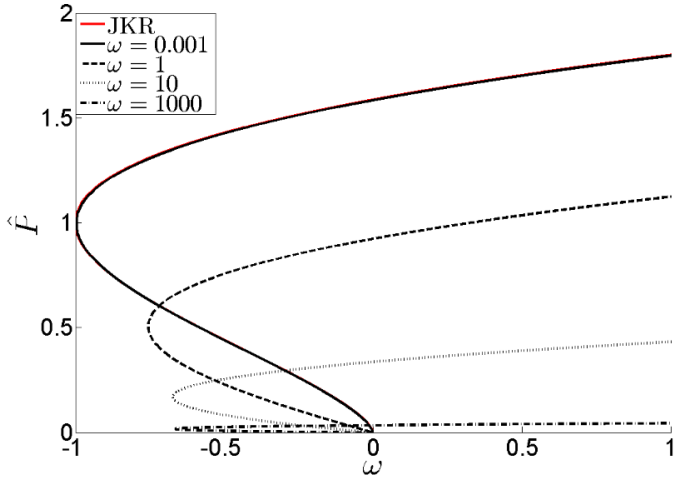

Fig. 4.7 Normalized contact radius versus normalized load for different ω.

4.3.7 Indentation depth versus contact radius

In a displacement controlled test, the relation between indentation depth and contact radius is obtained using (4.2b), (4.18a,b):

$$\hat{\delta} = 3\hat{a}^2 \bar{\delta}_H(\beta) - 4\phi\sqrt{\frac{\hat{a}}{\Lambda(\beta)}}\ , \tag{4.33}$$

where $\bar{\delta}_H$ is approximated by (4.30b). Eq. (4.33) reduces to the JKR theory (4.3c) in the limit of $\beta \to 0$ since $\bar{\delta}_H(\beta), \phi(\beta), \Lambda(\beta)$ approach *1* in this limit. The contact radius versus indentation depth for different elasto-capillary numbers ω is shown in Fig. 4.8.

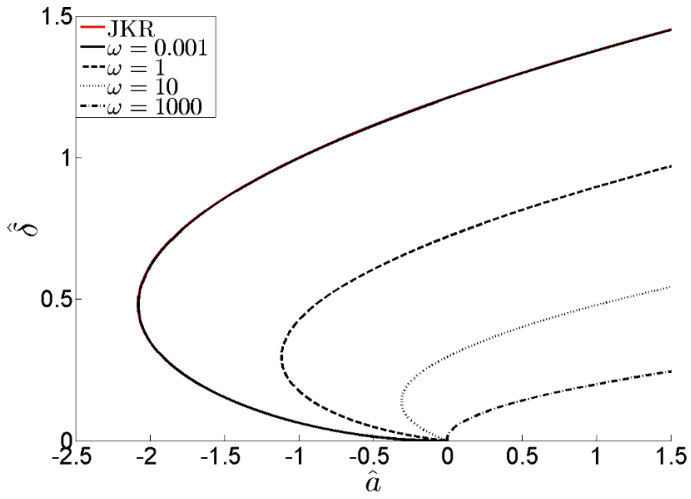

Fig. 4.8 Normalized contact radius versus normalized indentation depth for 4 different elasto-capillary numbers. Curves are generated using (4.30b) and (4.33) with $\bar{W}_{ad} = 0.1$. For $\omega = 0.001$ the JKR solution and the prediction given by (4.33) lies on top of each other.

Of great interest to experimentalists is the relation between applied load and indentation depth, which can be obtained by combining the results from Fig. 4.7 and Fig. 4.8 and is shown in Fig. 4.9.

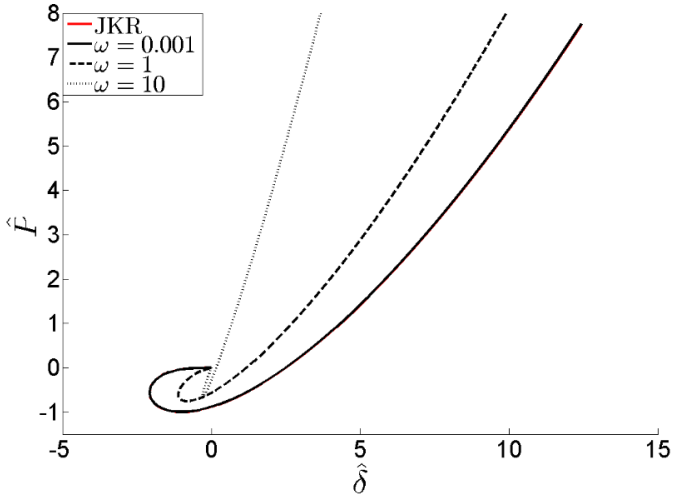

Fig. 4.9 Normalized load versus normalized indentation depth for different α with $\bar{W}_{ad} = 0.1$. Note that JKR and the solution for $\alpha = 0.001$ lies on top of each other.

4.4 Comparison with experiments

Style et al. [5] have recently measured the contact radius of small glass spheres adhering to the surface of silicone substrates under zero external load (the sphere are sufficiently small so that adhesive forces dominate gravity). Different contact radii are obtained by varying the radius of the sphere (from 3 to 30 μm) and the substrate's shear modulus μ (from 1 to 167kPa). Their results (symbols) are shown in Fig. 4.10. Xu et al. [6] previously analyzed the special case of the problem considered in the present work when force is zero, using a large-strain finite element (FEM) method. Their results were validated by fitting experimental data of Style et al. [5], with work of adhesion and surface tension extracted as two fitting parameters. While the analytical model developed in the present work extends the previous FEM analysis by allowing for applied indentation force, it is restricted by the assumptions that strains and displacements remain small. In Fig. 4.10, using the same parameters as found by Xu et al. [6], we compare the results of the small-strain theory developed in the present work with experiments of Style et al. [5]. The solid lines represent the full theory; the dotted lines represent the theory when air-substrate surface tension is neglected. Note that for the three stiffer materials, the present small-strain theory fits the data very well, even though the deformation is not that small. There is a systematic difference between results that do or do not include the effect of surface tension. For the most-compliant substrate, the small-strain theory significantly overestimates the contact radius. The breakdown of small strain theory in this regime is not surprising, since the small strain theory is expected to break down for this case except close to the non-wetting limit, where $W_{ad} / \sigma << 1$. To confirm that this discrepancy is due only to the very large deformation in the experiment, we modified our derivation of (4.8)

without making the small angle approximation and obtained the following relation between load and contact radius in the partial-wetting liquid-like limit:

$$P = \frac{2\pi\sigma a^2}{R} - 2\pi a\sigma\left[\frac{a\,\mathrm{W}_{ad}}{R\sigma} + \sqrt{1-(a/R)^2}\sqrt{1-(1-\mathrm{W}_{ad}/\sigma)^2}\right]. \qquad (4.34)$$

Note that, if the work of adhesion is indeed small in comparison with the surface tension and $a/R << 1$, then (4.34) reduces to the small strain theory solution given by (4.8). For the special case of $P = 0$, (4.34) reduces to a result in [6]:

$$a_0 = R\sqrt{1-(1-\mathrm{W}_{ad}/\sigma)^2}\,. \qquad (4.35)$$

This equation is used to fit the data in Fig. 4.10 for $\mu = 1kPa$. The almost perfect fit between model and experiments supports our claim that for very soft and adhesive samples the small deformation theory breaks down.

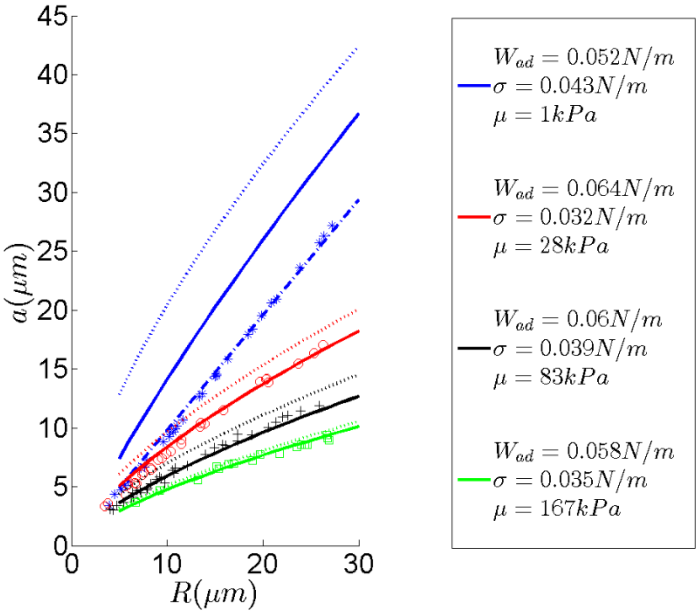

Fig. 4.10 Comparison with experimental data of Style *et al*. [5]. Symbols are experimental data. Solid lines are predictions based on small deformation theory with air-substrate surface tension. Dotted lines are based on small deformation theory without surface tension. Prediction of large strain solution in partial wetting liquid-

like limit (4.34) is shown as a dashed-dotted line. The parameters used for these fits are based on the paper by Xu *et al.* [6].

4.5 Summary and discussion

Equations (4.28a) and (4.33) extend the JKR theory to include the effect of surface tension. The extensions involve three dimensionless scalar factors, $\bar{P}_H, \bar{\delta}_H, \Lambda,$ which depends on the elasto-capillary number $\beta = \sigma/(2\mu a)$ only. Our analysis is strictly valid for a rigid sphere in no-slip contact with an incompressible isotropic elastic substrate. The incompressibility of the substrate is needed to ensure the vanishing of shear stress in the contact region. However, this incompressibility requirement can be relaxed since the interfacial shear stress due to a compressible substrate is typically small in comparison with the contact pressure, as noted by Johnson [1]. Therefore, our results are also approximately valid for compressible substrates provided that the shear modulus μ in our equations is replaced by $\mu\left[2(1-\nu)\right]^{-1}$.

Our analysis uses small deformation theory which requires the contact radius to be much less than the radius of the sphere. However, for soft materials the deformation can be very large. Fortunately, the works of Xu *et al.* [6] and Lin *et al.* [21] showed that the results of small deformation theory are surprisingly robust for this class of contact problems. This claim is also supported by our result in Fig. 4.10 which shows that small deformation theory is surprisingly accurate as long as the elasto-capillary number is not so large that one approaches the partial wetting liquid-like limit. The largest elasto-capillary number α corresponding to the case of $\mu = 1kPa$ in Fig. 4.10 is about 0.7. Note that small strain theory is valid even though $\alpha \geq 1$ as long as $W_{ad}/\sigma << 1$. If the condition $W_{ad}/\sigma << 1$ is violated and $\alpha \geq 1$, we suggest using (4.34) to approximate the relation between the indentation load and the contact radius.

Our calculation is strictly valid for no slip contact. For substrates such as hydrogels, the frictionless boundary condition could be more appropriate. Recall that the classical JKR theory is strictly valid for frictionless and no slip contact, as long as the substrate is incompressible. However, as pointed out in section 4.2, without the no-slip condition, one would have to introduce new physics into the model – that is, the tension of the substrate surface will change since it is in contact with the rigid surface. The problem is that the interfacial tension between a rigid surface and the surface of a compliant solid is not well defined, as a rigid surface can support any tension. From the mechanics view point, there is no consistent way to assign the tension acting on the substrate surface after contact. One way to deal with this difficulty is to assign the same tension to the substrate surface after contact, which is essentially the approach of Long *et al*. [19]. In this case the results of the present article apply without modification. However, the effect of this approximation could result in a work of adhesion that is different from that given by the Young-Dupre equation. This ad-hoc assumption is supported, at least partially by the fact that our theory is able to match the data of Style *et al*. [5].

We have not found any experiments that specifically measures the effect of surface tension on the relation between indentation and force. Therefore, our comparison is based on the special experimental case where the applied force is zero. It will be of great interest to test this theory against experiments involving finite indentation force.

APPENDIX 4.1

NUMERICAL IMPLEMENTATION

We divide the interval $[0,1]$ into *n* equal subintervals $[t_i, t_{i+1}]$, $i = 1,....,n+1$ with equal length $\Delta = 1/n$, so $t_i = (i-1)\Delta$, $i = 1,....,n+1$. Let the midpoints of these intervals to be denoted by

$$\frac{t_j + t_{j+1}}{2} = r_j = \frac{2j-1}{2}\Delta, \quad j = 1,...,n \tag{A4.1.1}$$

We discretize (4.16) into a $n \times n$ linear system of equations,

$$\frac{2}{\pi\beta}\int_0^1 \bar{t}\bar{p}(\bar{t},\beta)\int_0^\pi \psi\left(\bar{l}/\beta\right)d\theta d\bar{t} = \sum_{i=1}^{n} M_{ji}\bar{p}_i = \overline{\delta_H} - \frac{\bar{r}_j^{\,2}}{2}, \text{ j=1,...,n} \tag{A4.1.2}$$

where $\overline{p_i} = \bar{p}(\bar{t} = \bar{r}_i, \beta)$ and M_{ji} is the $n \times n$ matrix defined by

$$M_{ji} = \frac{2}{\beta\pi}\int_{t_i}^{t_{i+1}} \bar{t}k\left(\bar{t},\bar{r}_j,\beta\right)d\bar{t}, \; \mathrm{k}\left(\bar{t},\bar{r},\beta\right) = \int_0^\pi \psi\left(\sqrt{\bar{t}^2 + \bar{r}^2 - 2\bar{r}\bar{t}\cos\theta}/\beta\right)d\theta \tag{S3}$$

We find *n = 20* is enough to give us good results. The coefficients M_{ji} are obtained using standard quadrature rules. For any given β , the initial value of $\overline{\delta_H}$ is taken to be 1, and it is updated using the following shooting scheme:

Step 1: Solve (A4.1.2) using $\overline{\delta_H} = \bar{\delta}_1 = 1$.

Step 2: Solve (A4.1.2) using $\overline{\delta_H} = \overline{\delta_2} = 2\bar{\delta}_1$.

Step3: Examine the divergence of the pressure field near the contact line in step 1 and step 2. If pressure diverges to positive infinity at $\bar{\delta}_1$ and to negative infinity at $\bar{\delta}_2$, then the correct $\overline{\delta_H}$ must lie in between $\bar{\delta}_1$ and $\bar{\delta}_2$, then go to step 4. If both $\bar{\delta}_1$ and $\bar{\delta}_2$ lead to positive infinite pressure, then take $\bar{\delta}_1 = \bar{\delta}_2$ and go back to step 2.

Step4: Let $\bar{\delta}_3 = \dfrac{|d\bar{p}_2|\bar{\delta}_1 + |d\bar{p}_1|\bar{\delta}_2}{|d\bar{p}_1| + |d\bar{p}_2|}$, $d\bar{p}_1 = \bar{p}_n(\bar{\delta}_1) - \bar{p}_{n-1}(\bar{\delta}_1)$, $d\bar{p}_2 = \bar{p}_n(\bar{\delta}_2) - \bar{p}_{n-1}(\bar{\delta}_2)$.

Solve (A4.1.2) using $\bar{\delta}_H = \bar{\delta}_3$. Check whether the pressure converges at the edge (r=a). If not, take $\bar{\delta}_1 = \bar{\delta}_3$ if it diverges to positive infinity or take $\bar{\delta}_2 = \bar{\delta}_3$ if it diverges to negative infinity and then repeat step 4. During this loop, always check whether

pressure converges for $\overline{\delta_1}$ *and* $\overline{\delta_2}$. Whenever it converges we get the correct answer for both $\overline{\delta_H}$ and $\overline{P_H}$.

For each β, the numerical solution gives us the correct normalized displacement $\overline{\delta_H}(\beta)$, which should be a decreasing function of β. The total normalized Hertz-like force is finally computed using (4.15b).

The pressure distributions for different β are shown as below:

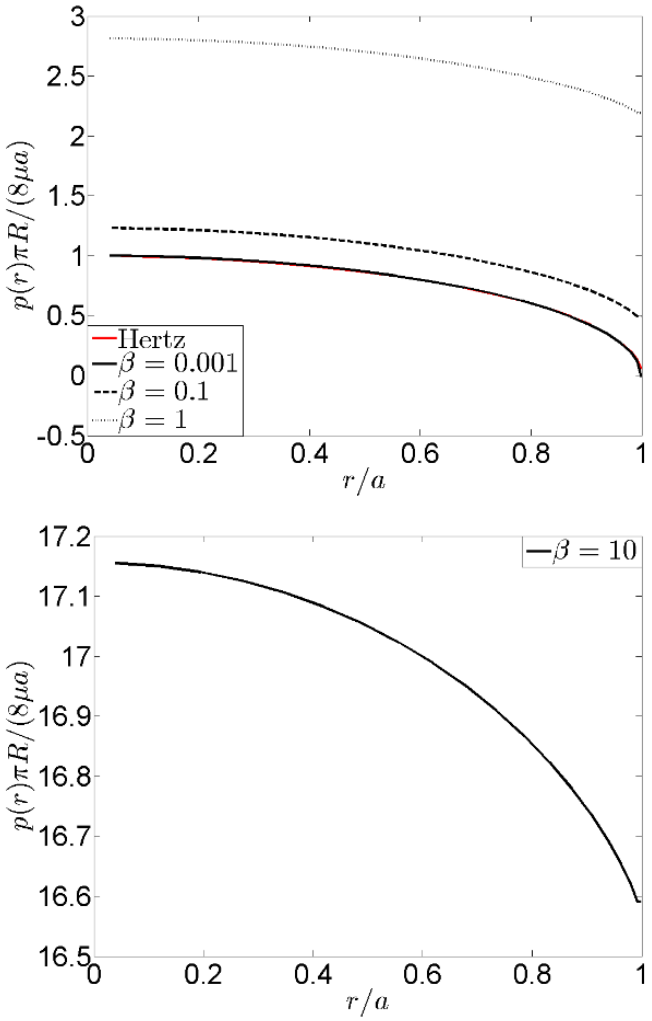

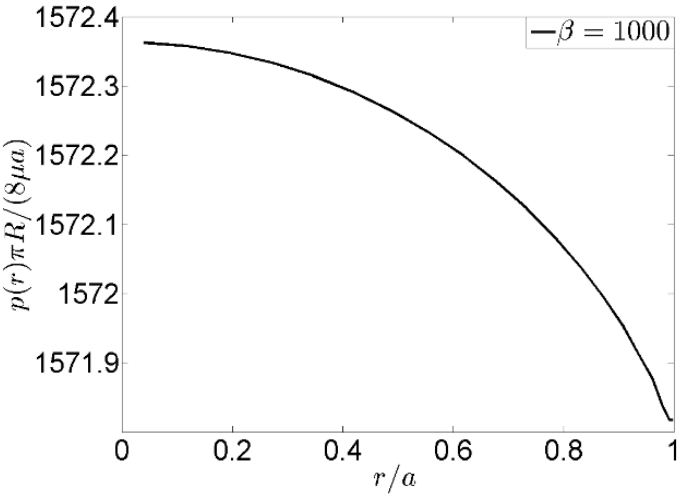

Fig. A.4.1.1 Pressure distributions for different β

APPENDIX 4.2

DERIVATION OF EQUATIONS (4.20) AND (4.28)

According to the properties of Bessel function of the second kind and Struve function,

$$\psi(\mathrm{x}\to 0)\approx -\frac{2}{\pi}[\ln(\frac{x}{2})+\gamma]\ , \tag{A4.2.1}$$

where γ is the Euler constant. Using (A4.2.1),

$$\begin{aligned}\psi(\bar{t}\,/\,\beta)-\frac{1}{\pi}\int_0^{\pi}\psi(\bar{l}\,/\,\beta)\,\mathrm{d}\,\theta &\approx -\frac{2}{\pi}[\ln(\bar{t})-\frac{1}{\pi}\int_0^{\pi}\ln(\sqrt{\bar{r}^2+\bar{t}^2-2\bar{r}\bar{t}\cos\theta})\,\mathrm{d}\,\theta] \\ &= \begin{cases} 0, & \bar{r}<\bar{t} \\ \dfrac{2}{\pi}\ln(\dfrac{\bar{r}}{\bar{t}}), & \bar{r}>\bar{t} \end{cases}\end{aligned} \tag{A4.2.2}$$

Equation (4.20) is obtained by substituting (A4.2.2) into (4.15a).

To derive (4.28), we equate the energy release rate from (4.2a) to the work of adhesion, resulting in

$$-\frac{1}{2}\frac{dC}{dA}(\mathrm{P}-\mathrm{P}_H)^2=W_{ad}\,, \tag{A4.2.3}$$

where $A=\pi a^2$ is the contact area. Using the normalization of (4.14) and (4.27), (A4.2.3) becomes:

$$\begin{aligned}-\frac{1}{2}\frac{dC}{dA}(\mathrm{P}-\mathrm{P}_H)^2 &= -\frac{1}{2}\frac{\Lambda(\beta)}{-16\pi\mu a^3}(\frac{16\mu R^2}{3})^2(\hat{P}-\bar{a}^3\overline{P_H})^2 \\ &= \frac{16\mu R}{9\pi\bar{a}^3}\frac{1}{2}\Lambda(\beta)(\hat{P}-\bar{a}^3\overline{P_H})^2 \\ &= W_{ad}\end{aligned} \tag{A4.2.4}$$

After rearrangement, (A4.2.4) becomes (4.28a).

REFERENCES

[1] K. L. Johnson, *Contact Mechanics* (Cambridge University Press, 1987).

[2] K. L. Johnson, K. Kendall, and A. D. Roberts, Proc. R. Soc. A Math. Phys. Eng. Sci. **324**, 301 (1971).

[3] D. . Rimai, D. . Quesnel, and A. . Busnaina, Colloids Surfaces A Physicochem. Eng. Asp. **165**, 3 (2000).

[4] A. Chakrabarti and M. K. Chaudhury, Langmuir **29**, 6926 (2013).

[5] R. W. Style, C. Hyland, R. Boltyanskiy, J. S. Wettlaufer, and E. R. Dufresne, Nat. Commun. **4**, 2728 (2013).

[6] X. Xu, A. Jagota, and C.-Y. Hui, Soft Matter **10**, 4625 (2014).

[7] Z. Cao, M. J. Stevens, and A. V. Dobrynin, Macromolecules **47**, 3203 (2014).

[8] A. W. C. Lau, M. Portigliatti, E. Raphaël, and L. Léger, Europhys. Lett. **60**, 717 (2002).

[9] T. Salez, M. Benzaquen, and É. Raphaël, Soft Matter **9**, 10699 (2013).

[10] J. M. Long, G. F. Wang, X. Q. Feng, and S. W. Yu, Int. J. Solids Struct. **49**, 1588 (2012).

[11] J.-M. Y. Carrillo and A. V Dobrynin, Langmuir **28**, 10881 (2012).

[12] R. Style, R. Boltyanskiy, Y. Che, J. Wettlaufer, L. A. Wilen, and E. Dufresne, Phys. Rev. Lett. **110**, 66103 (2013).

[13] C.-Y. Hui and A. Jagota, Langmuir **29**, 11310 (2013).

[14] J. H. Weijs, B. Andreotti, and J. H. Snoeijer, Soft Matter **9**, 8494 (2013).

[15] S. Vajpayee, C.-Y. Hui, and A. Jagota, Langmuir **24**, 9401 (2008).

[16] K. Kendall, J. Phys. D. Appl. Phys. **8**, 1449 (1975).

[17] C.-Y. Hui and A. Jagota, Proc. R. Soc. A Math. Phys. Eng. Sci. **470**, 20140085 (2014).

[18] M. K. Chaudhury, T. Weaver, C. Y. Hui, and E. J. Kramer, J. Appl. Phys. **80**, 30 (1996).

[19] J. M. Long and G. F. Wang, Mech. Mater. **56**, 65 (2013).

[20] M. A. Hajji, J. Appl. Mech. **45**, 320 (1978).

[21] Y.-Y. Lin and H.-Y. Chen, J. Polym. Sci. Part B Polym. Phys. **44**, 2912 (2006).

CHAPTER 5

ADHESIVE CONTACT OF A RIGID CIRCULAR CYLINDER TO A SOFT ELASTIC SUBSTRATE – THE ROLE OF SURFACE TENSION [4]

5.1 Introduction

A number of recent studies have demonstrated that surface tension can act as a significant and even dominant agent in the mechanics of compliant materials such as elastomers and gels. Examples include instabilities [1–3] and deformation driven by surface tension [4,5], violation of Young's equation for wetting [6–12], attenuation of driving forces for crack or void growth [13–16], and breakdown of conventional adhesive contact mechanics [17–21].

The last example cited above, i.e., the adhesive contact between non-conforming surfaces, is an important basic problem in adhesion science. For example, consider the contact of a rigid sphere with the flat surface of an elastic substrate. For small deformation, where the contact radius is small in comparison with the radius of the sphere, the solution is given by Hertz [22]. Hertz theory assumes adhesion-less contact; as a result, the traction on the contact region is compressive everywhere and vanishes at the contact line. In 1971, Johnson, Kendall and Roberts (JKR) [23] extended Hertz theory to allow for adhesion. The JKR theory has been extremely successful in describing the adhesive contact of elastic spheres [24]. However, recent observations of contact deformations on soft substrates, such as plasticized polystyrene [25], hydrogels [26] and silicone gels [17], caused by adhesion of hard microparticles or nanoparticles deviate considerably from JKR theory. For example, Style *et al.* [17] have reported that the exponent of power-law relationship between the contact radius a (indentation depth) and sphere radius R changes from $a \propto R^{2/3}$ ($\delta \propto \sqrt{R}$) to $a, \delta \propto R$ as the sphere reduces in size or the substrate becomes softer.

[4] Liu T, Jagota A., Hui C.Y., (2015). Soft Matter. **11**, 3844.

The transition in scaling observed in these experiments has been interpreted as a corresponding underlying transition from the JKR limit where deformation is resisted primarily by bulk elasticity, to the "liquid" limit where deformation is resisted primarily by surface tension. This transition in scaling is consistent with the molecular dynamics simulations by Cao *et al.* [27]. Using a large deformation Finite Element Model which incorporates both surface tension and non-linear elasticity, Xu *et al.* [18] have demonstrated the transition from the elasticity dominated regime where $a \propto R^{2/3}$ to the surface tension dominated regime where $a \propto R$ depend on a single elasto-capillary number $\alpha \equiv \sigma / 4\mu R$ - small α favors JKR theory whereas large α favors surface tension. Their numerical results are found to be in good agreement with the experiments reported by Style *et al* [17]. Xu *et al.*'s results are for rigid spheres that are subjected to zero load. The case of finite load has been recently considered by Hui *et al.* [19], who provided analytical expressions for the relations between indentation depth (contact radius) and applied load. They also examined the effect of surface tension on the pull-off load as a special case of their theory. It should be noted that similar transitions are predicted for soft particles on a rigid surface, as demonstrated by the theoretical works of Carrillo and Dobrynin [20] and Salez et al [28]. The dimensionless parameter $\omega = \dfrac{\sigma}{4(\mu R)^{2/3}(W_{ad}/2\pi)^{1/3}}$ which controls the transition between JKR and wetting limit was first suggested by Carrillo *et al.* [29] when they studied the adhesion of a soft nanoparticles *to a rigid substrate.*

Another geometry that is of practical interest is a circular rod or circular cylinder. This geometry arises whenever cylindrical or "hair-like" deformable objects adhere to each other or to a substrate. As explained in more detail below, the behavior of this two-dimensional problem differs qualitatively from the better studied three-dimensional (axisymmetric) problem of contact between a sphere and a flat substrate.

A Molecular Dynamic simulation combined with theory was performed by Cao *et al*. [30] to study the effect of surface energy on contact of spherical and cylindrical nano-particles with a soft solid without indentation force. The adhesive contact mechanics of an infinitely long rigid cylinder with an elastic half space in the absence of surface tension can be found in the works of Barquins [31] and Chaudhury *et al*. [32], while the two-dimensional Hertzian contact problem with surface tension has been studied by Long *et al*. [33].

In this Chapter, a different approach is used to include both adhesion and surface tension. Our derivation below follows the approach of JKR [23], that is, the adhesive force is confined to a region small compared with typical specimen dimensions, so that the contact edge can be viewed as the tip of traction free crack. In reality, adhesive forces acting outside the contact zone will serve to place a limit on the maximum stress that can be reached. To address this issue, Derjaguin, Muller, and Toporov [34] proposed a theory (DMT theory) that takes these forces into account, but assumes that they do not change the shape of the surface determined by the Hertz theory. This approximation leads to tensile stresses that are finite outside the contact line but are zero inside. A unifying theory of elastic contact of spheres was proposed by Maugis [35], who used a Dugdale-Barenblatt cohesive zone model to represent the surface forces outside the contact zone. This model removes the stress singularity of the JKR theory, and it also removes the stress discontinuity of the DMT theory. For the case of a rigid sphere on an incompressible elastic substrate, Maugis's result [35] showed that the transition from JKR to DMT theory depends on a single dimensionless parameter

$$\lambda = \sigma_c \left(\frac{R_s}{\mu^2 W_{ad}} \right)^{1/3}, \tag{5.1}$$

where σ_c is the cohesive stress, μ the shear modulus of the substrate, R_s the radius of the sphere and W_{ad} the work of adhesion. Typically, JKR theory is valid for $\lambda > 1$ and this is the typical situation in experiments using elastomeric spheres ($\mu \approx 10^6 Pa$) with radius around 1mm [36]. For very soft substrate where surface tension effect are important, $\mu < 10^5 Pa$. Since $\lambda \propto \left(R_s / \mu^2 \right)^{1/3}$ the reduction of modulus will extend the region of validity of the JKR model to micron size spheres. Indeed, Style *et al*'s experiments [17] showed that JKR theory works well for glass spheres with radii ranging from 3 to 30 microns on a silicon substrate with $\mu = 170 kPa$. In light of this, it is reasonable to adopt the JKR approach to study surface tension effect in the contact mechanics of soft materials. Finally, we note that the unified approach of Maugis [35] was also used by Baney *et al.* [37] and Leng *et al.* [38] to study two dimensional contact problems involving cylindrical geometry.

5.2 Statement of Problem and Summary of Approach

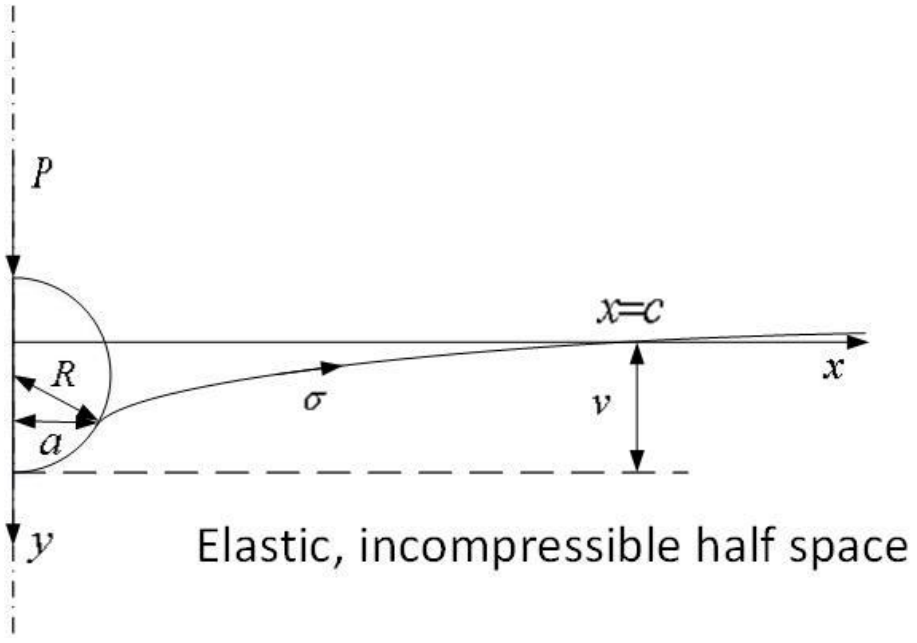

Fig. 5.1 A long rigid cylinder of radius *R* and length *L* >> *R* indents an isotropic and incompressible elastic half-space under the influence of a vertical line force *P*.

Indentation is resisted by the elasticity of the substrate as well as the surface tension of the elastic substrate.

Fig. 5.1 shows a rigid cylinder of radius R, with length $L >> R$ in the out-of-plane direction, brought into contact with the flat surface of a substrate by a vertical line force P (units = force/unit length, so total force acting on the cylinder is PL). Let (x,y,z) denote the position of a material point in the elastic half-space. Before deformation, the bottom of the cylinder touches the substrate surface at the origin, $x = y = z = 0$. The substrate occupies the half space $y > 0$ and is assumed to be linearly elastic, isotropic and *incompressible*, with shear modulus and Poisson's ratio $\nu = 0.5$. The contact zone is a long rectangular strip of width $2a$ and length L. We also assume that the surface stress tensor is isotropic, so it can be represented by the scalar surface tension. Just as in JKR theory, our analysis is based on small strain theory.

In contrast to the JKR theory, which assumes frictionless contact, we assume a no-slip contact condition. That is, a material point on the substrate surface is held fixed once it comes into contact with the rigid cylinder. Without the no-slip condition, one would have to introduce a new parameter into the model – the interfacial tension in the contact region. In general, the no-slip contact condition will cause non-zero shear traction in the contact region. However, a classical result in linear elasticity states that the no-slip boundary condition is consistent with a vanishing shear traction provided that the cylinder is rigid and the substrate is incompressible and infinite in extent [22]. Fortunately, the bulk modulus of most elastomers and hydrogels is much higher than their shear moduli, so incompressibility is an excellent approximation.

As in JKR theory, our basic approach is based on energy balance, that is, the relation between the contact radius and the applied load is obtained by setting the energy release rate G of the external crack (the air gap between the cylinder and the surface of the substrate outside the contact line) equal to the interfacial work of

adhesion W_{ad}. The key difference is the inclusion of surface tension in the calculation of the energy release rate. The procedure is as follows. First, we obtain the "Hertz-like" solution of a contact problem with surface tension. By this we mean the relationship between the line force $P_H(a)$, indentation displacement $\delta_H(a)$, and contact width $2a$ in the absence of adhesive forces. From this solution, we compute the instantaneous contact compliance, defined by

$$C(a) = d\delta_H / dP_H = \frac{d\delta_H}{da} / \frac{dP_H}{da}. \tag{5.2}$$

As shown by Vajpayee *et al.* [39], knowing the instantaneous contact compliance and the Hertz-like load P_H suffices to determine the energy release rate. Specifically, the energy release rate is given by[5]:

$$G = \frac{1}{4}\Lambda_H \left(P - P_H\right)^2, \quad \Lambda_H = -\frac{dC}{da}. \tag{5.3}$$

Finally, the relation between contact width *2a* and the applied line load *P* is obtained using the energy balance condition $G = W_{ad}$. Using (5.3), this relation is

$$P = P_H - 2\sqrt{W_{ad} / \Lambda_H}. \tag{5.4}$$

It is important to note that in general, dC/da and P_H are functions of the shear modulus, surface tension, cylinder radius, and the contact width. Once these two functions are determined (see below), equation (5.4) generalizes the JKR theory to include surface tension.

Equations (5.3-5.4) apply equally well to the three-dimensional indentation problem for which they were first derived [39] and for the two-dimensional cylindrical problem analyzed here, which is obtained by assuming that the cylinder is infinitely long. There is, however, a peculiarity of two-dimensional contact problems. As noted

[5] In Vajpayee et al. [39], $G = -\frac{1}{2}\frac{dC}{dA}\left(P - P_H\right)^2$, where A is the contact area. In our case, the area of contact is *2a* since the length of the cylinder is infinite. Note *P* and P_H has units of force per unit length.

by Johnson [22], the displacement of a point in an elastic half-space loaded by a line force (resulting in a two dimensional stress field) cannot be expressed relative to a datum at infinity, since the displacements decrease with distance *r* from the contact zone as ln *r*. Here we follow Johnson [22] by defining the displacements relative to an arbitrary point $x = c >> a$ (see Fig. 5.1) on the surface of the substrate. Thus, the indenter displacement δ_H in (5.2) can take any value depending on the choice of this point. Nevertheless, as shown below, d*C/da* in equations (5.3-5.4) does not depend on the choice of *c*, as long as $c >> a$.

5.2.1 The elasticity dominated limit

For an infinitely long cylinder ($L \to \infty$), in the limit where surface tension can be neglected and resistance to deformation is dominated by elasticity, the relation between contact width and load in the presence of adhesion has been derived earlier by Barquins [31] and Chaudhury *et al*. [32] using a different approach. Here, for uniformity of development, it is instructive to derive this relation using equation (5.4).

In the absence of surface tension and adhesion, the relationship between force and contact width is [22]

$$P_H = \frac{\pi \mu a^2}{R}. \tag{5.5}$$

Because of the two-dimensional nature of the problem, and the attendant dependence of displacements on choice of datum referred to above, determining the instantaneous contact compliance require special consideration. The normal surface displacement v for $|x| > a$ can be obtained using a result given in Johnson [22]:

$$v(|x| > a) = \frac{1}{R}\left[\frac{|x|}{2}\sqrt{x^2 - a^2} - \frac{a^2}{2}\ln\left||x| + \sqrt{x^2 - a^2}\right| - \frac{x^2}{2}\right] + b, \tag{5.6}$$

where *b* is an arbitrary constant. We pick a point at $x = c >> a$ as datum, i.e., we define the normal displacement at *c* to be zero, and this determines *b*. Continuity of v across the contact line implies that

$$\begin{aligned}\delta_H &= v\left(x=a\right)+\frac{a^2}{2R}\\ &= -\frac{1}{R}\left[\frac{c}{2}\sqrt{c^2-a^2}-\frac{a^2}{2}\ln\left|\frac{c+\sqrt{c^2-a^2}}{a}\right|-\frac{c^2}{2}\right], \text{ where } c >> a. \qquad (5.7)\\ &\approx \frac{a^2}{2R}\ln\left(\frac{2c}{a}\right)+\frac{a^2}{4R}\end{aligned}$$

The compliance, evaluated using (5.2), (5.5) and (5.7) is found to be:

$$C=\frac{1}{2\pi\mu}\ln\left[2c/a\right]\Rightarrow dC/da=-\Lambda_H(a)=\frac{1}{2\pi\mu a}. \qquad (5.8)$$

Substituting (5.5) and (5.8) into (5.4) recovers the JKR theory for a rigid cylinder in adhesive contact with an incompressible elastic half space [31], i.e.,

$$P=\frac{\pi\mu a^2}{R}-2\sqrt{2\pi\mu a W_{ad}}. \qquad (5.9a)$$

Note at zero load, the half contact width a_0 caused by adhesive forces is:

$$a_0=2\left(\frac{R^2W_{ad}}{\pi\mu}\right)^{1/3}. \qquad (5.9b)$$

The pull-off load is found to be [22],

$$P_{off}=-3\pi\mu R^{1/3}\left(\frac{W_{ad}}{2\pi\mu}\right)^{2/3}. \qquad (5.9c)$$

The contact half width at pull-off is:

$$a_{off}=R^{2/3}\left(\frac{W_{ad}}{2\pi\mu}\right)^{1/3}. \qquad (5.9d)$$

Recall that the pull-off load of a sphere is directly proportional to its radius and is independent of elastic modulus [23]. Equation (5.9c) shows that the scaling for pull-off is different for the case of cylinders.

5.2.2 The surface tension dominated limit

Before tackling the general problem of the transition from the elasticity dominated limit to surface tension dominated limit, we examine the latter limiting case. The free body diagram in Fig. 5.2 shows that force balance requires

$$P = 2\sigma \sin\left(\theta - \theta_p\right), \tag{5.10}$$

where $\theta = \sin^{-1}(a/R)$ and θ_p is the "peel" angle defined in Fig. 5.2.

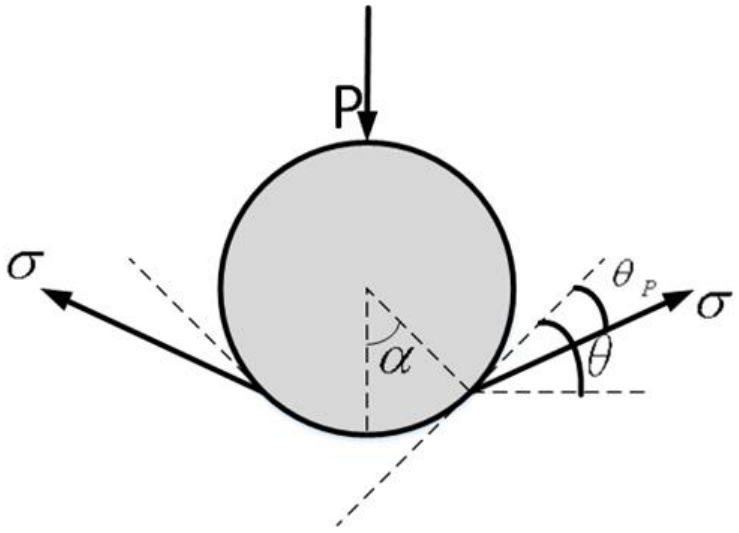

Fig. 5.2 Force balance and geometry in the surface tension limit.

The energy release rate G can be computed using Kendall's peel theory [40]:

$$G = \sigma\left(1 - \cos\theta_p\right), \tag{5.11}$$

Note, by setting $W_{ad} = \gamma_{SA} + \gamma_{CA} - \gamma_{CS}$ and use the fact that surface tension and surface energy has the same value for liquid (In general, this is not assumed in our calculation), the energy release-rate balance equation $G = W_{ad}$ is equivalent to Young-Dupre equation

$$\gamma_{CS} + \sigma\cos\left(\pi - \theta_p\right) = \gamma_{CA}, \tag{5.12}$$

where γ's are the surface energies, the subscripts C, S, A stand for rigid cylinder, compliant substrate and air, respectively. Setting $G = W_{ad}$ in (5.10) allows us to solve for θ_p. Substituting θ_p into (5.9) gives:

$$\frac{P}{2\sigma} = \frac{a}{R}\left(1 - \frac{W_{ad}}{\sigma}\right) - \sqrt{1 - \frac{a^2}{R^2}}\sqrt{1 - \left(1 - \frac{W_{ad}}{\sigma}\right)^2}. \tag{5.13}$$

Equation (5.13) is valid for large deformation. In the small deformation limit, the angles must be small, and (5.13) reduces to a linear relation between load and contact width, i.e.,

$$P = \frac{2\sigma a}{R} - 2\sqrt{2\sigma W_{ad}} \quad . \tag{5.14a}$$

The first term in (5.14a) can be identified as the Hertz-like load i.e., $(W_{ad} = 0)$,

$$P_H = 2\sigma a / R \, . \tag{5.14b}$$

which can also be found directly found using force balance (e.g. setting $\theta_P = 0$ in Fig. 5.2). Comparing (5.14a) and (5.4),

$$dC / da = -1/2\sigma \quad . \tag{5.14c}$$

The half contact width at zero load a_0 is easily found by setting $P = 0$ in (5.14a),

$$a_0 = 2R\sqrt{\frac{W_{ad}}{2\sigma}} \tag{5.15}$$

Note that a_0 is directly proportional to the cylinder radius, whereas in the elasticity dominated limit, this width scales with radius to the 2/3 power. The pull-off load in this limit is independent of the radius of cylinder, i.e.,

$$P_{off} = -2\sqrt{2\sigma W_{ad}} \, , \tag{5.16}$$

in contrast with the elasticity dominated limit, where the pull-off force scales with $R^{1/3}$. In particular, in the surface tension dominated limit, the cylinder pulls off at $a = 0$ whereas in the elasticity dominated limit the cylinder jumps out of contact at a *finite* width $a_{pull-off}$ given by (5.9d).

5.3 Transition between the elasticity and surface-tension-dominated limits

5.3.1 Formulation of the Hertz problem with surface tension

The transition between the elasticity and surface tension dominated limits is completely specified by the Hertz-load P_H and the derivative of the contact compliance Λ_H. To determine these quantities, we solve the indentation Hertz problem with surface tension (but without adhesion). The geometry is shown in Fig. 5.1. Due to surface tension, the normal stress can be discontinuous across the surface. We denote by

$$\lim_{y\to 0^{\pm}} \tau_{yy} \equiv \tau_{yy}^{\pm}(x) \tag{5.17a}$$

where $\tau_{yy}^{+}(x)$ and $\tau_{yy}^{-}(x)$ are the stress normal to the surface as it is approached from inside and outside of the solid. Outside the contact zone $x \in [-a,a], y = 0$, the normal surface traction approached from outside of the solid is zero, which is represented by

$$\lim_{y\to 0^{-}} \tau_{yy} \equiv \tau_{yy}^{-}(x) = 0, \quad x \notin [-a,a], \tag{5.17b}$$

The difference between the normal stress just inside and just outside the solid is given by the Laplace equation, which enforces force balance,

$$\tau_{yy}^{-} - \tau_{yy}^{+} = \sigma v'' \text{ , where } |x| < \infty \tag{5.17c}$$

where *v* is the normal component of surface displacement and we have assumed that curvature of the surface can be approximated by its second derivative with respect to '*x*'. That is, deformation of the surface outside the contact zone gives rise to a Laplace pressure. Therefore, even though the surface outside the contact zone is traction free, the normal component of the stress in the solid, τ_{yy}^{+}, as one approaches the surface *y = 0* from *y > 0* is not zero.

In addition, the incompressibility and traction-free assumption implies that

$$\tau_{xy}(|x| < \infty, y = 0) = 0 \tag{5.17d}$$

The starting point of our analysis begins with a well-known result in elasticity (see Johnson [22]), that the gradient of vertical surface displacement *v* of an incompressible elastic half space is related to the normal traction τ_{yy}^{+} on the surface *y = 0* by

$$\frac{dv}{dx} = \frac{1}{2\pi\mu} PV \int_{-\infty}^{\infty} \frac{\tau_{yy}^{+}(t)dt}{x-t} \quad , \tag{5.18}$$

where μ is the shear modulus of the substrate, *PV* stands for principal value integral and a prime denotes derivative with respect to *x*. As already mentioned, because of surface tension, even though the surface outside the contact zone is traction free, the normal component of the stress τ_{yy}^{+} as one approaches the surface *y = 0* from *y > 0* is not zero.

Using the Hilbert transform, we invert (5.18) obtaining:

$$\frac{1}{2\mu}\tau_{yy}^{+}(x) = -\frac{1}{\pi} PV \int_{-\infty}^{\infty} \frac{dv(t)/dt}{x-t} dt \tag{5.19}$$

To simplify the analysis, we introduce the following normalization:

$$\bar{x} = x/a, \bar{t} = t/a \;,\; \bar{x} = x/a,\; \bar{t} = t/a,\; \bar{v} = vR/a^2,\; s = \frac{\tau_{yy}^{+}(\bar{t})R}{4\mu a} \tag{5.20}$$

Using these normalized variables, (5.19) becomes:

$$s(\bar{x}) = -\frac{1}{2\pi} PV \int_{-\infty}^{\infty} \frac{\bar{v}'(\bar{t})\, d\bar{t}}{\bar{x}-\bar{t}} \;, \tag{5.21}$$

where a prime denotes derivative with respect to $\bar{x}$. While the displacement outside the contact zone is unknown, the displacement inside the contact zone is given by the contact condition. In normalized form, this condition is:

$$\bar{v}'(|\bar{x}|<1) = \frac{d\bar{v}}{d\bar{x}} = -\bar{x} \tag{5.22}$$

Due to symmetry, σ_{yy}^{+} and $\bar{v}'$ are even and odd function of $\bar{x}$ respectively. Using (5.22) and integrating by parts, after some calculations, (5.21) reduces to

$$s(\bar{x}) = -\frac{1}{2\pi}\left[\int_{1}^{\infty} \bar{v}''(\bar{t}) \ln\left|\bar{t}^2 - \bar{x}^2\right| d\bar{t} + \left(2 + \bar{x}\ln\left|\frac{\bar{x}-1}{\bar{x}+1}\right| - \ln\left|\bar{x}^2-1\right|\right)\right] \tag{5.23}$$

It should be noted that, in carrying out integration by parts, we enforced the continuity of $\bar{v}'$ across the contact line – ensuring bounded stress. The traction free boundary condition outside the contact zone requires $\tau_{yy}^{-}(|x|>a)=0$, so it follows from (5.17c) that τ_{yy}^{+} alone must balance the Laplace pressure induced by the surface curvature, v'':

$$-\tau_{yy}^{+} = \sigma v'' \Rightarrow s = -\beta \bar{v}'' \;, \qquad |\bar{x}|>1 \tag{5.24a}$$

where

$$\beta \equiv \frac{\sigma}{4\mu a}, \tag{5.24b}$$

is the ratio of the elasto-capillary length σ/μ and the contact width. Substituting (5.24a) in (5.23) gives the integral equation for the unknown vertical displacement outside the contact zone:

$$2\pi\beta\bar{v}''(\bar{x}) = \int_1^\infty \bar{v}''(\bar{x}) \ln\left|\bar{t}^2 - \bar{x}^2\right| d\bar{t} + \left(2 + \bar{x} \ln\left|\frac{\bar{x}-1}{\bar{x}+1}\right| - \ln\left|\bar{x}^2 - 1\right|\right), \quad |\bar{x}| > 1 \tag{5.25}$$

Equation (5.25) implies that $\bar{v}''$ depends on *the single dimensionless parameter* β introduced in (5.24b). Once $\bar{v}''$ is found outside the contact zone, we use (5.23) and (5.20) to determine the normal stress τ_{yy}^{+} inside the contact zone. Finally, it can be shown that, in the elasticity dominated limit where $\beta = 0$, the exact solution of (5.25) is identical to the classical Hertz solution given by (5.6).

It should be noted that our formulation is exact within the assumption of small strain and linear elasticity. Because the Green's function of the line load problem does not have a close form solution, we do not use this approach. Instead, in our formulation the surface tension appears as a boundary condition, as given by (5.17c). This equation is coupled to (5.19), which relates the deformation of the free surface to the normal stress distribution. Note that (5.19) uses the conventional Green's function of the 2D elasticity problem. In our method, we could recover the Green's function of the surface tension problem by solving the integral equation (5.23) numerically. It can be shown that this Green's function decays logarithmically at distances *far* from the line of application of the line force and this will lead to a divergence of the displacement field at infinity, as stated in the last paragraph before section 5.2.1.

5.3.2 Determination of P_H *and* $\Lambda_H = -dC/da$

The extended JKR theory, (5.4), can be written in the normalized form:

$$\hat{P} = \frac{\bar{P}_H \hat{a}^2}{3} - \frac{4}{3}\sqrt{\hat{a}/\bar{\Lambda}_H} \tag{5.26}$$

where

$$\hat{P} = \frac{P}{3\pi\mu R^{1/3}\left(\frac{W_{ad}}{2\pi\mu}\right)^{2/3}}, \quad \bar{P}_H \equiv \frac{R}{\pi\mu a^2} P_H, \quad \hat{a} = \frac{a}{R^{2/3}\left(\frac{W_{ad}}{2\pi\mu}\right)^{1/3}}, \quad \bar{\Lambda}_H = 2\pi\mu a \Lambda_H, \tag{5.27}$$

are the normalized indentation force, Hertz load with surface tension, half contact width and derivative of compliance respectively. Note that indentation load *P* and half

contact width a are normalized by the magnitude of pull-off load and pull-off radius in elasticity dominated limit. In the absence of adhesion, P_H must be balanced entirely by τ_{yy}^-. Using (5.17c) and (5.22), this condition is

$$P_H = -\int_{-a}^{a} \tau_{yy}^-(x)dx = -\int_{-a}^{a} \tau_{yy}^+(x)dx + \frac{2\sigma a}{R} \Rightarrow \bar{P}_H = \frac{4}{\pi}\left[2\beta - \int_{-1}^{1} s(\bar{x},\beta)d\bar{x}\right]. \qquad (5.28)$$

The last equality in (5.28) shows that $\bar{P}_H$ *is a function* of β *only*. Since $\bar{P}_H(\beta = 0) = 1$, this normalization measures the deviation of the Hertz-like load from the elastic limit. It is evaluated by solving (5.25) for $\bar{v}''$, then use (5.23) to evaluate $s(\bar{x},\beta)$ for $|\bar{x}| < 1$. The numerical method we used to solve the integral equation (5.25) is given in the Appendix; here we state the relevant results. As shown in Fig. 5.3, $\bar{P}_H$ can be well approximated by the expression:

$$\bar{P}_H = 1 + \left(\frac{8\beta}{\pi}\right)\left(\frac{\beta^2 + 1.819\beta + 0.1146}{\beta^2 + 1.164\beta + 0.03607}\right) \qquad (5.29)$$

It should be noted that (5.29) gives the correct asymptotic behaviors for small and large β, which correspond to the elasticity and surface tension dominated limits, respectively.

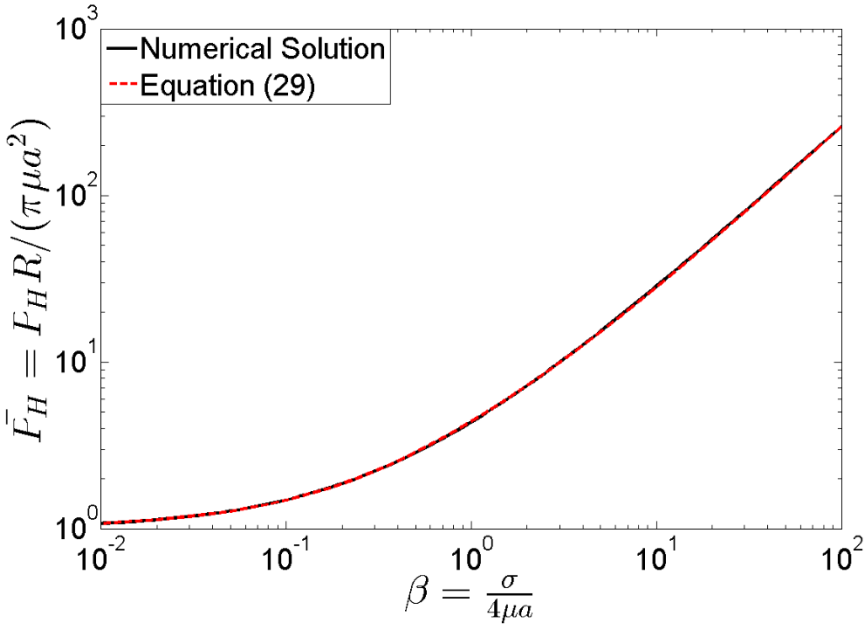

Fig. 5.3 Normalized Hertz-like load $\bar{P}_H$ versus normalized surface tension β. In this plot, the numerical solution is indistinguishable from (5.29). This result matches well with the results of Long *et al*. [33], and here a fitted formula is provided.

To expedite the analysis, it is convenient to define a normalized indentation depth $\bar{\delta}_H$ as

$$\bar{\delta}_H \equiv \delta_H R / a^2 \ . \tag{5.30}$$

Same as in the elasticity limit, we fixed a point *c* at a distance much greater than the contact width, and define the displacement there to be zero; as a result,

$$\begin{aligned} \bar{\delta}_H &= \bar{v}\big|_{\bar{x}=0} - \bar{v}\big|_{\bar{x}=\bar{c}} = \left(\bar{v}\big|_{\bar{x}=0} - \bar{v}\big|_{\bar{x}=1}\right) + \left(\bar{v}\big|_{\bar{x}=1} - \bar{v}\big|_{\bar{x}=\bar{c}}\right) \\ &= \frac{1}{2} - \int_1^{\bar{c}} \bar{v}'(\bar{x})d\bar{x} = \frac{1}{2} + \int_1^{\bar{c}} \left[1 - \int_1^{\bar{x}} \bar{v}''(\bar{t},\beta)d\bar{t} \right] d\bar{x} = \bar{c} - \frac{1}{2} - \int_1^{\bar{c}}\int_1^{\bar{x}} \bar{v}''(\bar{t},\beta)d\bar{t}\,d\bar{x} \end{aligned} \tag{5.31}$$

where $\bar{c} = c/a$. Equation (5.31) allows us to determine $\bar{\delta}_H$ using the solution of the integral equation (5.25). However, unlike $\bar{P}_H$, which depends only on β, $\bar{\delta}_H$ is a function of both $\bar{c}$ and β; thus the normalized instantaneous contact compliance in

general depends on $\bar{c}$ and β, even though $\bar{\Lambda}_H$ is independent of $\bar{c}$. In the Appendix, we show that $\bar{\Lambda}_H$ can be fitted by

$$\bar{\Lambda}_H(\beta) = \frac{\pi\beta^2 + 9.102\beta + 1}{4\beta^3 + 20.82\beta^2 + 12.75\beta + 1}. \tag{5.32}$$

It should be noted that (5.32) gives the correct asymptotic behavior for small and large β.

5.3.3 Extended JKR theory with surface tension

Equations (5.26), (5.29) and (5.32) completely specify the relation between applied load (indentation force) and the contact width. We call this relation the extended JKR theory; it is the main result of this work. Although $\bar{\Lambda}_H$ and $\bar{P}_H$ are functions only of β, the contact width is normally an unknown, so it is convenient to define a different dimensionless quantity ω,

$$\omega = \beta\hat{a} = \frac{\sigma}{4(\mu R)^{2/3}(W_{ad}/2\pi)^{1/3}}. \tag{5.33}$$

Since $\bar{P}_H$ and $\bar{\Lambda}_H$ in (5.26) depend only on $\beta = \omega/\hat{a}$, (5.26) states that the extended JKR theory ($\hat{P} - \hat{a}$ relation) is controlled by a *single* dimensionless parameter ω which is consistent with the work of Cao *et al.* [30]. Fig. 5.4 plots the normalized contact radius $\hat{a}$ versus the normalized load $\hat{P}$ for different ω using (5.26), (5.29) and (5.32). The limiting case of $\omega = 0$ (JKR, elastic limit) is plotted in the same figure as a reference.

Pull-off load and radius

For the elastic limit, it is well known that in a load controlled test, the cylinder suddenly jumps off the substrate at a finite contact width given by (5.9d) with pull-off load given by (5.9c). Fig. 5.4 shows that, the contact width at pull-off decreases with increasing ω and eventually vanishes at a critical value at $\omega \approx 1.6$. From Fig. 5.4, it is

shown that $\left.\frac{d\hat{P}}{d\hat{a}}\right|_{\hat{a}=0} = 0$ at this critical value. From (5.26) and use the fact that $\frac{d\beta}{d\hat{a}} = \frac{d(\omega/\hat{a})}{d\hat{a}} = -\frac{\omega}{\hat{a}^2}$,

$$\left.\frac{d\hat{P}}{d\hat{a}}\right|_{\hat{a}=0} = \frac{8\omega}{3\pi} - \frac{2}{3}\sqrt{\frac{1}{\hat{a}\bar{\Lambda}_H}}\left(1 + \frac{\beta}{\bar{\Lambda}_H}\frac{d\bar{\Lambda}_H}{d\beta}\right) \tag{5.34a}$$

Since $\beta = \omega/\hat{a}$, $\beta \to \infty$ when $\hat{a} \to 0$. Using (5.32), we found

$$\frac{\beta}{\bar{\Lambda}_H}\frac{d\bar{\Lambda}_H}{d\beta} = -1 + \frac{2.30774}{\beta} + o(\frac{1}{\beta^2}) \tag{5.34b}$$

Substituting this relationship into (5.34a) gives

$$\left.\frac{d\hat{P}}{d\bar{a}}\right|_{\bar{a}=0} = \frac{8\omega}{3\pi} - 1.736\sqrt{\frac{1}{\omega}} \tag{5.35}$$

Setting (5.35) equal to zero gives the critical value of ω, $\omega_c \approx 1.6$.

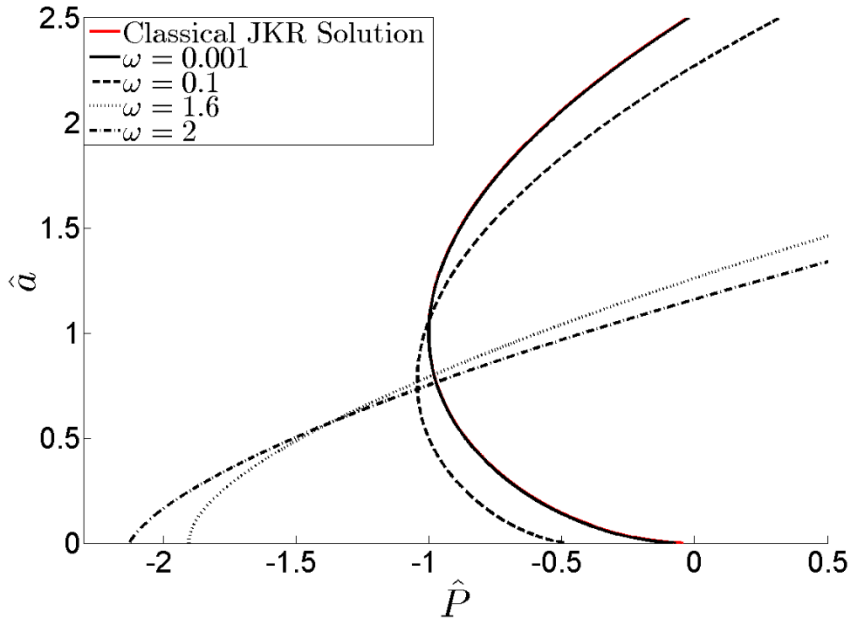

Fig. 5.4 Normalized contact radius versus normalized indentation force for different values of ω.

Thus, our theory predicts that for $\omega > \omega_c$, the cylinder pulls off at zero contact width from the substrate.

Fig. 5.5 highlights the surface tension effect on pull-off load and pull-off width and the way we normalize the load and radius reflect the deviation of pull-off behavior from the elasticity dominated limit (classical JKR solution). It should be noted that under this normalization, both pull-off load and pull-off width depend only on a single dimensionless parameter ω defined by (5.33).

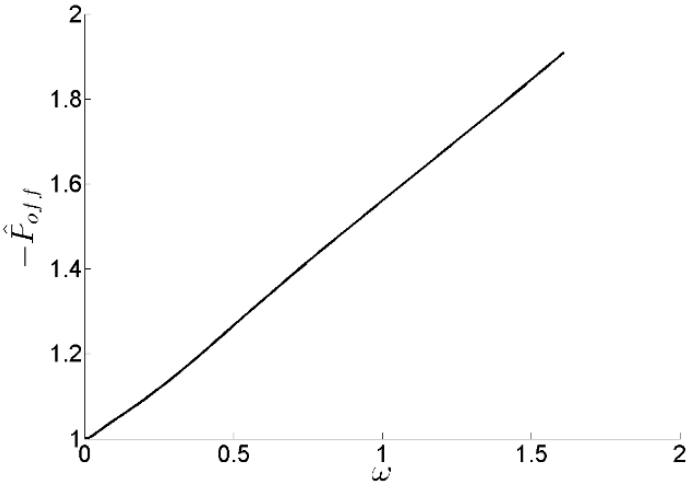

(a)

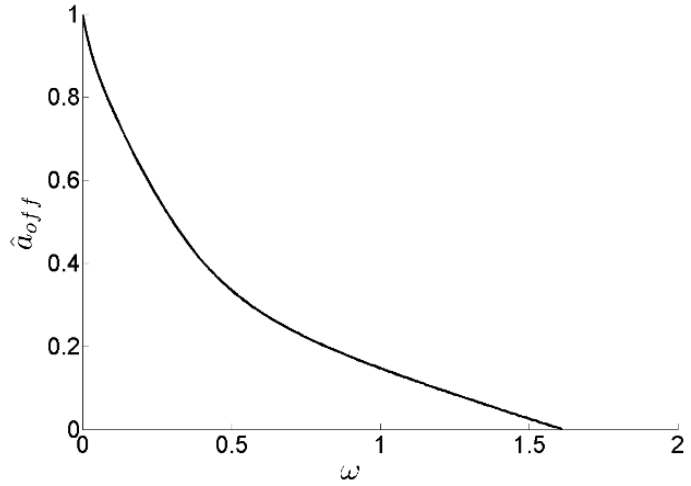

(b)

Fig. 5.5 (a) Normalized pull-off load versus ω (b) Normalized contact half width versus ω.

5.4 Summary and discussion

In this Chapter we analyzed the adhesive contact mechanics of a rigid cylinder indenting an elastic half-space, extending previous analyses to account for the influence of surface tension. Specifically, we show that the classical JKR theory without surface tension can be extended to include surface tension by modifying the Hertz load and the compliance. By introducing the normalization in (5.27), we manage to collapse the classical JKR solution (5.9a) and the liquid-like limit solution (5.14a) into a single relation (5.26) which is completely specified by a single dimensionless parameter ω. Physically, ω is essentially the ratio of the elasto-capillary length σ/μ to a characteristic length $R^{2/3}\left(W_{ad}/\mu\right)^{1/3}$ where adhesion acts (the pull-off width).

There is a significant difference between the pull-off mechanics of a rigid sphere and a rigid long cylinder in contact with a soft elastic substrate. For a sphere with radius R_s, Hui *et al.* [19] has recently shown that the pull-off load is found to vary between $-3\pi R_s W_{ad}/2$ and $-R_s W_{ad}$ for the elasticity dominated and surface tension dominated limit respectively. Note that the pull-off force in both limit is directly proportional to the radius of the sphere and the work of adhesion. In particular, pull-off always occur at a finite contact radius. This is not the case for a rigid cylinder, where the pull-off force is directly proportional to the square root of the product of the surface tension and the work of adhesion, and is independent of the cylinder radius in the liquid limit. In addition, the contact radius at pull-off vanishes above a critical value of ω, $\omega_c \approx 1.6$ implying that surface tension could strongly affect pull-off behavior for long cylinder objects. The deformed shape in the surface-tension-dominated limit also depends on whether the contactor is a sphere or a long cylinder. For example, Carrillo *et al* [20] found that it is necessary to assume the particle deforms into a spherical cap plus a cylindrical neck in order for their model to agree with their molecular dynamics simulation in the surface tension dominated limit. The

deformed shape of our substrate do not looked like a neck, despite the fact that our analysis does contain the "necking" limit, by which we mean the limit in which surface tension dominates. An important difference is that our analysis is in two-dimensions whereas that of Carrillo *et al* [20] is for a deformable axisymmetric spherical particle. Therefore, in the absence of gravity, the shape of the surface near the cylinder must be planar (which does not "look" like a neck) in the surface-tension-dominated limit. Finally, we are not aware of any experiments on contact mechanics of cylinders on substrates where surface tension effects are important. It will be very interesting to see whether our prediction is consistent with future experimental observations.

There are obvious limitations in our model, we use small strain theory where the contact radius is assumed to be small in comparison with the radius of the cylinder. This condition is not expected to hold in experiments involving very soft substrates. For a rigid sphere in contact with soft substrates, it has been found that the small strain theory is amazingly good for contact radius as large as 75% of the sphere radius (in liquid limit $W_{ad} << \sigma$ is assumed) [19]. Of course, the same conclusion may not apply for the cylindrical geometry. In a future work, we will use large deformation theory to quantity the limitations of the small strain theory. Also, our calculation is strictly valid for no-slip contact. For substrates such as hydrogels, the frictionless boundary condition could be more appropriate. Recall that the classical JKR theory is strictly valid for frictionless and no slip contact, as long as the substrate is incompressible. However, as pointed out in section 5.2, without the no-slip condition, one would have to introduce new physics into the model since the tension of the substrate surface will change once it is in contact with the rigid surface. The problem is that the interfacial tension between a rigid surface and the surface of a compliant solid is not well defined, as a rigid surface can support any tension. From the mechanics point of view,

there is no consistent way to assign the tension acting on the substrate surface after contact. One way to deal with this difficulty is to assign the same tension to the substrate surface after contact, which is essentially the approach of Long *et a.l* [33]. In this case the results in this Chapter apply without modification. However, the effect of this approximation could result in a work of adhesion that is different from that given by the Young-Dupre equation. Whether this ad-hoc assumption is justified will depend on future experimental data.

APPENDIX 5.1

NUMERICAL IMPLEMENTATION

The governing equation of this problem is equation (5.24):

$$2\pi\beta\bar{v}''(\bar{x}) = \int_1^{\infty} \bar{v}''(\bar{x}) \ln\left|\bar{t}^{\,2} - \bar{x}^2\right| d\bar{t} + \left(2 + \bar{x} \ln\left|\frac{\bar{x}-1}{\bar{x}+1}\right| - \ln\left|\bar{x}^2 - 1\right|\right), \quad |\bar{x}| > 1$$

Which is a Fredholm integral equation of the second kind defined on the interval $(1,\infty)$. To solve the equation numerically, we first change the interval to be finite by taking $\bar{t} = \tan(\frac{p}{2})$, $\bar{x} = \tan(\frac{q}{2})$. Now, the integral is changed to:

$$\int_1^{\infty} \bar{v}''(\bar{t}) \ln\left|\bar{t}^{\,2} - \bar{x}^2\right| d\bar{t} = \int_{\pi/2}^{\pi} \frac{\bar{v}''\left(\tan\left(\frac{p}{2}\right)\right)}{2\cos^2\left(\frac{p}{2}\right)} \ln\left|\tan\left(\frac{p}{2}\right)^2 - \tan\left(\frac{q}{2}\right)^2\right| dp \qquad \text{(A5.1.1)}$$

Define $F(\mathrm{p}) = \dfrac{\bar{v}''\left(\tan\left(\frac{p}{2}\right)\right)}{2\cos^2\left(\frac{p}{2}\right)}$, $G(\mathrm{q}) = 2 + \tan\left(\frac{q}{2}\right) \ln\left|\dfrac{\tan\left(\frac{q}{2}\right)-1}{\tan\left(\frac{q}{2}\right)+1}\right| - \ln\left|\tan^2\left(\frac{q}{2}\right)-1\right|$,

equation (5.24) is changed into:

$$\int_{\pi/2}^{\pi} F(p) \ln\left|\tan\left(\frac{p}{2}\right)^2 - \tan\left(\frac{q}{2}\right)^2\right| dp - 4\pi\beta\cos^2\left(\frac{q}{2}\right)\mathrm{F}(\mathrm{q}) = -G(\mathrm{q}) \qquad \text{(A5.1.2)}$$

The integral interval is now changed to $(\pi/2, \pi)$. Divide this interval into n subinterval $(\mathrm{p}_1, \mathrm{p}_2], ..., [\mathrm{p}_i, \mathrm{p}_{i+1}], ..., [\mathrm{p}_n, \mathrm{p}_{n+1})$ with equal length $\Delta = \pi/(2\mathrm{n})$ and take $q_i = \dfrac{p_i + p_{j+1}}{2}$, where $p_i = (\mathrm{i}-1)\Delta$. Based on this discretization, the integral $\int_{\pi/2}^{\pi} F(\mathrm{p}) \ln\left|\tan\left(\frac{p}{2}\right)^2 - \tan\left(\frac{q}{2}\right)^2\right| dp$ can be evaluated approximately as:

$$\int_{\pi/2}^{\pi} F(\mathrm{p}) \ln \left| \tan\left(\frac{p}{2}\right)^2 - \tan\left(\frac{q}{2}\right)^2 \right| du$$

$$= \int_{\pi/2}^{\pi} F(p) \ln \left| \frac{\tan\left(\frac{p}{2}\right)^2 - \tan\left(\frac{q}{2}\right)^2}{p-q} \right| dp + \int_{\pi/2}^{\pi} F(\mathrm{p}) \ln|p-q| dp \qquad \text{(A5.1.3)}$$

$$\approx \sum_{j=1}^{N} F(\mathrm{q}_j) \int_{p_j}^{p_{j+1}} \ln \left| \frac{\tan\left(\frac{p}{2}\right)^2 - \tan\left(\frac{q}{2}\right)^2}{p-q} \right| dp + \sum_{j=1}^{N} F(\mathrm{q}_j) \int_{p_j}^{p_{j+1}} \ln|p-q| dp$$

According to (A5.1.3), equation (A5.1.2) can be changed into discretized form:

$$\sum_{i=1}^{n} K_{ij} F(\mathrm{q}_j) = -G(\mathrm{q}_i) \qquad \text{(A5.1.4)}$$

Where $$K_{ij} = \int_{p_j}^{p_{j+1}} \ln \left| \frac{\tan\left(\frac{p}{2}\right)^2 - \tan\left(\frac{q_i}{2}\right)^2}{p-q_i} \right| dp + \int_{p_j}^{p_{j+1}} \ln|p-q_i| dp - 4\pi\beta \cos^2\left(\frac{q_i}{2}\right)\delta_{ij}$$ (no sum on i). The integral can be easily evaluated and therefore K_{ij} can be expressed as:

$$K_{ij} = \begin{cases} (p_{j+1}-p_j) \ln \left| \dfrac{\tan^2(\mathrm{q}_j/2) - \tan^2(\mathrm{q}_i/2)}{q_j - q_i} \right| \\ -(\mathrm{p}_{j+1}-p_j) + (\mathrm{p}_{j+1}-q_j) \ln|p_{j+1}-q_i| + (\mathrm{q}_i - p_j) \ln|p_j - q_i|, \ \mathrm{i} \neq \mathrm{j} \\ (\mathrm{p}_{j+1}-p_j) \ln \left| \dfrac{\tan\left(\frac{q_i}{2}\right)}{\cos^2\left(\frac{q_i}{2}\right)} \right| - 4\pi\beta \cos^2\left(\frac{q_i}{2}\right) \\ -(\mathrm{p}_{j+1}-p_j) + (\mathrm{p}_{j+1}-q_j) \ln|p_{j+1}-q_i| + (\mathrm{q}_i - p_j) \ln|p_j - q_i|, \ \mathrm{i=j} \end{cases} \qquad \text{(A5.1.5)}$$

Substitute equation (A5.1.5) into equation (A5.1.4), $F(\mathrm{q}_j)$ can be solved numerically and $\bar{v}''(\tan(\mathrm{q}_j/2)) = 2F(\mathrm{q}_j)\cos^2(\mathrm{q}_j/2)$.

APPENDIX 5.2

CALCULATION OF $\overline{\Lambda_H}$

First, we need to calculate the Compliance C:

$$C = \frac{d\delta_H}{dP_H} = \frac{d\delta_H / da}{dP_H / da}$$
$$= \frac{d(\overline{\delta_H} a^2 / R) / \mathrm{d}(\bar{a}\,\mathrm{R})}{d(\overline{P_H}\pi\mu a^2 / R) / \mathrm{d}(\bar{a}\,\mathrm{R})} = \frac{1}{\pi\mu}\frac{\bar{a}d\overline{\delta_H} / d\bar{a} + 2\overline{\delta_H}}{\bar{a}d\overline{P_H} / d\bar{a} + 2\overline{P_H}} \tag{A5.2.1}$$

Where $\bar{a} = a / R$. It is easy to show that $\overline{\Lambda_H} = 2\pi\mu a\Lambda_H$ is calculated as:

$$\overline{\Lambda_H} = -2[(2\overline{P_H} - \beta\frac{d\overline{P_H}}{d\beta})(\beta^2\frac{\partial^2\overline{\delta_H}}{\partial\beta^2} + 2\beta\bar{c}\frac{\partial^2\overline{\delta_H}}{\partial\beta\partial\bar{c}} + \bar{c}^2\frac{\partial^2\overline{\delta_H}}{\partial\bar{c}^2} - \beta\frac{\partial\overline{\delta_H}}{\partial\beta} - \bar{c}\frac{\partial\overline{\delta_H}}{\partial\bar{c}})$$
$$+(\beta\frac{\partial\overline{\delta_H}}{\partial\beta} + \bar{c}\frac{\partial\overline{\delta_H}}{\partial\bar{c}} - 2\overline{\delta_H})(\beta^2\frac{d^2\overline{P_H}}{d\beta^2} - \beta\frac{d\overline{P_H}}{d\beta})] / (2\overline{P_H} - \beta\frac{d\overline{P_H}}{d\beta})^2 \tag{A5.2.2}$$

Since $\overline{P_H}$ is only a function of β and $\overline{\delta_H}$ is a function of β and $\bar{c}$, $\overline{\Lambda_H}$ is at most a function of β and $\bar{c}$ (or equivalently, $\alpha, c/R, \bar{a}$). However, since the general JKR solution can't depend on where we select our dictum plane, $\overline{\Lambda_H}$ can only be a function of β. To prove this point, different values of c/R and a/R are taken to compute $\overline{\Lambda_H}$:

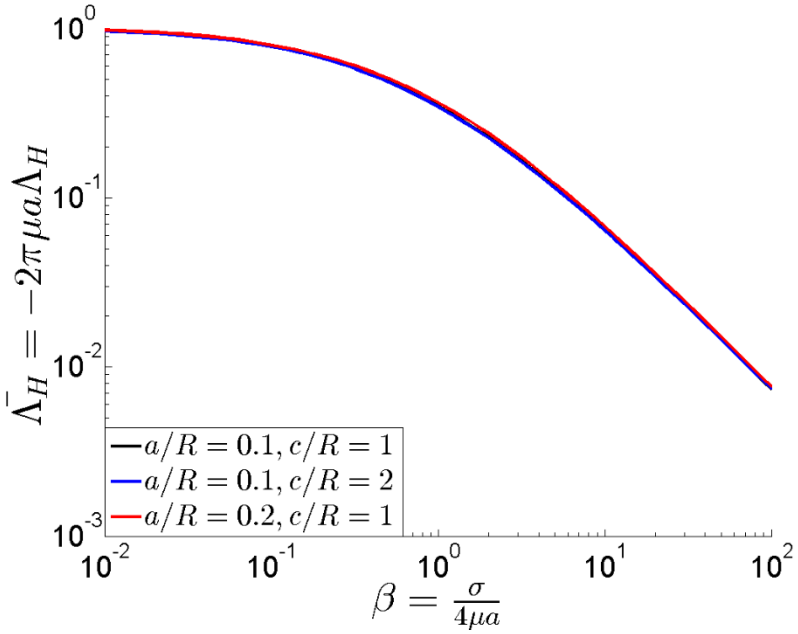

Fig. A5.2.1 $\overline{\Lambda_H}$ vs elasto-capillary number

From the plot shown above, it can be seen that different value of c/R and a/R result in almost same $\overline{\Lambda_H} - \alpha$ curve. This curve can be fitted by:

$$\bar{\Lambda}_H(\alpha) = \frac{\pi\alpha^2 + 9.102\alpha + 1}{4\alpha^3 + 20.82\alpha^2 + 12.75\alpha + 1} \qquad \text{(A5.2.3)}$$

REFERENCES

[1] S. Mora, T. Phou, J.-M. Fromental, L. M. Pismen, and Y. Pomeau, Phys. Rev. Lett. **105**, 214301 (2010).

[2] S. Mora, M. Abkarian, H. Tabuteau, and Y. Pomeau, Soft Matter **7**, 10612 (2011).

[3] D. L. Henann and K. Bertoldi, Soft Matter **10**, 709 (2014).

[4] A. Jagota, D. Paretkar, and A. Ghatak, Phys. Rev. E **85**, 51602 (2012).

[5] S. Mora and Y. Pomeau, (2014).

[6] L. A. Lubbers, J. H. Weijs, L. Botto, S. Das, B. Andreotti, and J. H. Snoeijer, J. Fluid Mech. **747**, R1 (2014).

[7] E. R. Jerison, Y. Xu, L. A. Wilen, and E. R. Dufresne, Phys. Rev. Lett. **106**, 186103 (2011).

[8] N. Nadermann, C.-Y. Hui, and A. Jagota, Proc. Natl. Acad. Sci. U. S. A. **110**, 10541 (2013).

[9] C.-Y. Hui and A. Jagota, Proc. R. Soc. A Math. Phys. Eng. Sci. **470**, 20140085 (2014).

[10] L. Limat, Eur. Phys. J. E. Soft Matter **35**, 9811 (2012).

[11] J. B. Bostwick, M. Shearer, and K. E. Daniels, Soft Matter **10**, 7361 (2014).

[12] T. Kajiya, P. Brunet, L. Royon, A. Daerr, M. Receveur, and L. Limat, Soft Matter **10**, 8888 (2014).

[13] T. Liu, R. Long, and C.-Y. Hui, Soft Matter **10**, 7723 (2014).

[14] J. B. Bostwick and K. E. Daniels, Phys. Rev. E **88**, 42410 (2013).

[15] S. Bhuyan, F. Tanguy, D. Martina, A. Lindner, M. Ciccotti, and C. Creton, Soft

Matter **9**, 6515 (2013).

[16] R. W. Style, R. Boltyanskiy, B. Allen, K. E. Jensen, H. P. Foote, J. S. Wettlaufer, and E. R. Dufresne, Nat. Phys. **11**, 82 (2014).

[17] R. W. Style, C. Hyland, R. Boltyanskiy, J. S. Wettlaufer, and E. R. Dufresne, Nat. Commun. **4**, 2728 (2013).

[18] X. Xu, A. Jagota, and C.-Y. Hui, Soft Matter **10**, 4625 (2014).

[19] C.-Y. Hui, T. Liu, T. Salez, E. Raphael, and A. Jagota, Proc. R. Soc. A Math. Phys. Eng. Sci. **471**, 20140727 (2015).

[20] J.-M. Y. Carrillo and A. V Dobrynin, Langmuir **28**, 10881 (2012).

[21] A. Chakrabarti and M. K. Chaudhury, Langmuir **30**, 4684 (2014).

[22] K. L. Johnson, *Contact Mechanics* (Cambridge University Press, 1987).

[23] K. L. Johnson, K. Kendall, and A. D. Roberts, Proc. R. Soc. A Math. Phys. Eng. Sci. **324**, 301 (1971).

[24] C. L. Mowery, A. J. Crosby, D. Ahn, and K. R. Shull, Langmuir **13**, 6101 (1997).

[25] D. . Rimai, D. . Quesnel, and A. . Busnaina, Colloids Surfaces A Physicochem. Eng. Asp. **165**, 3 (2000).

[26] A. Chakrabarti and M. K. Chaudhury, Langmuir **29**, 6926 (2013).

[27] Z. Cao, M. J. Stevens, and A. V. Dobrynin, Macromolecules **47**, 6515 (2014).

[28] T. Salez, M. Benzaquen, and É. Raphaël, Soft Matter **9**, 10699 (2013).

[29] J.-M. Y. Carrillo, E. Raphael, and A. V Dobrynin, Langmuir **26**, 12973 (2010).

[30] Z. Cao, M. J. Stevens, and A. V. Dobrynin, Macromolecules **47**, 3203 (2014).

[31] M. Barquins, J. Adhes. **26**, 1 (1988).

[32] M. K. Chaudhury, T. Weaver, C. Y. Hui, and E. J. Kramer, J. Appl. Phys. **80**, 30 (1996).

[33] J. M. Long, G. F. Wang, X. Q. Feng, and S. W. Yu, Int. J. Solids Struct. **49**, 1588 (2012).

[34] B. . Derjaguin, V. . Muller, and Y. . Toporov, J. Colloid Interface Sci. **53**, 314 (1975).

[35] D. Maugis, J. Colloid Interface Sci. **150**, 243 (1992).

[36] M. K. Chaudhury and G. M. Whitesides, Langmuir **7**, 1013 (1991).

[37] J. M. Baney and C.-Y. Hui, J. Adhes. Sci. Technol. **11**, 393 (1997).

[38] Y. S. Leng, Y. Z. Hu, and L. Q. Zheng, Proc. R. Soc. A Math. Phys. Eng. Sci. **456**, 185 (2000).

[39] S. Vajpayee, C.-Y. Hui, and A. Jagota, Langmuir **24**, 9401 (2008).

[40] K. Kendall, J. Phys. D. Appl. Phys. **8**, 1449 (1975).

CHAPTER 6

HOW DOES SURFACE TENSION AFFECTS ENERGY RELEASE RATE OF CRACKS LOADED IN MODE I?[6]

6.1 Introduction

The characteristic length scale that controls the deformation of a solid due to its surface tension σ is given by the ratio between the surface tension and its shear modulus *G*. For hard materials such as metals and ceramics, this "capillary" length σ/G is smaller than atomic dimensions, hence surface tension effect can be ignored. However, the capillary length of soft materials such as hydrogels and elastomers range from tens of nm to hundreds of μm. For this class of materials, surface tension can drive shape change, for example, a sharp corner in a soft material cannot remain sharp because of surface tension [1,2]. Surface tension can also flatten surfaces of structures made by replica molding [3,4]. Surface tension can cause Plateau instability in thin gel filaments [5]. Surface tension can also resist deformation, for example, both experiments and theory has shown that the contact mechanics of spheres and cylinders on soft elastic substrates can be affected by solid surface tension [6–11]. Liu et al. [12] have shown that surface tension induced Laplace pressure can cause closure of a crack inflated by hydrostatic pressure.

There are very few experimental studies examining the role of surface stress in fracture since actual measurements of surface stresses are very difficult to make. The first theoretical study on the influence of surface stress on the fracture of elastic solids were carried out by Thomson, Chuang and Lin [13] in 1986 (hence forth referred as TCL). In their model, they ignored the curvature of the deformed crack faces, and the effect of surface stresses is modelled as line forces acting at the crack tip. Their analysis showed that even though the

[6] Hui C.Y., Liu T., Schwaab M.E., (2015), Extreme Mechanics Letter, **6**, 31-36

singularities due to these line forces are much higher than the typical inverse square root singularity in linear elastic fracture mechanics, they have no effect on the crack tip energy release rate [see remarks after eq. 42 in their paper].

It is interesting to compare TCL's result with the more recent studies of Kim, Schiavone and Ru [14,15] (hence forth refer as KSR). Using the surface constitutive model of Gurtin and Murdoch [16], KSR [14] in 2010 formulated a small strain theory of fracture to study the effect of surface tension on fracture of a plane strain crack loaded in Mode I and Mode II. Their numerical results showed that the stress field directly ahead of a Mode I crack is bounded, *irrespective of the magnitude of the surface stress* (as long as it is not exactly zero). In a later paper [14], KSR reexamined their numerical solution in greater details and concluded that the stress field directly ahead of the crack tip of a Mode I crack has a weaker logarithmic singularity. In both cases their numerical results imply that the stress intensity factor (or the local stress intensity factor $K_{local} = K_A + K_{ST}$) is *exactly* zero. In other words, the applied stress intensity factor K_A is cancelled by the negative stress intensity factor K_{ST} caused by the curvature induced Laplace pressure acting to close the crack faces. Since a zero local stress intensity factor implies that local energy release rate is also zero, their result is the exact opposite of TCL's. Furthermore, because surface tension is represented as a line force, the stress field near the crack tip in Thomson's model is more singular than the inverse square root singularity of the classical theory and this result also contradicts the result of KSR.

The goal of this letter is resolve this paradox. To simplify the analysis, we focus on Mode *I* cracks and the surface stress $\sigma_{\alpha\beta}$ is assumed to be isotropic and is a constant independent of surface strain, that is, $\boldsymbol{\sigma} = \sigma \boldsymbol{I}$ where σ is the surface tension (force/length). To focus attention on the crack tip, we consider

the "Small Scale Surface tension" problem in which the effect of surface tension is confined to a region that is small with respect to typical specimen dimensions. As in Small Scale Yielding in classical fracture theory [17], the crack is semi-infinite and lies on the negative x axis, as shown in Fig. 6.1. The boundary condition is that at distances far from the crack tip, the stress and deformation field approaches the usual inverse square root singularity of the classical elasticity solution. More details will be given in the next section.

The curvature induced Laplace pressure p_L resisting the opening of the crack (see Fig. 6.1) is related to the surface tension σ and the curvature of the deformed crack faces κ by:

$$p_L = \sigma\kappa, \text{ where } \kappa = \frac{\mathrm{v}''}{\left[1+\left(\mathrm{v}'\right)^2\right]^{3/2}}, \tag{6.1}$$

where v is the crack opening displacement and a prime denotes differentiation with respect to x. In KSR, v' is assumed to be small everywhere and κ is approximated by:

$$\kappa = \mathrm{v}'' \tag{6.2}$$

Due to this approximation, the governing equation describing the crack tip field is linear and the full machinery of analytic function theory can be used to formulate the crack problem. In contrast, TCL avoided this issue all together by placing a line force at the crack tip - the curvature induced Laplace pressure appears as a delta function in their formulation [12].

It is easy to understand why K_{local} had to be zero in KSR's analysis, that is, the local stress field near the crack tip cannot have an inverse square root singularity. Indeed, assuming K_{local} is positive, the crack opening for the upper crack face near the crack tip is:

$$\mathrm{v} = \frac{2(1-\upsilon)K_{\mathrm{local}}}{G\sqrt{2\pi}}\sqrt{-x}, \quad x<0 \tag{6.3}$$

where υ is the Poisson's ratio and *G* the shear modulus. Substituting (6.3) into $\kappa = \mathrm{v}''$ gives

$$\kappa \propto K_{\text{local}} |x|^{-3/2}, \; x \to 0^- \tag{6.4}$$

Equations (6.4) and (6.1) imply that the Laplace pressure has a *non-integrable* singularity; such a singular pressure field will induce an *infinite* negative stress intensity factor at the crack tip, which means that K_{local} goes to negative infinity. This is a contradiction to the original assumption that K_{local} is positive so the only possibility is $K_{\text{local}} = 0$, which implies that the stress is bounded or has a weaker singularity.

The fact that $K_{\text{local}} = 0$ brings up the possibility a line force can exist at the crack tip. Indeed, in linear elasticity fracture mechanics, the crack tip deforms into a cusp shape if the stress is bounded at the tip - the Dugdale-Barenblatt model being a prime example [17–19]; whereas a logarithmic singularity in stress implies the crack tip opens into a wedge [see Appendix]. In both cases the curvature has a delta function behavior which corresponds to existence of a line force acting at the crack tip. Thus, the crack tip stress field in the KSR model can still be singular since the singularity in curvature can causes a singular field similar to those studied by TCL. Specifically, an implicit assumption of KSR is that curvature is non-singular; otherwise a concentrated line force can act at the crack tip.

The key idea in this letter is that these difficulties can be resolved using the full curvature expression. To see this, let us assume that the local crack tip field has form given by standard theory (6.3), then (6.1) implies that

$$\kappa\left(x \to 0^-\right) \to \frac{\mathrm{v}''}{|\mathrm{v}'|^3} = \frac{-\pi G^2}{2(1-\nu)^2 K_{local}^2} \tag{6.5}$$

The key feature is that v'' and $(v')^3$ has exactly the same singularity, so the curvature is *bounded* at the crack tip. This result implies that the curvature induced Laplace pressure is finite everywhere along the crack face *including the crack tip*. Thus, for sufficiently small surface tensions, the local stress intensity factor is well defined and positive (hence there is a non-zero energy release rate). In addition, the existence of finite curvature eliminates the possibility of a singular line force acting at the crack tip.

6.2 Formulation and analysis

To quantify our idea, we employed the usual small scale yielding formulation where the crack is modeled as semi-infinite and lies on the negative *x* axis with its tip at *x = 0*. For our case, the plastic zone is replaced by replaced by a zone where surface curvature is significant. This formulation is valid in the limit where the capillary length σ / G is much smaller than the crack length *a*. For example, the shear modulus of a soft hydrogel is on the order of 100 to 1000 Pa, using a crack length of 1cm, σ /Ga ranges from 0.07 to 0.007, where we have taken the surface tension of the hydrogel to be equal to the surface tension of water, which is about 0.07N/m. Thus, for most soft materials, the region of dominance of surface tension is expected to be localized at the crack tip. Let K_A denote the applied stress intensity factor. It is the stress intensity factor in the absence of surface tension. The displacement of the upper crack face v_A due to the applied K_A field is

$$v_A = \frac{2(1-\nu)K_A}{G}\sqrt{-x/2\pi},\ x<0 \tag{6.6}$$

Surface tension σ caused a restraining pressure $p_L(x)$ to close the crack, see (6.1). The crack face displacement v_p due to an arbitrary pressure field p acting on the crack faces is well known [20]; setting $p = p_L(x)$ gives:

$$v_p = \frac{(1-\nu)}{G\pi}\int_{-\infty}^{0} p_L(t)\ln\left|\frac{\sqrt{|x|}+\sqrt{|t|}}{\sqrt{|x|}-\sqrt{|t|}}\right|dt \tag{6.7}$$

The actual crack opening displacement is the sum of (6.6) and (6.7)

$$v = v_A + v_p\,. \tag{6.8}$$

The Laplace pressure is related to the curvature of the crack opening displacement v by (6.1). Substituting this into (6.6-6.7), (6.8) becomes:

$$v(x) = \frac{2(1-\nu)K_A}{G}\sqrt{-x/2\pi} + \frac{(1-\nu)\sigma}{\pi G}\int_{-\infty}^{0}\frac{v''(t)}{\left[1+\left(v'(t)\right)^2\right]^{3/2}}\ln\left(\frac{\sqrt{-x}+\sqrt{-t}}{\sqrt{-x}-\sqrt{-t}}\right)dt,\quad x<0 \tag{6.9}$$

For a given applied stress intensity factor, (6.9) is a non-linear integral equation for the unknown crack opening displacement v. Equation (6.9) can be reduced to a more standard form by differentiating both sides by x, resulting in:

$$v'(x) = -\frac{(1-\nu)K_A}{G}\sqrt{\frac{-1}{2\pi x}} + \frac{(1-\nu)\sigma}{G\sqrt{-x}}PV\left[\int_{-\infty}^{0}\frac{\sqrt{-t}}{t-x}\frac{v''(t)}{\left[1+v'(t)\right]^{3/2}}dt\right],\ x<0 \tag{6.10}$$

where PV denotes principal value. More insight can be obtained by normalizing x by the elasto-capillary number and the opening displacement v by the opening displacement of a traction free crack evaluated at a distance equal to the elasto-capillary length behind the crack tip, i.e.,

$$\eta = \frac{\pi G}{(1-\nu)\sigma}x,\ \mathrm{v} = \frac{2(1-\nu)K_A}{G}\sqrt{\frac{(1-\nu)\sigma}{2\pi^2 G}}\bar{v} \tag{6.11}$$

Using these normalized variables, the governing equation (6.10) becomes:

$$\dot{\bar{v}}(\eta) = \frac{-1}{2\sqrt{-\eta}} + \frac{1}{\sqrt{-\eta}}\int_{-\infty}^{0}\frac{\sqrt{-\xi}}{\xi-\eta}\frac{\ddot{\bar{v}}(\xi)}{\left[1+\beta\left(\dot{\bar{v}}(\xi)\right)^2\right]^{3/2}}d\xi,\ \eta<0 \tag{6.12a}$$

where a dot denote differentiation with respect to the normalized distance η and

$$\beta \equiv \frac{2(1-\upsilon)K_A^2}{G\sigma} = 4\left(J_A/\sigma\right) \tag{6.12b}$$

is a dimensionless parameter. It is proportional to the ratio of the energy release rate without surface tension, J_A , to the surface tension. It is particular interesting to note that if the approximation $\kappa \approx v''$ is used, (6.12a) becomes

$$\dot{\bar{v}}(\eta) = \frac{-1}{2\sqrt{-\eta}} + \frac{1}{\sqrt{-\eta}} \int_{-\infty}^{0} \frac{\sqrt{-\xi}}{\xi - \eta} \ddot{\bar{v}}(\xi) d\xi, \ \eta<0. \tag{6.13}$$

Note that there is no free parameter in (6.13). The absence of β means that the near tip fields is universal, that is, increasing or decreasing the surface tension could only change the region of asymptotic validity of the near tip fields, but not its form. Our asymptotic analysis of (6.13) supports the numerical results of KSR [14] - the normal stress σ_{yy} directly ahead of the crack tip has a logarithmic singularity. This analysis is given in the appendix for completeness.

The local stress intensity factor K_{local} can be expressed by adding the applied stress intensity factor to the stress intensity factor induced by the Laplace pressure. This can be done by examining the behavior of $v'(x \to 0^+)$ in (6.10) or by using a standard expression in fracture mechanics [20]:

$$K_{local} = K_A + \sigma \sqrt{\frac{2}{\pi}} \int_{-\infty}^{0} \frac{v''(t)}{\left[1 + v'(t)\right]^{3/2}} \frac{dt}{\sqrt{-t}} \tag{6.14}$$

In normalized form, (6.14) is

$$\frac{K_{local}}{K_A} = 1 + \chi(\beta), \ \chi(\beta) = 2 \int_{-\infty}^{0} \frac{\ddot{\bar{v}}(\xi)}{\left(1 + \beta \dot{\bar{v}}^2(\xi)\right)^{3/2}} \frac{d\xi}{\sqrt{-\xi}} \tag{6.15}$$

Note that $\chi(\beta)$ is in general negative ($\ddot{\bar{v}}(\xi) < 0$) there is a reduction in stress intensity factor. In this letter we limit our study to small surface tension where $\beta >> 1$. In this limit, the integral term in (6.12a) is small compare with the first term so that

$$\dot{\bar{v}}(\eta) = \frac{-1}{2\sqrt{-\eta}} + O(1/\beta). \tag{6.16}$$

Therefore a first order estimate of K_{local} can be determined by substituting $\dot{\bar{v}}(\eta) \approx \frac{-1}{2\sqrt{-\eta}}$ in (6.16) into (6.15) and evaluating $\chi(\beta)$. The resulting integral can be evaluated exactly and we found

$$\frac{K_{local}}{K_A} = 1 - \frac{4}{\pi\beta},\ \beta << 1. \tag{6.17}$$

Since the energy release rate is proportional to the square of the stress intensity factor, (6.17) is equivalent to

$$\frac{J_{local}}{J_A} = \left(1 - \frac{4}{\pi\beta}\right)^2,\ \text{where } \beta << 1. \tag{6.18}$$

where J_{local} is the energy release rate at the crack tip. Equation (6.18) shows that surface tension reduces applied energy release rate gradually and smoothly.

6.3 Discussion

Our model gives a satisfactory resolution of the differences in result between the work of TCL and KSR. To summarize, in TCL, the curvature of the deformed crack faces are ignored, the surface tension acts on the un-deformed flat crack faces. The line force boundary condition corresponds to the sudden change of slope at the crack tip. In contrast, KSR imposed a closing pressure on the undeformed crack faces which is proportional to the curvature of the deformed crack faces. These two different approaches gave very different results: in TCL, surface tension has no effect on the applied energy release rate, but increases the stress singularity at the crack tip; while for KSR, surface tension eliminates the local energy release rate by reducing the stress singularity at the crack tip.

Our approach is to treat the surface tension induced Laplace pressure as a cohesive traction acting on the crack faces. Cohesive traction (force) model was introduced by Barenblatt [19] to study brittle fracture. His idea is that the separation of perspective

fracture surfaces directly ahead of a crack is resisted by atomic cohesive forces. Since its introduction cohesive force model has been used to study a wide variety of fracture phenomenon. In the standard theory, the cohesive traction is a nonlinear function of crack opening displacement. For our case, the cohesive traction depend only on the curvature of the crack face (or the first and second derivatives of the crack opening displacement). Our model is mathematically equivalent to KSR, except we retain the nonlinear terms in the evaluation of curvature. Retaining this nonlinear term smooth over the curvature field and avoids the dominance of surface tension over elasticity near the crack tip. The result is that for small surface tensions, the local stress field has the same square root singularity, but with a reduce stress intensity factor. The applied energy release rate is also reduced by surface tension. Of course, if β is small, that is, if the surface tension is large or the applied stress intensity factor small, then the Laplace pressure could close the crack and eliminate the inverse square singularity at the crack tip. We did not study this scenario, but a recent paper by Liu et al [12] showed that the local energy release of an internally pressurized crack subjected to large deformation can vanish or even become negative for sufficiently large surface tensions or small internal pressures.

Our approach can be readily applied to finite cracks in elastic solids, as long as the Green's function for line load acting on the crack faces is known. Consider for example a plane strain crack of length *2a* in an infinite elastic block subjected to remote tension σ_A. For this case, the crack opening displacement due to the Laplace pressure v_p is related to the actual crack opening displacement *v* by

$$v_p = \frac{(1-\nu)\sigma}{G\pi}\int_{-a}^{a}\frac{v''(t)}{\left[1+\left(v'(t)\right)^2\right]^{3/2}}\ln\left|\frac{\sqrt{a^2-x^2}+\sqrt{a^2-t^2}}{\sqrt{a^2-x^2}-\sqrt{a^2-t^2}}\right|dt \qquad (6.19)$$

where we have used a standard result [20]. The crack opening displacement v_A due to the applied remote tension σ_A is

$$v_A = \frac{(1-\upsilon)\sigma_A}{G}\sqrt{a^2 - x^2} \tag{6.20}$$

The integral equation governing the unknown v is obtained by combining (6.19-6.20):

$$\begin{aligned} v(x) &= \frac{(1-\upsilon)\sigma_A}{G}\sqrt{a^2 - x^2} \\ &+ \frac{(1-\nu)\sigma}{G\pi}\int_{-a}^{a} \frac{v''(t)}{\left[1+\left(v'(t)\right)^2\right]^{3/2}} \ln\left|\frac{\sqrt{a^2-x^2}+\sqrt{a^2-t^2}}{\sqrt{a^2-x^2}-\sqrt{a^2-t^2}}\right| dt, \text{ where } |x| < a \end{aligned} \tag{6.21}$$

There is obvious limitation to the small strain approach used in this work, especially for very soft solids where the deformation can be exceeding large near the crack tip. An example of a crack subjected to very large deformation can be found in Sun et al. [21]. The fact that we need to retain the nonlinear term in curvature suggests that large deformation matters. Therefore, a consistent approach is to carry out a fully nonlinear large deformation analysis such as those recently performed by Liu et al [12]. The stress free reference configuration for a cracked elastic solid can be obtained by imagining turning off surface tension (e.g. treating the crack surfaces with a self-assembled monolayer) in the absence of external load. Starting from this stress free configuration, imagine turning on the surface tension without applying any external load (removing the monolayer). This sudden engagement of surface tension will immediately give a very concentrated line force at the crack tip. This line force will pull the crack tip inwards and resulting in the opening the crack faces. Since the surface stresses depend on the deformed configuration, the line force will be smooth over by the deformation, the curvature of the crack faces is expected to be continuous. This picture is consistent with Liu et al's simulation of a penny-shape crack in a neo-Hookean solid [12].

Finally, we mention that the reduction of energy release rate in our analysis is consistent with the earlier analysis by Wu [22] where an artificial finite tip radius was

introduced to avoid the singularity of curvature. This finite tip radius approach was also used in later works by Fu et al. [23] and Wang et al. [24].

APPENDIX 6.1

ASYMPTOTIC BEHAVIOR OF (6.13)

Let $f(\eta)=\dot{v}(\eta)$, then (6.13) can be rewritten as:

$$f(\eta)=\frac{-1}{2\sqrt{-\eta}}-\frac{1}{\sqrt{-\eta}}\int_{-\infty}^{0}\frac{\sqrt{-\xi}\,\dot{f}(\xi)}{\xi-\eta}d\xi \qquad \text{(A6.1.1)}$$

Define

$$\phi(z)\equiv\frac{1}{2\pi i}\int_{-\infty}^{0}\frac{\sqrt{-\xi}\,\dot{f}(\xi)}{\xi-z}d\xi, \text{ where } z\notin(-\infty,0] \qquad \text{(A6.1.2)}$$

where $z=\eta+i\zeta$ is a complex variable. The function ϕ is analytic in the entire complex *z* plane with the exception of the cut $(-\infty,0]$. Using the Plemeli formulae, we have, for $\eta\in(-\infty,0)$,

$$\phi^{+}(\eta)-\phi^{-}(\eta)=\sqrt{-\eta}\,\dot{f}(\eta) \qquad \text{(A6.1.3a)}$$

$$\phi^{+}(\eta)+\phi^{-}(\eta)=\frac{1}{\pi i}\int_{-\infty}^{0}\frac{\sqrt{-\xi}\,\dot{f}(\xi)}{\xi-\eta}d\xi \qquad \text{(A6.1.3b)}$$

where the superscripts $\pm$ denote the values of ϕ as *z* approaches the cut $(-\infty,0]$ from above or below respectively. Also, the integral in (A6.1.3b) is interpreted as a principal value integral. The asymptotic analysis is easiest to carry out if we formulate (A6.1.1) as a functional equation, as shown below. Equation (A6.1.3b) implies that

$$\pi i\left[\phi^{+}(\eta)+\phi^{-}(\eta)\right]=\int_{-\infty}^{0}\frac{\sqrt{-\xi}\,\dot{f}(\xi)}{\xi-\eta}d\xi \qquad \text{(A6.1.4)}$$

Substituting (A6.1.4) into (A6.1.1), (A6.1.1) becomes,

$$f(\eta)=\frac{-1}{2\sqrt{-\eta}}-\frac{\pi i}{\sqrt{-\eta}}\left[\phi^{+}(\eta)+\phi^{-}(\eta)\right], \text{ for } \eta\in(-\infty,0) \qquad \text{(A6.1.5)}$$

Now differentiate (A6.1.5) with respect to η, it becomes

$$\dot{f}(\eta)=\frac{-1}{4(-\eta)^{3/2}}-\frac{\pi i}{2(-\eta)^{3/2}}\left[\phi^{+}(\eta)+\phi^{-}(\eta)\right]-\frac{\pi i}{(-\eta)^{1/2}}\frac{d\left[\phi^{+}(\eta)+\phi^{-}(\eta)\right]}{d\eta} \qquad \text{(A6.1.6)}$$

Substituting (A6.1.6) into (A6.1.3a), we have

$$\begin{aligned}
&\phi^+(\eta)-\phi^-(\eta)\\
&=\sqrt{-\eta}\left\{\frac{-1}{4(-\eta)^{3/2}}-\frac{\pi i}{2(-\eta)^{3/2}}\left[\phi^+(\eta)+\phi^-(\eta)\right]-\frac{\pi i}{(-\eta)^{1/2}}\frac{d\left[\phi^+(\eta)+\phi^-(\eta)\right]}{d\eta}\right\} \qquad \text{(A6.1.7)}\\
&=\frac{1}{4\eta}+\frac{\pi i}{2\eta}\left[\phi^+(\eta)+\phi^-(\eta)\right]-\pi i\frac{d\left[\phi^+(\eta)+\phi^-(\eta)\right]}{d\eta}
\end{aligned}$$

The form of (A6.1.7) suggest that as $\eta\to 0^-$, the RHS of (A6.1.7) should dominate the LHS, so that the first order asymptotic behavior of ϕ can be examined by studying the equation

$$\frac{1}{4\eta}+\frac{\pi i}{2\eta}\left[\phi^+(\eta)+\phi^-(\eta)\right]-\pi i\frac{d\left[\phi^+(\eta)+\phi^-(\eta)\right]}{d\eta}=0,\ \text{for } \eta\to 0^- \qquad \text{(A6.1.8)}$$

Let $g(\eta)\equiv\left[\phi^+(\eta)+\phi^-(\eta)\right]$, then (A6.1.7) implies that

$$\frac{dg}{d\eta}-\frac{g}{2\eta}=\frac{1}{4\pi i\eta},\ \eta\to 0^- \qquad \text{(A6.1.9)}$$

The general solution of (A6.1.8) is

$$g(\eta)\equiv\left[\phi^+(\eta)+\phi^-(\eta)\right]=-\frac{1}{2\pi i}+iA(-\eta)^{1/2} \qquad \text{(A6.1.10)}$$

where *A* is an arbitrary real constant (this is because *g* is purely imaginary according to (A6.1.3b)). Substituting (A6.1.10) into (A6.1.5), we have

$$f(\eta)=\frac{-1}{2\sqrt{-\eta}}-\frac{\pi i}{\sqrt{-\eta}}\left[-\frac{1}{2\pi i}+iA(-\eta)^{1/2}\right]=\pi A \qquad \text{(A6.1.11)}$$

Thus, the asymptotic behavior of f as $\eta\to 0^-$ is a constant, and since

$$f(\eta)=\dot{\bar{v}}(\eta)\Rightarrow\bar{v}(\eta)=\pi A\eta \qquad \eta\to 0^- \qquad \text{(A6.1.12)}$$

For non-zero negative *A*, the local shape of crack tip is a wedge. (A6.1.12) implies that the $\sigma_{yy}(x)$ has a logarithmic singularity. For consistency, we should check that the LHS of (A6.1.7) is indeed small in comparison with terms of the RHS as $\eta\to 0^-$. To do this, we solve (A6.1.10) and found

$$\phi=-\frac{1}{4\pi i}-\frac{iA}{2\pi}\sqrt{z}ln(z) \qquad \text{(A6.1.13)}$$

To check that (A6.1.13) indeed satisfies (A6.1.6), we note that

$$\phi^{+} = -\frac{1}{4\pi i} - \frac{iA}{2\pi}\sqrt{-\eta}\, i[ln(-\eta) + \pi i]$$
$$\phi^{-} = -\frac{1}{4\pi i} - \frac{iA}{2\pi}\sqrt{-\eta}\,(-i)[ln(-\eta) - \pi i] \qquad \text{(A6.1.14)}$$

Therefore, $\phi^{+}(\eta) + \phi^{-}(\eta) = -\frac{1}{2\pi i} + iA\sqrt{-\eta}$. From (A6.1.3a) and (A6.1.14), we found

$$\phi^{+}(\eta) - \phi^{-}(\eta) = \sqrt{-\eta}\,\dot{f}(\eta) \to 0, \text{ as } \eta \to 0^{-} \qquad \text{(A6.1.15)}$$

which means the term on the LHS of (A6.1.7) can be neglected compare with any term on the RHS of (A6.1.7). Our result (A6.1.12) shows that $\dot{\bar{v}}(\eta)$ is a constant. We now show that $\bar{\sigma}_{yy}(\eta)$ as η approach the crack tip at $\eta = 0$ has a logarithmic singularity.

To see this, recall that any Mode I crack (with or without traction on its faces) can be viewed as a continuous distribution of dislocations [17]; in particular, for an semi-infinite crack lying on the negative *x* axis,

$$\sigma_{yy}(x) = \frac{G}{2\pi(1-\upsilon)}\int_{-\infty}^{0}\frac{\mu(x')}{x-x'}dx', \text{ for } x \neq 0 \qquad \text{(A6.1.16)}$$

where $\mu(x') = -2dv/dx'$ is the dislocation density. Using (6.11), the normalized form of (A6.1.16) is:

$$\bar{\sigma}_{yy}(\eta) = \frac{1}{2\pi}\int_{-\infty}^{0}\frac{\bar{\mu}(\xi)}{\eta-\xi}d\xi \qquad \text{(A6.1.17)}$$

where $\bar{\sigma}_{yy}$ and $\bar{\mu}$ are the normalized stress and dislocation density defined by

$$\bar{\sigma}_{yy} = \frac{G\sqrt{\beta}}{\pi(1-\upsilon)}\sigma_{yy},\ \bar{\mu}(\xi) = -2\dot{\bar{v}}(\xi) = -\frac{2}{\pi}\sqrt{\beta}\frac{dv}{dx'} \qquad \text{(A6.1.18)}$$

The asymptotic behavior of $\bar{\sigma}_{yy}$ as η approach the crack tip $(\eta = 0)$ can be found using a result of Muskhelishvili [22] where he showed that for $\dot{\bar{v}}(\eta \to 0^{-}) \to \pi A$ (see (A6.1.12)),

$$\bar{\sigma}_{yy}(\eta \to 0^{+}) = \pi A \ln \eta \qquad \text{(A6.1.19)}$$

This result is consistent with a numerical finding of KSR [15].

REFERENCES

[1] C. Y. Hui*, A. Jagota, Y. Y. Lin, and E. J. Kramer, (2002).

[2] S. Mora and Y. Pomeau, J. Phys. Condens. Matter **27**, 194112 (2015).

[3] A. Jagota, D. Paretkar, and A. Ghatak, Phys. Rev. E **85**, 51602 (2012).

[4] D. Paretkar, X. Xu, C.-Y. Hui, and A. Jagota, Soft Matter **10**, 4084 (2014).

[5] S. Mora, T. Phou, J.-M. Fromental, L. M. Pismen, and Y. Pomeau, Phys. Rev. Lett. **105**, 214301 (2010).

[6] R. W. Style, C. Hyland, R. Boltyanskiy, J. S. Wettlaufer, and E. R. Dufresne, Nat. Commun. **4**, 2728 (2013).

[7] J.-M. Y. Carrillo and A. V Dobrynin, Langmuir **28**, 10881 (2012).

[8] Z. Cao, M. J. Stevens, and A. V. Dobrynin, Macromolecules **47**, 6515 (2014).

[9] T. Salez, M. Benzaquen, and É. Raphaël, Soft Matter **9**, 10699 (2013).

[10] X. Xu, A. Jagota, and C.-Y. Hui, Soft Matter **10**, 4625 (2014).

[11] C.-Y. Hui, T. Liu, T. Salez, E. Raphael, and A. Jagota, Proc. R. Soc. A Math. Phys. Eng. Sci. **471**, 20140727 (2015).

[12] T. Liu, R. Long, and C.-Y. Hui, Soft Matter **10**, 7723 (2014).

[13] R. Thomson, T.-J. Chuang, and I.-H. Lin, Acta Metall. **34**, 1133 (1986).

[14] C. I. Kim, P. Schiavone, and C.-Q. Ru, J. Elast. **104**, 397 (2011).

[15] C. Kim, C.-Q. Ru, and P. Schiavone, Math. Mech. Solids **18**, 59 (2013).

[16] M. Gurtin and A. Ian Murdoch, Arch. Ration. Mech. Anal. **57**, (1975).

[17] J. R. Rice, Math. Fundam. **2**, 191 (1968).

[18] D. S. Dugdale, J. Mech. Phys. Solids **8**, 100 (1960).

[19] G. I. Barenblatt, Adv. Appl. Mech. **7**, 55 (1962).

[20] H. Tada, P. C. Paris, and G. R. Irwin, *The Stress Analysis of Cracks Handbook, Third Edition* (ASME, Three Park Avenue New York, NY 10016-5990, 2000).

[21] J.-Y. Sun, X. Zhao, W. R. K. Illeperuma, O. Chaudhuri, K. H. Oh, D. J.

Mooney, J. J. Vlassak, and Z. Suo, Nature **489**, 133 (2012).

[22] C. H. Wu, J. Mech. Phys. Solids **47**, 2469 (1999).

[23] X. L. Fu, G. F. Wang, and X. Q. Feng, Int. J. Fract. **151**, 95 (2008).

[24] G.-F. Wang, X.-Q. Feng, T.-J. Wang, and W. Gao, J. Appl. Mech. **75**, 11001 (2008)

CHAPTER 7

A CLOSED FORM LARGE DEFORMATION SOLUTION OF PLATE BENDING WITH SURFACE EFFECT [7]

7.1 Introduction

Classical elasticity theory usually neglects the effect of surface stress on deformation. However, these stresses can significantly affect deformation of soft materials or of nanostructures made of stiff materials [1]. For example, experiments have shown that the Young's modulus of nanowires is strongly size-dependent [2–6]. This size-dependence has been attributed to the presence of surface stress. A linearized beam theory modified to account for the additional bending resistance due to surface stress was found to be in good agreement with experimental data [7–13]. In this linearized theory, the effect of surface stress and bulk elasticity can be decoupled due to the principle of superposition.

Recent interest in biological materials has motivated many researchers to develop ultra-soft materials such as hydrogels with shear modulus on the order of kilopascals or lower. In soft materials surface stress effects can manifest at the macroscale [14,15]. For example, a sharp corner of a soft solid, after releasing from a mold made of a stiff solid, is rounded to minimize its surface energy [16–21]. Soft solids can exhibit both solid- and liquid-like behavior. For example, liquid-like Rayleigh-Plateau instabilities have been observed for soft elastic cylinders [22]. When a rigid sphere is brought into contact with an elastic substrate, contact size depends on the sphere radius and substrate elasticity. Experiments [23] have shown that very soft substrates resist indentation like a liquid would – the indentation force is balanced by the surface stress of the solid. In contrast, for stiff substrates, the indentation force is balanced primarily by bulk elasticity. To explain these observations, theories based on linear

[7] Liu T., Jagota A., Hui C.Y., (2016), submitted to Soft Matter.

elasticity and/or molecular simulations have been developed and the predictions are found to be consistent with experiments [19,24–33]. In most of these works, surface stress is assumed to be isotropic and independent of surface strain, and hence can be represented by a curvature dependent Laplace pressure. If the displacement and strains are small, then the curvature can be linearized and the additional displacements due to the Laplace pressure can be superimposed on the classical elastic solution. Of course, linearization is permissible only when slopes are small which may not be true in some situations such as near a crack tip [34]. Typically, the deformation of soft solids is large, hence large deformation models are required to correctly capture the physics and mechanics of surface stress.

The theoretical framework of finite surface elasticity in which large deformation is explicitly accounted for has been known for a long time, due mostly to the seminal work of Gurtin and Murdoch [35]. Their formulation include surface elasticity as a special case. In surface elasticity, the surface stress tensor can be obtained by taking the derivative of a surface work function with respect to the deformation gradient tensor. An example is the Shuttleworth equation. More recent works have extended Shuttleworth equation into large deformation regime [36–43]. Large deformation introduces complexity in several ways. First, the equations describing the kinematics of deformation are nonlinear. Second, the surface stresses depends on the geometry of the deformed surface, which is unknown. Finally, the relation between deformation and stresses can be highly nonlinear, i.e., the strains are not proportional to stress, as assumed in linear elasticity. Because of these difficulties, there are very few analytical solutions in the literature. In this work we focus on a problem which admits an analytical solution. Specifically, we consider the pure bending of an isotropic, incompressible plate with finite thickness. Unlike the linearized version of this theory, bulk and surface effects cannot be decoupled in our large deformation calculation. Our

results add to the very limited library of analytical solutions for large deformations of soft materials including surface effects.

In this work, we assume that the surface stress tensor of the plate is isotropic: it consists of a part which is effectively a residual tension and a part which increases with the surface area. Most analytical models of elasto-capillarity are based on keeping only the first term. Here we extend this model to include effect of area stretch on the surface stress. Our model is an extension of Gibbs surface elasticity (with surface shear modulus = 0) to the large deformation regime.

The plan of this Chapter is as follows. We summarize the basic theory of surface elasticity in section 7.2. In section 7.3, we formulate the plate bending problem with surface stress. The solutions are analytically determined up to some unknown constants which are solved in section 7.4. This is followed by a discussion of the results. The summary and conclusions are given in section 7.5.

7.2 Large deformation surface elasticity

7.2.1 Kinematics: Surface deformation gradient

Let $\partial\Omega_0$ denote the surface of a body occupying the region Ω_0 in the reference configuration. After deformation, this body occupies Ω and the initial surface $\partial\Omega_0$ becomes $\partial\Omega$. Assume that the material points initially on the surface remain on surface after deformation. The deformation $\mathbf{x}(\mathbf{X}) \in \partial\Omega,\ \forall \mathbf{X} \in \partial\Omega_0$ carries the position of a surface material point $\mathbf{X}$ in the reference configuration to its position $\mathbf{x}(\mathbf{X})$ in current configuration. We assume the deformation is continuously differentiable everywhere including on the surface. The surface deformation gradient tensor, by definition, is

$$\mathbf{F_S} = \nabla_{S_0}\mathbf{x}(\mathbf{X}). \tag{7.1}$$

where ∇_{S_0} is the surface gradient [25].

It should be noted that, by continuity, for any infinitesimal vector $d\mathbf{X}$ lying on the un-deformed surface, both the *bulk deformation gradient tensor* $\mathbf{F}$ and the surface deformation gradient tensor $\mathbf{F}_S$ will map it to the deformed vector $d\mathbf{x}$ on the deformed material surface, i.e.,

$$d\mathbf{x} = \mathbf{F}_S \cdot d\mathbf{X} = \mathbf{F} \cdot d\mathbf{X} \quad \text{for } \forall \, d\mathbf{X} \text{ on the un-deformed surface.} \tag{7.2}$$

This relation is later used to determine the components of the surface gradient tensor for any given curvilinear coordinate system.

7.2.2 Constitutive Model

Consider the thermodynamics for an arbitrary region of the surface. Define η, ω as the entropy and the heat absorbed per unit un-deformed area, respectively, $\mathbf{q}$ as the heat flow per unit un-deformed length through the boundary of a specified surface region S_0 (See Fig. 1). η and ω may come from the environment or the bulk.

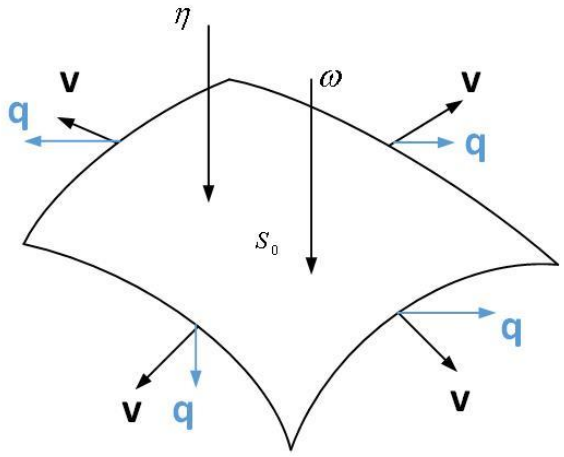

Fig. 7.1 Thermodynamic analysis for an arbitrary region of surface in the reference configuration. Unit vector **v** are tangent to the surface but normal to the boundary. η and ω are the entropy and heat from the bulk or environment and **q** is the heat flow to the adjacent surface.

The Clausius-Duhem inequality for region S_0 is

$$\frac{d}{dt}\int_{S_0} \eta dA + \int_{\partial S_0} \frac{\mathbf{q}}{T} \cdot \mathbf{v} dL - \int_{S_0} \frac{\omega}{T} dA \geq 0 \ , \tag{7.3}$$

where T is the temperature and $\mathbf{v}$ is the unit vector that is tangent to the surface but normal to the boundary of S_0. Using surface divergence theorem, the local form of Clausius-Duhem inequality can be written as

$$\dot{\eta} + div_{S_0}\left(\frac{\mathbf{q}}{T}\right) - \frac{\omega}{T} \geq 0 \ , \tag{7.4}$$

where the dot means the derivative with respect to time.

On the other hand, the energy balance for region S_0 is

$$\begin{aligned}
\frac{d}{dt}\int_{S_0} U dA &= -\int_{\partial S_0} \mathbf{q}\cdot\mathbf{v} dl + \int_{S_0} \omega dA + \int_{\partial S_0} \left(\boldsymbol{\Sigma}\cdot\mathbf{v}\right)\cdot\mathbf{u} dl + \int_{S_0} \left(\mathbf{T_S} - \mathbf{S}\cdot\mathbf{N}\right)\cdot\mathbf{u} dA \\
&= -\int_{S_0} div_s \mathbf{q} dA + \int_{S_0} \omega dA + \int_{S_0} \left(div_{S_0}\boldsymbol{\Sigma}\cdot\mathbf{u} + \boldsymbol{\Sigma}\cdot\nabla_{S_0}\mathbf{u}\right) dA + \int_{S_0} \left(\mathbf{T_S} - \mathbf{S}\cdot\mathbf{N}\right)\cdot\mathbf{u} dA \\
&= \int_{S_0} \left(-div_{S_0}\mathbf{q} + \boldsymbol{\Sigma}\cdot\nabla_{S_0}\mathbf{u} + \omega\right) dA + \int_{S_0} \left(div_{S_0}\boldsymbol{\Sigma} + \mathbf{T_S} - \mathbf{S}\cdot\mathbf{N}\right)\cdot\mathbf{u} dA \\
&= \int_{S_0} \left(-div_{S_0}\mathbf{q} + \boldsymbol{\Sigma}\cdot\nabla_{S_0}\mathbf{u} + \omega\right) dA
\end{aligned} \ , \tag{7.5}$$

where U is the internal energy per unit un-deformed area, $\mathbf{u}$ is the velocity of a material point, $\boldsymbol{\Sigma}_\mathbf{S}$ is the first Piola Kirchoff surface stress, $\mathbf{T_S}$ is the applied surface traction per unit un-deformed area, $\mathbf{S}$ is the first Piola Kirchoff stress for the bulk evaluated at the surface and $\mathbf{N}$ is the unit outward normal to the un-deformed surface. Note that the local form of surface equilibrium equation

$$div_{S_0}\left(\boldsymbol{\Sigma}_\mathbf{S}\right) + \mathbf{T_S} - \mathbf{S}\cdot\mathbf{N} = \mathbf{0} \ , \tag{7.6}$$

[25] is used in the last step.

From (7.5), the local form of energy balance is simply:

$$\dot{U} = -div_{S_0}\mathbf{q} + \boldsymbol{\Sigma}\cdot\nabla_{S_0}\mathbf{u} + \omega \, . \tag{7.7}$$

Substituting (7.7) into (7.4) and using the relation between surface internal energy and surface Helmholtz free energy $\Gamma = U - \eta T$, the inequality (7.4) can be further simplified as

$$\dot{\Gamma} + \eta\dot{T} - \boldsymbol{\Sigma}_\mathbf{S}\cdot\dot{\mathbf{F}}_\mathbf{S} + \frac{\mathbf{q}}{T}\cdot\nabla_{S_0}T \leq 0 \, . \tag{7.8}$$

Assuming Γ is a function of $\mathbf{F_S}$, T and $\nabla_{S_0}T$, (7.8) can be written as

$$\left(\eta+\frac{\partial\Gamma}{\partial T}\right)\dot{T}-\left(\boldsymbol{\Sigma}_{\mathbf{S}}-\frac{\partial\Gamma}{\partial\mathbf{F}_{\mathbf{S}}}\right)\cdot\dot{\mathbf{F}}_{\mathbf{S}}+\frac{\partial\Gamma}{\partial\nabla_{S_0}T}\cdot\dot{\nabla_{S_0}T}+\frac{\mathbf{q}}{T}\cdot\nabla_{S_0}T\le 0. \qquad (7.9)$$

Since $\dot{T}$, $\dot{\mathbf{F}}_{\mathbf{S}}$, $\dot{\nabla_{S_0}T}$ are independent and arbitrary, (12) implies that

$$\boldsymbol{\Sigma}_{\mathbf{S}}=\frac{\partial\Gamma}{\partial\mathbf{F}_{\mathbf{S}}},\quad \eta=-\frac{\partial\Gamma}{\partial T},\quad \frac{\partial\Gamma}{\partial\nabla_{S_0}T}=0,\quad \frac{\mathbf{q}}{T}\cdot\nabla_{S_0}T\le 0. \qquad (7.10a\text{-}d)$$

The equation $\boldsymbol{\Sigma}_{\mathbf{S}}=\dfrac{\partial\Gamma}{\partial\mathbf{F}_{\mathbf{S}}}$ in (7.10) extends the classical small strain surface constitutive relation $\boldsymbol{\sigma}_{\mathbf{S}}=\dfrac{\partial\gamma}{\partial\epsilon}$ into a general constitutive relation with large deformation surface strain and stress measures. This result is consistent with previous theories[21,26–30]. By repeating the above derivation for deformed surface, one can readily show that the Cauchy surface stress is

$$\boldsymbol{\sigma}_{\mathbf{S}}=\frac{1}{J_S}\frac{\partial\Gamma}{\partial\mathbf{F}_{\mathbf{S}}}\mathbf{F}_{\mathbf{S}}^{T}, \qquad (7.11)$$

where $J_S=\det\left(\mathbf{F}_{\mathbf{S}}\right)$ is the ratio of the deformed and the un-deformed surface area. The surface equilibrium equation in the deformed configuration is

$$div_S\boldsymbol{\sigma}_{\mathbf{S}}+\mathbf{t}_{\mathbf{S}}-\boldsymbol{\tau}\cdot\mathbf{n}=\mathbf{0}. \qquad (7.12)$$

In section 7.2.4, (7.11) is linearized and is shown that it is exactly the classical Shuttleworth equation.

7.2.3 Isotropic surface

For the special case of an isotropic surface, Γ depends only on two surface scalar invariants, I_s, II_s of the surface right Cauchy-Green tensor $\mathbf{C}_{\mathbf{S}}=\mathbf{F}_{\mathbf{S}}^{\mathbf{T}}\mathbf{F}_{\mathbf{S}}$ where

$$I_s=trace\left(\mathbf{C}_{\mathbf{S}}\right)\text{ and }II_s=\det\left(\mathbf{C}_{\mathbf{S}}\right)=\left(\det\mathbf{F}_{\mathbf{S}}\right)^2=J_s^2, \qquad (7.13a,b)$$

where $J_s=\det\mathbf{F}_{\mathbf{S}}>0$. Standard manipulation shows that

$$\boldsymbol{\Sigma}_{\mathbf{S}}=\frac{\partial\Gamma}{\partial\mathbf{F}_{\mathbf{S}}}=\left(2\frac{\partial\Gamma}{\partial I_s}\mathbf{F}_{\mathbf{S}}+J_s\frac{\partial\Gamma}{\partial J_s}\mathbf{F}_{\mathbf{S}}^{-T}\right). \qquad (7.14)$$

The Cauchy surface stress $\boldsymbol{\sigma}_{\mathbf{S}}$ is related to the 1st Piola surface stress $\boldsymbol{\Sigma}_{\mathbf{S}}$ by (7.11)

$$\boldsymbol{\sigma}_{\mathbf{S}}=\frac{1}{J_s}\boldsymbol{\Sigma}\mathbf{F}_{\mathbf{S}}^{T}=\frac{2}{J_s}\frac{\partial\Gamma}{\partial I_s}\mathbf{F}_{\mathbf{S}}\mathbf{F}_{\mathbf{S}}^{T}+\frac{\partial\Gamma}{\partial J_s}\mathbf{1}, \qquad (7.15)$$

where $\mathbf{1}$ is the surface identity tensor. Note that Cauchy surface stress is intrinsically symmetric, so angular momentum balance is automatically satisfied.

Since ratio of the surface area of a material element in the current and reference configuration is J_S, the surface free energy density in the deformed (γ) and un-deformed configuration (Γ) is related by

$$\Gamma = \gamma J_s \ . \tag{7.16}$$

Substituting (7.16) into (7.15), we obtain Shuttleworth equation for large deformation for an isotropic surface:

$$\boldsymbol{\sigma}_\mathbf{S} = 2\frac{\partial \gamma}{\partial I_s}\mathbf{F}_\mathbf{S}\mathbf{F}_\mathbf{S}^T + \left(J_S \frac{\partial \gamma}{\partial J_s} + \gamma \right)\mathbf{1}. \tag{7.17a}$$

In general, the surface stress need not be isotropic even in this case. Only for the special case where γ depends only on J_s, can the surface not support shear stress, and then the Cauchy surface stress is related to the current surface energy density γ by

$$\boldsymbol{\sigma}_\mathbf{S} = \left(J_S \frac{\partial \gamma}{\partial J_s} + \gamma \right)\mathbf{1}. \tag{7.17b}$$

As an example, the simplest model for Γ is obtained by keeping the linear terms of a Taylor series expansion of the energy density about its equilibrium state, i.e.,

$$\Gamma = aI_s + bJ_s, \tag{7.18}$$

where a and b are material constants that can be determined from atomistic simulations [47] or experiments. For this case, using (18), the Cauchy surface stress is related to the surface deformation by

$$\boldsymbol{\sigma}_\mathbf{S} = 2\frac{a}{J_S}\mathbf{F}_\mathbf{S}\mathbf{F}_\mathbf{S}^T + b\mathbf{1}. \tag{7.19}$$

It is readily seen that $2a$ is like the surface shear modulus and $b \equiv \sigma_o$ is the surface tension of the interface.

For the special case of $a = 0$, the surface stress is isotropic and its magnitude is a constant which is *independent* of surface deformation – the surface is fluid-like. (7.16) and (7.18) show that the surface free energy per unit deformed area is

$$\gamma = \sigma_0 , \tag{7.20}$$

consistent with classical theory of a fluid interface – surface free energy is numerically equal to surface tension even though they are physically different quantities. If a term quadratic in J_s is added in the expression of surface free energy Γ, then the surface stress becomes

$$\Gamma = \sigma_o J_s + \frac{k_s}{2}\left(J_s - 1\right)^2 \Rightarrow \boldsymbol{\sigma}_\mathbf{S} = \left(\sigma_o + k_s\left(J_s - 1\right)\right)\mathbf{1}, \tag{7.21}$$

where k_s is the surface bulk modulus, the surface tension σ_o is a residual stress and surface stress remains isotropic.

7.2.4 Linearized theory – Classical Shuttleworth equation

Define the right Cauchy-Green surface deformation tensor as $\mathbf{C}_\mathbf{S} = \mathbf{U}_\mathbf{S}{}^2 = \mathbf{F}_\mathbf{S}{}^T\mathbf{F}_\mathbf{S} d$, and according to Gurtin and Murdoch [25],

$$\mathbf{U}_\mathbf{S} \approx \mathbf{1} + \boldsymbol{\varepsilon}_\mathbf{S}, \tag{7.22}$$

where $\boldsymbol{\varepsilon}_\mathbf{S}$ is the infinitesimal surface strain tensor. From equation (7.11) and the relation $\Gamma = J_S\gamma$ between surface free energy defined per unit undeformed versus deformed areas, the Cauchy surface stress is simply

$$\boldsymbol{\sigma}_\mathbf{S} = \gamma\mathbf{1} + \frac{\partial\gamma}{\partial\mathbf{F}_\mathbf{S}}\mathbf{F}_\mathbf{S}{}^T . \tag{7.23}$$

Substituting (7.22) into (7.23), the constitutive relation can be linearized as

$$
\begin{aligned}
\boldsymbol{\sigma}_{\mathbf{S}} &= \gamma \mathbf{1} + \frac{\partial \gamma}{\partial \mathbf{F}_{\mathbf{S}}} \mathbf{F}_{\mathbf{S}}^{T} \\
&= \gamma \mathbf{1} + \frac{\partial \gamma}{\partial \mathbf{U}_{\mathbf{S}}} \cdot \frac{\partial \mathbf{U}_S}{\partial \mathbf{F}_S} \mathbf{F}_S^{T} \\
&= \gamma \mathbf{1} + \frac{\partial \gamma}{\partial \mathbf{U}_S} \mathbf{U}_S \\
&\approx \gamma \mathbf{1} + \frac{\partial \gamma}{\partial \boldsymbol{\varepsilon}_{\mathbf{S}}}
\end{aligned}
\quad . \tag{7.24}
$$

(7.24) is the classical Shuttleworth equation.

7.2.5 Indicial form for given curvilinear coordinates

For convenience of calculation, here the constitutive relation and equilibrium equations are expressed in indicial form for given curvilinear coordinates. Summation convention of summing over repeated indices will be used.

Let the un-deformed surface $\partial\Omega_0$ be parameterized by surface coordinates L^1 and L^2, and the deformed surface $\partial\Omega$ be parameterized by l^1 and l^2. The corresponding surface basis vectors are given by

$$
\begin{aligned}
\mathbf{D}_{\mathbf{1}} &= \frac{\partial \mathbf{X}}{\partial L^1},\ \mathbf{D}_{\mathbf{2}} = \frac{\partial \mathbf{X}}{\partial L^2} \\
\mathbf{d}_{\mathbf{1}} &= \frac{\partial \mathbf{x}}{\partial l^1},\ \mathbf{d}_{\mathbf{2}} = \frac{\partial \mathbf{x}}{\partial l^2}
\end{aligned}
\tag{7.25}
$$

The corresponding surface reciprocal bases are defined by

$$
\begin{aligned}
\mathbf{D}_{\boldsymbol{\alpha}} \cdot \mathbf{D}^{\boldsymbol{\beta}} &= \delta_{\alpha}^{\beta} \\
\mathbf{d}_{\boldsymbol{\alpha}} \cdot \mathbf{d}^{\boldsymbol{\beta}} &= \delta_{\alpha}^{\beta}
\end{aligned}
\tag{7.26}
$$

where α, β vary from 1 to 2 and δ_{α}^{β} is the Kronecker delta. In the following derivation, Greek letters range from 1 to 2 while English letters range from 1 to 3.

Using (7.2), the covariant components of surface deformation gradient tensor relative to the bases defined in (7.25) is determined by

$$
\left(F_S\right)_{\alpha\beta} = \mathbf{d}_{\boldsymbol{\alpha}} \cdot \mathbf{F}_{\mathbf{S}} \cdot \mathbf{D}_{\boldsymbol{\beta}} = \mathbf{d}_{\boldsymbol{\alpha}} \cdot \mathbf{F} \cdot \mathbf{D}_{\boldsymbol{\beta}}, \tag{7.27}
$$

where **F** is the bulk deformation gradient tensor evaluated on the surface.

The covariant components of $\boldsymbol{\sigma}_{\mathbf{s}}$ in (7.17) are

$$\left(\sigma_s\right)_{\alpha\beta} = 2\frac{\partial\gamma}{\partial I_s}\hat{F}_{\alpha}^{\cdot\xi}\hat{F}_{\beta\xi} + \left(J_S\frac{\partial\gamma}{\partial J_s} + \gamma\right)g_{\alpha\beta}, \tag{7.28}$$

where $g_{\alpha\beta} = \mathbf{d}_{\alpha}\cdot\mathbf{d}_{\beta}$ are the covariant components of the surface metric tensor $\boldsymbol{g}$ in the current configuration. The invariants I_S and J_S can be evaluated as

$$I_S = \left(F_S\right)_{\xi\alpha}\left(F_S\right)^{\xi\alpha},\ \mathrm{J}_S = \sqrt{\frac{I_S{}^2 - trace\left(\mathbf{C_S}^2\right)}{2}} = \sqrt{\frac{I_S{}^2 - \left(F_S\right)^{\xi\alpha}\left(F_S\right)_{\xi}^{\cdot\beta}\left(F_S\right)_{\cdot\beta}^{\zeta}\left(F_S\right)_{\zeta\alpha}}{2}}. \tag{7.29}$$

Correspondingly in (7.14), the covariant components of $\boldsymbol{\Sigma}_{\mathbf{S}}$ are

$$\left(\Sigma_S\right)_{\alpha\beta} = 2\frac{\partial\Gamma}{\partial I_S}\left(F_S\right)_{\alpha\beta} + J_S\frac{\partial\Gamma}{\partial J_S}\left(F_S\right)^{-T}{}_{\alpha\beta}. \tag{7.30}$$

In both equilibrium equations (9) and (15), the divergence of surface stress provides a jump of traction across the interface and can be written as [48]

$$\begin{aligned} div_S\left(\boldsymbol{\sigma}_{\mathbf{S}}\right) &= \left(\frac{\partial\left(\sigma_S\right)^{\alpha\xi}}{\partial l^{\xi}} + \left(\sigma_S\right)^{\xi\beta}\hat{\Gamma}_{\xi\beta}^{\alpha} + \left(\sigma_S\right)^{\alpha\beta}\hat{\Gamma}_{\beta\xi}^{\xi}\right)\mathbf{d}_{\alpha} + \left(\sigma_S\right)^{\alpha\beta}k_{\alpha\beta}\mathbf{n}, \\ div_{S_0}\left(\boldsymbol{\Sigma}_{\mathbf{S}}\right) &= \left(\frac{\partial\left(\Sigma_S\right)^{\alpha\xi}}{\partial L^{\xi}} + \left(\Sigma_S\right)^{\beta\gamma}\left(F_S\right)_{\cdot\gamma}^{\xi}\hat{\Gamma}_{\beta\xi}^{\alpha} + \left(\Sigma_S\right)^{\alpha\beta}\bar{\Gamma}_{\beta\xi}^{\xi}\right)\mathbf{d}_{\alpha} \\ &\quad + \left(\Sigma_S\right)^{\alpha\beta}k_{\alpha\xi}\left(F_S\right)_{\cdot\gamma}^{\xi}\mathbf{n}, \end{aligned} \tag{7.31a,b}$$

where

$$\boldsymbol{n} = \frac{\boldsymbol{d}_1\times\boldsymbol{d}_2}{\left|\boldsymbol{d}_1\times\boldsymbol{d}_2\right|}, \tag{7.31c}$$

is the unit outward normal to the deformed surface, and the surface Christoffel symbols $\hat{\Gamma}_{\alpha\beta}^{\xi}$, $\bar{\Gamma}_{\alpha\beta}^{\xi}$ and the surface curvature tensors $\boldsymbol{k}$, $\boldsymbol{K}$ in the current and reference configurations are related by [48]:

$$\begin{aligned} \frac{\partial\mathbf{d}_{\alpha}}{\partial l^{\beta}} &= \Gamma_{\alpha\beta}^{\xi}\mathbf{d}_{\xi} + k_{\alpha\beta}\mathbf{n}, \\ \frac{\partial\mathbf{D}_{\alpha}}{\partial L^{\beta}} &= \bar{\Gamma}_{\alpha\beta}^{\xi}\mathbf{D}_{\xi} + K_{\alpha\beta}\mathbf{N}. \end{aligned} \tag{7.32}$$

Note that a bar and a hat are added to distinguish the Christoffel symbols from the un-deformed surface energy.

If the surface is fluid-like i.e. $\boldsymbol{\sigma}_{\mathbf{S}} = \sigma_0\mathbf{1}$, then

$$\left(\sigma_S\right)^{\alpha\beta} = \sigma_0 \mathbf{d}^{\boldsymbol{\alpha}} \cdot \mathbf{d}^{\boldsymbol{\beta}} = \sigma_0 g^{\alpha\beta}. \tag{7.33a}$$

Substituting (7.33a) into (7.31a), the term inside the bracket vanishes and

$$div_S\left(\boldsymbol{\sigma}\right) = \sigma_0 k_\alpha^\alpha \mathbf{n}, \tag{7.33b}$$

where k_α^α is the mean curvature. Substituting (7.33b) back into the equation of surface force balance (7.12), one recovers the familiar Laplace equation [25],

$$\sigma_0 k_\alpha^\alpha \mathbf{n} + \mathbf{t_S} - \boldsymbol{\tau} \cdot \mathbf{n} = \mathbf{0}, \tag{7.34}$$

which states that the applied traction is balanced by the Laplace pressure and the traction provided by elastic bulk. However, that $div_s\left(\boldsymbol{\sigma}_\mathbf{S}\right)$ yields a simple pressure is only true for a fluid-like surface. When surface stress depends on surface strain, the traction caused by $div_s\left(\boldsymbol{\sigma}_\mathbf{S}\right)$ in general still has a shear component, that is, $\left(\frac{\partial \sigma^{\alpha\xi}}{\partial l^\xi} + \sigma^{\xi\beta}\hat{\Gamma}^\alpha_{\xi\beta} + \sigma^{\alpha\beta}\hat{\Gamma}^\xi_{\beta\xi}\right) \neq 0$, even if surface stress $\boldsymbol{\sigma}_\mathbf{S}$ is isotropic. For example, assume the Cauchy surface stress is given by (7.21), then direct evaluation of (7.20a) gives:

$$div_s\left(\boldsymbol{\sigma}_\mathbf{S}\right) = k_s \frac{\partial J_s}{\partial l^\xi} g^{\alpha\xi} \mathbf{d}_{\boldsymbol{\alpha}} + \left(\sigma_o + k_s\left(J_s - 1\right)\right) k_\alpha^\alpha \mathbf{n}. \tag{7.35}$$

Thus, unless the surface area ratio is a constant, the traction caused by the surface stress is not a Laplace pressure (normal to the surface), it has a component along the surface.

7.3 Bending of a plate with finite thickness

A well-known problem in nonlinear elasticity is the bending of a plate by an applied moment [46]. In this section, we consider the effect of surface stress on this bending and formulate the problem in the deformed configuration, i.e., using (7.12, 7.15). The un-deformed configuration corresponds to a stress-free plate without surface stress. Following Green and Zerna [46], the un-deformed configuration is defined by a Cartesian coordinate system $\left(X^1, \mathrm{X}^2, \mathrm{X}^3\right)$ with orthonormal basis

$\mathbf{E}_\mathrm{i}$, i=1,2,3. Specifically, the un-deformed plate is bounded by the planes $X^1 = c_1, \mathrm{X}^1 = c_2, \mathrm{X}^2 = \pm h, \mathrm{X}^3 = \pm d$. The cross-section of this plate in the X^1X^2 plane is shown in Fig. 7.2(a). The deformed plate is defined by a cylindrical coordinate system $\left(x^1, x^2, x^3\right) = \left(r, \theta, z\right)$ with orthogonal basis $\mathbf{e}_\mathrm{i} = \dfrac{\partial \mathbf{x}}{\partial x^i}$, i=1,2,3. Assuming the plate is incompressible, we seek a solution in which the deformation has the form:

$$r = \left(2\alpha X^1\right)^{1/2}, \ \theta = \beta X^2, \ z = \frac{X^3}{\alpha\beta} \tag{7.36}$$

where α and β are unknown constants to be determined. Geometrically, the deformation specified by (7.36) carries each plane initially normal to the X^1 axis to a portion of a curved surface of a cylinder whose axis is the X^3 axis. Also, planes initially normal to the X^2 axis rotate and become planes containing the X^3 axis, as shown in Fig. 7.2(b). The coefficients α and β are arranged in a way such that the incompressibility condition is satisfied.

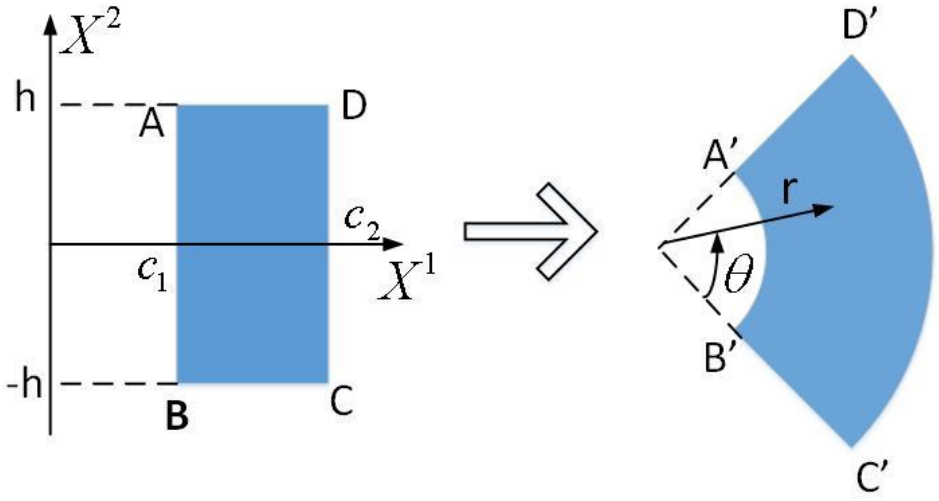

(a) (b)

Fig. 7.2 (a) Cross-section plot for the reference configuration of a finite thickness plate, axis X^3 is perpendicular to the plane. (b) Cross-section plot for the deformed configuration of the plate.

Using (7.36), the bulk deformation gradient tensor $\mathbf{F} = F^i_{\cdot J}\mathbf{e}_\mathrm{i}\mathbf{E}^\mathbf{J}$ is:

$$\mathbf{F} = \sqrt{\frac{\alpha}{2X^1}}\mathbf{e_1}\mathbf{E^1} + \beta\mathbf{e_2}\mathbf{E^2} + \frac{1}{\alpha\beta}\mathbf{e_3}\mathbf{E^3}, \tag{7.37a}$$

where

$$\mathbf{E^j} = \mathbf{E_j},\ \mathbf{e_1} = \frac{\partial \mathbf{x}}{\partial r} = \mathbf{e_r} = \mathbf{e^1},\ \mathbf{e_2} = \frac{\partial \mathbf{x}}{\partial \theta} = r\mathbf{e}_\theta,\ \mathbf{e^2} = \frac{1}{r}\mathbf{e_\theta},\ \mathbf{e^3} = \mathbf{e_3} = \mathbf{e}_z. \tag{7.37b}$$

Next, we assume the bulk behaves as an ideal rubber or a neo-Hookean solid, that is, the energy density function of the bulk *W*, is given by [45]

$$W = \frac{\mu}{2}\left[trace\left(\mathbf{F}^T\mathbf{F}\right) - 3\right], \tag{7.38}$$

The Cauchy stress tensor in the bulk, $\boldsymbol{\tau}$ associated with *W* is given by [45]

$$\boldsymbol{\tau} = -P\boldsymbol{I} + \mu\mathbf{B} \tag{7.39a}$$

Where μ is the small strain bulk shear modulus, $\boldsymbol{I}$ is the 3D identity tensor, *P* is the unknown pressure needed to enforce incompressibility and $\mathbf{B} = \mathbf{F}\mathbf{F}^T$ is the bulk left Cauchy-Green tensor. Using (7.37a), it is

$$\mathbf{B} = \mathbf{F}\mathbf{F}^T = \frac{\alpha^2}{r^2}\mathbf{e_1}\mathbf{e_1} + \beta^2\mathbf{e_2}\mathbf{e_2} + \frac{1}{\alpha^2\beta^2}\mathbf{e_3}\mathbf{e_3}. \tag{7.39b}$$

Substituting (7.39b) into (7.39a), the true stress in the bulk is:

$$\boldsymbol{\tau} = \left(-P + \mu\frac{\alpha^2}{r^2}\right)\mathbf{e}_r\mathbf{e}_r + \left(-P + \mu\beta^2 r^2\right)\mathbf{e}_\theta\mathbf{e}_\theta + \left(-P + \frac{\mu}{\alpha^2\beta^2}\right)\mathbf{e}_z\mathbf{e}_z. \tag{7.40}$$

The physical components of the true stress tensor are:

$$\begin{aligned} \tau_{rr} &= -P + \mu\frac{\alpha^2}{r^2} \\ \tau_{\theta\theta} &= -P + \mu\beta^2 r^2 \\ \tau_{zz} &= -P + \frac{\mu}{\alpha^2\beta^2}. \end{aligned} \tag{7.41a-c}$$

In the absence of body force, we determine *P* by substituting (7.41) into the equilibrium equations $div(\boldsymbol{\tau}) = \mathbf{0}$ and integrating to find

$$P = \frac{\mu\alpha^2}{2r^2} - \frac{\mu\beta^2 r^2}{2} + C, \tag{7.42}$$

where *C* is an integration constant.

The unknown constants α, β and C are determined by enforcing the surface stress boundary conditions (7.12) at $r = r_1$ and $r = r_2$. The surface deformation gradient tensor $\mathbf{F_S} = \nabla_{S_0}\mathbf{x}$ is evaluated using (7.36), assuming continuity of displacements,

$$\begin{aligned}\mathbf{F_S} &= \frac{\partial\left(r\mathbf{e_r} + x^3\mathbf{e_z}\right)}{\partial X^2}\mathbf{E_2} + \frac{\partial\left(r\mathbf{e_r} + x^3\mathbf{e_z}\right)}{\partial X^3}\mathbf{E}_3 \\ &= r\beta\mathbf{e_\theta}\mathbf{E_2} + \frac{1}{\alpha\beta}\mathbf{e_z}\mathbf{E_z}\end{aligned} \tag{7.43}$$

Using (7.43), the right Cauchy surface strain tensor $\mathbf{C_S} = \mathbf{F_S}^T\mathbf{F_S}$ is

$$\mathbf{C_S} = r^2\beta^2\mathbf{E_2}\mathbf{E_2} + \frac{1}{\alpha^2\beta^2}\mathbf{E_z}\mathbf{E_z} \tag{7.44}$$

Using (7.44), the two surface invariants of $\mathbf{C_S}$, I_s, II_s are:

$$I_s = \beta^2 r^2 + (\alpha\beta)^{-2}, \quad II_s = r^2/\alpha^2 = J_s^2. \tag{7.45}$$

As mentioned in the introduction, we assume that surface energy density function is independent of I_s. For simplicity, we assume that the surface stress is a linear function of the area stretch ratio J_s, i.e., the surface energy density is quadratic in $(J_S - 1)$:

$$\gamma = \sigma_o + \frac{k_s}{2J_s}(J_s - 1)^2 \tag{7.46}$$

The surface stress is obtained using (7.15), (7.46) and (7.45):

$$\boldsymbol{\sigma}_S = \left(\sigma_o + k_s(J_s - 1)\right)\mathbf{1} = \left(\sigma_o + k_s\left(\frac{r}{\alpha} - 1\right)\right)\mathbf{1}. \tag{7.47}$$

The first term in (7.47) corresponds to a constant residual surface stress $\sigma_0\mathbf{1}$ which models a liquid-like surface. Note that when $J_S = 1$, surface stress is numerically equal to surface energy density. In general, this needs not to be true since $J_S\left.\frac{\partial\gamma}{\partial J_S}\right|_{J_S=1}$ in Eq (7.15) can be a non-zero constant. The second term models the stress induced by increase in surface area, where k_s is the surface modulus.

The surface divergence on the traction free surfaces $X^1 = c_1$ and $X^1 = c_2$ can be computed readily:

$$div_S(\boldsymbol{\sigma}) = -\left(\frac{\sigma_0}{r} + \frac{k_S}{\alpha} - \frac{k_S}{r}\right)\mathbf{e}_r, \text{ at } r = r_1 \equiv \sqrt{2\alpha c_1} \text{ or } r = r_2 \equiv \sqrt{2\alpha c_2} \tag{7.48}$$

For our problem, the surface divergence is the Laplace pressure acting on the surface and is normal to the deformed surface.

To further simplify the solution, let us assume that there is no stretch in the X^3 direction (i.e. deformation is plane strain), this gives one of the conditions that determine the unknown constants, $\alpha\beta = 1 \Rightarrow \beta = 1/\alpha$. This plane strain assumption means the plate is either long or constrained in X^3 direction so that the rounding of edges due to surface stress can be neglected. The other two constants, α and C are determined using the traction free boundary conditions at $r = r_1$ and $r = r_2$, i.e.,

$$\begin{aligned} -\frac{\mu\alpha}{4c_1} - \mu\beta c_1 + C &= -\left(\frac{\sigma_0}{\sqrt{2\alpha c_1}} + \frac{k_S}{\alpha} - \frac{k_S}{\sqrt{2\alpha c_1}}\right) \\ \frac{\mu\alpha}{4c_2} + \mu\beta c_2 - C &= -\left(\frac{\sigma_0}{\sqrt{2\alpha c_2}} + \frac{k_S}{\alpha} - \frac{k_S}{\sqrt{2\alpha c_2}}\right). \end{aligned} \tag{7.49a,b}$$

The system of equations (7.49a,b) and $\alpha\beta = 1$ determine α, β, C for any given values of c_1 and c_2 $(c_2 > c_1)$.

Determination of Moment and Curvature

Once α, β, C are solved, we determine the force resultant and moment at the ends of the plate ($X^2 = \pm h$). Radial equilibrium yields

$$\frac{\partial \tau_{rr}}{\partial r} + \frac{\tau_{rr} - \tau_{\theta\theta}}{r} = 0. \tag{7.50}$$

Integrating (7.50) and using the boundary conditions $(r\tau_r)\big|_{r=r_1} = \sigma\big|_{r=r_1} \equiv \sigma_1, (r\tau_r)\big|_{r=r_2} = \sigma\big|_{r=r_2} \equiv \sigma_2 s$, we obtain

$$\sigma_1 + \sigma_2 + \int_{r_1}^{r_2} \tau_{\theta\theta} dr = 0. \tag{7.51}$$

Equation (7.51) states that the force resultant is zero. The moment on the plate is

$$M = \int_{r_1}^{r_2} r\tau_{\theta\theta} dr + r_1\sigma_1 + r_2\sigma_2 = -\int_{r_1}^{r_2} r\tau_{rr} dr . \tag{7.52}$$

Substituting (7.41a) and (7.42) into (7.52), the moment is

$$M = -\frac{\mu\alpha^2}{2}\ln\frac{r_2}{r_1} - \frac{\mu\beta^2\left(r_2^4 - r_1^4\right)}{8} + \frac{C\left(r_2^2 - r_1^2\right)}{2} . \tag{7.53}$$

In the following, we present results by normalizing all lengths by the initial width of the plate, $c_2 - c_1$ which is a constant. The normalized moment is denoted by $\bar{M}$ which is:

$$\bar{M} \equiv \frac{M}{\mu\left(c_2 - c_1\right)^2} = -\frac{\bar{\alpha}^2}{4}\ln\frac{\bar{c}_2}{\bar{c}_1} - \frac{\bar{c}_1 + \bar{c}_2}{2} + \bar{\alpha}\bar{C} , \tag{7.54a}$$

where

$$\bar{\alpha} = \alpha/(c_2 - c_1), \bar{c}_2 = c_2/\left(c_2 - c_1\right), \bar{c}_1 = c_1/\left(c_2 - c_1\right) . \tag{7.54b}$$

The kinematic assumption (7.36) implies that the plate bends with a given curvature $\kappa = 1/\sqrt{\alpha\left(c_1 + c_2\right)}$; the normalized curvature is

$$\bar{\kappa} = 1/\sqrt{\bar{\alpha}\left(\bar{c}_1 + \bar{c}_2\right)} . \tag{7.55}$$

Equations (7.54a) and (7.52) indicate that the curvature and moment can be expressed in terms of $\bar{\alpha}$ and $\bar{C}$. It can be readily verified that the relation between normalized moment and curvature depends on two dimensionless parameters

$$\bar{\sigma}_0 = \frac{\sigma_0}{\mu\left(c_2 - c_1\right)} \text{ and } \bar{k}_S = \frac{k_S}{\mu\left(c_2 - c_1\right)} \tag{7.56}$$

The quantity $\bar{\sigma}_0$ is usually called elasto-capillary number. Numerical solutions are presented in the next section.

7.4 Results and discussion

We first assume the surfaces at $X^1 = c_1$ and $X^1 = c_2$ have identical surface property, that is, their surface stresses are given by (7.47). The moment-curvature relations for different $\bar{\sigma}_0$ and $\bar{k}_S$ are shown in Fig. 7.3.

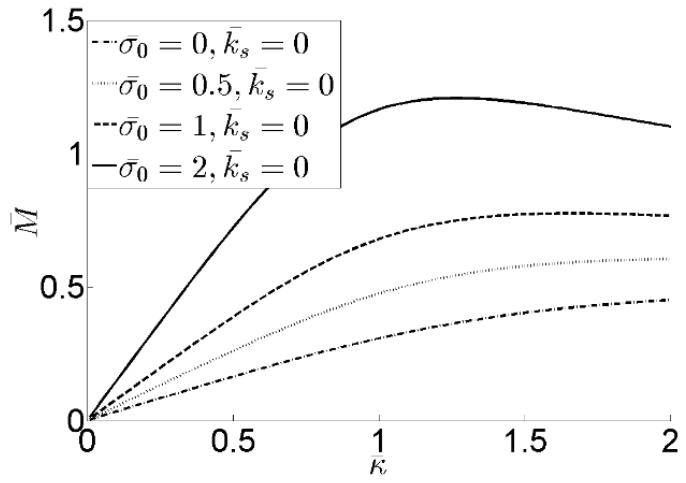

(a)

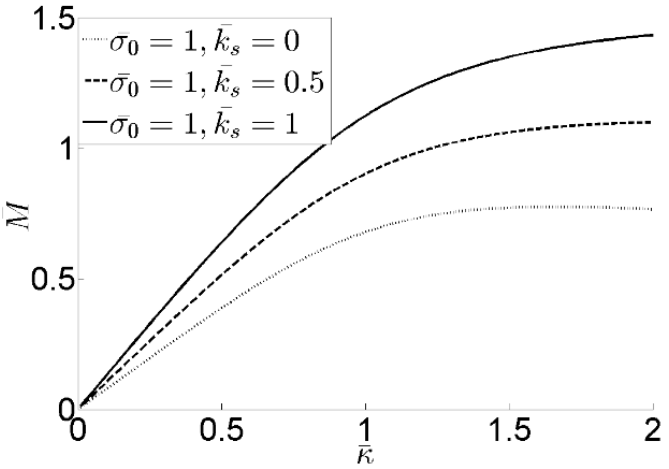

(b)

Fig. 7.3 Normalized moment versus normalized curvature. (a) surface stress is a constant. (b) surface stress linearly depends on surface strain with different surface stiffness.

Fig. 7.3(a,b) show that surface stress can substantially increase the bending moment required to achieve a given curvature. As expected, a positive surface stiffness k_s also increases the overall stiffness of the structure, making the plate harder to bend. Surprisingly, the moment is essentially linearly proportional to curvature as

long as $\bar{\kappa}$ is less than 1 even though the problem has both geometric and material nonlinearity.

Although linear theory works very well for moderately large deformations, there are interesting effects that it cannot capture. The top curve in Fig. 7.3(a) shows that for sufficiently large elasto-capillary number σ_0, bending becomes unstable at a critical curvature. Specifically, in a displacement control test, the moment decreases with curvature once a critical value is reached; in a load control test, once the moment reaches its maximum, the structure will collapse. To gain physical insights on this instability, we consider the special case where there is no surface stiffness, that is $k_S = 0$. As illustrated in Fig.7.4 (a), if $\boldsymbol{\sigma}\big|_{r=r_1} = \boldsymbol{\sigma}\big|_{r=r_2} = \sigma_0 \mathbf{1}$, the *direct* contribution to total moment about the center line of the plate due to surface stress is zero. However, surface residue stress σ_0 can indirectly contribute to moment by changing the distribution of bulk stresses $\tau_{\theta\theta}$ and τ_{rr}. The results in Fig. 7.4 (b) suggest that the presence of surface residue stress will make $\tau_{\theta\theta}$ more compressive. This change is more severe as it approach the inner boundary of the plate ($\bar{r} = \bar{r}_1$). This stress concentration makes an additional contribution to the total moment for a given curvature. The schematic in Fig. 7.4 (a) and the results in Fig. 7.4 (c) both show that the inner part of the plate is radially stretched while the outer part is compressed. As a result, the thickness of the plate ($\bar{t} \equiv t/(c_2 - c_1)$) may vary over the bending process – this is a nonlinear process that cannot be captured by linear theory. Our results in Fig. 7.4(c) show that the plate thickness goes down rapidly with increasing curvature. When the decrease due to the thinning effect is more significant than the increase due to the stress concentration effect, the total moment required to bend the plate goes down with further increase of curvature. It should be noted that this unstable behavior is not discovered in previous studies of thin plate bending because of the use of linear theory.

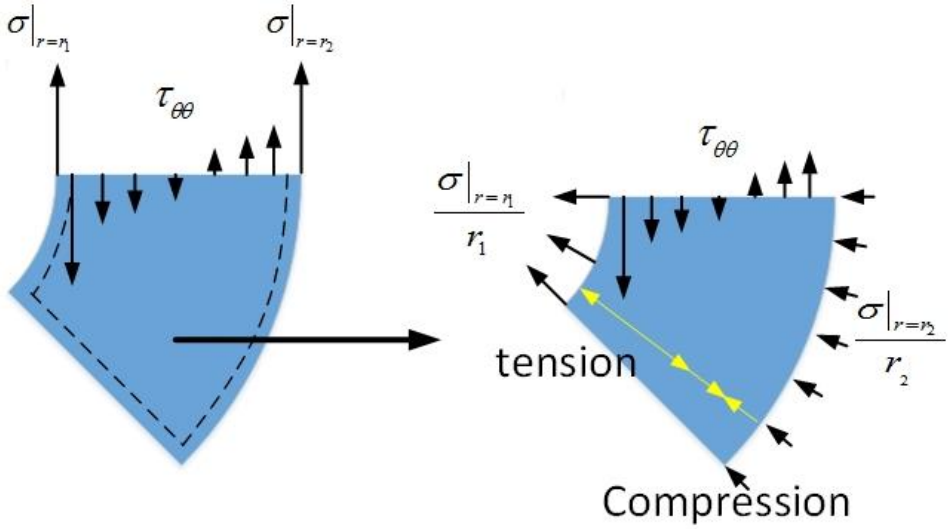
$\sigma|_{r=r_1}$
$\sigma|_{r=r_2}$
$\tau_{\theta\theta}$
$\tau_{\theta\theta}$
$\frac{\sigma|_{r=r_1}}{r_1}$
tension
$\sigma|_{r=r_2}$
r_2
Compression

(*a*)

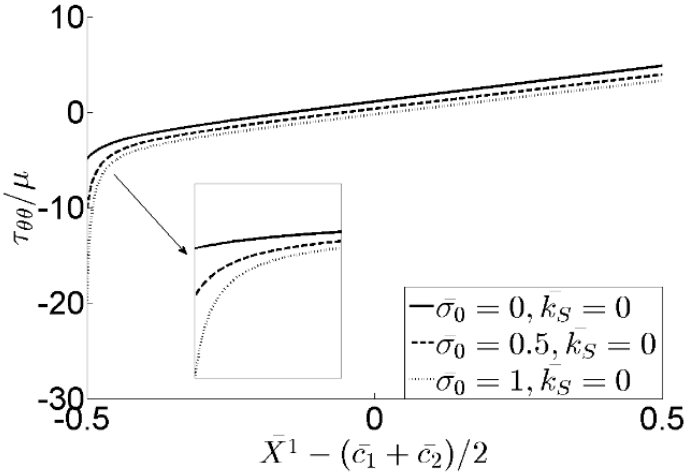
10
0
-10
-20
-30
-0.5
0
0.5
$\tau_{\theta\theta}/\mu$
$\bar{X}^1 - (\bar{c}_1 + \bar{c}_2)/2$
$\bar{\sigma}_0 = 0, \bar{k}_S = 0$
$\bar{\sigma}_0 = 0.5, \bar{k}_S = 0$
$\bar{\sigma}_0 = 1, \bar{k}_S = 0$

(*b*)

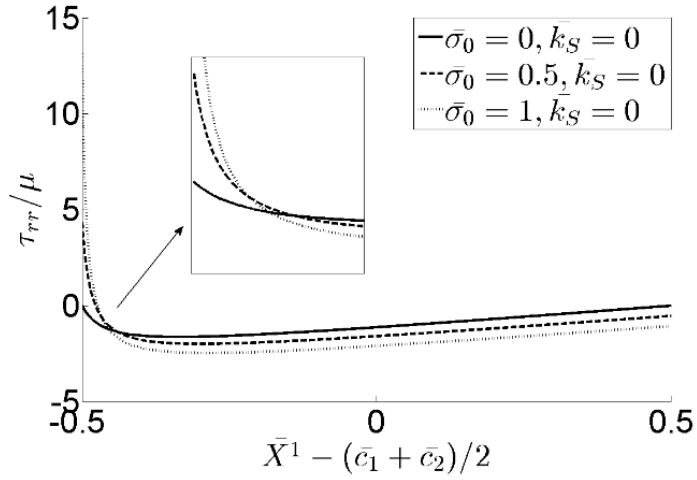

(c)

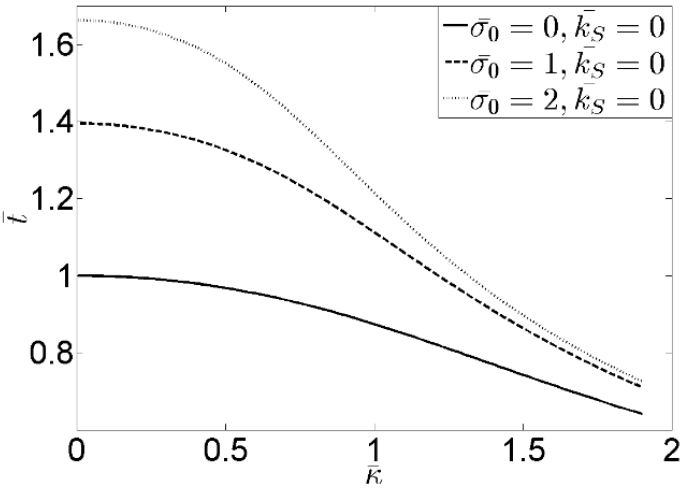

(d)

Fig. 7.4 (a) Schematic of the cross-section stress distribution, the two line forces represent surface stress. By removing the skin which carries surface stress, a radial traction (Laplace pressure) is felt on the surface of the remaining solid. (b) Circumferential stress distribution for different value of residue isotropic surface stress at fixed curvature $\bar{\kappa}=1.5$ with surface stiffness $\bar{k_s}=0$. (c) Radial stress distribution for different value of residue isotropic surface stress at fixed curvature $\bar{\kappa}=1.5$ with surface stiffness $\bar{k_s}=0$ (d) Plate thickness decreases with bending curvature. Note that when there is residue surface stress, the plate is thicker than the un-deformed plate

even at zero curvature. This is because the plate is under compression due to surface stress.

As shown in Fig. 7.3 (b), the instability discussed above can be eliminated by increasing the surface stiffness k_S. The effects of surface stiffness on the bulk elastic stress field are shown in Fig. 7.5. Increasing surface stiffness can reverse the concentration of stress at $\bar{r} = \bar{r}_1$ caused by the residual surface stress $\overline{\sigma_0}$. This relief of stress concentration decreases the moment due to bulk elasticity, causing the effective stiffness to decrease. However, the results in Fig. 7.3 (b) shows the reverse. This is because the inner surface is under compression while the outer surface of the plate is under tension. The difference in surface strains times the surface stiffness give rise to a difference in surface stress ($\bar{\sigma}_1 < \bar{\sigma}_2$) which directly generates a moment that contributes to stiffness and eliminates the instability.

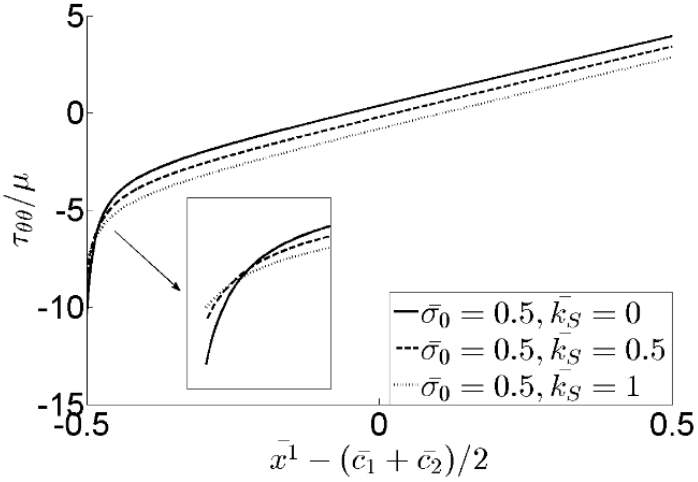

(a)

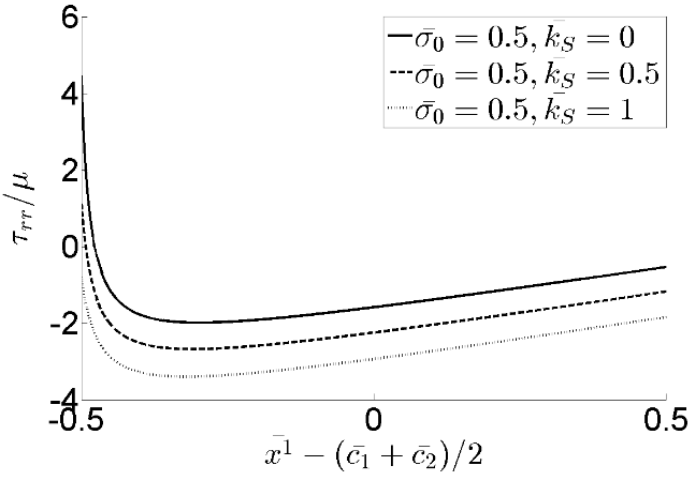

(b)

Fig. 7.5 Stress distribution for different value of surface stiffness. The curvature $\bar{\kappa}$ is fixed to be 1.5 and residue surface stress $\bar{\sigma}_0 = 0.5$ (a) circumferential stress component distribution (b) radial stress distribution.

Mora et al. showed experimentally that asymmetry of geometry can cause a slender soft material to be bent by its own surface stress [20]. Here we demonstrate that asymmetry in surface properties can also cause the plate bent by itself. Suppose we perform surface modification on one side of the plate so that it has a different surface stress than the other side, i.e., the surface stress on $\bar{r} = \bar{r}_1$ and $\bar{r} = \bar{r}_2$ are different. Then the plate will be bent toward the side where surface stress is larger. To demonstrate this effect, we assume surface stress is zero on one side ($\bar{r} = \bar{r}_2$) and positive on the other ($\bar{r} = \bar{r}_1$). Intuitively, the surface tension on $\bar{r} = \bar{r}_1$ generate a moment which needs to be balanced by the moment caused by bulk stress field as shown in Fig. 7.6 (b). The required bulk stress distribution can be provided by a pure bending deformation. Fig. 7.6 (a) shows that the increase in surface tension on $\bar{r} = \bar{r}_1$ results in an increase of self-bending curvature $\bar{\kappa}_0$.

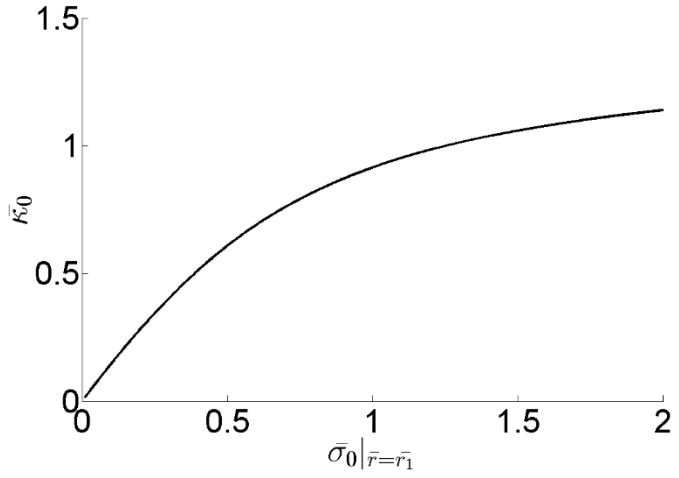

(a)

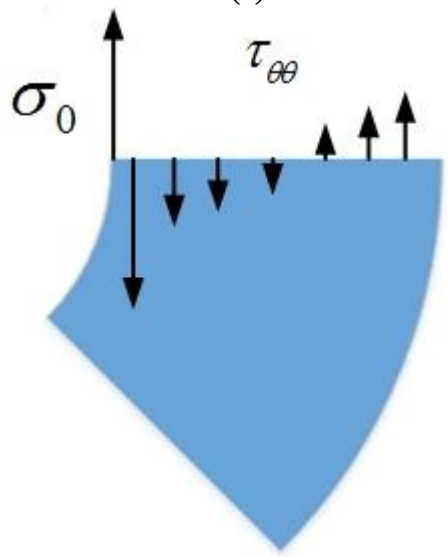

(b)

Fig. 7.6 On $\bar{r}=\bar{r}_2$, $\bar{\sigma}_0=\bar{k}_S=0$, on $\bar{r}=\bar{r}_1$, $\bar{\sigma}_0>0$ while $\bar{k}_S=0$. (a) The normalized equilibrium curvature $\bar{\kappa}_0$ increase with $\bar{\sigma}_0$ on $\bar{r}=\bar{r}_1$ surface. (b) Schematic of bulk stress distribution induced by the self-bending.

7.5 Summary and conclusions

We consider the surface stress effect on the pure bending of a plate. Both bulk elastic response and surface stress are formulated using finite deformation theory. The

deformation is obtained analytically and the solutions are solved numerically. It is found that both residual surface stress and surface stiffness can improve the structure's overall stiffness, one by modifying the stress distribution in the bulk and the other one directly generate moment through the difference in surface strain. We also explore the possibilities of having different surface stress on different boundaries of the plate which can bend the structure without external moment. The equilibrium curvature increases with the difference of surface stress.

Our solution assumes that the plate behaves as an ideal rubber (Neo-Hookean material) where resistance to deformation is attributed to increase in entropy. It has been known that this model underestimates the stresses at very large deformations, e.g. when the polymer chains are fully stretched. There is no difficulty to extend our model to account for strain stiffening effects. This can be accomplished using a more realistic strain hardening model for the work function defined in (6). Many such models has been proposed in the literature [45]. We can also use a more general form of the description of our surface stress as long as there is no shear component in surface stress tensor.

For more complex surface behavior or for structures with complex boundary conditions, our approach will not work. For example, if the assumption of plane strain were relaxed, the Poisson effect may cause the plate to have non-uniform displacement along the X^3 direction where the surface stress may resist this deformation and hence affect the behavior of τ_{zz}. In this situation, a guess for an admissible deformation is extremely difficult and hence our semi-inverse method is no longer valid. It should also be noted that we do not consider the rounding of edges due to surface stress in our formulation, so our solution is only valid away from the edges. More importantly, we imposed a specific deformation field in our solution, which may not be the only solution – for example, at very high Elasto-capillary number the plate

may buckle without external load. For problems with complex boundary conditions, numerical methods such as finite element method (FEM) can be used. Our solution can be used as a test for FEM formulations and also allow us to gain insight on the effect of surface stress on bending specimens which are easy to fabricate and commonly use in structural mechanics.

REFERENCES

[1] J. Wang, Z. Huang, H. Duan, S. Yu, X. Feng, G. Wang, W. Zhang, and T. Wang, Acta Mech. Solida Sin. **24**, 52 (2011).

[2] K. Babaei Gavan, H. J. R. Westra, E. W. J. M. van der Drift, W. J. Venstra, and H. S. J. van der Zant, Appl. Phys. Lett. **94**, 233108 (2009).

[3] G. Y. Jing, H. L. Duan, X. M. Sun, Z. S. Zhang, J. Xu, Y. D. Li, J. X. Wang, and D. P. Yu, Phys. Rev. B **73**, 235409 (2006).

[4] S. Cuenot, C. Frétigny, S. Demoustier-Champagne, and B. Nysten, Phys. Rev. B **69**, 165410 (2004).

[5] K. R. Pirota, E. L. Silva, D. Zanchet, D. Navas, M. Vázquez, M. Hernández-Vélez, and M. Knobel, Phys. Rev. B **76**, 233410 (2007).

[6] C. Q. Chen, Y. Shi, Y. S. Zhang, J. Zhu, and Y. J. Yan, Phys. Rev. Lett. **96**, 75505 (2006).

[7] J. He and C. M. Lilley, Nano Lett. **8**, 1798 (2008).

[8] J. He and C. M. Lilley, Appl. Phys. Lett. **93**, 263108 (2008).

[9] G.-F. Wang and X.-Q. Feng, J. Phys. D. Appl. Phys. **42**, 155411 (2009).

[10] G.-F. Wang and X.-Q. Feng, Appl. Phys. Lett. **94**, 141913 (2009).

[11] Z.-Q. Wang, Y.-P. Zhao, and Z.-P. Huang, Int. J. Eng. Sci. **48**, 140 (2010).

[12] G. Yun and H. S. Park, Phys. Rev. B **79**, 195421 (2009).

[13] R. Ansari and S. Sahmani, Int. J. Eng. Sci. **49**, 1244 (2011).

[14] B. Andreotti, O. Baeumchen, F. Boulogne, K. E. Daniels, E. R. Dufresne, H. Perrin, T. Salez, J. H. Snoeijer, and R. W. Style, Soft Matter **12**, 2993 (2016).

[15] R. W. Style, A. Jagota, C.-Y. Hui, and E. R. Dufresne, (2016).

[16] D. Paretkar, X. Xu, C.-Y. Hui, and A. Jagota, Soft Matter **10**, 4084 (2014).

[17] A. Jagota, D. Paretkar, and A. Ghatak, Phys. Rev. E **85**, 51602 (2012).

[18] J. B. Lee, S. Peng, D. Yang, Y. H. Roh, H. Funabashi, N. Park, E. J. Rice, L.

Chen, R. Long, M. Wu, and D. Luo, Nat. Nanotechnol. **7**, 816 (2012).

[19] S. Mora and Y. Pomeau, (2014).

[20] S. Mora, C. Maurini, T. Phou, J.-M. Fromental, B. Audoly, and Y. Pomeau, Phys. Rev. Lett. **111**, 114301 (2013).

[21] C. Y. Hui*, A. Jagota, Y. Y. Lin, and E. J. Kramer, (2002).

[22] S. Mora, T. Phou, J.-M. Fromental, L. M. Pismen, and Y. Pomeau, Phys. Rev. Lett. **105**, 214301 (2010).

[23] R. W. Style, C. Hyland, R. Boltyanskiy, J. S. Wettlaufer, and E. R. Dufresne, Nat. Commun. **4**, 2728 (2013).

[24] C.-Y. Hui, T. Liu, T. Salez, E. Raphael, and A. Jagota, Proc. R. Soc. A Math. Phys. Eng. Sci. **471**, 20140727 (2015).

[25] T. Liu, A. Jagota, and C.-Y. Hui, Soft Matter (2015).

[26] J. B. Bostwick, M. Shearer, and K. E. Daniels, Soft Matter **10**, 7361 (2014).

[27] E. R. Jerison, Y. Xu, L. A. Wilen, and E. R. Dufresne, Phys. Rev. Lett. **106**, 186103 (2011).

[28] C.-Y. Hui and A. Jagota, Proc. R. Soc. A Math. Phys. Eng. Sci. **470**, 20140085 (2014).

[29] J. M. Long and G. F. Wang, Mech. Mater. **56**, 65 (2013).

[30] G. F. Wang and X. R. Niu, Acta Mech. Sin. **31**, 531 (2015).

[31] C. I. Kim, P. Schiavone, and C.-Q. Ru, J. Elast. **104**, 397 (2011).

[32] Z. Cao, M. J. Stevens, and A. V. Dobrynin, Macromolecules **47**, 6515 (2014).

[33] Z. Cao, M. J. Stevens, and A. V. Dobrynin, Macromolecules **47**, 3203 (2014).

[34] C.-Y. Hui, T. Liu, and M.-E. Schwaab, *How Does Surface Tension Affect Energy Release Rate of Cracks Loaded in Mode I?* (2016).

[35] M. Gurtin and A. Ian Murdoch, Arch. Ration. Mech. Anal. **57**, (1975).

[36] G. Yun and H. S. Park, Comput. Methods Appl. Mech. Eng. **197**, 3337 (2008).

[37] A. Papastavrou, P. Steinmann, and E. Kuhl, J. Mech. Phys. Solids **61**, 1446 (2013).

[38] A. Javili and P. Steinmann, Comput. Methods Appl. Mech. Eng. **198**, 2198 (2009).

[39] A. Javili and P. Steinmann, Comput. Methods Appl. Mech. Eng. **199**, 755 (2010).

[40] P. H. Saksono and D. Perić, Comput. Mech. **38**, 251 (2005).

[41] P. H. Saksono and D. Perić, Comput. Mech. **38**, 265 (2005).

[42] Z. P. Huang and J. Wang, Acta Mech. **182**, 195 (2006).

[43] X. Gao, Z. Huang, J. Qu, and D. Fang, J. Mech. Phys. Solids **66**, 59 (2014).

[44] R. Shuttleworth, Proc. Phys. Soc. Sect. A **63**, 444 (1950).

[45] G. A. Holzapfel, *Nonlinear Solid Mechanics: A Continuum Approach for Engineering* (Wiley, 2000).

[46] A. E. Green and W. Zerna, *Theoretical Elasticity* (Courier Corporation, 2002).

CHAPTER 8

ENERGY RELEASE RATE OF A PENNY-SHAPED CRACK SUBJECTED TO INTERNAL PRESSURE: EFFECT OF SURFACE TENSION AND LARGE DEFORMATION [8]

8.1 Introduction

Understanding how surface tension affects the energy release rate of cracks in soft materials is fundamental to many problems related to material processing, such as adhesion and contact mechanics. For example, when an elastic sphere is in adhesive contact to a flat rigid substrate, the contact radius is determined by a balance of surface energy and the energy release rate of the interface crack exterior to the contact zone, as shown by Johnson-Kendall-Roberts (JKR) theory [1]. Recent experimental and theoretical works by Xu et al [2] and Style et al [3] has demonstrated that JKR theory breaks down for very soft elastic substrates. However, these new experimental results are consistent with a theory that accounts for the effect of surface tension on the energy release rate of the interface crack.

The characteristic length scale that describes the deformation of a solid due to its surface tension σ is given by the ratio between the surface tension and its Young's modulus E. For engineering materials such as metals and ceramics, this "elasto-capillary" length is smaller than atomic dimensions. However, in the past decade, new applications such as replica molding and drug delivery drove the synthesis of soft materials such as hydrogels and elastomers with Young's modulus ranging from 10^2 to 10^6 Pa. The elasto-capillary length of these soft materials ranges from tens of nm to hundreds of μm; as a result, the role of surface tension in driving shape change and deformation of solids can be considerable, as demonstrated by recent experiments and simulations [4–10].

[8] Liu T., Long R., Hui C.Y., (2014), Soft Matter, **10**, 7723

For most liquids, surface tension is isotropic and is numerically equal to surface energy. The problem is far more complex for solids since surface stress is not necessary isotropic [11]. In addition, surface stress and surface energy are different physical quantities which need not be numerically equal, even if surface stress is isotropic. In 1975, Gurtin and Murdoch [12] proposed a continuum formulation of surface stress where surface stress can be decomposed into a residual stress component and a surface strain dependent component. For soft material such as elastomer or hydrogel, which is the primary interest of this work, it is reasonable to assume that surface stress is isotropic. As a first-order approximation, in the following we shall assume that the surface tension σ is a material constant independent of surface strain.

There are few studies examining the role of surface stress in fracture since actual measurements of surface stresses are very difficult to make. In 1986, a theoretical analysis of the elastic fracture behavior under the influence of surface stresses was carried out by Thomson et al [13] in which the surface tension was modeled as line forces acting on the crack tip. More relevant to this present work is the paper by Wu (1999) [14] and Kim et al (2010, 2012) [15,16]. Wu's paper in 1999 suggested that the stress intensity factor at the crack tip is reduced by surface stresses. However, the numerical solution of Kim et al in 2010 [15] showed that for a plane strain crack loaded in Mode I and Mode II, the near tip stress field is bounded, irrespective of the magnitude of the surface stress (as long as it is not exactly zero). In a later paper, Kim et al (2012) [16] reexamined their numerical solution in greater details and showed that the near tip stress field for a Mode I crack has a logarithmic singularity. In both cases their numerical results suggested that the stress intensity factor near the crack tip (or the local stress intensity factor $K_{local} = K_A + K_{ST}$) is exactly zero. In other words, the applied stress intensity factor K_A is cancelled by the negative stress intensity

factor K_{ST} due to surface stresses. Since a zero local stress intensity factor implies that local energy release rate is also zero, there seems to be a discrepancy between the results of Wu's [14] and Kim et al's [15,16]. However, in Wu's analysis [14], a finite tip radius was introduced to remove the negative stress intensity factor induced by surface tension. This finite tip radius approach was also used in later works of Fu et al [17], Wang et al [18] and Wang and Li [19].

The use of a finite tip radius however, is only one way of dealing with the unbounded negative stress intensity factor due to surface tension. A simple way to understand how this occurs is to consider a plane strain Mode I crack lying on the negative x axis, with the crack tip at $x = 0$. Without loss in generality, we assume surface stress $\sigma_{\alpha\beta}$ to be isotropic, that is, $\sigma = \sigma\delta_{\alpha\beta}$ where σ is the surface tension (force/length). For this case, the Laplace pressure P_L resisting the opening of the crack (see Fig. 8.1) is directly proportional to the curvature κ which can be written as

$$\kappa = \frac{\mathrm{v}''}{\left[1+\left(\mathrm{v}'\right)^2\right]^{3/2}} \tag{8.1}$$

where v is the crack opening displacement and a prime denotes differentiation with respect to x. In the analyses of Wu [14] and Kim et al [15], they assumed that v' is small everywhere and the curvature κ is approximated by $v"$. Due to this approximation, the governing equation describing the crack tip field is linear and the full machinery of analytic function theory can be used to formulate the crack problem.

We can now understand why K_{local} had to be zero in these analyses, that is, the local stress field near the crack tip cannot have an inverse square root singularity. Indeed, assuming K_{local} is positive, the crack opening displacement near the crack tip must have the form:

$$\mathrm{v} \propto K_{\mathrm{local}}\sqrt{-x},\ x<0 \tag{8.2}$$

Since $\kappa = \mathrm{v}''$,

$$\kappa \propto K_{\text{local}} |x|^{-3/2},\ x \to 0^- \tag{8.3}$$

Thus, the Laplace pressure induced by the deformed crack has a non-integrable singularity. It can be shown that such a singular pressure field will induce an infinite negative stress intensity factor at the crack tip, which means that K_{local} goes to negative infinity. This is a contradiction to the original assumption that K_{local} is positive so the only possibility is $K_{\text{local}} = 0$, which means either that the stress is bounded or has a weaker singularity. On the other hand, if v' is retained, then

$$\kappa = \frac{\mathrm{v}''}{\left[1+\left(\mathrm{v}'\right)^2\right]^{3/2}} \approx \frac{\mathrm{v}''}{\left(\mathrm{v}'\right)^3},\ x \to 0^- \tag{8.4}$$

Note that v'' and $\left(\mathrm{v}'\right)^3$ has exactly the same singularity, so that κ is bounded at the crack tip. As a result, it is possible for the local stress intensity factor to be non-zero. Therefore, it is not necessary to introduce a finite tip radius for the undeformed crack if one is willing to deal with a nonlinear boundary condition (i.e., using the full expression for radius of curvature).

The above discussion and analysis illustrates one of the difficulties of using small strain theory to study fracture. The problem arises since the strains and displacement gradient are no longer small near the crack tip, but the linear elasticity theory assumes that these quantities are small and this assumption can result in paradoxes like the one noted above. A more consistent way to approach the fracture problem is to use large deformation theory. We emphasize that our primary objective in this work is to study fracture in soft materials where large deformation cannot be avoided.

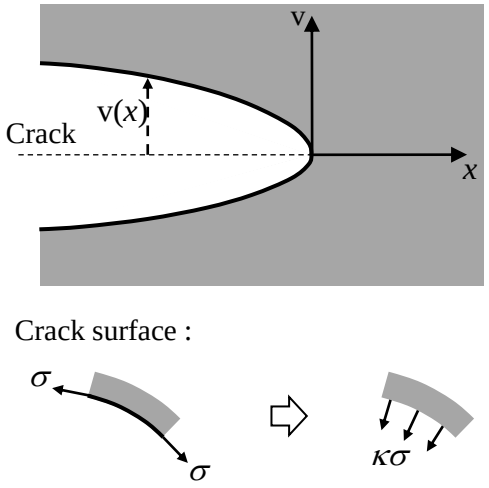

Fig. 8.1 Surface tension on crack face

The analysis in this work is based on the fully nonlinear equilibrium theory of incompressible hyperelastic solid which allows for arbitrary large deformation. The surface stress is assumed to be isotropic and constant. A newly developed surface tension element [4] is used in conjunction with a commercial finite element code ABAQUS to evaluate the energy release rate. The plan of this Chapter is as follows. The energy argument for the calculation of energy release rate is established in section 8.2. Section 8.3 introduces the mesh and basic procedures used in our finite element calculation. Results are shown in section 8.4 and section 8.5 gives an approximated expression for energy release rate. Discussion and summary is given in section 8.6.

8.2 Geometry and derivation of Energy Release Rate

Our goal is to determine the energy release rate G of a penny-shaped or circular crack with undeformed radius *a*. The crack lies in the interior of an infinite block of incompressible hyperelastic solid where the strain energy density *W* has the form

$$W = E\Phi\left(I_1\right) \tag{8.5a}$$

where *E* is the small strain Young's modulus and I_1 is the trace of the Cauchy-Green tensor. The function $\Phi\left(I_1\right)$ is assumed to be smooth and obeys [20]

$$\Phi\left(I_1 \geq 3\right) \geq 0, \Phi\left(I_1 = 3\right) = 0 \tag{8.5b}$$

The crack is loaded by imposing an internal pressure P on the crack faces. For incompressible solids, this is equivalent to applying a remote hydrostatic tensile stress with magnitude P while keeping the crack surface free of loading except surface tension.

A classical way to calculate G is to use a virtual crack extension method (VCEM). However, this method requires an accurate solution of the stress and strain fields [21]. Due to large deformation, the mesh near the crack tip is highly distorted, so the local stress and deformation fields near the crack tip determined by FEM are much less accurate than global quantities such as the deformed crack volume V. In the following, we derive a simple expression for the energy release rate in terms of P, V and the deformed crack area A. This expression allows us to evaluate G accurately even though the mesh near the crack tip is highly distorted.

The initial configuration is a traction free crack in a stress free solid with no surface tension, and the crack area in this configuration is $A_0 = 2\pi a^2$. It is convenient to "load" the crack in two steps. In the first step, surface tension is increased gradually to its full value σ at zero pressure. At the end of this step, the original flat crack will deform and reduce its area to A_s, with a volume given by V_s. This step is followed by inflating the deformed crack by a hydrostatic pressure P, for example by pushing an incompressible fluid into the crack cavity (see Fig. 8.2). Let V be the volume of the deformed crack when the applied pressure is P. Since the solid is elastic, the deformation and energy of the system should be independent of loading history and depends only on the final state. In other words, the order of application of surface tension and pressure will not affect our results.

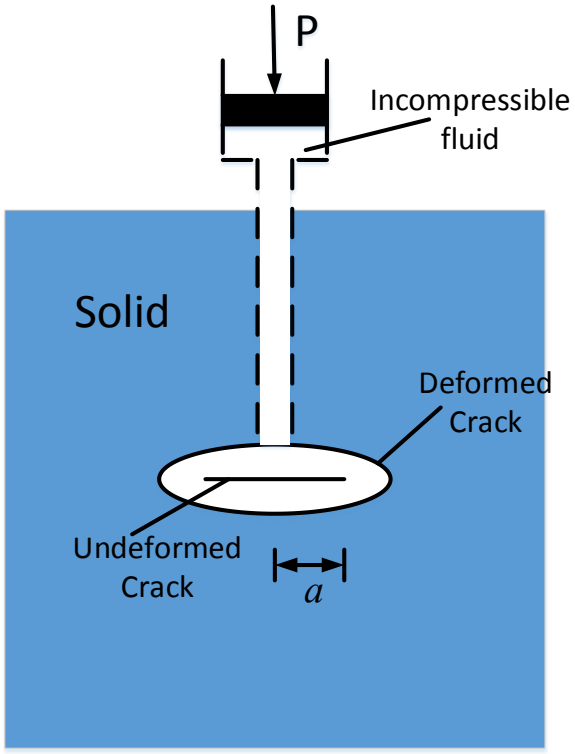

Fig. 8.2 Schematic of the mechanical loading process.

In the process of turning on the surface tension at zero pressure, the work done by surface tension on the elastic body is

$$-\int_{A_0}^{A_s} \sigma(P=0,\mathrm{A})dA \tag{8.6}$$

Note that the surface tension in this stage is not a constant as it increases from zero to its final value σ. At the end of this step, the potential energy of the surface is σA_s and the elastic energy of the body is given by Eq. (8.6). Note that since $A_s < A_0$, this energy is positive.

In the second step, the crack is pressurized, the work done by the pressure is

$$\int_{V_s}^{V} P(V^*)dV^* \tag{8.7}$$

This work is used to increase the strain energy of the solid as well as stretching the surface. The potential energy of the pressure load is given by

$$-PV \tag{8.8}$$

where V is the volume of the crack at the end of the second step. To understand this term, one can imagine that the pressure is applied by a stack of weights. Thus, the system consists of the weights, the elastic solid and its surface. As fluid is forced into the crack, the weight drops and the system lost mechanical potential energy which is given by Eq. (8.8).

Adding all the energies, the total potential energy of the system PE is:

$$PE = -\int_{A_0}^{A_s} \sigma(P=0,A)dA + \int_{V_s}^{V} P\left(V^*\right)dV^* - PV + \sigma A_s \tag{8.9}$$

After integration by parts, Eq. (8.9) is simplified as

$$PE = -\int_0^P V\left(P^*\right)dP^* + \int_0^\sigma A\left(P=0,\sigma^*\right)d\sigma^* \tag{8.10}$$

Dimensional analysis implies that

$$V = a^3\bar{V}\left(\bar{P},\omega\right),\ A\left(P=0,\sigma\right)=a^2\bar{A}\left(\omega\right) \tag{8.11a}$$

where $\bar{V}$ and $\bar{A}$ are dimensionless functions and

$$\omega = \frac{\sigma}{Ea},\quad \bar{P}=P/E\ , \tag{8.11b}$$

are the elasto-capillary number and normalized pressure respectively. Substituting Eq. (8.11a) and Eq. (8.11b) into Eq. (8.10) gives:

$$PE = -Ea^3\left(\int_0^{\bar{P}} \bar{V}\left(\bar{P}^*,\omega\right)d\bar{P}^* - \int_0^{\omega} \bar{A}\left(\omega^*\right)d\omega^*\right) \tag{8.12}$$

The energy release rate G is, by definition,

$$\begin{aligned} G &= -\frac{1}{2\pi a}\frac{\partial PE}{\partial a}\bigg|_P \\ &= \frac{E}{2\pi a}\frac{\partial}{\partial a}\left[a^3\int_0^{\bar{P}} \bar{V}\left(\bar{P}^*,\omega\right)d\bar{P}^* - a^3\int_0^{\omega} \bar{A}\left(\omega^*\right)d\omega^*\right] \\ &= \frac{Ea}{2\pi}\left[3\Psi - \omega\frac{\partial\Psi}{\partial\omega}\right] \end{aligned} \tag{8.13a}$$

where

$$\Psi\left(\bar{P},\omega\right) \equiv \int_0^{\bar{p}} \bar{V}\left(\bar{P}^*,\omega\right) d\bar{P}^* - \int_0^{\omega} \bar{A}\left(\omega^*\right) d\omega^* \tag{8.13b}$$

It is convenient to define a normalized energy release rate Γ by

$$\Gamma \equiv G / Ea = \frac{1}{2\pi}\left[3\Psi - \omega \frac{\partial \Psi}{\partial \omega} \right] \tag{8.14}$$

If surface tension is neglected, then the normalized energy release rate is a function of pressure only, and reduces to an earlier expression derived by Lin and Hui [22].

8.3 Finite Element Method

We used a commercial FEM software, ABAQUS, to calculate the displacement field of the crack corresponding to different $\overline{P}$ and elastocapillary number ω. All numerical calculations are carried out by assuming that the elastic solid is incompressible and neo-Hookean, i.e.,

$$W = \frac{E}{6}\left(I_1 - 3\right) \tag{8.15}$$

The built-in hyperelastic function in ABAQUS was used to model the incompressible neo-Hookean material. Symmetry allows us to mesh only the upper half of the elastic solid (see Fig. 8.3). All lengths are normalized by the undeformed crack radius *a*. The built-in axisymmetric quadrilateral elements (CAX4RH) are used, and on the crack face, a user subroutine (UEL) written in FORTRAN is used to enforce a uniform tension along the crack face. Details about implementation of surface tension element can be found in Xu et al [4]. Eq. (8.14) is used to evaluate the energy release rate in our FEM. Specifically, in the FEM, the applied pressure and surface tension are changed incrementally from zero. At each step, the deformed crack volume and deformed crack faces area are obtained from the computed crack opening displacement. Using Eq. (8.13b), Ψ can be calculated by numerical integration and Γ is evaluated using numerical differentiation. Unlike stress fields, the total crack volume *V* and the crack face area *A* are relatively insensitive to the distortion of

elements near the crack tip, hence the energy release rate calculated using Eq. (8.14) is expected to be much more accurate than VCEM. When the elements are too distorted, a re-mesh program is used to ensure convergence and accuracy. A typical mesh used in our simulation is shown in Fig. 8.4.

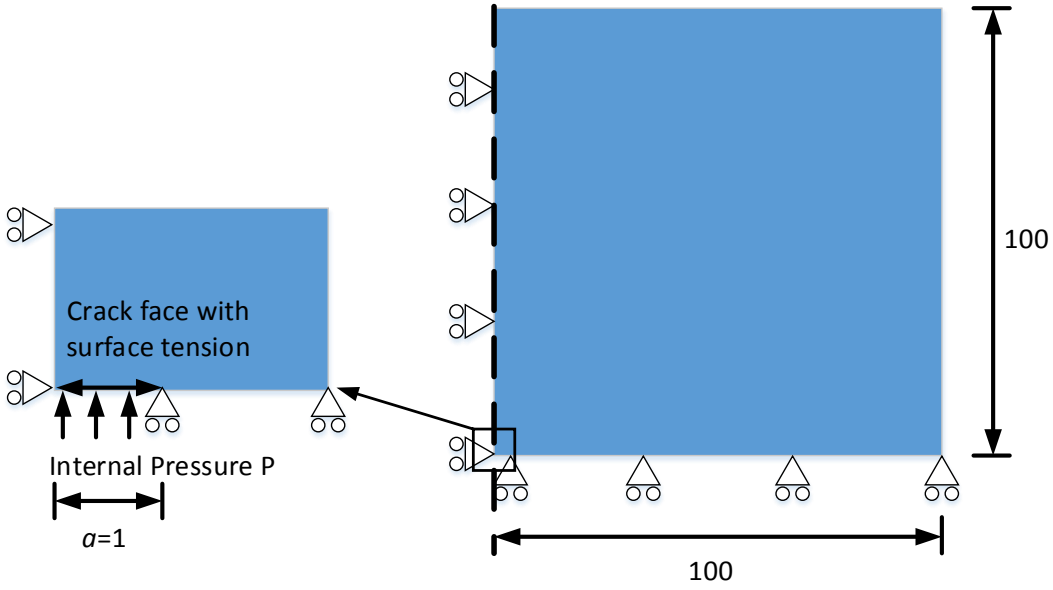

Fig. 8.3: The geometry and boundary conditions used in our finite element calculation. All lengths are normalized by initial crack radius a. The right and upper boundaries are traction free. Symmetry boundary conditions are applied on the left and lower boundaries. Internal pressure and surface tension are applied on crack faces.

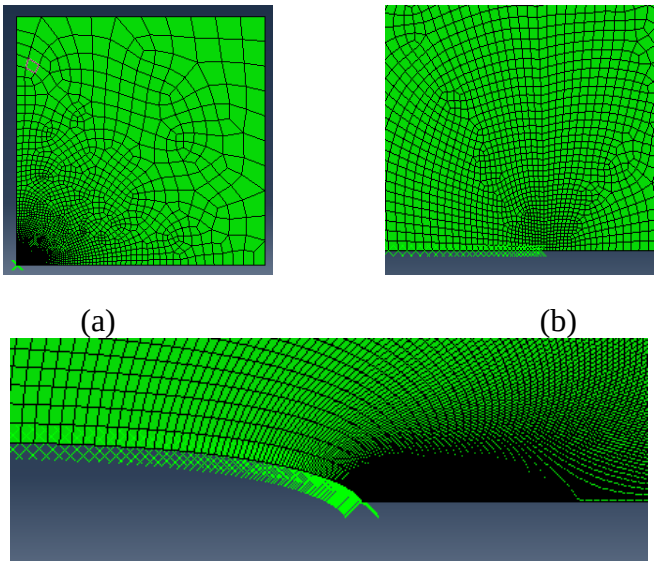

Fig. 8.4 Mesh used in our FEM calculation: (a) mesh of the full model. (b) zoom-in view of the original coarse mesh near the crack tip. (c) Re-mesh on deformed configuration.

8.4 Results

The elasto-capillary number is the only material parameter that controls our solution. We give an order of estimate for the elasto-capillary number ω for a soft material with a small crack. If the crack radius is 1mm and the surface tension is 0.1J/m^2, then $\omega = 10^2 (J/m^3)/E$. For a very soft gel with modulus on the order of tens of pascals, ω is of order unity. For rubbers, where the modulus is on the order of $10^6 Pa$, $\omega \approx 10^{-4}$. Fig. 8.5 (a) plots the normalized crack volume $\bar{V}(\bar{p}, \omega)$ versus the elasto-capillary number ω for three different values of applied pressure. It shows that for soft materials, the reduction of crack volume due to surface tension can be significant.

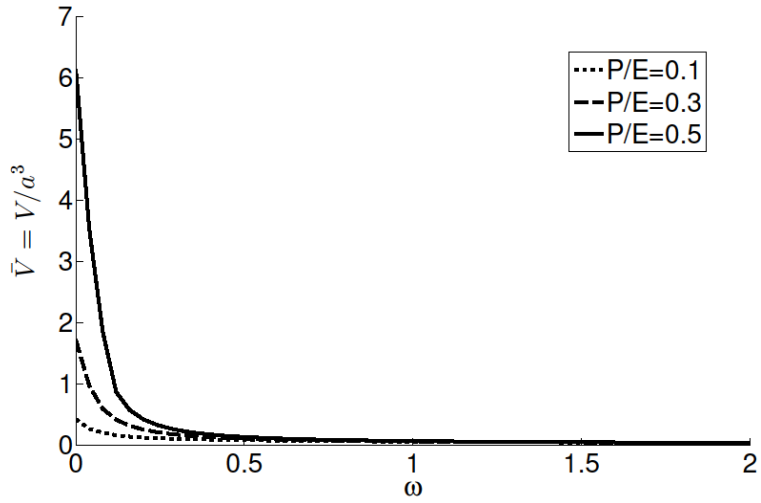

(a)

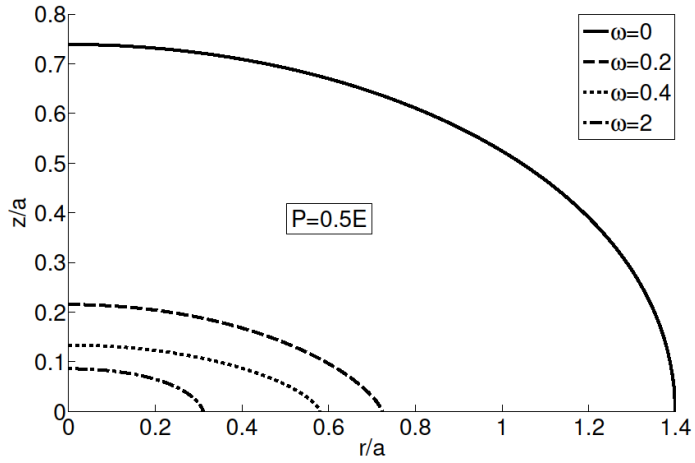

(b)

Fig. 8.5 (a) Normalized crack volume versus elasto-capillary number ω for different pressures. (b) Crack opening displacements for different elasto-capillary numbers when $p = 0.5E$

Fig. 8.5(b) shows the crack opening profile for different elasto-capillary number when the applied pressure is $0.5E$. Note that as ω increases, the crack shrinks both in the horizontal and vertical directions. The results shown above are for reasonably large pressures. For low pressures, for example, $P = 0.02E$, the results are shown in Fig.

8.6(a,b). For the case of no surface tension, $\omega = 0$ (point A), the crack is opened by the pressure. As ω is increased from A to B, the crack shrinks in both directions as shown in Fig. 8.6 (b). In this regime, the inward Laplace pressure caused by the surface tension resist crack opening. From B to C, the crack continues to shrink in horizontal direction but opens more in the middle. After the crack volume reaches its maximum at C, the crack opening displacement continues to increase until ω reaches ω_D. After D, the crack starts to shrink in both directions again and eventually the crack volume approaches zero as ω increases. Thus, for a fixed pressure, our results suggest that the crack volume will go to zero in the limit of infinite surface tension or $\omega \to \infty$.

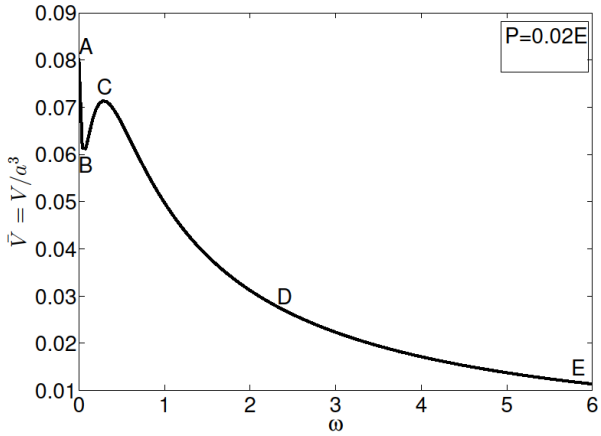

(a)

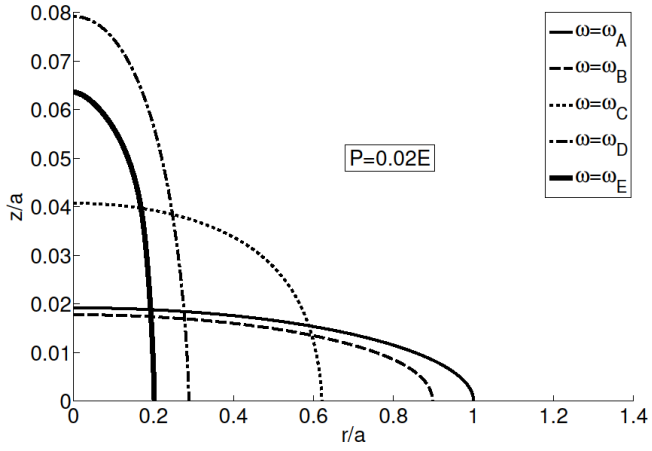

(b)

Fig. 8.6 (a) Normalized crack volume versus elasto-capillary number ω for $P = 0.02E$. (b) Crack opening displacements for different elasto-capillary numbers when $P = 0.02E$.

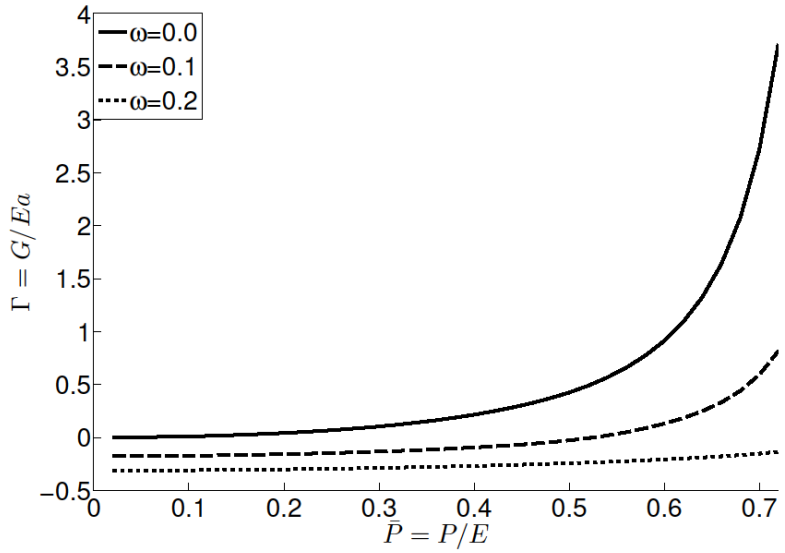

Fig. 8.7 Change of normalized energy release rate with respect to normalized pressure for different elasto-capillary number

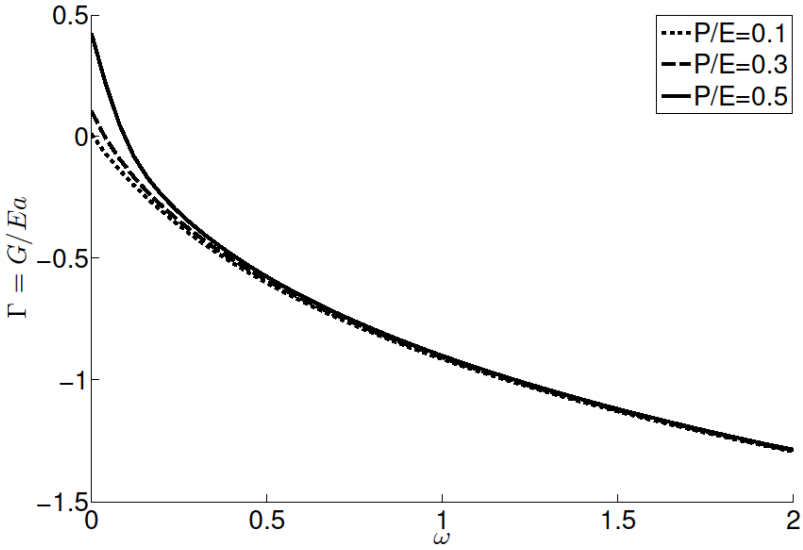

Fig. 8.8 Change of normalized energy release rate with respect to elasto-capillary number for different normalized pressure

Fig. 8.7 plots the normalized energy release rate versus normalized pressure for three different elasto-capillary numbers. For zero surface tension, the energy release rate is always positive and increases with pressure. This result is identical to the previous work of Lin and Hui [22]. For $\omega = 0.1$ and $\omega = 0.2$, the energy release rate is

negative when pressure is below some critical value. Physically, this means that the crack will have a tendency to heal since the potential energy of the system will decrease when the crack heals.

The dependence of Γ on ω for fixed normalized pressures is shown in Fig. 8.8. This result suggests that, for any fixed applied pressure, the energy release rate is a monotonic decreasing function of ω so that in the liquid limit, the crack will be closed under a constant pressure load. One may imagine that in the liquid limit, the crack would deform into a sphere with a finite radius, but a straight forward analysis of the potential energy of spherical solution in this limit shows that this solution is unstable under pressure control and thus the sphere will collapse.

8.5 Approximation for energy release rate

In this section, we give an approximate linearized formula for energy release rate in the limit of very small $\omega = \sigma / Ea$.

Let $\Gamma_0 \equiv \Gamma\left(\bar{P}, \omega = 0\right)$ denote the normalized energy release rate for the case with no surface tension. As shown in Fig. 8.9, the Γ_0 versus $\bar{P}$ curve of our FEM result can be fitted very well by the expression:

$$\Gamma_0 = \frac{3}{\pi}\bar{P}^2 exp\left[\frac{-1.333\bar{P}^3 + 1.021\bar{P}^2 + 0.0747\bar{P}}{0.72 - \bar{P}}\right] \tag{8.16}$$

Note Eq. (8.16) agrees with the energy release rate in the small strain limit, where

$$\Gamma_0 = \pi\bar{P}^2 / 3,\ \bar{P} << 1 \tag{8.17}$$

In the previous work of Lin and Hui [22] and Rong and Hui [23], it was found numerically that the energy release rate tends to diverge at a finite value of $\bar{P} \approx 0.72$. This feature is also included in Eq. (8.16). However, it must be noted that this divergence is restricted to neo-Hookean solid which underestimates the amount of

strain hardening effect. Lin and Hui [22] has shown that the energy release rate does not diverge for materials that exhibit high strain hardening.

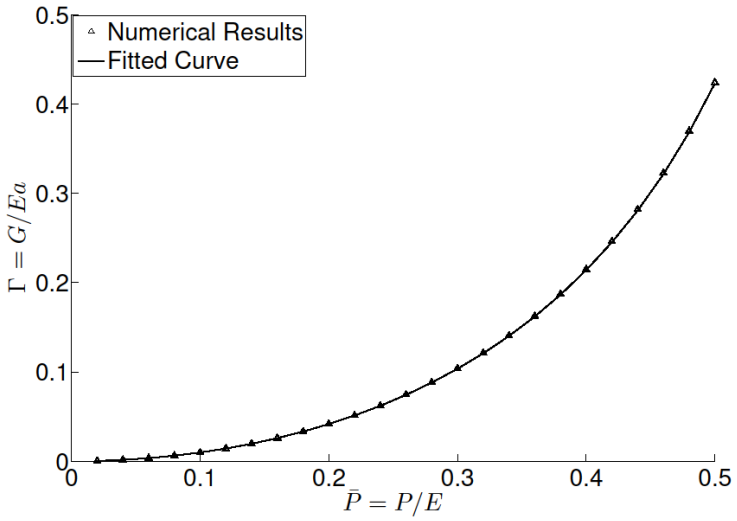

Fig. 8.9 Normalized energy release rate versus normalized pressure $\bar{P}$, when $\omega = 0$.

The numerical result in Fig. 8.8 suggests that the normalized energy release rate can be approximated by a linear function of ω when ω is sufficiently small, that is,

$$\Gamma = \Gamma_0 + s(\bar{P})\omega, \ \omega << 1 \tag{8.18}$$

where s is the slope of the $\Gamma - \omega$ curve when $\omega \to 0$, which depends on the normalized pressure $\bar{P}$. The region of validity of Eq. (8.18) depends on the normalized pressure, as can be seen in Fig. 8.8. The dependence of s on $\bar{P}$ is shown in Fig. 8.10.

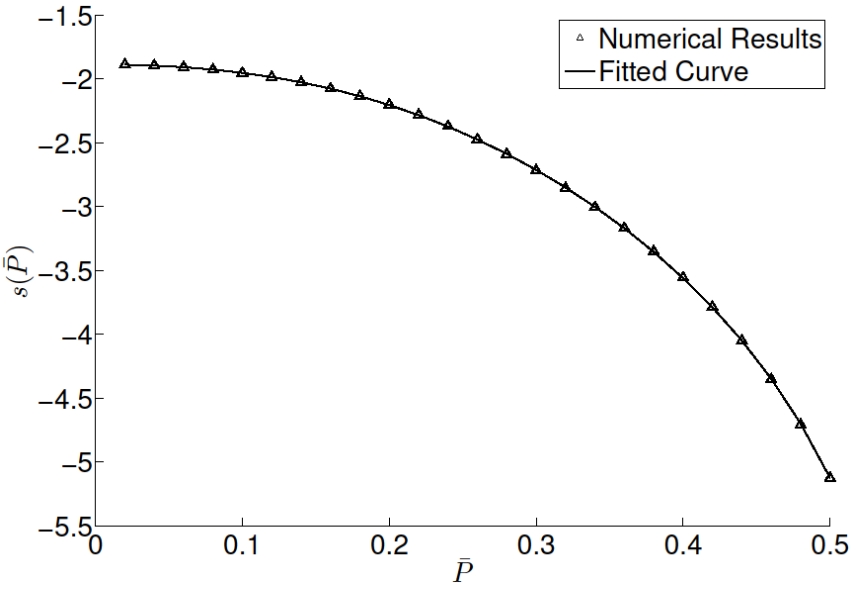

Fig. 8.10 $s\left(\bar{P}\right)=\partial\Gamma/\partial\omega\big|_{\omega=0}$ versus normalized pressure $\bar{P}$.

A fit for the *s* versus $\bar{P}$ curve is

$$s(\bar{P})=-1.885-5.123\bar{P}^2\exp\left[\frac{4.109\bar{P}^3-5.328\bar{P}^2+2.045\bar{P}}{0.72-\bar{P}}\right] \tag{8.19}$$

Eq. (8.19), combined with the Eq. (8.16), allow us to find an approximate expression for the energy release rate in the limit of small $\omega=\sigma/Ea$, that is,

$$\begin{aligned}\Gamma=&\frac{3}{\pi}\bar{P}^2 exp\left[\frac{-1.333\bar{P}^3+1.021\bar{P}^2+0.0747\bar{P}}{0.72-\bar{P}}\right]\\&-\left[1.885+5.123\bar{P}^2\exp\left(\frac{4.109\bar{P}^3-5.328\bar{P}^2+2.045\bar{P}}{0.72-\bar{P}}\right)\right]\omega\end{aligned} \tag{8.20}$$

which provides a good fit to our numerical results in Fig. 8.8 in the small ω limit.

8.6 Summary and discussion

The effect of surface tension on the energy release rate of a penny-shaped crack under internal pressure is determined by the dimensionless elasto-capillary number $\omega=\sigma/Ea$. A simple expression of the energy release rate which involves only the deformed crack volume, deformed crack area, elasto-capillary number and the applied

pressure is derived. For a neo-Hookean solid, our finite element results show that the energy release rate is significantly reduced due to surface tension. For pressure lower than a critical value which depends on the elasto-capillary number, the energy release rate is negative which means the crack has a tendency to heal. This is a nonlinear phenomenon that cannot be captured by the linearized theory. For small ω, an approximated linear function to evaluate the normalized energy release rate Γ is given by

$$\Gamma = \Gamma_0(P/E) + s(P/E)\omega \tag{8.21}$$

where Γ_0 is the energy release rate without surface tension and is given by Eq. (8.16), and s is a dimensionless function that depends on the normalized applied pressure.

Surface energy also plays an important role in fracture energy. For ideally brittle elastic solids, the fracture energy or fracture toughness is twice the surface energy. However, this is rarely the case for most materials because of additional dissipation mechanism. For materials relevant to this work, such as elastomers, the fracture energy is found to be much greater than surface energy, which can be estimated by taking the energy required to break a carbon-carbon bond and multiplying it by the number of bonds crossing a unit area of the fracture plane [24]. Lake and Thomas [24] suggested that most of the energy stored in the chains up to the point of bond rupture is dissipated, so fracture energy in elastomers is amplified by the number of bonds per chain. In this Chapter, we show that for soft materials, although surface energy is not the dominant factor in setting the fracture energy, surface tension can significantly affect the material deformation and stress field and thus reduces the energy release rate. This is a new and interesting way in which surfaces resist fracture.

Finally, our work assumes that the surface tension is positive but it can be negative [11]. We did not investigate this possibility since a compressive surface stress may cause a buckling instability of the crack faces, which will lead to complications in

our numerical method. Whether a negative surface tension will increase the energy release rate is an interesting question subjected to further investigation.

REFERENCES

[1] K. L. Johnson, K. Kendall, and A. D. Roberts, Proc. R. Soc. A Math. Phys. Eng. Sci. **324**, 301 (1971).

[2] X. Xu, A. Jagota, and C.-Y. Hui, Soft Matter **10**, 4625 (2014).

[3] R. W. Style, C. Hyland, R. Boltyanskiy, J. S. Wettlaufer, and E. R. Dufresne, Nat. Commun. **4**, 2728 (2013).

[4] X. Xu, A. Jagota, S. Peng, D. Luo, M. Wu, and C.-Y. Hui, Langmuir **29**, 8665 (2013).

[5] S. Mora, C. Maurini, T. Phou, J.-M. Fromental, B. Audoly, and Y. Pomeau, Phys. Rev. Lett. **111**, 114301 (2013).

[6] A. Marchand, S. Das, J. H. Snoeijer, and B. Andreotti, Phys. Rev. Lett. **109**, 236101 (2012).

[7] R. W. Style, R. Boltyanskiy, Y. Che, J. S. Wettlaufer, L. A. Wilen, and E. R. Dufresne, Phys. Rev. Lett. **110**, 66103 (2013).

[8] R. W. Style and E. R. Dufresne, Soft Matter **8**, 7177 (2012).

[9] A. Jagota, D. Paretkar, and A. Ghatak, Phys. Rev. E **85**, 51602 (2012).

[10] B. Roman and J. Bico, J. Phys. Condens. Matter **22**, 493101 (2010).

[11] R. C. Cammarata and K. Sieradzki, Annu. Rev. Mater. Sci. **24**, 215 (1994).

[12] M. Gurtin and A. Ian Murdoch, Arch. Ration. Mech. Anal. **57**, (1975).

[13] R. Thomson, T.-J. Chuang, and I.-H. Lin, Acta Metall. **34**, 1133 (1986).

[14] C. H. Wu, J. Mech. Phys. Solids **47**, 2469 (1999).

[15] C. I. Kim, P. Schiavone, and C.-Q. Ru, J. Elast. **104**, 397 (2011).

[16] C. Kim, C.-Q. Ru, and P. Schiavone, Math. Mech. Solids **18**, 59 (2013).

[17] X. L. Fu, G. F. Wang, and X. Q. Feng, Int. J. Fract. **151**, 95 (2008).

[18] G.-F. Wang, X.-Q. Feng, T.-J. Wang, and W. Gao, J. Appl. Mech. **75**, 11001 (2008).

[19] G. F. Wang and Y. Li, Eng. Fract. Mech. **109**, 290 (2013).

[20] A. J. M. (Anthony J. M. Spencer, *Continuum Mechanics* (Dover Publications, 2004).

[21] D. M. Parks, Comput. Methods Appl. Mech. Eng. **12**, 353 (1977).

[22] Y. Y. Lin and C. Y. Hui, Int. J. Fract. **126**, 205 (2004).

[23] R. Long and C.-Y. Hui, Soft Matter **6**, 1238 (2010).

[24] G. J. Lake and A. G. Thomas, Proc. R. Soc. London A Math. Phys. Eng. Sci. **300**, (1967).

CHAPTER 9

EFFECT OF SURFACE TENSION ON THE ADHESION BETWEEN A RIGID FLAT PUNCH AND A SEMI-INFINITE NEO-HOOKEAN HALF-SPACE [9]

9.1 Introduction

The indentation of a rigid flat circular punch into an elastic half space is a classic problem in mechanics. It was first solved by Boussinesq [1]. His solution can be readily extended to determine the force required to retract the indenter when the indenter/substrate interface is adhesive [2–5], and this is a fundamental result in adhesion science. However, this force is a lower bound since it ignores the resistance due to elasto-capillarity, that is, it assumes that surface stress of the elastic substrate plays no role in resisting deformation. For soft materials, this assumption can cause substantial errors, as demonstrated by recent experiments [6–9] and theories [10–13]. More references on the effect of surface stress on the mechanical behavior of soft materials can be found in a recent review by Style et al. [14]. In general, whether or not surface stresses are important depends on the elasto-capillary number ω, defined as the ratio of the elasto-capillary length σ / E to the characteristic length scale of the problem of interest. For the adhesion problem in this work, this length is *a*, the radius of the indenter. Thus, elasto-capillarity comes into play when the size of the indenter is small or when the substrate is very compliant.

Another limitation to the Boussinesq's solution is that it assumes small strain linear elasticity (*SSLE*). Experiments have demonstrated that large deformations are often associated with elasto-capillary phenomenon [7,9]. Therefore, the Boussinesq solution is not expected to work for problems where $\omega \geq 1$.

The adhesion problem considered in this work is closely related to adhesive contact mechanics of spheres and cylinders. Recently, several research groups have

[9] Liu T., Jagota A., Hui C.Y., (2016), Extreme Mechanics Letter

shown that surface stress can significantly affect the contact mechanics of these objects when $\omega \geq 1$ [15–20]. A simple way to model the mechanics of contact is to view the air gap between the contacting surfaces as an external traction-free crack; the crack front being the contact line. The equilibrium position of the contact line is determined by setting the energy release rate of this crack to the work of adhesion, W_{ad}. It is interesting to note that the energy release rate of this crack can be deduced from the "Hertz" solution in which the stress singularity at the contact line is suppressed by enforcing continuity of slope [15,16,19]. Finally, it should be noted that the analyses in [15–20] are based on small strain linear elasticity (*SSLE*). One of the main objectives of this work is to study how the energy release rate depends on the applied load and the surface stress for large deformation.

The plan of this Chapter is as follows. Section 9.2 states the problem and section 9.3 describes the finite element method. A formula for calculation of energy release rate is derived in section 9.4. Numerical results for the effect of surface tension on the deformation field, energy release rate and pull-off behavior are presented in section 9.5, and a discussion and summary are given in section 9.6.

9.2 Statement of problem

9.2.1 Problem definition

The geometry of the problem under consideration is shown in Fig. 9.1 A rigid flat circular punch of radius a is in contact with an elastic half space. We assume that contact is adhesive so the interface can support tension. The half space is assumed to be isotropic, homogeneous and incompressible, and its elasticity is described by a neo-Hookean material model.

To describe the mechanical behavior of the surface, we restrict our attention to soft materials such as polymer gels and elastomers, for which the surface can be

considered to be isotropic. For these materials, the surface stress tensor $\boldsymbol{\Sigma} = \sigma \boldsymbol{I}_s$ is isotropic, where $\boldsymbol{I}_s$ is the surface identity tensor, and σ is a scalar defined as the surface tension. We further assume that σ is constant, independent of surface strain. As noted by Gibbs [21], surface tension in solids need not be the same as surface energy. However, for hydrogels where the bulk of the surface material is liquid, the surface tension is expected to be constant with a value approximately equal to the surface energy. This statement is consistent with many experimental studies on soft hydrogels as well as soft elastomers [22–26]. Consistent with an adhesive interface, we impose no-slip condition on the interface between punch and substrate. As noted in our previous work [15,16], by this assumption we need not consider a separate interfacial tension in the contact region.

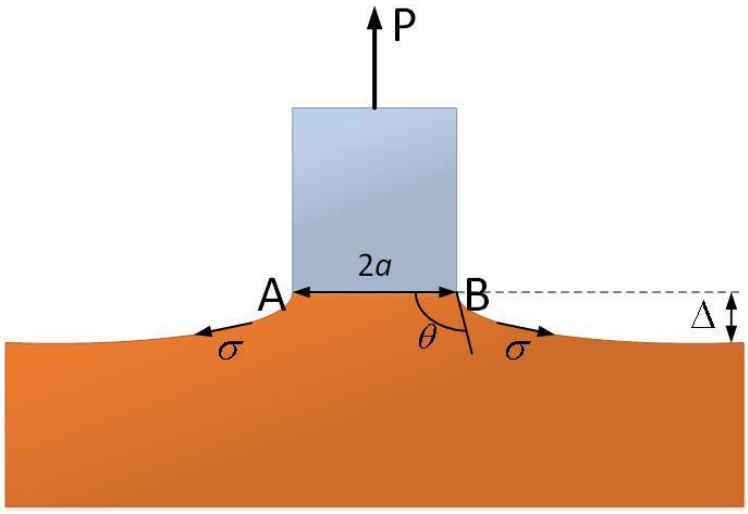

Fig. 9.1 the contact between a rigid punch with radius *a* and a semi-infinite elastic half-space under retraction P. The retraction displacement is Δ, and the contact angle between the substrate-air interface and the punch bottom is denoted by θ.

9.2.2 Limiting cases: Elasticity and Liquid-like limit

Before tackling the general problem with surface tension, we consider two limits. In the first, elasticity dominates and surface tension is negligible ($\omega \to 0$). In the second, the material is liquid-like with $\omega \to \infty$.

9.2.2.1 Elastic limit, $\omega \to 0$

In the limit of vanishing elasto-capillary number and assuming *SSLE*, the pressure distribution under the punch is [1]:

$$p(r) = \frac{P}{2\pi a^2}\left(1-\frac{r^2}{a^2}\right)^{-1/2}, \; r < a \tag{9.1}$$

where $P > 0$ is the retraction load (see Fig. 9.1). It should be noted that Boussinesq's solution assumes frictionless contact. Fortunately, due to incompressibility, the interfacial shear traction is also zero for no-slip contact. The relation between the retraction load P and the indenter displacement $\Delta > 0$ is given by

$$P = \frac{8}{3} Ea\Delta \tag{9.2}$$

where E is the Young's modulus. Eqs. (9.1, 9.2) apply for both indentation and retraction as long as deformation is small. Fig. 9.2 illustrates that contact line can be viewed as the front of an external interface crack. The energy release rate G of this crack is [27]:

$$G = \frac{3P^2}{32\pi E a^3} = \frac{2E\Delta^2}{3\pi a} \tag{9.3}$$

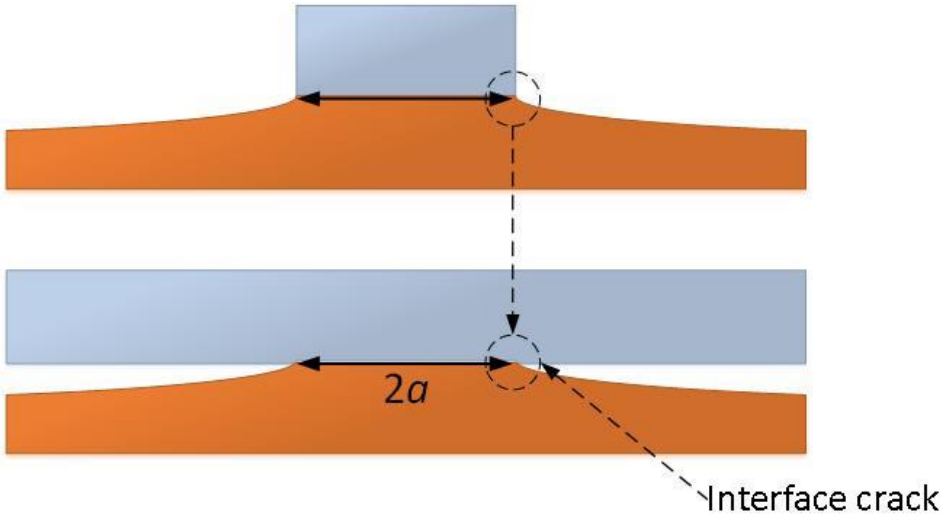

Fig. 9.2 During retraction, the edge of contact can be seen as the front of an external interface crack. This is because the indenter is rigid, so changing its shape outside the contact zone does not affect the stress and strain field in the substrate.

When the energy release rate is equal to the work of adhesion W_{ad}, the interface crack becomes unstable resulting in the punch suddenly jumping out of contact. The critical load and displacement associate with this instability are called pull-off force and displacement respectively and they are given by (9.3):

$$\Delta_{off}^{(e)} = \sqrt{\frac{3\pi a W_{ad}}{2E}},\ \mathrm{P}_{off}^{(e)} = 8a\sqrt{\frac{\pi a E W_{ad}}{6}}\ , \tag{9.4}$$

where the superscript (*e*) denotes the small strain elastic limit. Thus, the pull-off force/displacement can be used to determine the work of adhesion assuming that the modulus of the substrate is known.

For large deformation, exact results are not available. Kristnan *et al*. [27] have studied the punch problem using a finite element model without accounting for surface tension. These results are used to check the validity of our finite element model for the special case of $\omega \to 0$.

9.2.2.2 Liquid-like limit $\omega \to \infty$

In this limit, elasticity can be neglected in a large region surrounding the punch. We assume gravity is negligible, so the pressure in the liquid-like "solid" is uniform and equals to atmosphere pressure and the free surface of the substrate is a zero mean curvature surface as shown in Fig. 9.3.

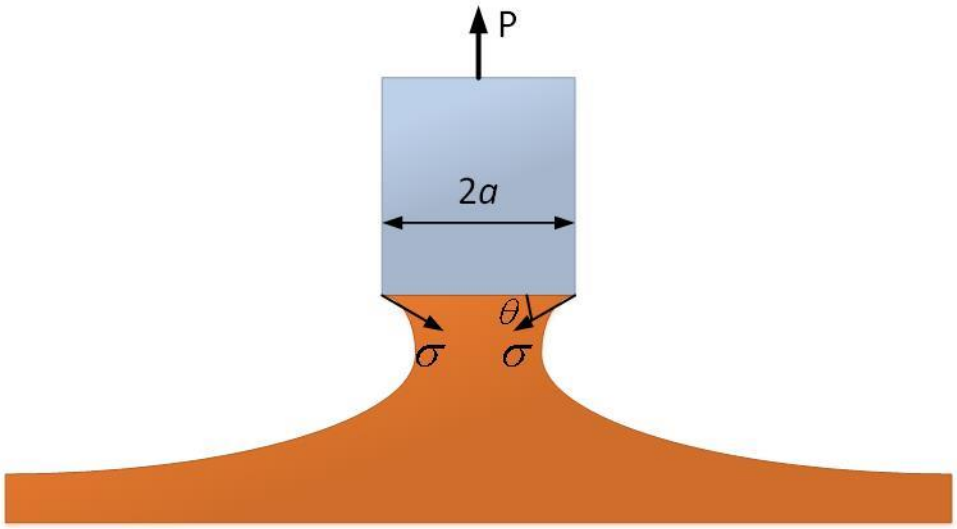

Fig. 9.3 Deformed shape of the substrate surface (zero mean curvature surface when gravity is neglected) in the liquid like limit, θ denotes the contact angle of the contact line.

In this limit, the contact angle θ at the punch edge (see Fig. 9.3) is determined by energy balance, which is equivalent to Young-Dupre's equation assuming contact line is on lower surface[10] [11]:

$$\sigma(1+\cos\theta) = W_{ad} \tag{9.5}$$

Force balance in z-direction (the direction of *P*) yields

$$2\pi a\sigma \sin\theta = P \tag{9.6}$$

The pull-off load is determined by combining (9.5) and (9.6), i.e.,

[10] In practice, (5) is a lower bound since the contact angle can be anywhere between what is given by (5) and $3\pi/2$ because perfectly sharp corner does not exist.

$$P_{off}^{(l)} = 2\pi a\sigma\sqrt{2\frac{W_{ad}}{\sigma} - \left(\frac{W_{ad}}{\sigma}\right)^2} \tag{9.7a}$$

where the superscript *l* denotes the liquid limit. In this limit, large contact angle ($\theta \gg \phi$) *implies small deformation*, for this case, $W_{ad}/\sigma \ll 1$ so (9.7a) reduces to

$$P_{off}^{(l)} \approx 2\pi a\sqrt{2\sigma W_{ad}}, \text{ for } W_{ad}/\sigma \ll 1. \tag{9.7b}$$

Finally, it should be noted that the displacement of the punch is not defined in the liquid like limit for an *infinite* substrate. Indeed, the deformed substrate has a zero mean curvature surface, and surface displacement increases logarithmically with the size of the substrate.

9.3 Finite Element (FE) Method

Our FE model is shown schematically in Fig. 4. A commercial FEM software, ABAQUS® , is used to compute the deformation of the substrate which is assumed to be an incompressible neo-hookean solid with strain energy density *W* given by

$$W = \frac{E}{6}(I_1 - 3) \tag{9.8}$$

where $I_1 = \sum_{i=1}^{3} \lambda_i^2$ is the first invariant of the right Cauchy-Green strain tensor with the principle stretches denoted by λ_i. The built-in Neo-Hookean function in ABAQUS is selected to model this material behavior. In our model, all lengths are normalized by *a* and retraction load *P* is normalized by its corresponding value in the elastic limit with displacement equal to *a* (see Eq. (9.2)), that is

$$\bar{P} = 3P/(8Ea^2),\ \bar{\Delta} = \Delta/a,\ \bar{r} = r/a \tag{9.9}$$

With this normalization, the dimensionless solution depends only on a single dimensionless parameter, the elasto-capillary number $\omega = \sigma/(Ea)$. The infinite cross-section of the substrate is approximated by a square with a length of 100 dimensionless units (the contact extends over a radial distance of one). We have checked that increasing the size of the square does not affect the solution of the stress

and deformation fields near the punch. On boundary 1 (see Fig. 9.4), a given displacement is prescribed in the z-direction while the radial displacement is fixed to be zero to enforce the no-slip condition. No radial displacement is allowed on boundaries 2 and 4 while the z- displacement and shear traction are both zero on boundary 3. On boundary 5, a user-defined surface element (UEL) is used to model surface tension. Details about the implementation of this surface element in ABAQUS can be found in the work of Xu *et al.* [28]. The built-in element CAX4RH is selected as bulk element type. We monitor the distortion of elements and, when the distortion is too large, a re-meshing python script is run to generate a new mesh on the deformed configuration to ensure proper convergence and accuracy of calculation.

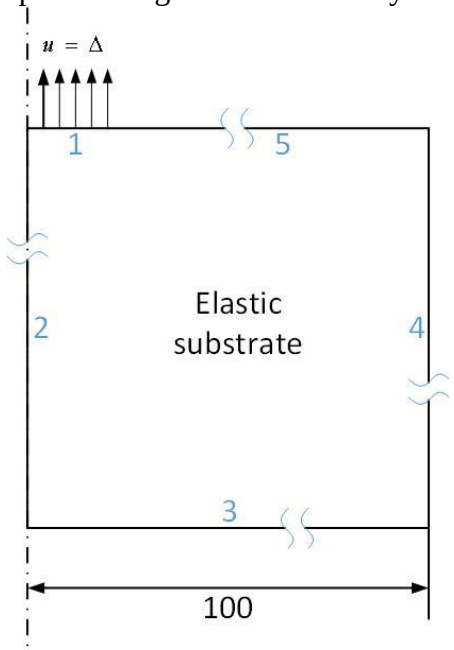

Fig. 9.4 A schematic of our model used in finite element calculation. All length are normalized by the punch radius. The elastic half-space is approximated by a square with length equal to 100 unit.

9.4. Calculation of energy release rate G

Our main objective is to determine the relation between the load and displacement during retraction. The pull-off load and displacement are determined by the energy balance equation, i.e., the energy release rate of the interface crack is equal to the work of adhesion,

$$G = W_{ad} \tag{9.10}$$

In the literature, calculation of energy release rate usually requires local stress or displacement field near crack tip. Because of the high gradients at the crack tip, these quantities are much more susceptible to error in comparison with global quantities like indenter load, indenter displacement and total elastic energy. Here we introduce a formulation which takes advantage of this fact.

In a displacement controlled test, the energy release rate is given by

$$G = \left.\frac{\partial \Gamma}{\partial A}\right|_{\Delta}, \tag{9.11}$$

where Γ is the total energy of the substrate and $A = \pi a^2$ is the contact area. The normalized total energy $\bar{\Gamma} = \Gamma / \left(\frac{8}{3} E a^3\right)$ is the work done by the normalized load acting on the normalized displacement, i.e.,

$$\bar{\Gamma} = \int_0^{\bar{\Delta}} \bar{P}\left(\bar{\Delta}', \omega\right) d\bar{\Delta}' \tag{9.12}$$

Dimensional consideration imply that the normalized total energy $\bar{\Gamma}$ and normalized load $\bar{P}$ is a *function of* $\bar{\Delta}$ *and* ω *only*. Since both $\bar{\Delta}$ *and* ω in (9.11) contain $a = \sqrt{A/\pi}$, the derivative of Γ in (9.11) consists of three terms given by (see Appendix for details)

$$G = \frac{4Ea}{\pi}\left(\bar{\Gamma}\left(\bar{\Delta}, \omega\right) - \frac{1}{3}\frac{\partial\left(\bar{\Gamma}\left(\bar{\Delta}, \omega\right)\right)}{\partial\left(\bar{\Delta}\right)}\bar{\Delta} - \frac{1}{3}\frac{\partial\left(\bar{\Gamma}\left(\bar{\Delta}, \omega\right)\right)}{\partial\left(\omega\right)}\omega\right) \tag{9.13}$$

After normalizing energy release rate by $\frac{4Ea}{\pi}$, i.e., $\bar{G} = \frac{pG}{4Ea}$, Eq. (9.13) becomes:

$$\bar{G} = \frac{\pi G}{4Ea} = \bar{\Gamma}\left(\bar{\Delta}, \omega\right) - \frac{1}{3}\frac{\partial \bar{\Gamma}\left(\bar{\Delta}, \omega\right)}{\partial \bar{\Delta}}\bar{\Delta} - \frac{1}{3}\frac{\partial \bar{\Gamma}\left(\bar{\Delta}, \omega\right)}{\partial \omega}\omega \qquad (9.14)$$

Eq. (9.14) allows us to evaluate the energy release rate using global quantities such as strain energy and its variations with the normalized displacement and elasto-capillary number. Specifically, the first term of Eq. (9.14) is computed by numerical integration using Eq. (9.12) and the last two terms are evaluated by a first order central finite difference method. In post-processing, the sum of *z*-direction reaction force on boundary 3 is used to compute the normal load in Eq. 12. Note that while (9.13) is strictly valid for a semi-infinite substrate, a correction term needs to be added when a finite substrate is considered (see Appendix).

9.5 Numerical Results

The local surface displacement profiles for different retraction displacement are shown in Fig. 9.5 for five different elasto-capillary numbers. In the absence of surface tension ($\omega = 0$), *SSLE* theory predicts that the contact angle should be exactly 90°; however, the free surface actually deforms into a neck like region with the local contact angle close to zero. As shown in Fig. 9.5, the neck becomes more severe as retraction increases from 0.1 to 1. This result is consistent with the earlier analysis by Krishnan *et al.* [27] where $\omega = 0$. As shown in Fig. 9.5, the local kink at the contact line flattened as elasto-capillary number increases, consistent with the intuition that surface tension always mitigate local curvature.

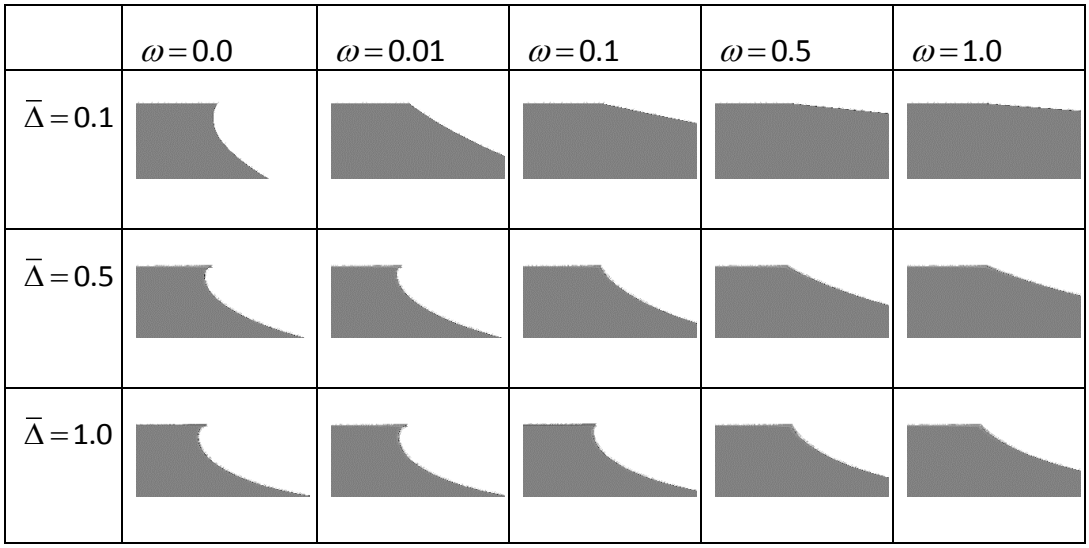

Fig. 9.5 Near edge deformation field for retraction of punch. The gray part is the deformed shape of the substrate near the punch edge. With increase of elasto-capillary number, the substrate becomes more flat and the local contact angle becomes larger.

The stiffness of the system *k* is defined as the ratio of the indenter force over the indenter displacement. In linear theory, *k* depends on a, ω and is independent of Δ. However, for large deformation or nonlinear material behavior, this need not be the case. Because the normalized load is a function only of $\bar{\Delta}$ and ω, it is convenient to define a normalized stiffness $\bar{k} = \bar{P} / \bar{\Delta}$, so

$$k = P / \Delta = \frac{8Ea}{3} \bar{k} \left(\bar{\Delta}, \omega \right) \tag{9.15}$$

Surprisingly, our FEM results in Fig. 9.6 show that the force versus indentation displacement curve is practically linear for $\Delta \le a$, that is, the normalized stiffness is a function of ω only in this range, i.e.,

$$\bar{k} \left(\bar{\Delta}, \omega \right) \simeq \bar{k} \left(\omega \right), \bar{\Delta} \le 1 \tag{9.16}$$

Note that the normalized stiffness increases with the elasto-capillary number. Also, in Fig. 9.6, we compared our results with the *SSLE* results of Wang et al. [29] which are

shown as red lines . Our result shows that SSLE underestimates the stiffness and the error increases with increasing elasto-capillary number. One source of error of SSLE comes from the fact that the contact angle at the contact edge cannot be correctly predicted by linear theory.

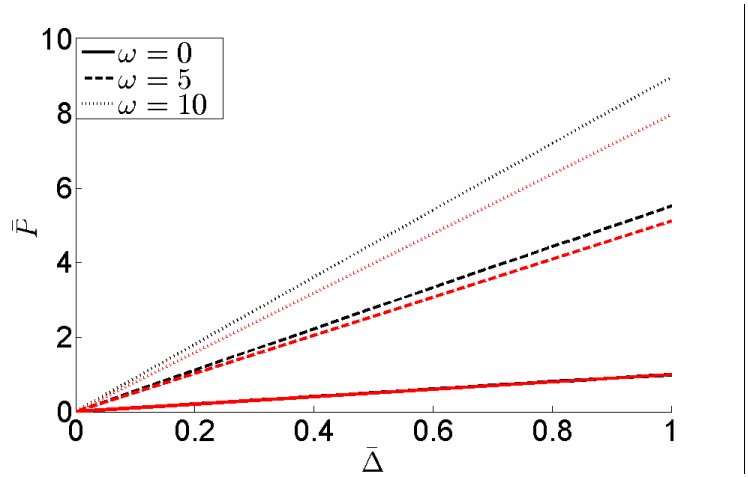

(a)

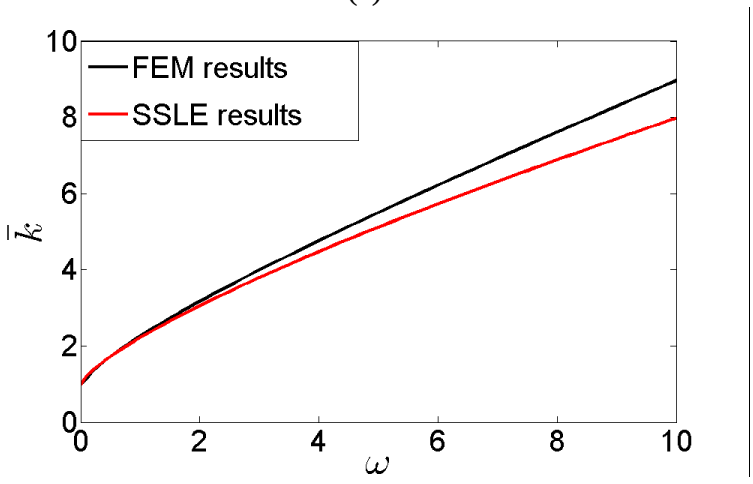

(b)

Fig. 9.6 (a) Normalized load-displacement relation for retraction of punch for three different elasto-capillary numbers. The three red lines are the corresponding SSLE results given by Wang et al [29]. (b) Comparison of stiffness with SSLE results. SSLE tends to underestimate the stiffness.

Results for the normalized energy release rate are shown in Fig. 9.7 (a, b).

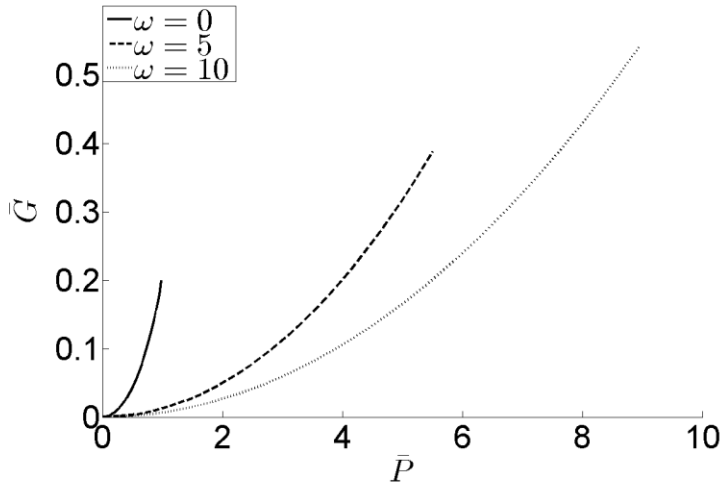

(a)

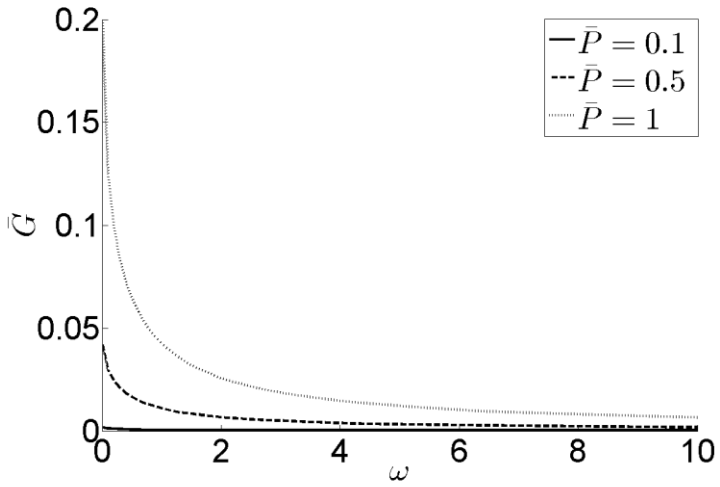

(b)

Fig. 9.7 (a) Normalized energy release rate vs normalized load for different values of elasto-capillary number (b) Normalized energy release rate vs elaso-capillary number for different normalized load.

Physically, one expects that, for a fixed elasto-capillary number ω, a higher external load will provide a higher driving force to propagate the crack and hence

corresponds to a higher energy release rate, as shown in Fig. 9.7 (a). On the other hand, the presence of surface stress tends to close the crack as suggested by a previous calculation [30]. Therefore, for a fixed external load, the energy release rate will decrease with elasto-capillary number as shown in Fig. 9.7 (b).

Once the energy release rate is obtained, the pull-off load and displacement can be determined using the energy balance equation $G = W_{ad}$. Fig 9.8 (a,b) plots the pull-off load and displacement normalized by their corresponding value in the elasticity dominated limit (Eq. (9.4)) to highlight the effect of surface tension.

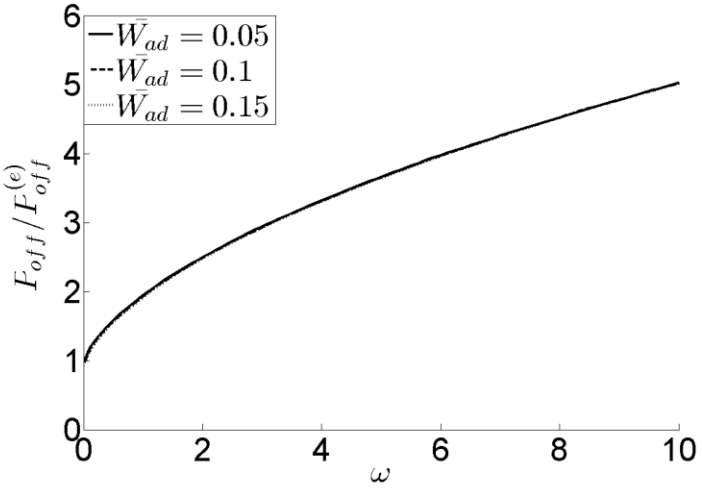

(a)

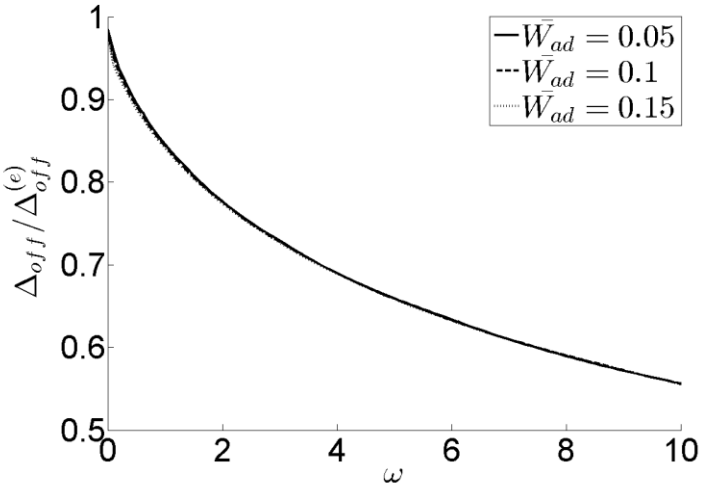

(b)

Fig. 9.8 (a) normalized pull-off load vs elasto-capillary number (b) normalized pull-off displacement vs elasto-capillary number. The curves with different normalized work of adhesion $\overline{W_{ad}} = \dfrac{\pi W_{ad}}{4Ea}$ essentially lie on top of each other.

Fig. 9.8 (a,b) show an important result, *the curves for different normalized* $\overline{W_{ad}} = \dfrac{\pi W_{ad}}{4Ea}$ *lie on top of each other*. Thus, the normalized pull-off load/displacement *depend only on* the elasto-capillary number, i.e.,

$$P_{off} = 8a\sqrt{\frac{\pi a E W_{ad}}{6}}\,\widehat{P_{off}}(\omega)$$
$$\Delta_{off} = \sqrt{\frac{3\pi a W_{ad}}{2E}}\,\widehat{\Delta_{off}}(\omega) \qquad (9.17a,b)$$

Note that the pull-off load increases with the elasto-capillary number while the pull-off displacement *decreases* with it, consistent with the intuition that surface tension opposes deformation. These results are also consistent with previous work for spherical indenter [16] and 2-D cylindrical indenter [15]. In the Appendix, we show that (17a,b) is exact if the stiffness of the system depends only on ω. In the range of our calculation, $0 \le \omega \le 10$, $P_{off}(\omega)$ and $\Delta_{off}(\omega)$ can be fitted accurately by the following expressions:

$$P_{off}(\omega) = \frac{2.4934\omega + 1.54\omega^{1/2} + 1}{1.6244\omega^{1/2} + 1}$$
$$\Delta_{off}(\omega) = \frac{0.5035\omega^{1/2} + 1}{0.1678\omega + 0.6225\omega^{1/2} + 1} \qquad (9.18)$$

Since gravity is ignored in our calculation, the indenter displacement is not defined (or depend on the scale of the substrate) in the liquid limit, so these formulae should be used within the range of $0 \le \omega \le 10$.

9.6. Discussion and summary

9.6.1 Discussion

Our finite element results shows that the indentation load-displacement curve is practically linear for $\bar{\Delta} \le 1$, as a result, the normalized stiffness is a function of elasto-capillary number alone. This result suggested that solid surface tension can be measured by evaluating the slope of the loading curve if one can independently measure the elastic modulus of the solid. In many applications, the Elasto-capillary number is quite small. For example, the elasto-capillary number of a punch with a 1mm diameter and a soft silicone gel with modulus on the order of 1KPa [7] is about

0.1. For these cases, Fig. 9.6 (b) shows that the normalized stiffness is not so sensitive to elasto-capillary number, as a result, the change in stiffness due to surface tension may not be significant enough to be detected. However, Fig. 9.5 shows that the deformation near the contact line is very sensitive to ω when it is small. Hence, for small ω, an alternative way to determine substrate surface tension is to measure the "apparent contact angle" θ. Fig. 9.9 plots the apparent contact angle as a function of the elasto-capillary number for $\bar{\Delta}=1.0$. Note that θ increases very rapidly for small ω. On the other hand, for an ultra-soft hydrogel with modulus on the order of 10Pa [31], ω is about 10, for this case the substrate stiffness should be used to determine the surface tension.

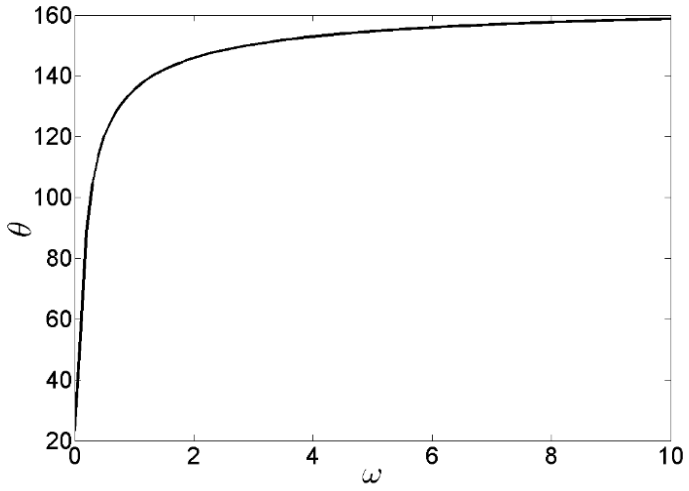

Fig. 9.9 Apparent contact angle vs elasto-capillary number for $\bar{\Delta}=1.0$

An important subset of problem of practical interest we did not fully address here is the effect of surface tension on indentation, where $P < 0$. This is because indentation can cause the side wall of the indenter to come into contact with the surface of the substrate, as shown by our FE calculations which is included in the Appendix. These FE results show that as long as the amount of indentation does not exceed the contact

radius and the elasto-capillary number is greater or equal to 0.1, sidewall contact does not occur and Eq. (9.15) holds for both indentation and retraction. In general, side contact will affect the indenter force even if frictionless boundary condition were imposed between the sidewall and substrate. Of course, in reality, some friction will exist, and this will provide additional resistance to indentation and further complicates the analysis.

9.6.2 Summary

Finite element simulations are used to investigate the effects of surface tension on the adhesive contact between a rigid flat circular punch and an elastic substrate. The elasto-capillary number $\omega = \frac{\sigma}{Ea}$ is used to quantify surface tension effects. Our calculation shows that surface tension can significantly mitigate the local concentration of curvature near the edge of the punch. This change of local deformation is very sensitive to elasto-capillary number when it is small. For fixed indentation load, it is shown that energy release rate goes down when ω increases which suggests that the presence of surface tension makes the propagation of an interface crack more difficult. An examination of pull-off behavior shows that a higher external load but a *smaller displacement* is required to pull the punch out of contact when there is surface tension. Finally, we propose that the loading curve slope and the "contact angle" at the punch edge for fixed displacement is a function of elasto-capillary number only and may be used as a method to measure the substrate surface tension. We also provide approximate expressions for the pull-off load and displacement.

In a previous work of a rigid sphere in contact with an elastic substrate, Karpitscha *et al*. [32] found that the local contact angle is always determined by Young's

equation, assuming surface energies equal to surface tensions. Our pull-off results are consistent with their theory even though the geometry is different (see Appendix).

There are limitations in our work. We have not been able to consider very large deformation where $\Delta > a$. Such large deformation requires a considerable amount of remeshing which affects the accuracy of the FE solution. We assume the surface stress is isotropic and can be represented by a constant surface tension σ independent of surface strain, so our surface model can only be applied to a restricted class of soft materials. It is also assumed that the contact line is perfectly circular whereas in reality the presence of defect may cause small error when compared with theory. Finally, we assume adhesion is sufficiently strong so that the interface does not slip before it fails.

APPENDIX 9.1

INDENTATION BEHAVIOR

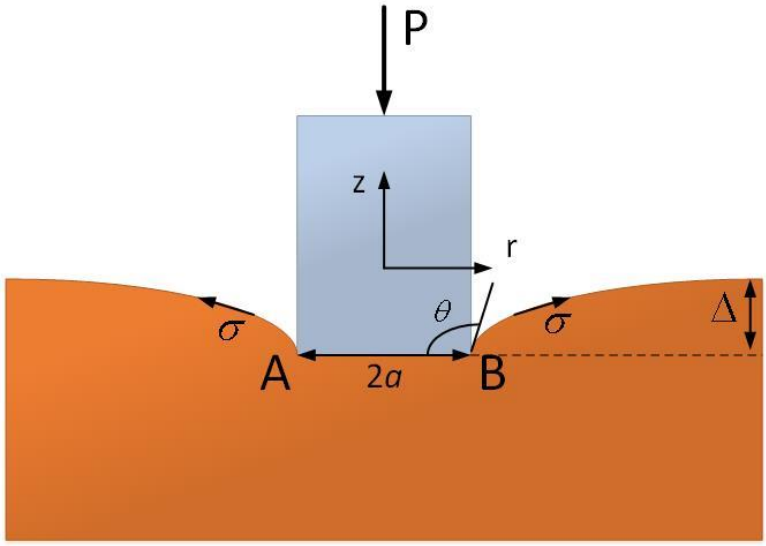

Fig. A9.1.1 Scheme of a rigid punch indenting on an elastic solid, i.e. $P,\ \Delta < 0$.

In this section, similar calculation of deformation and load vs displacement curve are carried out for indentation behavior, i.e. $P,\ \Delta < 0$. The FEM results in Fig. A9.1.2 shows that the angle θ (see Fig. A9.1.1) is *less* than $\pi/2$ in the absence of surface tension ($\omega = 0$) which is different from the prediction of small strain theory where $\theta = \pi/2$. Fig. A9.1.2 shows that for large indentation ($\bar{\Delta} \geq 0.5$) and small elasto-capillary number $\omega \leq 0.01$, the substrate comes into contact with the lateral surface of the punch. Such sideway contact is not observed for $\omega \geq 0.1$ even for $\bar{\Delta} = 1$. Indeed, as ω increases, θ becomes larger than $\pi/2$, and the substrate surface "flattens".

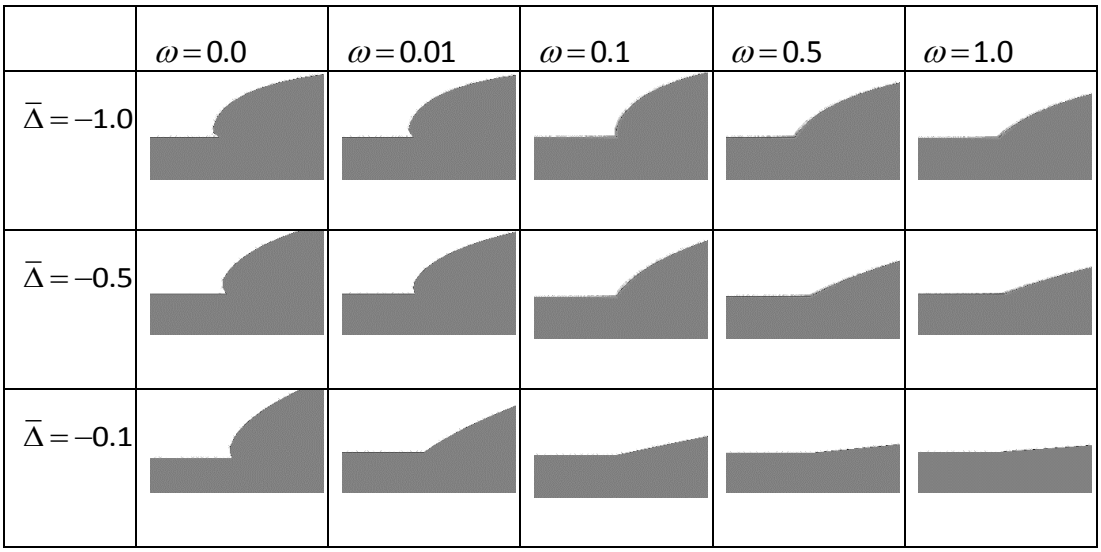

Fig. A9.1.2 Near edge deformation field for indentation

Similar to retraction, the deformation near the contact line is very sensitive to ω. For example, for $\bar{\Delta} = -0.1$ even very small surface tension ($\omega = 0.01$) can significantly flatten the deformed surface and reduces the local concentrated curvature predicted by the classical crack tip solution. For larger deformation ($\bar{\Delta} = -0.5$), higher surface tension is required to flatten the deformed surface.

As expected, surface tension resists deformation, that is, for same indentation displacement a higher load is required. This behavior is shown in Fig. A9.1.3 for different Elasto-capillary number.

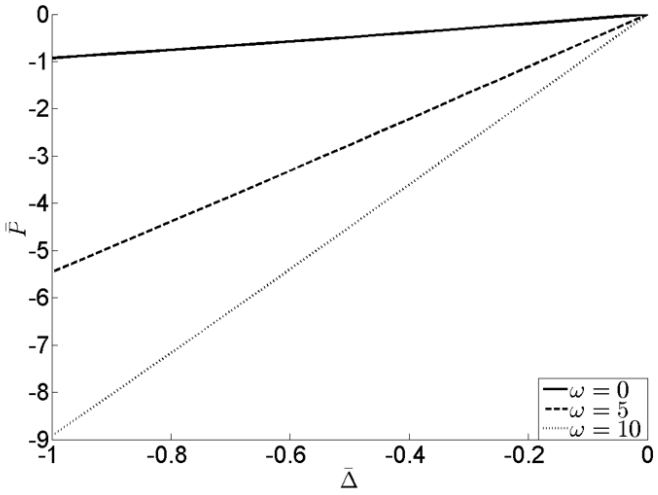

Fig. A9.1.3 Normalized load-displacement relation for indentation with different elasto-capillary number.

Figure A9.1.3 also shows that the indentation force is directly proportional to the indentation displacement, as in the case of retraction. Hence the normalized stiffness (as in Eq. 9.15) is approximately independent of the indentation depth and depends only on the elasto-capillary number. However, this behavior may not be accurate for large indentation and small elasto-capillary number, since sideway contact is not taken into account in our FE model.

APPENDIX 9.2

DERIVATION OF ENERGY RELEASE RATE

According to the definition of energy release rate and the fact that $\bar{\Gamma} = \Gamma / \left(\frac{8}{3} Ea^3 \right)$

$$G = \left. \frac{\partial \Gamma}{\partial A} \right|_{\Delta} = \left. \frac{1}{2\pi a} \frac{\partial \left(\frac{8Ea^3}{3} \bar{\Gamma}(\bar{\Delta}, \omega) \right)}{\partial a} \right|_{\Delta} \tag{A9.1}$$

Since $\bar{\Delta} = \frac{\Delta}{a}, \omega = \frac{\sigma}{Ea}$, equation (A9.1) can further be simplified as

$$\begin{aligned} G &= \frac{1}{2\pi a} \left(8Ea^2 \bar{\Gamma}(\bar{\Delta}, \omega) - \frac{8Ea^3}{3} \frac{\partial \bar{\Gamma}(\bar{\Delta}, \omega)}{\partial \bar{\Delta}} \frac{\bar{\Delta}}{a} - \frac{8Ea^3}{3} \frac{\partial \bar{\Gamma}(\bar{\Delta}, \omega)}{\partial \omega} \frac{\omega}{a} \right) \\ &= \frac{4Ea}{\pi} \left(\bar{\Gamma}(\bar{\Delta}, \omega) - \frac{1}{3} \bar{\Delta} \frac{\partial \bar{\Gamma}(\bar{\Delta}, \omega)}{\partial \bar{\Delta}} - \frac{1}{3} \omega \frac{\partial \bar{\Gamma}(\bar{\Delta}, \omega)}{\partial \omega} \right) \end{aligned} \tag{A9.2}$$

The above derivation is strictly valid for an infinite substrate, however, in our finite element calculation, we can only simulate a substrate with a finite size $R = 100a$. When surface tension is considered, the normalized total energy $\bar{\Gamma}$ should also be a function of $\bar{R} = \frac{R}{a}$. Hence, a correction term needs to be added in the expression of energy release rate:

$$\begin{aligned} G &= \left. \frac{1}{2\pi a} \frac{\partial \left(\frac{8Ea^3}{3} \bar{\Gamma}(\bar{\Delta}, \omega, \bar{R}) \right)}{\partial a} \right|_{\Delta} \\ &= \frac{4Ea}{\pi} \left(\bar{\Gamma}(\bar{\Delta}, \omega, \bar{R}) - \frac{1}{3} \bar{\Delta} \frac{\partial \bar{\Gamma}(\bar{\Delta}, \omega, \bar{R})}{\partial \bar{\Delta}} - \frac{1}{3} \omega \frac{\partial \bar{\Gamma}(\bar{\Delta}, \omega, \bar{R})}{\partial \omega} - \frac{1}{3} \bar{R} \frac{\partial \bar{\Gamma}(\bar{\Delta}, \omega, \bar{R})}{\partial \bar{R}} \right) \end{aligned} \tag{A9.3}$$

APPENDIX 9.3

PULL-OFF LOAD AND DISPLACEMENT NORMALIZATION

The goal of this analysis is to show that if $\bar{P}-\bar{\Delta}$ relation is linear and the stiffness is a function of ω only, then $\frac{\Delta_{off}}{\Delta^{(e)}_{off}}$ and $\frac{P_{off}}{P^{(e)}_{off}}$ are function of ω only.

Proof: If $\bar{P}=k(\omega)\bar{\Delta}$, then

$$\bar{\Gamma}=\frac{1}{2}k(\omega)\bar{\Delta}^2 \tag{A9.4}$$

Therefore, according to Eq. (9.14) in the main text,

$$\bar{G}=\frac{\bar{\Delta}^2}{6}\left(k(\omega)-k'(\omega)\omega\right) \tag{A9.5}$$

Take $\bar{G}=\overline{W_{ad}}$, and because $k(0)=1$,

$$\frac{\Delta_{off}}{\Delta^{(e)}_{off}}=\sqrt{\frac{1}{k(\omega)-k'(\omega)\omega}} \tag{A9.6}$$

and

$$\frac{P_{off}}{P^{(e)}_{off}}=k(\omega)\sqrt{\frac{1}{k(\omega)-k'(\omega)\omega}} \tag{A9.7}$$

APPENDIX 9.4

COMPARISON WITH KARPITSCHA ET AL.

In our calculation, we evaluate the energy release rate without imposing a fracture or pull-off condition. As long as we do not impose the pull-off condition (Eq. (9.10)), the contact angle is dependent on the displacement of the punch. In Karpitscha *et al.*'s paper [32], they always impose energy equilibrium, that is, $G = W_{ad}$, hence their displacement is equivalent to Δ_{off} in this work.

Strictly speaking, our theory should recover the result of Karpitscha *et al.* [32], which states that the contact angle is determined locally by the liquid limit, that is, by Young's equation when we impose the pull-off condition. However, It should be noted for very mall elasto-capillary numbers (stiff solids, small surface tension), the region of validity of Young's equation is too small to be detected in our FEM calculations. Here we check by comparing the pull-off angle predicted by our finite element result and the liquid limit theory. As shown in Fig. A9.4.1 below, for $\omega > 0.5$, the FEM result and the contact angle predicted by Young's equation essentially lie on top of each other, suggesting that our calculation does agree with Karpitscha *et al.*'s results [32].

Finally, it should be noted that, both Karpitscha *et al*. and us assumed that the contact line has no length scale. The molecular length scale (say *d*) of the contact line can introduce a different length scale in the problem, and this new length scale allows elasticity to dominate surface stress in stiff solids – for this case the local contact angle in the limit of small elasto-capillary number is not given by the Young's equation. A discussion of this can be found in C.Y. Hui and A. Jagota [33].

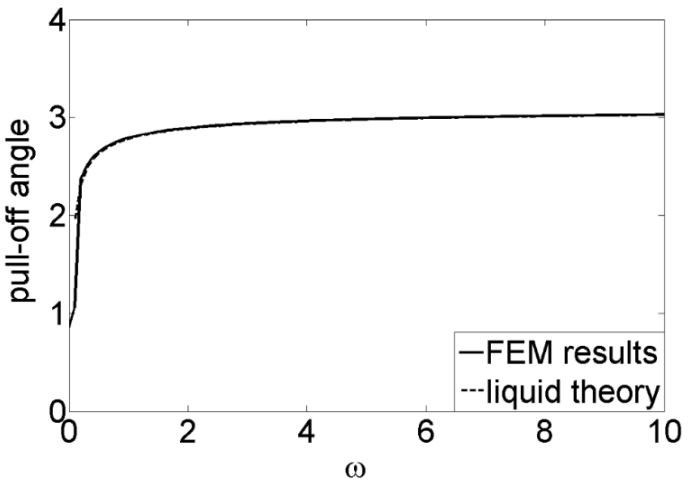

Fig. A9.4.1 Comparison between the contact angle at pull-off predicted by both FEM results and liquid theory when $\overline{W_{ad}}$ is fixed to be 0.05.

REFERENCES

[1] J. Boussinesq, (1885).

[2] K. L. Johnson, *Contact Mechanics* (Cambridge University Press, 1987).

[3] K. L. Johnson, K. Kendall, and A. D. Roberts, Proc. R. Soc. A Math. Phys. Eng. Sci. **324**, 301 (1971).

[4] B. . Derjaguin, V. . Muller, and Y. . Toporov, J. Colloid Interface Sci. **53**, 314 (1975).

[5] D. Maugis, J. Colloid Interface Sci. **150**, 243 (1992).

[6] K. E. Jensen, R. Sarfati, R. W. Style, R. Boltyanskiy, A. Chakrabarti, M. K. Chaudhury, and E. R. Dufresne, Proc. Natl. Acad. Sci. U. S. A. **112**, 14490 (2015).

[7] R. W. Style, C. Hyland, R. Boltyanskiy, J. S. Wettlaufer, and E. R. Dufresne, Nat. Commun. **4**, 2728 (2013).

[8] B. Andreotti, O. Baeumchen, F. Boulogne, K. E. Daniels, E. R. Dufresne, H. Perrin, T. Salez, J. H. Snoeijer, and R. W. Style, 5 (2015).

[9] A. Chakrabarti and M. K. Chaudhury, Langmuir **30**, 4684 (2014).

[10] D. Tabor, J. Colloid Interface Sci. **58**, 2 (1977).

[11] C.-Y. Hui and A. Jagota, Proc. R. Soc. A Math. Phys. Eng. Sci. **470**, 20140085 (2014).

[12] A. Jagota, D. Paretkar, and A. Ghatak, Phys. Rev. E **85**, 51602 (2012).

[13] X. Xu, A. Jagota, S. Peng, D. Luo, M. Wu, and C.-Y. Hui, Langmuir **29**, 8665 (2013).

[14] R. W. Style, A. Jagota, C.-Y. Hui, and E. R. Dufresne, (2016).

[15] T. Liu, A. Jagota, and C.-Y. Hui, Soft Matter (2015).

[16] C.-Y. Hui, T. Liu, T. Salez, E. Raphael, and A. Jagota, Proc. R. Soc. A Math. Phys. Eng. Sci. **471**, 20140727 (2015).

[17] J. M. Long, G. F. Wang, X. Q. Feng, and S. W. Yu, Int. J. Solids Struct. **49**, 1588 (2012).

[18] J. M. Long and G. F. Wang, Mech. Mater. **56**, 65 (2013).

[19] X. Gao, F. Hao, Z. Huang, and D. Fang, Int. J. Solids Struct. **51**, 566 (2014).

[20] X. Gao, F. Hao, D. Fang, and Z. Huang, Int. J. Solids Struct. **50**, 2620 (2013).

[21] C.-Y. Hui and A. Jagota, Langmuir **29**, 11310 (2013).

[22] R. Style, R. Boltyanskiy, Y. Che, J. Wettlaufer, L. A. Wilen, and E. Dufresne, Phys. Rev. Lett. **110**, 66103 (2013).

[23] S. Mora, T. Phou, J. M. Fromental, L. M. Pismen, and Y. Pomeau, Phys. Rev. Lett. **105**, 214301 (2010).

[24] S. Mora, M. Abkarian, H. Tabuteau, and Y. Pomeau, Soft Matter **7**, 10612 (2011).

[25] S. Mora, C. Maurini, T. Phou, J.-M. Fromental, B. Audoly, and Y. Pomeau, Phys. Rev. Lett. **111**, 114301 (2013).

[26] X. Xu, A. Jagota, D. Paretkar, and C.-Y. Hui, Soft Matter **12**, 5121 (2016).

[27] V. R. Krishnan and C.-Y. Hui, Soft Matter **4**, 1909 (2008).

[28] X. Xu, A. Jagota, and C.-Y. Hui, Soft Matter **10**, 4625 (2014).

[29] G. F. Wang and X. R. Niu, Acta Mech. Sin. **31**, 531 (2015).

[30] T. Liu, R. Long, and C.-Y. Hui, Soft Matter **10**, 7723 (2014).

[31] A. Chakrabarti and M. K. Chaudhury, Langmuir **29**, 6926 (2013).

[32] S. Karpitschka, L. van Wijngaarden, and J. H. Snoeijer, 5 (2015).

[33] C.-Y. Hui and A. Jagota, Proc. R. Soc. A Math. Phys. Eng. Sci. **470**, 20140085 (2014).

CHAPTER 10

CONCLUSIONS AND FUTURE WORK

This dissertation starts by considering the coupling of liquid/vapor surface tension with elastic deformation of solid structures. Two experiments are presented to demonstrate the possibilities of deforming the solid structure by liquid capillary force and use the deformation in turn to drive the motion of droplets. Specifically, we show that droplets separated by a thin elastic film can interact with each other and droplets sitting on a film terminated fibrillar structure can move spontaneously and chaotically. Further studies can be carried out to explore their applications especially in the field of micro-fluidics. For example, a device can be developed to manipulate motion of droplets on side of the film using droplets on the other side. More studies on the instabilities caused by size-changing and periodic potential need to be done to completely understand the phenomenon presented in Chapter 3. For example, one may want to change the chemistry of the droplets to see how vaporization affects motion. With better understanding, it may be possible to use this mechanism to produce controlled motion of droplets using, for example, a variation in inter-fibril spacing.

In Chapter 4 and 5, we develop an adhesive contact theory between a rigid cylinder/sphere and a semi-infinite elastic substrate accounting for surface stresses. In these works, we consider normal contact where the role of interfacial shear stresses is not significant. Further studies should include friction and to understand how surface stresses can resist side-way load.

In Chapters 7, 8 and 9, we use large deformation theory to study the effect of solid surface stress. We find a closed-form solution for the pure bending of a finite-thickness plate with strain-dependent surface stress. One limitation in this work is we are not able to consider the surface stress effect near the edge of the plate where there is a singularity in un-deformed curvature. Hence our solution is only valid far away

from the edges. In Chapter 8 and 9, a finite element method that consider both large deformation and solid surface stress effect is used to study a penny-shaped crack problem and a rigid circular punch indentation problem respectively. In both problems, an energy argument is used to calculate the energy release rate. Instead of evaluating the stress and deformation field near the crack tip, only global quantities such as crack volume or load and displacement are required in our calculation. Therefore, the amount of computational effort can be greatly reduced while the accuracy of the calculation can be still guaranteed. In our finite element calculations, we assume the surface stress is isotropic and strain-independent – similar to liquid surface behavior. In the future, the surface element subroutine should be extended to consider the non-isotropic stress component and surface strain-dependency [3]. This improvement has the potential to predict some interesting phenomena that has not been explored before. Furthermore, recent experiments has shown that strain in hydro-gel may lead to phase separation which can cause change in surface properties [4]. A large deformation finite element model with porous material and surface elements may be used to capture this phenomenon.

REFERENCES

[1] N. J. Cira, A. Benusiglio, and M. Prakash, Nature **519**, 446 (2015).
[2] S. Karpitschka, A. Pandey, L. A. Lubbers, J. H. Weijs, L. Botto, S. Das, B. Andreotti, and J. H. Snoeijer, Proc. Natl. Acad. Sci. U. S. A. **113**, 7403 (2016).
[3] Z. P. Huang and J. Wang, Acta Mech. **182**, 195 (2006).
[4] K. E. Jensen, R. Sarfati, R. W. Style, R. Boltyanskiy, A. Chakrabarti, M. K. Chaudhury, and E. R. Dufresne, Proc. Natl. Acad. Sci. U. S. A. **112**, 14490 (2015).